
On the origin and evolution of perturbations in the early universe

by

Rajeev Kumar Jain

Harish-Chandra Research Institute, Allahabad



A Thesis submitted to the
Board of Studies in Physical Science Discipline
in partial fulfillment of the requirements
for the degree of

DOCTOR OF PHILOSOPHY
of
Homi Bhabha National Institute



June 2009

Certificate

This is to certify that the Ph.D. thesis entitled **On the origin and evolution of perturbations in the early universe** submitted by **Rajeev Kumar Jain** for the award of the degree of Doctor of Philosophy is a record of bona fide research work done under my supervision. It is further certified that the thesis represents the independent work done by the candidate and collaboration was necessitated by the nature and scope of the problems dealt with.

Date: June 2009

Dr. L. Sriramkumar
(Thesis Supervisor)

Declaration

This thesis is a presentation of my original research work. Whenever contributions of others are involved, every effort is made to indicate this clearly, with due reference to the literature and acknowledgment of collaborative research and discussions.

The work is original and has not been submitted earlier as a whole or in part for a degree or diploma at this or any other institution or university.

This work was done under the guidance of Dr. L. Sriramkumar, at Harish Chandra Research Institute, Allahabad, India.

Date: June 2009

Rajeev Kumar Jain

(Ph.D. Candidate)

Dedicated to
my parents

Acknowledgment

I would like to thank my supervisor Dr. L. Sriramkumar for his patient guidance, support and encouragement. His immense enthusiasm for doing research is admirable. He made me think harder about the problems than I otherwise would have. I would also like to thank him for his criticism which helped in improving the quality of the thesis.

It is indeed a pleasure to thank Dileep Jatkari, Pravabati Chingangbam and Tarun Souradeep for very fruitful discussions and collaborations during this thesis. I would specially like to thank Pravabati Chingangbam for helping me at various stages of the work.

I would like to thank all my friends and colleagues for their help, support and encouragement.

I would also like to thank all my teachers for teaching me the subject of physics.

I would like to acknowledge the use of the High Performance Scientific Computing facility at the Harish-Chandra Research Institute, Allahabad, India.

Lastly, and most importantly, I wish to thank my father and my brothers for their love, encouragement and relentless support.

Synopsis

The inflationary scenario is possibly the most promising scenario to describe the early stages of the universe. The scenario not only offers an elegant explanation for the extent of homogeneity and isotropy of the background universe, but also provides an attractive causal mechanism to generate the inhomogeneities. The inflationary epoch amplifies the small quantum fluctuations present at the beginning of the epoch into classical perturbations, which in turn leave their imprints as anisotropies in the Cosmic Microwave Background (CMB). These anisotropies in turn act as seeds for the formation of the large scale structures that we observe at the present time as galaxies and clusters of galaxies. The ever-increasing precision of the measurements of the anisotropies in the CMB offer us an unprecedented scope to test the predictions of inflation. The simplest models of inflation wherein the accelerated expansion of the universe is driven by a single, slowly rolling scalar field, generically predict a nearly scale invariant spectrum of primordial perturbations, which seems to be in good agreement with the recent observations of the CMB.

In the conventional picture, the inflationary epoch is expected to be followed by a period of reheating, a regime during which the energy is transferred perturbatively from the inflaton to radiation in order to recover the hot big bang phase of the universe. It used to be believed that reheating may not affect the evolution of the perturbations and, as a result, the post-inflationary dynamics of the perturbations were often ignored when using the CMB observations to constrain the various inflationary models. However, over the past few years, it has been realized that post-inflationary dynamics can alter the amplitude of the curvature perturbations at super-Hubble scales, in particular, when more than one component of matter is present. In such a situation, the resulting effects of the post-inflationary dynamics have to be taken into account when constraining the inflationary models using the CMB observations.

This thesis work is aimed at studying issues related to the origin and evolution of cosmological perturbations during inflation and reheating, and the resulting signatures on the CMB. With this goal in mind, in this thesis, the following problems have been investigated: (i) deviations from slow roll inflation and the amplification or suppression of the curvature perturbations at super-Hubble scales, (ii) generating features in the primordial spectrum so as to lead to a better fit to the data at the low CMB multipoles, (iii) effects of departure from slow roll inflation on the tensor power spectrum and the tensor-to-scalar ratio, (iv) reheating and its effects on the large scale perturbations, and (v) non-gravitating scalar field in the Friedmann universe. We have briefly described these issues below.

It is well known that, in the slow roll inflationary scenario, the amplitude of the curvature perturbations approaches a constant value soon after the modes leave the Hubble radius. However, recently, it was shown that the amplitude of the curvature perturbations induced by the canonical scalar field can grow at super-Hubble scales if there is either a brief transition to fast roll inflation or if inflation is interrupted for some period of time. We extend the earlier analysis to the case of a non-canonical scalar field described by the tachyonic action. With the help of a specific example, we show that, if there is a period of deviation from slow roll inflation, then the asymptotic amplitude of the modes that leave the Hubble radius just before the deviation are enhanced when compared to their value at Hubble exit. While modes that leave well before the deviation remain unaffected, it is found that there exists an intermediate range of modes whose amplitudes are actually *suppressed* at super-Hubble scales. We also illustrate as to how the growth of the intrinsic entropy perturbations (i.e. the non-adiabatic pressure perturbation associated with the tachyon) during the fast roll regime proves to be responsible for the change in the amplitude of the curvature perturbations at super-Hubble scales. Furthermore, following the earlier analysis for the canonical scalar field, we show that the power spectrum evaluated in the long wavelength approximation matches the exact power spectrum obtained numerically very well.

As we have mentioned above, a nearly scale invariant primordial spectrum fits the recent CMB data rather well. However, there exist a few points at the lower multipoles which lie outside the cosmic variance. Even as the debate about the statistical significance of the outliers in the CMB data continues, a variety of scenarios have been proposed to explain the possible physical reasons behind these outliers. In particular, there has been an inter-

est in exploring whether spectra with features that are generated by deviations from slow roll inflation lead to a better fit to the data. Motivated by this possibility, we investigate inflationary scenarios driven by a class of potentials which are similar in form to those that arise in certain minimal supersymmetric extensions of the standard model. We find that these potentials allow a brief period of departure from inflation sandwiched between two stages of slow roll inflation, a scenario which we refer to as punctuated inflation. We show that such a background behavior leads to a step like feature in the scalar power spectrum. We set the scales such that the drop in the power spectrum occurs at a length scale that roughly corresponds to the Hubble radius today—a feature that seems necessary to explain the lower power observed in the quadrupole moment of the CMB anisotropies. We perform a Markov Chain Monte Carlo analysis to determine the values of the model parameters that provide the best fit to the recent WMAP 5-year data for the CMB angular power spectrum. We find that an inflationary spectrum with a suppression of power at large scales that we obtain leads to a much better fit (with just one extra parameter, χ^2_{eff} improves by 6.62) of the observed data when compared to the best fit reference Λ CDM model with a featureless, power law, primordial spectrum.

Almost all the efforts in the literature that have focused on suppressing the scalar power spectrum on large scales (so as to lead to a better fit at the low CMB multipoles) seem to have overlooked the corresponding effects on the tensors. With the help of specific examples from the canonical scalar field as well as tachyonic models, we illustrate that, in punctuated inflation, a drop in the scalar power generically leads to a rise in the tensor power. The increase in the amplitude of the tensor spectrum alongwith a drop in the scalar spectrum at large scales results in a dramatic rise in the tensor-to-scalar ratio r at these scales. Interestingly, we find that r actually exceeds well beyond unity over a small range of scales. We show that the rise in r on large scales translates to a rapid increase in the angular power spectrum, C_{ℓ}^{BB} , of the B-mode polarization of the CMB at the low multipoles. We also discuss the potential observational implications of these results.

An important assumption that is made when comparing the predictions of the inflationary models with the CMB observations is that the amplitude of the curvature perturbations, say, at Hubble exit—if no deviations from slow roll arise or, in general, at the end of inflation—is the same as their amplitude when the modes re-enter the Hubble radius at later epochs.

But, as we mentioned, of late, it has been realized that the amplitude of the curvature perturbations can be affected post-inflation due to the presence of the isocurvature perturbations when multiple fields and fluids are present. In such a situation, evidently, the spectrum of curvature perturbations evaluated at the end of inflation will not be the same as at the early stages of the radiation dominated epoch. Therefore, in such scenarios, the post-inflationary effects on the curvature perturbations have to be included when comparing the predictions with the observed data.

With the aim of understanding possible post-inflationary effects on the curvature perturbations, we investigate the problem of perturbative reheating and its effects on the evolution of the curvature perturbations in tachyonic inflationary models. We derive the equations governing the evolution of the scalar perturbations for a system consisting of a tachyon and a perfect fluid. Assuming the perfect fluid to be radiation, we solve the coupled equations for the system numerically and study the evolution of the perturbations from the sub-Hubble to the super-Hubble scales. In particular, we analyze the effects of the transition from tachyon driven inflation to the radiation dominated epoch on the evolution of the large scale curvature and non-adiabatic pressure perturbations. We consider two different potentials to describe the tachyon and study the effects of two possible types of decay of the tachyon into radiation. We plot the spectrum of curvature perturbations at the end of inflation as well as at the early stages of the radiation dominated epoch. We find that reheating does not affect the amplitude of the curvature perturbations in any of these cases. These results corroborate similar conclusions that have been arrived at earlier based on the study of the evolution of the perturbations in the super-Hubble limit. We illustrate that, before the transition to the radiation dominated epoch, the relative non-adiabatic pressure perturbation between the tachyon and radiation decays in a fashion very similar to that of the intrinsic entropy perturbation associated with the tachyon. Moreover, we show that, after the transition, the relative non-adiabatic pressure perturbation dies down extremely rapidly during the early stages of the radiation dominated epoch. It is these behavior which ensure that the amplitude of the curvature perturbations remain unaffected during reheating. We also discuss the corresponding results for the case of the canonical scalar field.

We have discussed above as to how quantum fluctuations during the inflationary epoch can be responsible for the generation of the inhomogeneities in the early universe. Apart

from the inflationary scenario, phase transitions that result in the formation of topological defects have been considered as an alternative source of the perturbations. With the aim of providing another possible mechanism for the origin of the perturbations, we consider the behavior of an inhomogeneous, interacting, scalar field that is coupled non-minimally to gravity in the Friedmann background. We show that for a specific choice of the interaction terms, the stress-energy tensor of the scalar field vanishes and, as a result, the scalar field does not gravitate. The naive space dependent solution to the equations of motion results in a singular field profile. We carefully analyze the stress-energy tensor for such a solution and show that the singularity of the solution gives a subtle contribution to the stress-energy tensor. The space dependent solution therefore is, actually, *not* non-gravitating. Our conclusion turns out to be applicable to other spacetime dependent non-gravitating solutions as well. We study the hybrid inflation scenario in this model when a purely time dependent non-gravitating field is coupled to another scalar field.

We conclude the thesis with a discussion on a couple of different avenues for further investigations. Two directions that we believe require immediate attention are: (i) the generation of large non-Gaussianities during inflation, and (ii) analyzing the effects of post-inflationary dynamics on the evolution of the perturbations in a broader class of scenarios. We have outlined these two issues below.

It is well known that models of inflation driven by single, slowly rolling, canonical scalar fields generically lead to a rather small amount of primordial non-Gaussianity. However, recent analysis of the CMB data seems to indicate a fairly large amount of non-Gaussianity. Theoretically, there seems to be only two possibilities to account for a large non-Gaussianity. We can consider non-canonical scalar fields such as the ones encountered in D-brane inflationary models, which seem to naturally produce sizeable non-Gaussianities. However, if one is restricted to consider only canonical scalar fields, there seems to be no option but to allow for features in the scalar power spectrum, which have been shown to lead to reasonably large non-Gaussianities. Under these conditions, it becomes imperative to evaluate the amount of non-Gaussianity generated in scenarios such as punctuated inflation. With more accurate measurements of the CMB anisotropies by forthcoming missions, non-Gaussianity can soon become a powerful tool to constrain inflationary models.

We have discussed as to how the amplitude of the curvature perturbations remains unaf-

fectured during reheating if the decay rate is either a constant, or a function of the inflaton. The warm inflationary scenario is an interesting possibility, wherein the decay rate, in addition to depending on the inflaton, can also depend on the temperature. It will be interesting to explore the effects of the transfer of the energy from the inflaton to radiation on the perturbations in these scenarios. Needless to add, in addition to such specific possibilities that can be considered, a comprehensive analysis of the effects of post-inflationary dynamics on the perturbations in a wider class of scenarios is called for.

List of publications and preprints

1. **Rajeev Kumar Jain**, P. Chingangbam and L. Sriramkumar, *On the evolution of tachyonic perturbations at super-Hubble scales*, JCAP **0710**, 003 (2007).
2. Nabamita Banerjee, **Rajeev Kumar Jain** and Dileep P. Jatkar, *Non-gravitating scalar field in the FRW background*, Gen. Rel. Grav. **40**, 93 (2008).
3. **Rajeev Kumar Jain**, P. Chingangbam, Jinn-Ouk Gong, L. Sriramkumar and Tarun Souradeep, *Punctuated inflation and the low CMB multipoles*, JCAP **0901**, 009 (2009).
4. **Rajeev Kumar Jain**, P. Chingangbam and L. Sriramkumar, *Reheating in tachyonic inflationary models: Effects on the large scale curvature perturbations*, arXiv:0902.1067 [astro-ph.CO].
5. **Rajeev Kumar Jain**, P. Chingangbam, L. Sriramkumar and Tarun Souradeep, *The tensor-to-scalar ratio in punctuated inflation*, arXiv:0904.2518 [astro-ph.CO].

Contents

1	Introduction and scope	1
1.1	The hot big bang model	1
1.2	The Friedmann line element	5
1.3	Observed values of the background cosmological parameters	6
1.4	Shortcomings of the hot big bang model	8
1.5	The inflationary paradigm	10
1.5.1	Driving inflation with scalar fields	14
1.5.2	Slow roll inflation	16
1.5.3	Inflationary models and their comparison with the observations	17
1.6	Reheating the universe after inflation	20
1.7	Scope of the thesis	22
1.7.1	Beyond slow roll inflation	22
1.7.2	Post-inflationary dynamics and its effects on the perturbations	24
1.8	Conventions and notations	25
2	Effects of deviations from slow roll inflation	27
2.1	Motivation	27
2.2	Essential cosmological perturbation theory	29
2.2.1	The background equations	29
2.2.2	The scalar perturbations	30
2.2.3	The tensor perturbations	37
2.2.4	The Bunch-Davies initial conditions	38
2.3	The scalar and tensor power spectra in slow roll inflation	39
2.4	The curvature perturbations induced by the tachyon	42

CONTENTS

2.5	Evolution of the curvature perturbations at super-Hubble scales	44
2.5.1	A specific example	45
2.6	Entropy perturbations as the source of evolution	49
2.7	The long wavelength approximation	52
2.8	Non-trivial evolution of the curvature perturbations	56
2.8.1	Example I	57
2.8.2	Example II	58
2.9	Summary and discussion	62
3	Punctuated inflation and the low CMB multipoles	65
3.1	Motivation	65
3.2	The inflaton potential and the background dynamics	68
3.3	The scalar power spectrum	71
3.3.1	Physical ‘expectations’	71
3.3.2	Numerical results	73
3.4	Comparison with the recent WMAP 5-year data	74
3.4.1	The parameters in our model and the priors we work with	75
3.4.2	The best fit values and the joint constraints	77
3.4.3	The CMB angular power spectra for the best fit values	78
3.5	Summary and discussion	81
3.5.1	Summary	82
3.5.2	Discussion	83
4	The tensor-to-scalar ratio in punctuated inflation	85
4.1	Introduction and motivation	85
4.2	Characteristics of the scalar and the tensor perturbation spectra in punctuated inflation	88
4.3	Punctuated inflation with canonical scalar fields	89
4.3.1	The model motivated by MSSM	90
4.3.2	A hybrid inflation model	91
4.4	An example of tachyonic punctuated inflation	94
4.5	The effects on the B-modes of the CMB	96

4.6	The evolution of the perturbations for a mode with $r > 1$	99
4.7	Conclusions	99
5	Reheating and its effects on large scale perturbations	103
5.1	Inflationary and post-inflationary effects on the perturbations	103
5.2	Transition from tachyon driven inflation to the radiation era	107
5.2.1	Background equations in the presence of interacting components . . .	107
5.2.2	The case of the tachyon and a perfect fluid	108
5.2.3	Tachyonic inflationary models, different possible Γ and reheating . . .	109
5.3	Equations of motion governing the scalar perturbations	111
5.3.1	First order Einstein equations	113
5.3.2	Equations of motion describing the perturbed matter components . .	114
5.3.3	The coupled perturbation variables and the initial conditions	115
5.4	Effects of reheating on the scalar power spectrum	118
5.4.1	Evolution of the curvature perturbations and the scalar power spectrum	118
5.4.2	Evolution of the entropy perturbations	120
5.5	The case of the canonical scalar field and a perfect fluid	125
5.5.1	Background equations	125
5.5.2	Equations governing the scalar perturbations	127
5.5.3	Evolution of the curvature perturbations and the scalar power spectrum	129
5.5.4	Evolution of the entropy perturbations	129
5.6	Summary and discussion	131
6	Non-gravitating scalar field in the Friedmann universe	135
6.1	Introduction	135
6.2	Non-gravitating scalar field in various backgrounds	137
6.2.1	The Minkowski background	139
6.2.2	The Friedmann background	140
6.2.3	The AdS background	141
6.3	The regularized stress-energy tensor	143
6.3.1	The Minkowski background	144
6.3.2	The Friedmann background	145

CONTENTS

6.4	The hybrid inflation model	146
6.4.1	Conformal transformation	148
6.5	Discussion and summary	149
7	Summary and outlook	151
7.1	Summary	151
7.2	Outlook	153

List of Tables

3.1	The priors on the various parameters describing the reference Λ CDM model with a power law primordial spectrum and the $n = 3$ MSSM case	77
3.2	The mean values and the $1\text{-}\sigma$ constraints on the various parameters that describe the reference model and the $n = 3$ MSSM case.	81
5.1	Achieving inflation: The values for the parameters of the tachyon potential and the initial conditions for the inflaton that we work with.	110
5.2	Achieving inflation <i>and</i> reheating: The values of the initial energy density of radiation and the parameters describing the decay rates that we work with, when the interaction of the tachyon with radiation is taken into account. . . .	111

List of Figures

1.1	The sky maps from the observations by COBE and WMAP.	4
1.2	The evolution of the physical wavelengths and the Hubble radius d_H as a function of the scale factor a on a logarithmic plot during the radiation and the matter dominated epochs.	9
1.3	The evolution of the physical wavelengths and the Hubble radius d_H as a function of the scale factor a on a logarithmic plot during inflation and the radiation dominated epoch.	12
1.4	The WMAP 5-year data for the CMB angular power spectrum and the theoretical curve for the best fit, concordant Λ CDM cosmological model with a power law primordial spectrum.	19
1.5	The two-dimensional marginalized constraints with $1-\sigma$ and $2-\sigma$ confidence levels on the scalar spectral index n_s , and the tensor-to-scalar ratio r from WMAP 5-year data and WMAP+BAO+Supernovae datasets.	20
2.1	The evolution of the quantity $(z'/z\mathcal{H})$ as a function of the number of e -folds N for a tachyonic model exhibiting a period of deviation from slow roll.	47
2.2	The evolution of the amplitude of the curvature perturbation \mathcal{R}_k as a function of the number of e -folds N for the modes with wavenumbers $k = 0.03 \text{ Mpc}^{-1}$ and $k = 0.1 \text{ Mpc}^{-1}$ in the specific tachyonic model.	48
2.3	The evolution of the amplitude of the entropy perturbation S_k as a function of the number of e -folds N for the two modes $k = 0.03 \text{ Mpc}^{-1}$ and $k = 0.1 \text{ Mpc}^{-1}$ in the tachyonic model.	51
2.4	The evolution of the effective speed of sound c_s^2 as a function of the number of e -folds N	54

LIST OF FIGURES

2.5	The evolution of the quantity z^2 as a function of the number of e -folds N . . .	55
2.6	Plots of the scalar power spectrum that has been evaluated at the end of inflation through the numerical integration of the modes as well as the spectrum that has been obtained using the long wavelength approximation.	56
2.7	The evolution of the amplitude of the curvature perturbation \mathcal{R}_k as a function of the number of e -folds N for the mode with wavenumber $k = 0.01 \text{ Mpc}^{-1}$. .	59
2.8	The spectrum of the curvature perturbations $\mathcal{P}_s(k)$ as a function of the wavenumber k	60
2.9	The evolution of the amplitude of the curvature perturbation \mathcal{R}_k as a function of the number of e -folds N for the mode with wavenumber $k = 0.01 \text{ Mpc}^{-1}$. .	61
2.10	The spectrum of the curvature perturbations $\mathcal{P}_s(k)$ as a function of the wavenumber k	62
3.1	Illustration of the inflaton potential for the $n = 3$ MSSM case.	69
3.2	The phase portrait of the scalar field in the case of the $n = 3$ MSSM model. . .	70
3.3	The background quantity $(z'/z \mathcal{H})$ as a function of the number of e -folds N , for the cases of $n = 3$ and $n = 4$	74
3.4	The evolution of the scalar field in the plane of the first two HSR parameters ϵ_H and δ_H in the case of $n = 3$	75
3.5	The scalar power spectrum $\mathcal{P}_s(k)$ as a function of the wavenumber k for the cases of $n = 3$ and $n = 4$	76
3.6	The one-dimensional mean and marginalized likelihood curves for all the input parameters (and the derived parameter H_0) in the $n = 3$ case.	79
3.7	The $1\text{-}\sigma$ and $2\text{-}\sigma$ two-dimensional joint constraints on the different input parameters (and the derived parameter H_0) in the $n = 3$ case.	80
3.8	The CMB angular power spectrum for the best fit values of the $n = 3$ MSSM case and the best fit power law, reference model.	82
4.1	The scalar power spectrum $\mathcal{P}_s(k)$ and the tensor power spectrum $\mathcal{P}_T(k)$ as a function of the wavenumber k for the $n = 3$ and $n = 4$ MSSM cases.	92
4.2	The tensor-to-scalar ratio $r(k)$ for the cases of $n = 3$ and $n = 4$ as a function of the wavenumber k	93

4.3	The scalar power spectrum $\mathcal{P}_s(k)$, the tensor power spectrum $\mathcal{P}_t(k)$ and the corresponding tensor-to-scalar ratio $r(k)$ as a function of the wavenumber k for the hybrid inflation model.	95
4.4	The scalar and the tensor power spectra and the corresponding tensor-to-scalar ratio for the case of the tachyonic punctuated inflationary model. . . .	97
4.5	The B-mode CMB angular power spectrum C_ℓ^{BB} as a function of the multipole ℓ for the best fit values of the $n = 3$ and $n = 4$ MSSM models.	98
4.6	The evolution of the amplitudes of the curvature perturbation \mathcal{R}_k and the tensor perturbation \mathcal{U}_k as a function of the number of e -folds N for a mode with the tensor-to-scalar ratio $r > 1$	100
5.1	In the left column, the evolution of the quantities Ω_T and Ω_γ as a function of the number of e -folds N for the tachyon potential $V_1(T)$ and the two cases of Γ , viz. $\Gamma_1 = \text{constant}$ and $\Gamma_2 = \Gamma(T)$. In the right column, the evolution of the first HSR parameter ϵ_H and the equation of state parameter of the entire system w as a function of the number of e -folds N	112
5.2	In the left column, the evolution of the amplitudes of the curvature perturbations associated with the tachyon $ \mathcal{R}_T $ and radiation $ \mathcal{R}_\gamma $ as well as the weighted sum of the two $ \mathcal{R} $ as a function of the number of e -folds N for the two possible types of Γ . In the right column, the scalar power spectrum towards the end of inflation and soon after complete reheating has been achieved for the two cases of Γ	121
5.3	The evolution of the amplitudes of the Bardeen potential $ \Phi $, the intrinsic entropy perturbation $ \delta p_T^{\text{NA}} $ and the isocurvature perturbation $ \delta p_{T\gamma}^{\text{NA}} $ as a function of the number of e -folds N for the two types of Γ	124
5.4	In the left column, the evolution of the quantities Ω_ϕ and Ω_γ as a function of the number of e -folds N for the two types of Γ in the case of the popular chaotic inflation model. In the right column, the evolution of the first HSR parameter ϵ_H and the equation of state parameter w of the entire system as a function of the number of e -folds N	126

LIST OF FIGURES

- 5.5 In the left column, the evolution of the amplitudes of the curvature perturbations associated with the scalar field $|\mathcal{R}_\phi|$, radiation $|\mathcal{R}_\gamma|$ and the total curvature perturbation of the entire system $|\mathcal{R}|$ as a function of the number of e -folds N for the two types of the decay rate. In the right column, the scalar power spectrum before and after the transition. 130
- 5.6 The evolution of the amplitudes of the Bardeen potential $|\Phi|$, the intrinsic entropy perturbation $|\delta p_\phi^{\text{NA}}|$ and the isocurvature perturbation $|\delta p_{\phi\gamma}^{\text{NA}}|$ as a function of the number of e -folds N for the two types of Γ 132
- 6.1 The generic form of the potential for the non-gravitating field in the Friedmann background, and the square of the classical solution at a fixed time. . . 142

Chapter 1

Introduction and scope

Cosmology is certainly one of the most exciting disciplines in research amongst all the areas of physical sciences. It endeavors to use scientific methods to provide answers to the fundamental questions about the origin, the content, the evolution and the ultimate fate of the entire universe. Like any other field of science, cosmology involves the formulation of theories or hypotheses about the universe which lead to specific predictions for phenomena that can be tested with observations. Depending on the outcome of the observations, the theories need to be abandoned, revised or extended to accommodate the conclusions from the data. Cosmology is indeed the interlink between the observation and the theory: the theory should be based on the results of the observations, however, the proper interpretation of the observations requires the correct theory. With extremely accurate data available from the observations, over the last couple of decades, cosmology has grown into a precision science.

1.1 The hot big bang model

The prevailing theory about the origin and the evolution of our universe is the so-called big bang model¹. Theoretically, the model rests on two key ideas that date back to the early half of the twentieth century: general theory of relativity and the cosmological principle. According to the general theory of relativity, it is no longer sufficient to describe gravity

¹As used by the cosmologists, the term 'big bang' broadly refers to the notion that the universe has expanded from primordial dense initial conditions at some finite time in the past, and continues to expand to the present time. Often, big bang is also used to refer to the point in time, early in the universe, where the matter densities and the spacetime curvature diverge. Actually, the term reflects our ignorance than knowledge! Close to this point in time, general theory of relativity is expected to break down, and quantum gravitational effects are expected to take over.

by a Newtonian potential. Rather, gravitation is supposed to be a distortion of space and time itself, and the theory essentially establishes the connection between the geometry of spacetime and the distribution of matter. The cosmological principle states that the matter content in the universe is homogeneous and isotropic when averaged over sufficiently large scales. These two ideas form the theoretical basis for the big bang cosmology, and they lead to very specific predictions for the observable properties of the universe. So far, all the observational evidence that have been gathered provide overwhelming support for the big bang model. It is now regarded as the best available theory for the origin and the evolution of the cosmos, and virtually all the theoretical work in cosmology involves extensions and refinements of the big bang theory. The theory is indeed so successful in explaining the results from various observations that it is considered an essential ingredient of the current standard model of cosmology (for a detailed discussion, see any of the following texts [1, 2, 3, 4, 5, 6, 7]).

The success of the big bang model rests on three significant observational pillars. The first of these observations essentially indicates that the universe is expanding. It was discovered that most of the galaxies outside our own Milky Way were continuously receding from us [8]. Moreover, the velocities of these galaxies turn out to be proportional to their distances. The more distant a galaxy, the faster it was moving away which is, nothing but, a result of the expansion of the universe. The Hubble diagram is a plot of the recessional velocities, say, v of these galaxies with respect to their proper distances, say, d . The linear relationship is known as the Hubble's law, and is usually written as

$$v = H_0 d, \quad (1.1)$$

where H_0 is the Hubble constant which determines the present rate of expansion of the universe. Its value is usually parametrized in terms of the dimensionless quantity h as follows:

$$h = H_0 / (100 \text{ km s}^{-1} \text{ Mpc}^{-1}). \quad (1.2)$$

Direct observations indicate that the value of h is given by [9]

$$h = 0.72 \pm 0.1 \quad (1.3)$$

The Hubble's law is considered a fundamental relation, while the Hubble diagram still remains one of the most direct evidence we have that the universe is expanding.

The second most important observation is the existence of an exceedingly isotropic (to about one part in 10^5) background radiation of relic photons, known as the Cosmic Microwave Background radiation (CMB). Though the existence of the CMB was predicted quite a while back, it was first accidentally discovered somewhat later [10]. The CMB has an almost perfect black body spectrum, and it has a temperature of 2.725 K today [11]. Since the energy density of radiation falls faster with the expansion than matter, the above two observations immediately suggest that the universe was radiation dominated at early times², and the CMB reflects the fact that matter and radiation were in thermal equilibrium during these early stages. The transition to the more recent matter dominated epoch occurs when the radiation density falls sufficiently low such that the photons cease to interact with matter, and the CMB is nothing but the relic radiation which is reaching us from this epoch of decoupling. In the beginning of the previous decade, for the first time, the Cosmic Background Explorer satellite (COBE) detected tiny fluctuations (anisotropies) in the CMB [12, 13, 14, 15]. More recently—in the early part of the present decade—the Wilkinson Microwave Anisotropy Probe satellite (WMAP) provided more accurate measurements of these anisotropies [16, 17, 18]. In Fig. 1.1, we have displayed the sky maps of the anisotropies in the CMB as seen by COBE and WMAP. The pattern of these fluctuations offer us a direct snapshot of the universe at the epoch of decoupling. As we shall discuss, the structure of the observed fluctuations provide a compelling ground in favor of the hot big bang theory [19, 20, 21, 22].

Another significant observation in support of the big bang model is the primordial abundance of the light elements which are in good agreement with the predictions coming from the theory of Big Bang Nucleosynthesis (BBN) (for a recent review, see Ref. [23]). The process of BBN, which begins about three minutes after the big bang, is considered to be responsible for the formation of the light elements during the early, hot radiation dominated phase of the universe. The abundances of all the light elements depend on a single parameter, viz. the ratio of the number density of baryons to the photons in the universe. Since this ratio does not change with time, its value allows us to determine the baryon density at a given epoch. The measured abundances of the light elements agree reasonably well with those predicted from the single value of this ratio. The observations of the light elements place a

²This is the reason behind the often used adjective ‘hot’ to the big bang model.

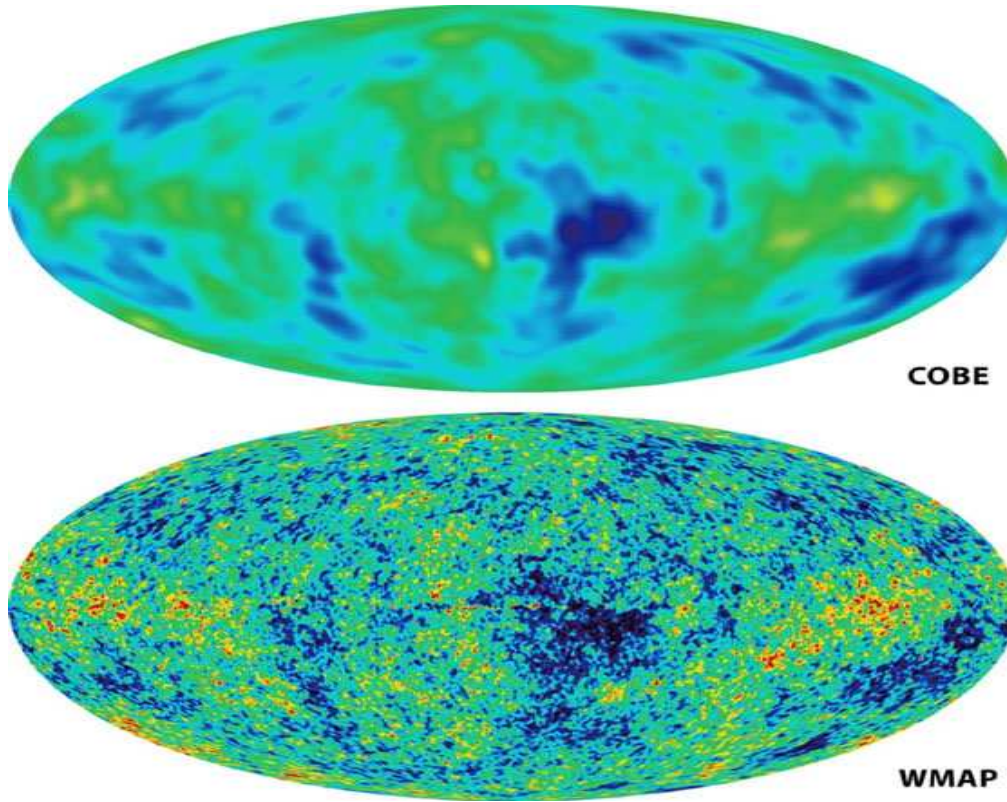


Figure 1.1: The sky maps as obtained from the observations by COBE (on top) and the WMAP 5-year data (at the bottom). The precise measurements of WMAP provide more information about the structure of the CMB anisotropies as compared to COBE.

stringent constraint on the baryon density today (see, for instance, Ref. [24]). The theory of BBN is considered one of the cornerstones of modern cosmology, and the reasonably good agreement between the theoretical predictions and the measurements is regarded as a strong evidence for the hot big bang model.

These three observational signatures—viz. the Hubble’s law, the perfect blackbody spectrum alongwith the detailed structure of the anisotropies in the CMB, and the primordial abundance of the light elements—firmly support the hot big bang model.

1.2 The Friedmann line element

As we mentioned earlier, the standard hot big bang model is based upon the cosmological principle which requires the universe to be homogeneous and isotropic on sufficiently large scales (see, for instance, Ref. [25]). The general relativistic description of a homogeneous and isotropic universe is characterized by the Friedmann line element, and is given by [26, 27, 28, 29, 30, 31]

$$ds^2 = dt^2 - a^2(t) \left[\frac{dr^2}{(1 - \mathcal{K} r^2)} + r^2 (d\theta^2 + \sin^2 \theta d\phi^2) \right], \quad (1.4)$$

where t is the cosmic time and $a(t)$ denotes the scale factor. The constant \mathcal{K} represents the spatial curvature which describes the spatial geometry of the universe. The universe is spatially flat if $\mathcal{K} = 0$, finite or closed if $\mathcal{K} > 0$, and infinite or open if $\mathcal{K} < 0$. Apart from the cosmic time, another time variable which we shall frequently use is known as the conformal time η , and is defined as

$$\eta = \int \frac{dt}{a(t)}. \quad (1.5)$$

In terms of the conformal time coordinate, the Friedmann line element (1.4) reduces to

$$ds^2 = a^2(\eta) \left[d\eta^2 - \frac{dr^2}{(1 - \mathcal{K} r^2)} - r^2 (d\theta^2 + \sin^2 \theta d\phi^2) \right]. \quad (1.6)$$

Let ρ and p denote the energy density and the pressure of, say, a matter field or a perfect fluid that is driving the expansion of the universe. Then, the Einstein's equations corresponding to the Friedmann line element (1.4) lead to the following two Friedmann equations describing the evolution of the scale factor $a(t)$:

$$H^2 = \left(\frac{8\pi G}{3} \right) \rho - \frac{\mathcal{K}}{a^2}, \quad (1.7a)$$

$$\frac{\ddot{a}}{a} = - \left(\frac{4\pi G}{3} \right) (\rho + 3p). \quad (1.7b)$$

where $H = (\dot{a}/a)$ is the Hubble parameter which indicates the rate of expansion of the universe at any epoch, and the overdots denote derivative with respect to the cosmic time. Upon combining the above Friedmann equations, we can arrive at the following equation for the energy density of the matter field or fluid

$$\dot{\rho} + 3H(\rho + p) = 0, \quad (1.8)$$

an equation that is also referred to as the continuity equation. The evolution of the universe depends on the equation of state parameter w which is defined as $w = (p/\rho)$. For example, the radiation has the equation of state parameter $w = (1/3)$, while the non-relativistic matter (i.e. dust) has $w = 0$. It may be noted that the continuity equation (1.8) also follows from the conservation of the stress-energy tensor of the perfect fluid.

The first Friedmann equation (1.7a) can be rewritten as

$$\Omega - 1 = \frac{\mathcal{K}}{a^2 H^2}, \quad (1.9)$$

where the dimensionless density parameter Ω is defined as the ratio of the energy density to the critical density, i.e.

$$\Omega = \frac{\rho}{\rho_c}, \quad (1.10)$$

with ρ_c being the critical density which is given by

$$\rho_c = \frac{3 H^2}{8 \pi G} \quad (1.11)$$

The critical density is a particular value of the energy density for which the universe is spatially flat (i.e. $\Omega = 1$). The value of the density parameter Ω determines the sign of the spatial curvature \mathcal{K} . If the energy density of the matter content of the universe is less than the critical density (so that $\Omega < 1$), the universe is open and infinite. On the other hand, if the matter density is greater than the critical density (i.e. when $\Omega > 1$), the universe is closed and finite.

1.3 The background cosmological parameters and the observed values

Observations indicate that the present value of Ω is within a few percent of unity. (We should emphasize that, hereafter, Ω shall always refer to the density parameter evaluated *today*.) The strongest constraint on Ω comes from the observations of the anisotropies in the CMB. The recent WMAP observations constrain the value of Ω to be [20]

$$\Omega = 1.099 \pm 0.085, \quad (1.12)$$

which, in turn, indicates that the universe is extremely close to being spatially flat.

1.3. OBSERVED VALUES OF THE BACKGROUND COSMOLOGICAL PARAMETERS

In the previous section, we had discussed two forms of matter, viz. radiation and baryons. While radiation is composed of massless (and nearly massless) relativistic particles which includes photons present in the form of CMB and neutrinos, the term baryons refers to ordinary matter that makes up the atoms which are the building blocks of planets, stars, galaxies, and indeed all of us. The temperature of the CMB determines the density of radiation in the universe, and the corresponding density parameter, say, Ω_{r} , evaluated today can be expressed as [6]

$$\Omega_{\text{r}} h^2 \simeq 2.49 \times 10^{-5}. \quad (1.13)$$

The observed abundances of the light elements provide a direct constraint on the baryon density today, and the density parameter associated with baryons is found to be [23]

$$\Omega_{\text{b}} h^2 = 0.021 \pm 0.001. \quad (1.14)$$

Importantly, such a value for the baryon density is in good agreement with the results obtained from the structure of the fluctuations recently observed in the CMB [24].

In addition to radiation and baryonic matter, various observations indicate that the universe consists of two other types of matter: Cold Dark Matter (CDM) and dark energy. By CDM, one refers to non-relativistic matter that interacts only weakly with the ordinary baryonic matter. It is also assumed to be dissipationless and collisionless. The recent CMB observations seem to point towards the following density parameter for CDM [20]

$$\Omega_{\text{c}} h^2 = 0.1099 \pm 0.0062. \quad (1.15)$$

The dark energy is a truly bizarre form of matter that is characterized by negative pressure. The existence of dark energy seems inevitable if we are to explain the current, observed acceleration of the universe. In fact, dark energy seems to be the most dominant component of the universe today. Amongst various available candidates to account for dark energy, the cosmological constant Λ with $w = -1$ seems to be the most promising candidate. Such a Λ CDM model, often referred to as the concordance model, is in very good agreement with the observations. The recent observations of Type Ia supernovae constrain the density of the cosmological constant Λ to be [32]

$$\Omega_{\Lambda} = 0.713^{+0.027}_{-0.029}. \quad (1.16)$$

It should also be emphasized that this value is consistent with the earlier surveys of the supernovae observations as well as with the recent data from WMAP and the measurements of the Baryon Acoustic Oscillations (BAO) [20, 21].

1.4 Shortcomings of the hot big bang model

Despite the remarkable success of the hot big bang model in explaining the results from various observations and many other properties of our universe, it was soon realized that the theory has some serious shortcomings. It was unable to provide a satisfactory explanation to a few significant cosmological puzzles. These puzzles include the horizon problem, the flatness or the curvature problem, the origin of primordial density fluctuations, the density of unwanted relics, to name a few (for a detailed discussion in this regard, see, for example, any of the following texts [1, 2, 3]).

To start with, the horizon problem is the problem of determining why the universe appears statistically homogeneous and isotropic in accordance with the cosmological principle. In other words, why is the temperature of the CMB seen in the opposite directions of the sky almost the same? In the standard hot big bang cosmology, if one assumes that the universe was radiation dominated all the way from the time of big bang until decoupling, these opposite directions in the sky would have been much larger than the Hubble radius³, say, $d_H = H^{-1} = (\dot{a}/a)^{-1}$ at the time of decoupling. Therefore, these antipodal points would not have been in causal contact before this epoch and, hence, there is no way to establish thermal equilibrium over such a length scale. On the other hand, observations indicate that the CMB has virtually the same temperature (to about one part in 10^5) in all directions of the sky. The horizon problem is, therefore, the lack of an explanation as to why such a large number of (about 10^6) causally disconnected volumes had nearly the same temperature at the time of decoupling. As shown in Fig. 1.2, there is another way of stating the horizon problem. The physical wavelengths associated with the perturbations, say, λ_p , always grow as the scale factor, i.e. $\lambda_p \propto a$. Whereas, during the radiation and the matter dominated

³Actually, it is the particle horizon that represents the size of the observable universe at any given epoch. It indicates the distance that light could have traveled from the big bang up to the given time. We shall be considering the Hubble radius rather than the particle horizon, since, in most of the cases, the Hubble radius is equivalent to the particle horizon up to a constant multiplicative factor. Moreover, being a local quantity, the Hubble radius often proves to be more handy to deal with than the horizon.

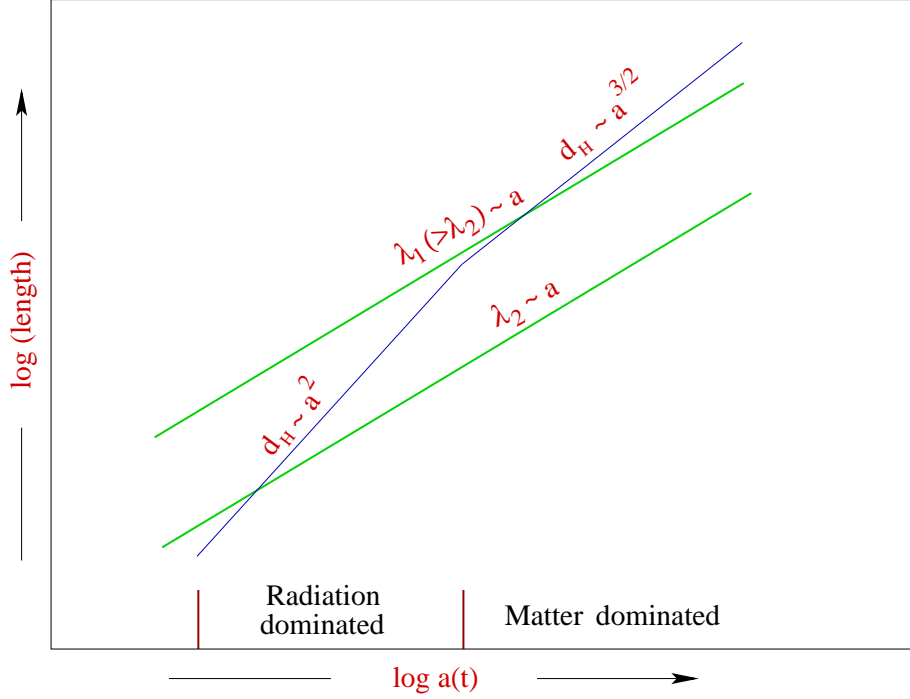


Figure 1.2: The evolution of the physical wavelengths λ_1 and λ_2 ($\lambda_p = a/k$) and the Hubble radius d_H have been plotted as a function of the scale factor a on a logarithmic plot during the radiation and the matter dominated epochs. In the standard hot big bang cosmology, a given length scale crosses the Hubble radius only once, and therefore, if one goes back in time, all the modes are outside the Hubble radius and, hence, not in causal contact at very early times. Nevertheless, the temperature of the CMB observed in the opposite directions of the sky is almost the same.

epochs, the Hubble radius, viz. d_H , behaves as a^2 and $a^{3/2}$ respectively. These behavior indicate that, during the radiation and the matter dominated epochs, the physical wavelength grows *faster* than the Hubble radius *as we go back in time* [1]. In other words, in the hot big bang model, the primordial perturbations have to be correlated at length scales much larger than the Hubble radius in order to result in the anisotropies that we observe in the CMB.

Another drawback of the standard hot big bang model referred to as the flatness problem is essentially a cosmological fine-tuning problem. It pertains to the fact that the current density of the universe is so close to its critical value such that the universe is exceedingly spatially flat today [cf. Eq. (1.12)]. As is evident from Eq. (1.9), if $\Omega = 1$, then it remains so for

all times. However, when $\Omega \neq 1$, it evolves with the expansion of the universe. The currently observed value implies that Ω is forced to be much closer to unity in the past. For instance, we require $|\Omega - 1| < \mathcal{O}(10^{-16})$ at the epoch of nucleosynthesis and $|\Omega - 1| < \mathcal{O}(10^{-64})$ at the Planck epoch. This appears to be an extreme fine tuning of the initial conditions. All the initial conditions other than these extremely fine tuned ones lead either to a closed universe that recollapses almost immediately, or to an open universe that very quickly enters the curvature dominated regime.

The spontaneous breakdown of the symmetries of high energy theories which are expected to be restored in the early universe typically lead to the production of many unwanted relics such as the magnetic monopoles, domain walls, cosmic strings and textures. Apart from these defects, these theories also predict supersymmetric particles such as gravitinos, Kaluza-Klein particles, and weakly coupled moduli fields. Since the energy densities of these massive relic particles turn out to be larger than the energy density of radiation at early times, these relics could become the dominant component of matter in the early universe. In the hot big bang model, there is no mechanism for getting rid of such relics that could have been produced in the early universe. On the other hand, no signatures of the presence of any of these relics have yet been provided by the current observations.

Finally, the most important problem in cosmology is to provide a causal physical mechanism to generate the primordial density fluctuations which are considered responsible for the formation of the structures that we see around us today. We had mentioned above that, in the hot big bang model, all the cosmological scales today prove to be much larger than the Hubble radius during the early stages of the universe. This, in turn, implies that any mechanism which is invoked for the generation of these primordial fluctuations has to be intrinsically acausal.

1.5 The inflationary paradigm

As we discussed above, though the hot big bang model was able to provide a satisfactory interpretation to the various observations, it had some serious shortcomings of its own. Almost three decades ago, it was realized that a phase of an accelerated expansion of the universe at very early times can indeed provide a solution to the various problems of the standard hot big bang cosmology that we have described above. Such a period of extremely

rapid expansion of the universe, known as *inflation* is not a replacement for the conventional hot big bang model, but rather an accessory feature attached to it that occurs at very early times without disturbing any of its successes. The inflationary model that was originally formulated has now been termed as old inflation [33]. To overcome the drawbacks of old inflation, the model was further refined in later years and has since been named as new inflation [34, 35]. In the last twenty five years or so, a large number of inflationary models have been proposed which are based on the various high energy theories, such as, for instance, the Minimal Supersymmetric Standard Model (MSSM) and string theory. However, a satisfactory model of inflation still eludes us.

The precise, and more physical definition of inflation is an epoch in the early universe during which λ_p decreases faster than the Hubble radius *as we go back in time*, i.e. if we have [3, 4]

$$-\frac{d}{dt} \left(\frac{\lambda_p}{d_H} \right) < 0. \quad (1.17)$$

This definition translates to an equivalent condition for inflation which is given by

$$\ddot{a} > 0. \quad (1.18)$$

Therefore, inflation corresponds to an epoch during which the scale factor of the universe is accelerating. In Fig. 1.3, the physical wavelength of two different modes and the Hubble radius have been plotted as a function of the scale factor during inflation and the radiation dominated epochs [1]. In plotting the figure, we have assumed that the inflationary phase is described by a power law expansion of the form $a \propto t^f$ with $f > 1$. In such a case, d_H behaves as $a^{(1/f)}$. Therefore, while the straight lines describing the evolution of the physical wavelengths will always have a unit slope, those describing the Hubble radius during the inflationary and the radiation dominated epoch will have a slope of much less than unity (say, for $f \gg 1$) and two, respectively. It is then evident from the figure that, *as we go back in time*, modes that leave the Hubble radius during the later epochs will not be inside the Hubble radius during the early stages of the universe *unless there exists a period of inflation*. Alternatively, these conditions allow the entire observable region of our universe to lie within a region that was well inside the Hubble radius at the onset of inflation. This property turns out to be the key point in solving the cosmological puzzles of the standard hot big bang cosmology. A useful quantity to describe the amount of inflation is the number

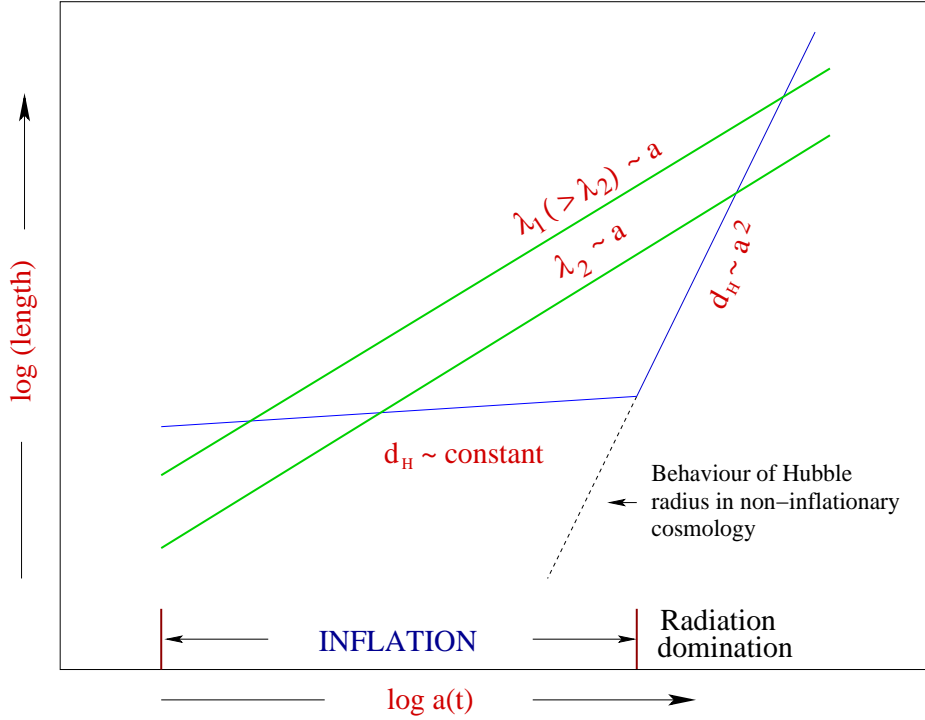


Figure 1.3: The evolution of the physical wavelengths λ_1 and λ_2 and the Hubble radius d_H have been plotted as a function of the scale factor a on a logarithmic plot during inflation and the radiation dominated epoch. In the hot big bang model, a given length scale crosses the Hubble radius only once, while in the inflationary cosmology, all scales are sub-Hubble at very early times. In other words, an epoch of inflation brings all the scales of cosmological interest inside the Hubble radius at a suitably early time which allows the initial conditions on these modes to be imposed in the sub-Hubble regime. These scales cross the Hubble radius during inflation, and re-enter during the subsequent post-inflationary epoch.

of e -foldings, which is quantified by the ratio of the scale factor at a given time t to its value at an initial time t_i , and is defined as

$$N \equiv \ln \left(\frac{a(t)}{a_i} \right) = \int_{t_i}^t H dt. \quad (1.19)$$

In order to overcome the horizon and the flatness problems associated with the hot big bang model, it turns out that about 60 e -folds of inflation are required [3, 4]. However, this number of e -folds actually depends on the energy scale associated with the inflationary regime. In fact, 60 e -folds seems to be an approximate observational upper bound which ensures that the largest scale observed today is inside the Hubble radius during the inflationary

epoch [36, 37].

In the previous section, we had briefly discussed the shortcomings of the standard hot big bang model. We shall now elaborate as to how an inflationary phase in the early universe provides a satisfactory solution to all these problems. As Fig. 1.3 indicates, the inflationary epoch allows one to bring the modes inside the Hubble radius, thereby helping us overcome the horizon problem. The observed isotropy of the CMB then follows from the fact that the largest regions were in causal contact with each other at early times.

Due to the accelerated expansion of the universe during the inflationary phase, the density parameter Ω is quickly driven towards unity, as is evident from Eq. (1.9). (Note that, during inflation, the Hubble parameter H is nearly constant, while the scale factor a grows rapidly.) Given that the inflationary expansion lasts sufficiently long for the required number of e -folds and drives Ω very close to unity, it will be driven further close to unity (rather than away from it) at later epochs. In other words, inflation does not alter the global geometrical properties of the universe. An open or a closed universe will remain open or closed irrespective of the occurrence of inflation. What inflation does is to increase the apparent size of the universe by such a large factor that it becomes locally flat to a very great precision. Thus, inflation provides a natural solution to the flatness problem as well.

As a byproduct, inflation also resolves the relic density problem. The 60 odd e -folds that seem to be needed to resolve the horizon problem dilute the number density of the magnetic monopoles and other unwanted relics to such an extent that their abundances fall below detectable levels.

Though originally unexpected, the most significant outcome of the inflationary scenario is to provide a causal mechanism for the origin of the primordial perturbations. The fluctuations in the quantum fields inside the Hubble radius during the early stages of inflation prove to be responsible for the generation of these perturbations. The drastic expansion of the universe during the inflationary epoch amplifies these small quantum fluctuations and turns them into classical perturbations whose amplitude generally freezes at super-Hubble scales [38, 39, 40, 41]. These perturbations leave their imprints as anisotropies in the CMB, which, in turn, act as seeds for the formation of the large scale structures that we observe at the present time as galaxies and clusters of galaxies. As we shall discuss in the next section, in general, in slow roll inflation, the spectrum of these perturbations turns out to be nearly

scale invariant, which is, basically due to the fact that the Hubble rate is almost constant during the inflationary epoch. The recent CMB observations seem to strongly favor such a perturbation spectrum (see, for instance, Ref. [20]). This is regarded as an important evidence in support of the inflationary paradigm. Thus, inflation not only explains the large scale homogeneity of the observed universe, but it also provides an elegant explanation for the pattern of inhomogeneities on the smaller scales.

1.5.1 Driving inflation with scalar fields

As discussed in the previous section, an accelerated evolution of the scale factor during inflation turns out to be the key property in solving the horizon problem of the hot big bang model. In order to have an inflationary phase in the early universe, it turns out that one needs to have a matter source with negative pressure as neither radiation nor matter allow for such a behavior of the scale factor. From the Friedmann equation (1.7b), it is evident that, for accelerated expansion, we require

$$(\rho + 3p) < 0. \quad (1.20)$$

It has been known for quite some time that scalar fields are one of the natural candidates, which can behave as matter sources with negative pressure and can indeed drive a phase of accelerated expansion at very early times. Most of the popular models of inflation are based on the scalar fields. The scalar field responsible for driving the inflationary phase is generally referred to as an inflaton. Among various other things, the scalar fields are one of the fundamental ingredients in modern theories of particle physics which are considered to be responsible for the physics of symmetry breaking. Although, as yet, there has been no direct observation of a fundamental scalar field (such as, say, the one describing the Higgs particle), the prediction of theories that take such fields into account have been tested against experiments. Inflationary cosmology is one arena where these scalar fields play a crucial role. The subject of particle physics has yet of offer a definitive view of the detailed properties of such fields. The unusual feature of the potential energy of a scalar field which may redshift very slowly with the expansion of the universe, corresponds to an effective equation of state with negative pressure. Due to such an uncommon characteristic of the scalar fields, they are considered promising candidates which can drive the inflationary phase during the

early stages of the universe. Based on the different functional forms of the potential energy of the scalar fields and perhaps various motivations from particle physics point of view, phenomenologically, there exists enormous freedom in building a wide range of different inflationary models.

One of the simplest and natural realization of a matter component with negative pressure is the case of a single, canonical and homogeneous scalar field, say, $\phi(t)$, that is minimally coupled to the gravity. In the homogeneous Friedmann background, the energy density ρ_ϕ and the pressure p_ϕ of the inflaton are given by

$$\rho_\phi = \frac{1}{2} \dot{\phi}^2 + V(\phi), \quad (1.21a)$$

$$p_\phi = \frac{1}{2} \dot{\phi}^2 - V(\phi). \quad (1.21b)$$

where $V(\phi)$ is the potential energy associated with the inflaton. For a spatially flat universe (i.e. $\mathcal{K} = 0$), the first Friedmann equation can be written as

$$H^2 = \left(\frac{8\pi G}{3} \right) \left[\frac{1}{2} \dot{\phi}^2 + V(\phi) \right]. \quad (1.22)$$

The equation of motion describing the inflaton is given by

$$\ddot{\phi} + 3H\dot{\phi} + V_\phi = 0, \quad (1.23)$$

where $V_\phi \equiv (dV/d\phi)$. In this equation, the $(3H\dot{\phi})$ term is generally referred to as the friction term which arises due to the expansion of the universe and leads to the damping of the motion of the inflaton. Using the above expressions for the energy density and the pressure for the inflaton, one finds that the condition for inflation (1.20) translates to

$$\dot{\phi}^2 < V(\phi), \quad (1.24)$$

which states that the universe can undergo a phase of an accelerated expansion if the potential energy of the inflaton dominates the kinetic energy. With a sufficiently flat potential, even if this condition is not satisfied initially, it can be achieved very quickly, provided that the inflaton is displaced far from the minima of its potential. The above condition eventually leads to a vacuum like ($w \simeq -1$) equation of state parameter for the inflaton, which, in turn, results in an accelerated phase of the universe.

1.5.2 Slow roll inflation

The conventional approximation that guarantees inflation is known as the slow roll approximation. Under this approximation, the kinetic energy of the inflaton is neglected when compared to its potential energy. Also, in order to lead to the required amount of inflation, the acceleration term is also ignored when compared to the friction term in the equation of motion for the inflaton. Upon imposing these conditions, i.e. $(\dot{\phi}^2/2) \ll V(\phi)$ and $|\ddot{\phi}| \ll 3H|\dot{\phi}|$, we arrive at the following equations:

$$H^2 \simeq \left(\frac{8\pi G}{3} \right) V(\phi), \quad (1.25a)$$

$$3H\dot{\phi} \simeq -V_\phi. \quad (1.25b)$$

It turns out that the slow roll approximation can be incorporated in the following two conditions [3, 5, 6, 7]:

$$\epsilon_V(\phi) \ll 1 \quad \text{and} \quad |\eta_V(\phi)| \ll 1, \quad (1.26)$$

where ϵ_V and η_V are known as the Potential Slow Roll (PSR) parameters, and are defined as

$$\epsilon_V = \left(\frac{1}{16\pi G} \right) \left(\frac{V_\phi}{V} \right)^2, \quad (1.27a)$$

$$\eta_V = \left(\frac{1}{8\pi G} \right) \left(\frac{V_{\phi\phi}}{V} \right), \quad (1.27b)$$

where $V_{\phi\phi} \equiv (d^2V/d\phi^2)$. Note that, by definition, the first PSR parameter ϵ_V is always positive, while the second PSR parameter η_V can also have negative values. In fact, one can define a complete hierarchy of the PSR parameters in terms of the derivatives of the potential. However, in almost all the cases of interest, the first two PSR parameters in the hierarchy—viz. ϵ_V and η_V —prove to be sufficient in studying the inflationary dynamics and quantifying its predictions. In a similar way, another hierarchy of parameters, known as the Hubble Slow Roll (HSR) parameters can be defined in terms of the derivatives of the Hubble parameter. While the PSR parameters prove to be handy, the HSR parameters turn out to be a better choice to describe the slow roll approximation (for a detailed discussion in this context, see, Ref. [42]; also see Ref. [43]).

The slow roll approximation—i.e. the smallness of the PSR parameters is a sufficient, but not a necessary condition for the occurrence of inflation. As the inflaton rolls down the

potential, the first PSR parameter ϵ_v grows and the inflationary phase ends when it becomes unity. In the slow roll approximation, the number of e -folds during the inflationary regime can be expressed as

$$N \equiv \ln \left(\frac{a}{a_i} \right) \simeq (8\pi G) \int_{\phi}^{\phi_i} \left(\frac{V}{V_\phi} \right) d\phi, \quad (1.28)$$

where ϕ_i is the value of the field at the initial time t_i . This expression is a convenient one, since, given a potential, it allows us to express the evolution of the field directly in terms of the number of e -folds, without the need to solve the equations of motion.

1.5.3 Inflationary models and their comparison with the observations

During the past two decades, ever since the original proposal of inflation, a plethora of inflationary models have been considered in the literature. Broadly, these models can be classified as single or multiple scalar field models. Amongst the models that are described by the canonical action, the single field models are often further divided into two classes based on the form of the effective potential. The first class consists of the large field models, in which the initial value of the inflaton is large (typically, larger than the Planck scale) and it slowly rolls down toward the minimum of the potential at smaller values of the field. Inflation ends when the minimum is approached, leading to a failure of the slow roll conditions. The chaotic inflationary models fall in this class [44]. The second class are called the small field models, since, in these models, inflation occurs at small values of the field and terminates when the field slowly evolves toward the minimum of the potential at large values of the field. New inflation [34, 35] and the natural inflation [45] are the examples of this class. Typical examples of multiple, canonical scalar field models are the hybrid inflation models [46] wherein there is, at least, one more field present, in addition to the slowly rolling inflaton. In these models, inflation ends when the second field is destabilized and settles down to a global minimum of the potential, when the value of the inflaton falls below some critical value. It should be added that inflationary models involving more than two scalar fields have also been considered in the literature (see, for instance, Refs. [47, 48]).

Apart from the class of canonical scalar field models discussed above, there also exist several other models of inflation which are described by non-canonical actions. Such models are often motivated by high energy theories such as, say, string theory. The tachyon [49, 50, 51, 52, 53, 54, 55, 56], and the Dirac-Born-Infeld (DBI) inflationary models [57, 58] are

popular examples that belong to this class. A phenomenological model that has attracted a lot of attention is k-inflation [59, 60], wherein a phase of the accelerated expansion of the universe is realized using the kinetic energy of the inflaton. Inflation has also been achieved without an inflaton, due to the presence of higher order curvature terms in the theory [61].

As we discussed above, a period of inflation at early times not only homogenizes the universe but also creates the small inhomogeneities. These inhomogeneities are actually generated due to the quantum fluctuations of the scalar field. These inhomogeneities, in turn, leave their imprints as anisotropies in the CMB. Measurements of the anisotropies in the CMB—from the early days of COBE which first detected the anisotropies, until the most recent observations of WMAP—have indicated a typical amplitude of about one part in 10^5 of these anisotropies. The spectrum of the scalar perturbations that leads to these anisotropies is usually assumed to be Gaussian in nature⁴, and is often characterized by two parameters, viz. its amplitude and the spectral index. The amplitude of the spectrum is essentially the power associated with a particular wavelength (called the pivot scale) and the spectral index determines the shape of the spectrum. It is useful to note that spectra with indices greater than or less than unity are often referred to as blue and red spectra, respectively. The case of the spectral index being unity corresponds to an exactly scale invariant power spectrum. Such a spectrum with no associated tensor contribution is known as the Harrison-Zel'dovich spectrum. The slow roll approximation generically leads to a perturbation spectrum with slight deviation from scale invariance. Such a spectrum seems to provide a remarkable fit to the observed data. As we shall discuss in the next chapter, the slow roll approximation allows us to determine the spectral amplitude and the index in terms of the background quantities. It, therefore, allows one to compare the predictions of different inflationary models with the data in a relatively model independent fashion.

The power law primordial spectrum that we mentioned above can be expressed as

$$\mathcal{P}_s(k) = A_s \left(\frac{k}{k_0} \right)^{n_s-1}, \quad (1.29)$$

where, A_s and n_s are the amplitude and the spectral index, while k_0 is the pivot scale. In Fig. 1.4, the recent WMAP 5-year data for the CMB angular power spectrum has been displayed. The figure also contains the angular power spectrum corresponding to the best fit

⁴In this thesis, we shall restrict our discussion to the linear order in the perturbations.

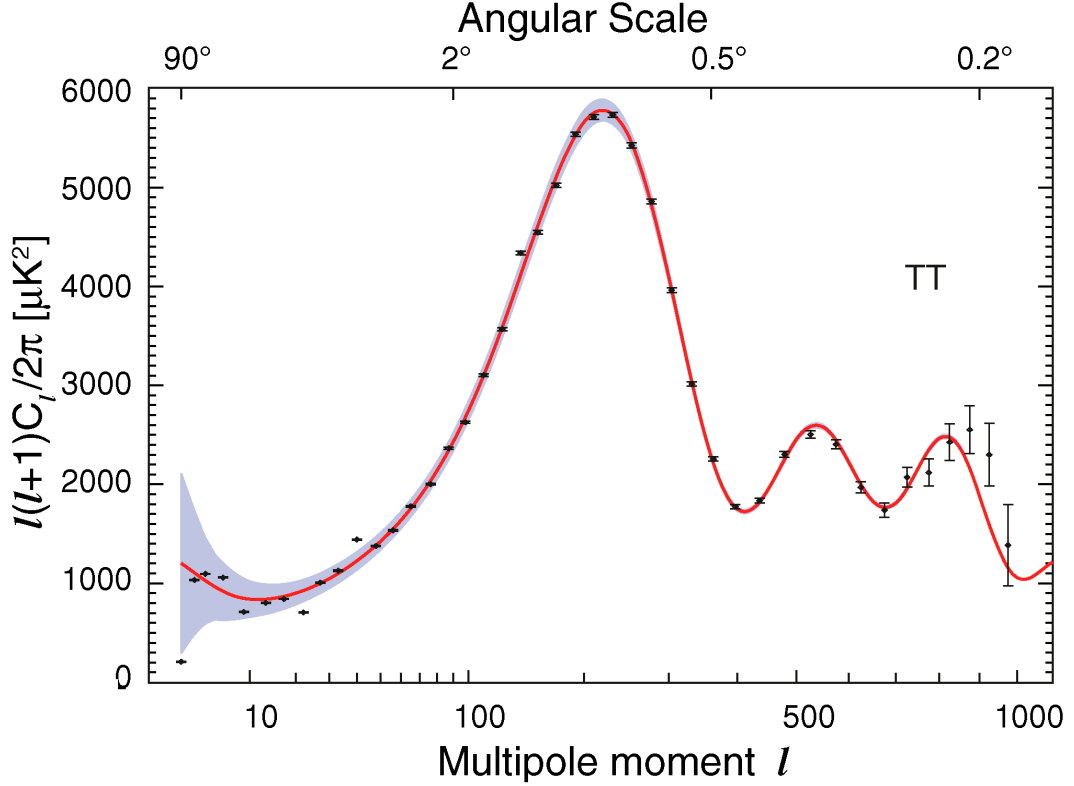


Figure 1.4: The WMAP 5-year data for the CMB angular power spectrum (the black dots with error bars) and the theoretical curve for the best fit Λ CDM model with a power law primordial spectrum (the solid red curve). The blue shaded region is the statistical uncertainty, known as the cosmic variance (see, for example, Refs. [4, 6, 7]). The concordant model seems to provide a reasonably good fit to the data. (This figure is from Ref. [22].)

Λ CDM model with the above power law primordial spectrum. The WMAP 5-year data constrains the amplitude of the scalar spectrum to be $A_s = (2.41 \pm 0.11) \times 10^{-9}$, while the spectral index is constrained to be $n_s = 0.963^{+0.014}_{-0.015}$ [20]. In addition to the scalar perturbations, inflation also generates tensor perturbations, i.e. gravitational waves. The WMAP 5-year data also provides an upper limit on the contribution of the tensors to the CMB anisotropies. For instance, when a scale invariant tensor contribution is assumed, the concordant model leads to the following upper bound on the tensor-to-scalar ratio r at $2\text{-}\sigma$ confidence level: $r < 0.43$. In Fig. 1.5, the two-dimensional marginalized constraints with $1\text{-}\sigma$ and $2\text{-}\sigma$ confidence levels on the scalar spectral index n_s , and the tensor-to-scalar ratio r , defined at the pivot scale

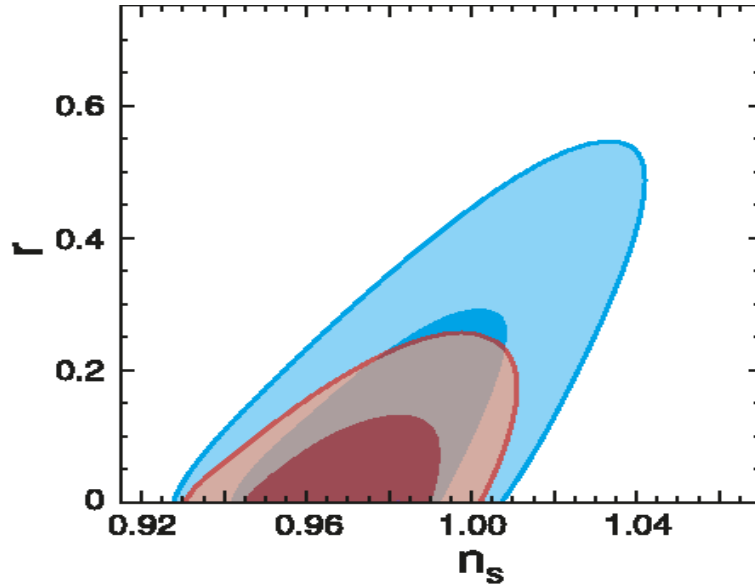


Figure 1.5: The two-dimensional marginalized constraints with $1\text{-}\sigma$ and $2\text{-}\sigma$ confidence levels on the scalar spectral index n_s , and the tensor-to-scalar ratio r , defined at the pivot scale of $k_0 = 0.002 \text{ Mpc}^{-1}$. The contours in blue are for WMAP 5-year data alone while the red contours represent the results for WMAP+BAO+Supernovae datasets. (This figure is from Ref. [21].)

of $k_0 = 0.002 \text{ Mpc}^{-1}$ for WMAP 5-year data alone, and also for WMAP+BAO+Supernovae datasets have been shown. These observations seem to provide strong evidence in favor of the inflationary paradigm.

1.6 Reheating the universe after inflation

Reheating, which is expected to occur after the end of the inflationary epoch, is a regime during which the energy of the inflaton is transferred to radiation to give way to the standard hot big bang phase of the universe. Due to the rapid expansion of the universe in a very short span of time during the inflationary phase, the universe is left in an effectively zero temperature state at the end of inflation. Therefore, any successful theory of inflation must also explain as to how the universe was reheated to lead to the standard hot big bang picture. Over the last few years, it has been realized that the process of reheating can have significant effects on the cosmological predictions of the preceding inflationary phase. In

what follows, we shall discuss a few reheating scenarios and shall also briefly mention the effects of reheating on the evolution of the perturbations in these scenarios.

The simplest scenario of reheating is often referred to as perturbative reheating. In this scenario, the decay of the inflaton into other particles is conceived in terms of a phenomenological decay term ($\Gamma\dot{\phi}$) which is introduced by hand in the equation of motion (1.23) of the inflaton [cf. Eq. (5.38)] (for a detailed discussion in this context, see, for instance, Ref. [1], also see Refs. [62, 63, 64, 65, 66]). Such a term turns out to be responsible for the transfer of the energy from the inflaton to radiation and other particles. Perturbative reheating is often achieved using a constant decay rate. In such a case, it has been shown that the amplitude of the large scale perturbations is not affected by the process of reheating [65, 66].

Another scenario wherein the transfer of energy from inflaton to other particles takes place in a non-perturbative fashion is known as preheating. After the end of inflation in chaotic inflationary models, the inflaton further rolls down and starts oscillating about the minima of the potential. These oscillations gradually decay due to the expansion of the universe. The coherent oscillations of the inflaton lead to a non-perturbative resonant transfer of energy from the field to the other particles which are indeed present in the full theory but are not considered, in particular, in the effective picture while studying the dynamics of inflation. The inherent non-linear dynamics involved in the preheating process leads to an explosive production of particles (see, for example, Refs. [67, 68, 69, 70, 71, 72, 73, 74, 75, 76, 77, 78, 79, 80]). It turns out that this non-perturbative mechanism of preheating can be much more efficient than the usual perturbative process for certain ranges of parameters of the theory. It has been noticed that, the parametric resonance due to the unstable oscillations of the inflaton during preheating can lead to an exponential growth in the amplitude of the large scale perturbations (see, for instance, Refs. [81, 82, 83, 84]).

Two other scenarios that are known to affect the large scale perturbations are the curvaton and the modulated reheating scenarios. In the curvaton scenario, the perturbations generated during inflation are amplified post-inflation due to the presence of the entropic perturbations [85, 86]. The modulated and/or the inhomogeneous reheating is another interesting scenario in which inflation is essentially required to resolve the horizon and the flatness problem, whereas the perturbations are generated due to an inhomogeneous de-

cay rate when the energy is being transferred from the inflaton to radiation through other fields [87, 88, 89, 90].

While there exist a large number of scenarios in the literature that address the phenomenon of reheating, the process of reheating and the underlying dynamics are yet to be completely understood. Though the simplest of the reheating processes do not affect the amplitude of the curvature perturbations, as we discussed above, there can be a non-trivial evolution of the large scale perturbations. However, this phenomenon seems to be highly model dependent. Evidently, in all these scenarios, the effects of the post-inflationary dynamics have to be taken into account while constraining the predictions of the inflationary models using the CMB observations (in this context, see, for instance, Ref. [91]).

1.7 Scope of the thesis

In this section, we shall briefly discuss the work that constitutes this thesis. The thesis work is aimed at studying some issues related to the origin and evolution of cosmological perturbations during the inflationary era and the reheating phase, and the resulting signatures on the CMB. With these goals in mind, the issues studied in this thesis can be broadly classified into two categories:

- Beyond slow roll inflation
- Post-inflationary dynamics and its effects on the perturbations

We shall describe these issues in detail below.

1.7.1 Beyond slow roll inflation

As is well known, in the slow roll inflationary scenario, the amplitude of the curvature perturbations approaches a constant value soon after the modes leave the Hubble radius. However, if there are deviations from slow roll, there can be a non-trivial evolution of the perturbations at super-Hubble scales which, in turn, lead to specific features in the power spectrum.

In chapter 2, we shall start with a brief discussion of the essential results from the linear cosmological perturbation theory. With the help of a specific example for the case of a non-canonical scalar field described by the tachyonic action, we shall illustrate that, if there is

either a transition to fast roll inflation, or if inflation is interrupted for some period of time, the amplitude of the curvature perturbations can be enhanced or suppressed (when compared to its value at Hubble exit) at super-Hubble scales. We shall explicitly show that it is the growth of the intrinsic entropy perturbation associated with the scalar field during the fast roll regime which turns out to be responsible for the change in the amplitude of the curvature perturbations at super-Hubble scales. We shall also show that the power spectrum of curvature perturbations evaluated in the long wavelength approximation matches the exact power spectrum obtained numerically very well. Interestingly, in such scenarios with deviations from slow roll, the power spectrum no more remains scale invariant. Towards the end of this chapter, we shall construct two simple analytically tractable examples in the context of the canonical scalar field. We shall discuss the evolution of the curvature perturbations at large scales in these cases and also present the power spectrum evaluated analytically.

In chapter 3, we shall investigate inflationary scenarios driven by a class of potentials which are similar in form to those that arise in certain minimal supersymmetric extensions of the standard model. We find that these potentials allow a brief period of departure from inflation sandwiched between two stages of slow roll inflation, a scenario which we shall refer to as punctuated inflation. We shall show that such background behavior leads to a step like feature in the scalar power spectrum. We set the scales such that the drop in the power spectrum occurs at a length scale that corresponds to the Hubble radius today—a feature that seems necessary to explain the lower power observed in the quadrupole moment of the CMB anisotropies. We shall perform a Markov Chain Monte Carlo analysis to determine the values of the model parameters that provide the best fit to the recent WMAP 5-year data for the CMB angular power spectrum. We shall find that an inflationary spectrum with a suppression of power at large scales that we obtain leads to a much better fit of the observed data when compared to the best fit reference Λ CDM model with a featureless, power law, primordial spectrum.

In chapter 4, we shall discuss the effects of punctuated inflation on the tensor power spectrum and, in particular, the tensor-to-scalar ratio. With examples from the canonical scalar field as well as the tachyonic models, we shall illustrate that, in punctuated inflation, a drop in the scalar power on large scales is always accompanied by a rise in the tensor power and, hence, an even more pronounced increase in the tensor-to-scalar ratio r at these scales. Inter-

estingly, we shall find that r actually exceeds well beyond unity over a small range of scales. We shall show that the rise in r on large scales translates to a rapid increase in the angular power spectrum, C_ℓ^{BB} , of the B-mode polarization of the CMB at the low multipoles. Although, in the specific models of punctuated inflation that we shall study, the C_ℓ^{BB} does not attain observable values, our work suggests that there could be models of punctuated inflation that fit the data well, and also predict observable levels of C_ℓ^{BB} . We shall also discuss the possible observational implications of our results.

1.7.2 Post-inflationary dynamics and its effects on the perturbations

It has been pointed out that, in tachyonic inflation, an epoch of matter domination (rather than radiation domination) generally arises at the end of inflation [55, 92]. This behavior is also known to lead to the formation of caustics [93]. With these issues in mind, in chapter 5, we shall investigate the problem of perturbative reheating and its effects on the evolution of the curvature perturbations in tachyonic inflationary models. We shall derive the equations governing the evolution of the scalar perturbations for a system consisting of a tachyon and a perfect fluid. Assuming the perfect fluid to be radiation, we shall solve the coupled equations for the system numerically and study the evolution of the perturbations from the sub-Hubble to the super-Hubble scales. In particular, we shall analyze the effects of the transition from tachyon driven inflation to the radiation dominated epoch on the evolution of the large scale curvature and non-adiabatic pressure perturbations. We shall consider two different potentials to describe the tachyon and shall study the effects of two possible types of decay of the tachyon into radiation. We shall plot the spectrum of curvature perturbations at the end of inflation as well as at the early stages of the radiation dominated epoch. We shall find that reheating does not affect the amplitude of the curvature perturbations in any of these cases. These results corroborate similar conclusions that have been arrived at earlier based on the study of the evolution of the perturbations in the super-Hubble limit. We shall illustrate that, before the transition to the radiation dominated epoch, the relative non-adiabatic pressure perturbation between the tachyon and radiation decays in a fashion very similar to that of the intrinsic entropy perturbation associated with the tachyon. Moreover, we shall show that, after the transition, the relative non-adiabatic pressure perturbation dies down extremely rapidly during the early stages of the radiation dominated

epoch. It is these behavior which ensure that the amplitude of the curvature perturbations remain unaffected during reheating. We shall also discuss the corresponding results for the case of the canonical scalar field.

With the aim of providing another possible mechanism for the generation of perturbations, in chapter 6, we shall consider the behavior of an inhomogeneous, interacting, scalar field that is coupled non-minimally to gravity in the Friedmann background. We shall show that for a specific choice of interaction terms, the stress-energy tensor of the scalar field vanishes, and as a result, the scalar field does not gravitate. We shall find that the naive space dependent solution to equations of motion gives rise to singular field profile. We shall carefully analyze the stress-energy tensor for such a solution and shall show that the singularity of the solution gives a subtle contribution to the stress-energy tensor. The space dependent solution is, therefore, not non-gravitating. We shall illustrate that our conclusions are applicable to other spacetime dependent non-gravitating solutions as well. We shall also study a hybrid inflation scenario in this model when purely time dependent non-gravitating field is coupled to another scalar field.

Finally, in chapter 7, we shall rapidly summarize the results obtained in this thesis and shall also briefly discuss a few related problems that we believe require immediate attention.

1.8 Conventions and notations

Before we proceed further, a few words on the conventions and notations we shall adopt in this thesis are in order.

- We shall always work in $(3 + 1)$ dimensions.
- In chapter 6, for calculational convenience, we shall work with the metric signature of $(-, +, +, +)$. Barring this chapter, in the rest of the thesis, we shall work with the metric signature of $(+, -, -, -)$.
- We shall set $\hbar = c = 1$ but shall often display G explicitly, and define the Planck mass to be $M_{\text{p}} = (8 \pi G)^{-1/2}$. And, we shall mention so whenever we set M_{p} to unity.
- Throughout our discussions in this thesis, we shall work in the spatially flat Friedmann background with $\mathcal{K} = 0$.

- We shall express the various quantities in terms of either the cosmic time t , or the conformal time η , as is convenient.
- As we had mentioned, an overdot shall denote differentiation with respect to the cosmic time t . And, an overprime shall denote derivative with respect to the conformal time η .
- It is useful to note here that, for any given function, say, f , we have

$$\dot{f} = (f'/a) \quad \text{and} \quad \ddot{f} = [(f''/a^2) - (f' a'/a^3)], \quad (1.30)$$

where a is the scale factor describing the Friedmann background.

Chapter 2

Deviations from slow roll inflation and the effects on the large scale perturbations

2.1 Motivation

It is well-known that, in the inflationary scenario, the amplitude of the curvature perturbations approaches a constant value soon after the modes leave the Hubble radius (see, for example, either of the following texts [3, 5, 6] or one of the following reviews [94, 95, 96, 97, 98]). But, what is not so commonly known is that this result is true *only* in slow roll or power law inflation and, in fact, the curvature perturbations can be amplified at super-Hubble scales if there is either a period of fast roll inflation or if there is a break in inflation. For the case of curvature perturbations induced by the canonical scalar field, this behavior was first noticed a few years back [99] and a general criterion for such an amplification to occur was also obtained [100]. In this chapter, our aim is to extend the earlier analysis [99, 100] to the case of curvature perturbations generated by a non-canonical scalar field. Interestingly, we find that, in addition to enhancing the amplitude of the curvature perturbations of a certain range of modes at super-Hubble scales, a period of deviation from slow roll inflation also leads to the suppression of the amplitude of another range of modes.

The non-canonical scalar field that we shall consider is the one that is described by the tachyonic action. Such scalar fields generically arise in the study of the dynamics of D-branes in string theory [49, 50, 51, 52]. In particular, the tachyon, which refers to an unstable scalar field that rolls down from the maxima of its potential near the origin to its minima at infinity, captures the essential dynamical features of the decay process of unstable branes (for the original discussion, see Refs. [53, 54]). Various cosmological applications of the tachyon

have been studied extensively in the literature (see, for instance, Refs. [101, 102, 103] and references therein) and, in particular, it has proved to be a fertile ground for inflationary model building (see, for example, Ref. [56] and references therein). It is also possible to have tachyons whose potential has a global minimum at the origin so that the field rolls down from a large value towards the origin (see, for example, Ref. [104]; for cosmological applications of such fields, see, for instance, Refs. [105, 106, 107, 108]). We shall consider such a scenario in this chapter. It should be pointed out here that the tachyon falls under a broader class of non-canonical scalar field models that are often referred to as the k-inflation models [59, 60].

With the help of a specific example, we shall illustrate that the amplitude of the curvature perturbations induced by the tachyon¹ can be enhanced or suppressed (when compared to its value at Hubble exit) at super-Hubble scales if there is a period of deviation from slow roll inflation. We shall also show that it is the growth of entropy perturbations during such a transition that turns out to be responsible for the change in the amplitude of the tachyonic perturbations. Moreover, following the earlier analysis for the canonical scalar field, we shall show that the power spectrum evaluated in the long wavelength approximation and the exact power spectrum obtained numerically match rather well. We shall also briefly comment on an interesting application of this phenomenon, which we shall utilize later to arrive at certain features in the primordial spectrum that lead to a better fit to the data.

The remainder of this chapter is organized as follows. In the following section, after briefly summarizing the essential background equations, we shall rederive the familiar equations describing the scalar perturbations for the cases of an arbitrary matter field and a canonical scalar field. We shall also discuss the corresponding equations for the tensor perturbations. In Sec. 2.3, we shall rapidly outline the standard derivation of the scalar and the tensor spectra as well as the spectral indices in the slow roll inflation. In Sec. 2.4, we shall derive the equations describing the scalar perturbations generated by the tachyon. In Sec. 2.5, we shall illustrate the amplification or suppression of the curvature perturbations at super-Hubble scales when there is a transition from slow roll to fast roll and back with the help of a specific example. In Sec. 2.6, we shall show as to how the entropy perturbations grow during

¹Actually, as we mentioned above, the term ‘tachyon’ refers to a non-canonical scalar field that is often described by a potential with a maxima near the origin. However, the specific potential that we shall consider in this chapter does not have this feature.

the period of fast roll inflation which in turn act as the source for the evolution of the curvature perturbations at super-Hubble scales. In Sec. 2.7, we extend an earlier result for the canonical scalar field to the tachyonic case and show that the power spectrum calculated in the long wavelength approximation agrees quite well with the exact power spectrum evaluated numerically. In Sec. 2.8, we shall present two simple examples wherein the amplitude of the curvature perturbations induced by the canonical scalar field is enhanced at super-Hubble scales, when compared to their values at Hubble exit. Finally, in Sec. 2.9, we close by commenting on an important application of our result, which we shall utilize in later chapters for the canonical scalar field.

2.2 Essential cosmological perturbation theory

In this section, we shall sketch essential cosmological perturbation theory. After quickly summarizing the equations corresponding to the Friedmann background, we shall discuss the equations describing the scalar perturbation for the cases of an arbitrary matter field and a canonical scalar field. We shall also arrive at the equations characterizing the tensor perturbations. We should again emphasize here that, in this thesis, we shall restrict our discussion to the linear order in the perturbations.

2.2.1 The background equations

As we had discussed in the previous chapter, a spatially flat, homogeneous and isotropic Friedmann universe is described by the line element:

$$ds^2 = dt^2 - a^2(t) d\mathbf{x}^2 = a^2(\eta) [d\eta^2 - d\mathbf{x}^2]. \quad (2.1)$$

The Einstein equations corresponding to this line element lead to the following Friedmann equations that describe the time evolution of the scale factor:

$$\left(\frac{\dot{a}}{a}\right)^2 = \left(\frac{8\pi G}{3}\right) \rho, \quad (2.2a)$$

$$\left(\frac{\ddot{a}}{a}\right) = -\left(\frac{4\pi G}{3}\right) (\rho + 3p). \quad (2.2b)$$

A very useful equation that can be obtained from these Friedmann equations is given by

$$\dot{H} = -4\pi G (\rho + p). \quad (2.3)$$

For a canonical scalar field with energy density ρ_ϕ and pressure p_ϕ as given in Eqs. (1.21), this equation reduces to

$$\dot{H} = -4\pi G \dot{\phi}^2. \quad (2.4)$$

2.2.2 The scalar perturbations

On taking into account the scalar perturbations to the background metric (2.1), the Friedmann line-element, in general, can be written as [3, 5, 94, 95, 96, 97, 109, 110]

$$ds^2 = a^2(\eta) \left[(1 + 2A) d\eta^2 - 2(\partial_i B) dx^i d\eta - ((1 - 2\psi) \delta_{ij} + 2\partial_i \partial_j E) dx^i dx^j \right], \quad (2.5)$$

where A , B , ψ and E are the scalar functions that describe the perturbations. The infinitesimal coordinate transformations, also referred to as the gauge transformations, can be written as

$$\eta \rightarrow \tilde{\eta} = \eta + \chi(\eta, \mathbf{x}), \quad (2.6a)$$

$$x^i \rightarrow \tilde{x}^i = x^i + \delta^{ij} \partial_j \xi(\eta, \mathbf{x}), \quad (2.6b)$$

where χ and ξ are two independent scalar functions of space and time coordinates and the tildes shall, hereafter, refer to the various quantities in the new coordinates. The metric perturbations are, in general, not invariant under such a change of coordinates. Under the gauge transformations (2.6), the scalar metric perturbations A , B , ψ and E transform as [5, 95]

$$A \rightarrow \tilde{A} = A - \left(\frac{1}{a} \right) (a\chi)', \quad (2.7a)$$

$$B \rightarrow \tilde{B} = B + \chi - \xi', \quad (2.7b)$$

$$\psi \rightarrow \tilde{\psi} = \psi + \mathcal{H}\chi, \quad (2.7c)$$

$$E \rightarrow \tilde{E} = E - \xi, \quad (2.7d)$$

where $\mathcal{H} = (a'/a)$ is the conformal Hubble parameter. Using the above gauge transformations, gauge-invariant variables can be constructed by taking the appropriate combinations of the functions A , B , ψ and E . The two gauge-invariant variables—known as the Bardeen variables [94, 95, 111]—that characterize the two degrees of freedom describing the scalar

perturbations are given by [3, 5, 94, 95, 96, 97, 109, 110, 111]

$$\Phi \equiv A + \left(\frac{1}{a}\right) [(B - E') a]', \quad (2.8a)$$

$$\Psi \equiv \psi - \mathcal{H} (B - E'). \quad (2.8b)$$

As another useful example, consider a scalar quantity that can be split into a background value and a perturbation as follows:

$$Q(\eta) + \delta Q(\eta, \mathbf{x}). \quad (2.9)$$

Under the gauge-transformations (2.6), the background value Q remains invariant while the perturbation δQ transforms as follows [5, 95]:

$$\delta Q \rightarrow \widetilde{\delta Q} = \delta Q - Q' \chi. \quad (2.10)$$

A combination of the perturbation in Q and the metric perturbations that remains gauge-invariant is given by

$$\delta \mathcal{Q} = \delta Q + Q' (B - E'). \quad (2.11)$$

At the linear order in the perturbations, the Einstein equations relating the perturbed Einstein tensor δG_ν^μ to the perturbed stress-energy tensor δT_ν^μ are given by

$$\delta G_\nu^\mu = 8 \pi G \delta T_\nu^\mu. \quad (2.12)$$

The components of the perturbed Einstein tensor corresponding to the line-element (2.5) are given by

$$\begin{aligned} \delta G_0^0 &= \left(\frac{2}{a^2}\right) \left(-3 \mathcal{H} (\mathcal{H} A + \psi') + \nabla^2 [\psi - \mathcal{H} (B - E')]\right) \\ &= \left(\frac{2}{a^2}\right) \left(-3 \mathcal{H} (\mathcal{H} \Phi + \Psi') + \nabla^2 \Psi + 3 \mathcal{H} (-\mathcal{H}' + \mathcal{H}^2) (B - E')\right), \end{aligned} \quad (2.13a)$$

$$\begin{aligned} \delta G_i^0 &= \left(\frac{2}{a^2}\right) \partial_i (\mathcal{H} A + \psi') \\ &= \left(\frac{2}{a^2}\right) \partial_i \left(\mathcal{H} \Phi + \Psi' + (\mathcal{H}' - \mathcal{H}^2) (B - E')\right), \end{aligned} \quad (2.13b)$$

$$\begin{aligned} \delta G_j^i &= -\left(\frac{2}{a^2}\right) \left([(2 \mathcal{H}' + \mathcal{H}^2) A + \mathcal{H} (A' + 2 \psi') + \psi'' + \nabla^2 (\mathcal{D}/2)] \delta_j^i - \partial^i \partial_j (\mathcal{D}/2)\right) \\ &= -\left(\frac{2}{a^2}\right) \left([(2 \mathcal{H}' + \mathcal{H}^2) \Phi + \mathcal{H} (\Phi' + 2 \Psi') + \Psi'' + \nabla^2 (\mathcal{D}/2)] \delta_j^i \right. \\ &\quad \left. + (\mathcal{H}'' - \mathcal{H} \mathcal{H}' - \mathcal{H}^3) (B - E') \delta_j^i - \partial^i \partial_j (\mathcal{D}/2)\right), \end{aligned} \quad (2.13c)$$

where

$$\mathcal{D} = \left[(A - \psi) + 2\mathcal{H} (B - E') + (B - E')' \right] = (\Phi - \Psi), \quad (2.14)$$

and, we have made use of the definitions (2.8) of the gauge-invariant potentials Φ and Ψ in arriving at the second equalities.

Under the gauge transformations (2.6), the components of the perturbed Einstein tensor δG_ν^μ transform as follows:

$$\delta G_0^0 \rightarrow \widetilde{\delta G_0^0} = \delta G_0^0 - G_0^{0'} \chi, \quad (2.15a)$$

$$\delta G_i^0 \rightarrow \widetilde{\delta G_i^0} = \delta G_i^0 - \left[G_0^0 - \left(\frac{1}{3} \right) G_k^k \right] \partial_i \chi, \quad (2.15b)$$

$$\delta G_j^i \rightarrow \widetilde{\delta G_j^i} = \delta G_j^i - G_0^{0'} \chi, \quad (2.15c)$$

where G_ν^μ denotes the Einstein tensor corresponding to the background line-element (2.1), and is given by

$$G_0^0 = \left(\frac{3}{a^2} \right) \mathcal{H}^2, \quad (2.16a)$$

$$G_i^0 = 0, \quad (2.16b)$$

$$G_j^i = \left(\frac{1}{a^2} \right) (2\mathcal{H}' + \mathcal{H}^2) \delta_j^i. \quad (2.16c)$$

As in the case of the scalar functions describing the metric perturbations, it is straightforward to construct gauge-invariant quantities corresponding to the perturbed Einstein tensor δG_ν^μ . The gauge-invariant, perturbed Einstein tensor, which we shall denote as $\delta \mathcal{G}_\nu^\mu$, can be written as follows [5, 95]:

$$\begin{aligned} \delta \mathcal{G}_0^0 &= \delta G_0^0 + G_0^{0'} (B - E') \\ &= \left(\frac{2}{a^2} \right) \left(-3\mathcal{H} (\mathcal{H} \Phi + \Psi') + \nabla^2 \Psi \right), \end{aligned} \quad (2.17a)$$

$$\begin{aligned} \delta \mathcal{G}_i^0 &= \delta G_i^0 + \left[G_0^0 - \left(\frac{1}{3} \right) G_k^k \right] \partial_i (B - E') \\ &= \left(\frac{2}{a^2} \right) \partial_i (\mathcal{H} \Phi + \Psi'), \end{aligned} \quad (2.17b)$$

$$\begin{aligned} \delta \mathcal{G}_j^i &= \delta G_j^i + G_j^{i'} (B - E') \\ &= - \left(\frac{2}{a^2} \right) \left([(2\mathcal{H}' + \mathcal{H}^2) \Phi + \mathcal{H} (\Phi' + 2\Psi') + \Psi'' + \nabla^2 (\mathcal{D}/2)] \delta_j^i \right. \\ &\quad \left. - \partial^i \partial_j (\mathcal{D}/2) \right), \end{aligned} \quad (2.17c)$$

and, we have made use of the expressions for the perturbed and the background Einstein tensor as in (2.13) and (2.16) in arriving at the second equalities. In a similar fashion, the gauge-invariant perturbed stress-energy tensor, which we shall denote as $\delta\mathcal{T}_\nu^\mu$, can be constructed and is given by [5, 95]

$$\delta\mathcal{T}_0^0 = \delta T_0^0 + T_0^{0'} (B - E'), \quad (2.18a)$$

$$\delta\mathcal{T}_i^0 = \delta T_i^0 + \left[T_0^0 - \left(\frac{1}{3} \right) T_k^k \right] \partial_i (B - E'), \quad (2.18b)$$

$$\delta\mathcal{T}_j^i = \delta T_j^i + T_j^{i'} (B - E'), \quad (2.18c)$$

where T_ν^μ denotes the stress-energy tensor corresponding to the background matter field. Upon using the background equations (2.2), the Einstein equations (2.12) governing the linear perturbations can be written in the following form

$$\delta\mathcal{G}_\nu^\mu = 8\pi G \delta\mathcal{T}_\nu^\mu. \quad (2.19)$$

Note that the quantities on both sides of the above equation are now explicitly gauge-invariant.

Gauge-invariant equations of motion for an arbitrary matter field

At the linear order in the perturbations, perfect fluids and scalar fields do not possess any anisotropic stresses. Under these conditions, the perturbed stress-energy tensor associated with these sources can be expressed as follows:

$$\delta T_0^0 = \delta\rho, \quad \delta T_i^0 = \partial_i \delta q \quad \text{and} \quad \delta T_j^i = -\delta p \delta_j^i, \quad (2.20)$$

where the quantities $\delta\rho$, δq and δp are the scalar quantities that denote the perturbations in the energy density, the momentum flux, and the pressure of the matter field, respectively. It is then clear that, in the absence of the anisotropic stresses, the non-diagonal, spatial component of the Einstein equations (2.19) leads to the relation: $\Phi = \Psi$. The first order gauge-invariant Einstein equations then lead to the following form of the equations [3, 5, 94, 95, 96, 97, 109, 110]

$$\nabla^2 \Phi - 3\mathcal{H} (\Phi' + \mathcal{H} \Phi) = (4\pi G a^2) [\delta\rho + \rho' (B - E')], \quad (2.21a)$$

$$\partial_i (\Phi' + \mathcal{H} \Phi) = (4\pi G a^2) [\partial_i \delta q + (\rho + p) \partial_i (B - E')], \quad (2.21b)$$

$$\Phi'' + 3\mathcal{H} \Phi' + (2\mathcal{H}' + \mathcal{H}^2) \Phi = (4\pi G a^2) [\delta p + p' (B - E')]. \quad (2.21c)$$

The first and the third of these Einstein equations can be combined to lead to the following differential equation for the gauge-invariant Bardeen potential Φ [3, 5, 94, 95, 96, 97, 109, 110]:

$$\Phi'' + 3\mathcal{H}(1 + c_A^2)\Phi' - c_A^2\nabla^2\Phi + [2\mathcal{H}' + (1 + 3c_A^2)\mathcal{H}^2]\Phi = (4\pi G a^2)\delta p^{\text{NA}}, \quad (2.22)$$

where we have made use of the standard relation [118]

$$\delta p = c_A^2 \delta \rho + \delta p^{\text{NA}}, \quad (2.23)$$

with $c_A^2 \equiv (p'/\rho')$ denoting the adiabatic speed of sound and δp^{NA} representing the non-adiabatic pressure perturbation². The curvature perturbation \mathcal{R} is defined in terms of the Bardeen potential Φ and its time derivative as [94, 95, 96, 97]

$$\mathcal{R} = \Phi + \left(\frac{2\rho}{3\mathcal{H}}\right) \left(\frac{\Phi' + \mathcal{H}\Phi}{\rho + p}\right). \quad (2.24)$$

Upon substituting this expression for the curvature perturbation in Eq. (2.22) describing the evolution of the Bardeen potential Φ and making use of the background equations (2.2), we obtain that [118]

$$\mathcal{R}' = -\left(\frac{\mathcal{H}}{\mathcal{H}' - \mathcal{H}^2}\right) \left[(4\pi G a^2)\delta p^{\text{NA}} + c_A^2\nabla^2\Phi\right]. \quad (2.25)$$

Note that, for adiabatic perturbations (i.e. perturbations for which $\delta p^{\text{NA}} = 0$), this equation implies that $\mathcal{R}' \simeq 0$ at super-Hubble scales, when the $(c_A^2\nabla^2\Phi)$ term can be neglected. In other words, the absence of the non-adiabatic perturbations leads to the conservation of the curvature perturbation at super-Hubble scales.

The curvature perturbations induced by the canonical scalar field

As we had discussed in the previous chapter, the most attractive feature of inflation is that it provides a natural mechanism for the generation of perturbations in a causal manner. The quantum fluctuations associated with the inflaton prove to be responsible for the generation of these perturbations. In what follows, we shall obtain the equation of motion for the curvature perturbations induced by the canonical scalar field which acts as the inflaton. The

²The quantities that appear within the square brackets on the right hand sides of the first order Einstein equations (2.21a) and (2.21c) are the gauge-invariant versions of $\delta\rho$ and δp . On using these expressions in the relation (2.23), it is straightforward to show that δp^{NA} is gauge-invariant as well.

scalar field can be decomposed into a homogeneous part ϕ and a perturbation $\delta\phi$. Under the gauge transformations (2.6), the perturbation $\delta\phi$ transforms as follows:

$$\delta\phi \rightarrow \widetilde{\delta\phi} = \delta\phi + \chi. \quad (2.26)$$

A quantity involving the perturbation in the scalar field $\delta\phi$ and the metric perturbations which remains invariant under the scalar gauge transformations (2.6) can be constructed to be

$$\delta\varphi = \delta\phi + \phi' (B - E'). \quad (2.27)$$

At the linear order, the components of the perturbed stress-energy tensor associated with the scalar field can be expressed as

$$\delta T_0^0 = \delta\rho_\phi = \left(\dot{\phi} \delta\dot{\phi} - \dot{\phi}^2 A + V_\phi \delta\phi \right), \quad (2.28a)$$

$$\delta T_i^0 = \partial_i \delta q_\phi = \partial_i \left(\dot{\phi} \delta\phi \right), \quad (2.28b)$$

$$\delta T_j^i = -\delta p_\phi \delta_j^i = -\left(\dot{\phi} \delta\dot{\phi} - \dot{\phi}^2 A - V_\phi \delta\phi \right) \delta_j^i. \quad (2.28c)$$

Note that these components of the perturbed stress-energy tensor are not gauge-invariant. Using Eqs. (2.18) and the definition of the Bardeen potential as in Eq. (2.8) alongwith the gauge-invariant definition of the perturbed scalar field in Eq. (2.27), the various gauge-invariant components of the perturbed stress-energy tensor can be written as

$$\delta \mathcal{T}_0^0 = \left(\dot{\phi} \delta\dot{\varphi} - \dot{\phi}^2 \Phi + V_\phi \delta\varphi \right), \quad (2.29a)$$

$$\delta \mathcal{T}_i^0 = \partial_i \left(\dot{\phi} \delta\varphi \right), \quad (2.29b)$$

$$\delta \mathcal{T}_j^i = -\left(\dot{\phi} \delta\dot{\varphi} - \dot{\phi}^2 \Phi - V_\phi \delta\varphi \right) \delta_j^i. \quad (2.29c)$$

As we mentioned earlier, at the linear order in the perturbations, the scalar field does not possess any anisotropic stress and, consequently, $\Phi = \Psi$ during inflation. As a result, only one independent degree of freedom characterizing the scalar perturbations remains to be dealt with. On substituting the expressions for $\delta\rho_\phi$, δq_ϕ and δp_ϕ as in Eqs. (2.28), in the first order Einstein equations (2.21) governing the scalar perturbations, one arrives at following equation for the Bardeen potential:

$$\Phi'' + 3\mathcal{H} (1 + c_A^2) \Phi' - c_A^2 \nabla^2 \Phi + [2\mathcal{H}' + (1 + 3c_A^2) \mathcal{H}^2] \Phi = (1 - c_A^2) \nabla^2 \Phi. \quad (2.30)$$

Upon comparing this equation for Φ with the general equation (2.22), it is evident that the non-adiabatic pressure perturbation associated with the inflaton is given by

$$\delta p^{\text{NA}} = \left(\frac{1 - c_A^2}{4 \pi G a^2} \right) \nabla^2 \Phi. \quad (2.31)$$

In such a case, equation (2.25) describing the evolution of the curvature perturbation simplifies to

$$\mathcal{R}' = - \left(\frac{\mathcal{H}}{\mathcal{H}' - \mathcal{H}^2} \right) \nabla^2 \Phi. \quad (2.32)$$

On differentiating this equation with respect to the conformal time and making use of the background equations (2.2a) and (2.4), the definition of the curvature perturbation (2.24) and the Bardeen equation (2.30), we find that the Fourier modes of the curvature perturbation induced by the canonical scalar field are described by the following equation [6, 97]:

$$\mathcal{R}_k'' + 2 \left(\frac{z'}{z} \right) \mathcal{R}_k' + k^2 \mathcal{R}_k = 0, \quad (2.33)$$

where the quantity z is given by

$$z = \left(\frac{a \dot{\phi}}{H} \right) = \left(\frac{a \phi'}{\mathcal{H}} \right). \quad (2.34)$$

Another useful variable which is often introduced while studying the evolution of the perturbations, is the Mukhanov-Sasaki variable v which is defined as [110, 112]

$$v = \mathcal{R} z. \quad (2.35)$$

The Fourier modes of the Mukhanov-Sasaki variable v_k satisfy the following differential equation which is referred to as the Mukhanov-Sasaki equation:

$$v_k'' + \left[k^2 - \left(\frac{z''}{z} \right) \right] v_k = 0. \quad (2.36)$$

On quantization, the variable $\mathcal{R}(\eta, \mathbf{x})$ becomes a quantum operator and can be expressed in terms of the Fourier modes \mathcal{R}_k as follows [6, 113]:

$$\hat{\mathcal{R}}(\eta, \mathbf{x}) = \int \frac{d^3 \mathbf{k}}{(2\pi)^{3/2}} \left[\hat{a}_{\mathbf{k}} \mathcal{R}_k(\eta) e^{i \mathbf{k} \cdot \mathbf{x}} + \hat{a}_{\mathbf{k}}^\dagger \mathcal{R}_k^*(\eta) e^{-i \mathbf{k} \cdot \mathbf{x}} \right], \quad (2.37)$$

where the creation and the annihilation operators $\hat{a}_{\mathbf{k}}$ and $\hat{a}_{\mathbf{k}}^\dagger$ obey the standard commutation relations. At the linear order in the perturbation theory, the power spectrum as well as

the other statistical properties of the scalar perturbations are completely characterized by the two point function of the quantum field $\hat{\mathcal{R}}$ and, therefore, the perturbations generated during inflation are often referred to as Gaussian perturbations. The power spectrum of the scalar perturbations $\mathcal{P}_s(k)$ is then given by the relation

$$\int_0^\infty \frac{dk}{k} \mathcal{P}_s(k) \equiv \int \frac{d^3(\mathbf{x} - \mathbf{x}')}{(2\pi)^3} \langle 0 | \hat{\mathcal{R}}(\eta, \mathbf{x}) \hat{\mathcal{R}}(\eta, \mathbf{x}') | 0 \rangle e^{-i\mathbf{k} \cdot (\mathbf{x} - \mathbf{x}')}, \quad (2.38)$$

where $|0\rangle$ is the vacuum state defined as $\hat{a}_{\mathbf{k}}|0\rangle = 0 \ \forall \mathbf{k}$. Using the decomposition as in Eq. (2.37), the spectrum of the scalar perturbations can be written in terms of the Fourier modes \mathcal{R}_k as [97]

$$\mathcal{P}_s(k) = \left(\frac{k^3}{2\pi^2} \right) |\mathcal{R}_k|^2 = \left(\frac{k^3}{2\pi^2} \right) \left(\frac{|v_k|}{z} \right)^2. \quad (2.39)$$

The perturbation spectrum should, in general, be evaluated at super-Hubble scales [i.e. when $(k/aH) = (k/\mathcal{H}) \ll 1$] when the amplitude of the curvature perturbations approaches a constant value. The spectral index associated with the scalar spectrum n_s is given by the logarithmic derivative of the spectrum and is defined as [97]

$$n_s - 1 = \left(\frac{d \ln \mathcal{P}_s}{d \ln k} \right). \quad (2.40)$$

Note that a scale invariant scalar spectrum corresponds to $n_s = 1$.

2.2.3 The tensor perturbations

Upon taking into account the tensor perturbations to the background metric (2.1), the Friedmann line-element can be described as [4, 5, 6, 7]

$$ds^2 = a^2(\eta) \left[d\eta^2 - (\delta_{ij} + \mathcal{U}_{ij}) dx^i dx^j \right], \quad (2.41)$$

where \mathcal{U}_{ij} is a symmetric, transverse and traceless tensor. The transverse and traceless conditions reduce the number of independent degrees of freedom of \mathcal{U}_{ij} to two, which correspond to the two types of polarization associated with the gravitational waves. The tensor perturbations can be quantized in a similar fashion as the curvature perturbations. In the absence of anisotropic stresses, one arrives at the following differential equation describing the Fourier amplitude \mathcal{U}_k of the gravitational waves [4, 5, 6, 7]:

$$\mathcal{U}_k'' + 2 \left(\frac{a'}{a} \right) \mathcal{U}_k' + k^2 \mathcal{U}_k = 0. \quad (2.42)$$

If we define

$$u = \mathcal{U} a, \quad (2.43)$$

then the differential equation satisfied by the Fourier modes of the variable u is given by

$$u_k'' + \left[k^2 - \left(\frac{a''}{a} \right) \right] u_k = 0. \quad (2.44)$$

It is useful to note that this equation is essentially the same as the Mukhanov-Sasaki equation (2.36) barring the fact that the quantity z is now replaced by the scale factor a . The spectrum of the tensor perturbations $\mathcal{P}_T(k)$ can then be expressed in terms of the Fourier modes \mathcal{U}_k and u_k as follows:

$$\mathcal{P}_T(k) = 2 \left(\frac{k^3}{2\pi^2} \right) |\mathcal{U}_k|^2 = 2 \left(\frac{k^3}{2\pi^2} \right) \left(\frac{|u_k|}{a} \right)^2. \quad (2.45)$$

As in the scalar case, the tensor spectrum should also be evaluated at super-Hubble scales. The additional factor of two in the above expression for the tensor spectrum takes into account the two independent states of polarization of the gravitational waves. The spectral index associated with the tensor spectrum n_T is given by the logarithmic derivative of the spectrum and is defined as [97]

$$n_T = \left(\frac{d \ln \mathcal{P}_T}{d \ln k} \right). \quad (2.46)$$

It should be stressed that, while $n_s = 1$ corresponds to a scale invariant scalar spectrum, a scale invariant tensor spectrum is described by $n_T = 0$. Finally, the tensor-to-scalar ratio r is defined as follows [97]:

$$r(k) \equiv \left(\frac{\mathcal{P}_T(k)}{\mathcal{P}_S(k)} \right). \quad (2.47)$$

As we had mentioned in the previous chapter, the scalar spectral index n_s and the tensor-to-scalar ratio r turn out to be two important inflationary parameters that can be constrained using the data from the various observations.

2.2.4 The Bunch-Davies initial conditions

Before we proceed further, the issue regarding the initial conditions on the perturbations needs to be discussed. Since the various modes exit the Hubble radius during inflation and re-enter during the subsequent radiation dominated epoch, the initial conditions on the perturbations should be imposed at a time when the modes are well inside the Hubble radius,

i.e. when $(k/aH) = (k/\mathcal{H}) \gg 1$. From Eqs. (2.36) and (2.44), it is evident that, in the sub-Hubble limit, the scalar and the tensor modes v_k and u_k behave in the Minkowskian form as $e^{\pm i k \eta}$. The scalar and tensor perturbations being in the vacuum state requires the solutions v_k and u_k to be the positive frequency modes at sub-Hubble scales with the asymptotic form [3, 5]

$$\lim_{(k/aH) \rightarrow \infty} [v_k(\eta), u_k(\eta)] \rightarrow \frac{1}{\sqrt{2k}} e^{-i k \eta}. \quad (2.48)$$

The vacuum state associated with the modes at very early times that exhibit such a behavior is often referred to as the Bunch-Davies vacuum [114].

2.3 The scalar and tensor power spectra in slow roll inflation

In this section, we shall rapidly derive the scalar and tensor power spectra and the spectral indices in the slow roll approximation. As we had discussed in the previous chapter, the HSR parameters turn out to be a better choice to describe the slow roll approximation than the PSR parameters as no additional condition needs to be satisfied for the approximation to be valid. Treating the Hubble parameter H as a function of the scalar field ϕ , the HSR parameters are defined in terms of the Hubble parameter and its derivatives. The first two dimensionless HSR parameters ϵ_H and η_H are defined as follows [42]:

$$\epsilon_H = 2 M_P^2 \left(\frac{H_\phi}{H} \right)^2, \quad (2.49a)$$

$$\eta_H = 2 M_P^2 \left(\frac{H_{\phi\phi}}{H} \right), \quad (2.49b)$$

where $H_\phi \equiv (dH/d\phi)$ and $H_{\phi\phi} \equiv (d^2H/d\phi^2)$. Upon using the background equations, these two parameters can be written as

$$\epsilon_H = - \left(\frac{\dot{H}}{H^2} \right), \quad (2.50a)$$

$$\eta_H = - \left(\frac{\ddot{\phi}}{H\dot{\phi}} \right) = \epsilon_H - \left(\frac{\dot{\epsilon}_H}{2H\epsilon_H} \right). \quad (2.50b)$$

In order to evaluate the scalar and the tensor spectra in slow roll approximation, we start by rewriting the various quantities that appear in the equation of motion for the scalar and the tensor perturbations in terms of these two HSR parameters. Using equation (2.4) and the

expression (2.50a) for the first HSR parameter ϵ_H , the quantity z defined in equation (2.34) can be written as

$$z = \sqrt{2} M_P a \sqrt{\epsilon_H}. \quad (2.51)$$

Using the expressions for z and the HSR parameters, the term (z'/z) that appears in the equation of motion describing the curvature perturbation (2.33) can be written as [99]

$$\left(\frac{z'}{z}\right) = \mathcal{H} (1 + \epsilon_H - \eta_H). \quad (2.52)$$

Again, using these expressions, the term (z''/z) that appears in the Mukhanov-Sasaki equation (2.36) can be expressed as [3, 96, 115, 116]

$$\left(\frac{z''}{z}\right) = \mathcal{H}^2 \left[2 - \epsilon_H + (\epsilon_H - \eta_H) (3 - \eta_H) + \left(\frac{\epsilon'_H - \eta'_H}{\mathcal{H}}\right) \right]. \quad (2.53)$$

Upon using the definition of ϵ_H as in Eq. (2.50a), it can be shown that

$$\left(\frac{a''}{a}\right) = \mathcal{H}^2 (2 - \epsilon_H). \quad (2.54)$$

It should be emphasized that the above expressions are exact and the slow roll approximation has not been imposed in arriving at these expressions. At the leading order in the slow roll approximation³, using the definitions of the first two HSR parameters ϵ_H and η_H and also assuming ϵ_H to be a constant at the same order, we can write

$$\mathcal{H} \simeq - \left[\frac{1}{(1 - \epsilon_H) \eta} \right]. \quad (2.55)$$

On using this relation for \mathcal{H} in the expressions (2.53) and (2.54), at the leading order in the slow roll approximation, we get

$$\left(\frac{z''}{z}\right) \simeq \left(\frac{2 + 6\epsilon_H - 3\eta_H}{\eta^2}\right), \quad (2.56a)$$

$$\left(\frac{a''}{a}\right) \simeq \left(\frac{2 + 3\epsilon_H}{\eta^2}\right), \quad (2.56b)$$

with the HSR parameters being treated as constants. From Eqs. (2.36) and (2.44), it is evident that the solutions to the variables v_k and u_k that satisfy the appropriate initial conditions (2.48) will be given in terms of the Hankel function as [43, 97, 117]

$$[v_k(\eta), u_k(\eta)] = \left(\frac{-\pi \eta}{4}\right)^{1/2} e^{i\pi/2 [\nu+1/2]} H_\nu^{(1)}(-k\eta), \quad (2.57)$$

³Here, by leading order, we refer to the linear order in the slow roll parameters. We shall ignore the terms which are higher order in the slow roll parameters.

where $H_\nu^{(1)}$ is the Hankel function of the first kind and of order ν . The quantity ν for the scalar and the tensor cases is given by

$$\nu_s \simeq \left(\frac{3}{2} + 2\epsilon_H - \eta_H \right), \quad (2.58a)$$

$$\nu_T \simeq \left(\frac{3}{2} + \epsilon_H \right). \quad (2.58b)$$

In order to evaluate the scalar and the tensor spectra in the super-Hubble limit, i.e. as $(-k\eta) \rightarrow 0$, the Hankel functions in the solutions (2.57) should be expanded as a series about the origin. The expansion then results in the following expressions for the scalar and the tensor spectra [3, 43, 97, 115]

$$\begin{aligned} \mathcal{P}_s(k) &= \left(\frac{1}{32\pi^2 M_P^2 \epsilon_H} \right) \left[\frac{|\Gamma(\nu_s)|}{\Gamma(3/2)} \right]^2 \left(\frac{k}{a} \right)^2 \left(\frac{-k\eta}{2} \right)^{(1-2\nu_s)} \\ &= \left(\frac{H^2}{2\pi\dot{\phi}} \right)^2 \left[\frac{|\Gamma(\nu_s)|}{\Gamma(3/2)} \right]^2 2^{(2\nu_s-3)} (1 - \epsilon_H)^{(2\nu_s-1)}, \end{aligned} \quad (2.59a)$$

$$\begin{aligned} \mathcal{P}_T(k) &= \left(\frac{1}{2\pi^2 M_P^2} \right) \left[\frac{|\Gamma(\nu_T)|}{\Gamma(3/2)} \right]^2 \left(\frac{k}{a} \right)^2 \left(\frac{-k\eta}{2} \right)^{(1-2\nu_T)} \\ &= \left(\frac{2H^2}{\pi^2 M_P^2} \right) \left[\frac{|\Gamma(\nu_T)|}{\Gamma(3/2)} \right]^2 2^{(2\nu_T-3)} (1 - \epsilon_H)^{(2\nu_T-1)}, \end{aligned} \quad (2.59b)$$

where the second equalities have been expressed in terms of the quantities evaluated at the Hubble exit [i.e. at $(-k\eta) = (1 - \epsilon_H)^{-1}$]. At the leading order in the slow roll approximation, the amplitudes of the scalar and the tensor spectra are given by [3, 43, 97]

$$\mathcal{P}_s(k) \simeq \left(\frac{H^2}{2\pi\dot{\phi}} \right)_{k=aH}^2, \quad (2.60a)$$

$$\mathcal{P}_T(k) \simeq \left(\frac{8}{M_P^2} \right) \left(\frac{H}{2\pi} \right)_{k=aH}^2, \quad (2.60b)$$

with the quantities on the right hand side to be evaluated when the modes cross the Hubble radius. In the slow roll limit, upon using the corresponding background equations (1.25), the scalar and the tensor spectral amplitudes can be expressed in terms of the potential and its derivative as follows [3, 43, 97]

$$\mathcal{P}_s(k) \simeq \left(\frac{1}{12\pi^2 M_P^6} \right) \left(\frac{V^3}{V_\phi^2} \right)_{k=aH}, \quad (2.61a)$$

$$\mathcal{P}_T(k) \simeq \left(\frac{2}{3\pi^2} \right) \left(\frac{V}{M_P^4} \right)_{k=aH}. \quad (2.61b)$$

Using the expressions (2.60) for the power spectra and the definitions (2.40) and (2.46) of the spectral indices, it can be easily shown that

$$n_s \simeq (1 - 4\epsilon_H + 2\eta_H), \quad (2.62a)$$

$$n_T \simeq -2\epsilon_H. \quad (2.62b)$$

It is evident from these expressions that, in the slow roll approximation, when the slow roll parameters are very small, the scalar and the tensor spectra will be nearly scale invariant. Moreover, in the slow roll limit, the tensor-to-scalar ratio is found to be

$$r \simeq 16\epsilon_H = -8n_T. \quad (2.63)$$

Since, $\epsilon_H \ll 1$ in the slow roll limit, the amplitude of the tensor perturbations prove to be smaller than the amplitude of the scalar perturbations. The above expression is the so-called consistency relation for single field slow roll inflation [3, 43, 96, 97].

2.4 The curvature perturbations induced by the tachyon

In this section, we shall first summarize the background equations in the presence of the tachyon, and then discuss the equations describing the curvature perturbations induced by the tachyon. For the case of the tachyon, say, T , described by the potential $V(T)$, the background energy density ρ_T and the pressure p_T are given by [54, 55, 92]

$$\rho_T = \left(\frac{V(T)}{\sqrt{1 - \dot{T}^2}} \right), \quad (2.64a)$$

$$p_T = - \left(V(T) \sqrt{1 - \dot{T}^2} \right). \quad (2.64b)$$

In the spatially flat, Friedmann background that we shall be considering, the equation of motion for the tachyon T is given by [55, 92]

$$\left(\frac{\ddot{T}}{1 - \dot{T}^2} \right) + 3H\dot{T} + \left(\frac{V_T}{V} \right) = 0, \quad (2.65)$$

where $V_T \equiv (dV/dT)$.

If we denote the perturbation in the tachyon as δT , then, it is straightforward to show that, the perturbations in the energy density, the momentum flux and the pressure of the tachyon

are given by

$$\delta\rho_T = \left(\frac{V_T \delta T}{\sqrt{1 - \dot{T}^2}} \right) + \left(\frac{V \dot{T}}{(1 - \dot{T}^2)^{3/2}} \right) (\delta\dot{T} - A \dot{T}), \quad (2.66a)$$

$$\partial_i \delta q_T = \left(\frac{V \dot{T}}{a \sqrt{1 - \dot{T}^2}} \right) (\partial_i \delta T), \quad (2.66b)$$

$$\delta p_T = - \left(V_T \delta T \sqrt{1 - \dot{T}^2} \right) + \left(\frac{V \dot{T}}{\sqrt{1 - \dot{T}^2}} \right) (\delta\dot{T} - A \dot{T}), \quad (2.66c)$$

where A is the metric perturbation that appears in the perturbed Friedmann line-element (2.5). As in the case of the canonical scalar field, the tachyons possess no anisotropic stress and, therefore, $\Phi = \Psi$. On substituting these expressions for $\delta\rho_T$, δq_T and δp_T in the first order Einstein equations (2.21), we find that the Bardeen potential Φ induced by the tachyonic perturbations satisfies the following differential equation:

$$\Phi'' + 3\mathcal{H} (1 + c_A^2) \Phi' - c_A^2 \nabla^2 \Phi + [2\mathcal{H}' + (1 + 3c_A^2) \mathcal{H}^2] \Phi = (c_s^2 - c_A^2) \nabla^2 \Phi, \quad (2.67)$$

where $c_s^2 = (1 - \dot{T}^2)$ is referred to as the effective speed of sound (see, for instance, Ref. [92]). Upon comparing the above equation with Eq. (2.22), we find that the non-adiabatic pressure perturbation associated with the tachyon is given by

$$\delta p_T^{\text{NA}} = \left(\frac{c_s^2 - c_A^2}{4\pi G a^2} \right) \nabla^2 \Phi. \quad (2.68)$$

The quantity δp_T^{NA} is usually related to the entropy perturbation \mathcal{S} as follows (see, for instance, Ref. [118]):

$$\delta p_T^{\text{NA}} = \left(\frac{p'_T}{\mathcal{H}} \right) \mathcal{S}. \quad (2.69)$$

On making use of Eqs. (2.68) and (2.69), we obtain the entropy perturbation \mathcal{S} to be [92]

$$\mathcal{S} = \left(\frac{\mathcal{H}}{4\pi G a^2 p'_T} \right) (c_s^2 - c_A^2) \nabla^2 \Phi. \quad (2.70)$$

Therefore, for the tachyonic case, the equation (2.25) describing the evolution of the curvature perturbation simplifies to

$$\mathcal{R}' = - \left(\frac{4\pi G a^2 p'_T}{\mathcal{H}' - \mathcal{H}^2} \right) \left(\frac{c_s^2}{c_s^2 - c_A^2} \right) \mathcal{S} = - \left(\frac{\mathcal{H} c_s^2}{\mathcal{H}' - \mathcal{H}^2} \right) \nabla^2 \Phi. \quad (2.71)$$

Upon using this relation alongwith the definition (2.24) and the equation (2.67) describing the evolution of the Bardeen potential, we find that the Fourier modes of the curvature perturbation induced by the tachyon are described by the differential equation [92]

$$\mathcal{R}_k'' + 2 \left(\frac{z'}{z} \right) \mathcal{R}_k' + c_s^2 k^2 \mathcal{R}_k = 0, \quad (2.72)$$

where the quantity z is given by

$$z = \left(\frac{a}{H} \right) \left(\frac{\rho_T + p_T}{c_s^2} \right)^{1/2} = \left(\frac{\sqrt{3} M_{\text{P}} a \dot{T}}{\sqrt{1 - \dot{T}^2}} \right). \quad (2.73)$$

The Mukhanov-Sasaki variable v for the tachyon can be defined as in the case of the canonical scalar field [cf. Eq. (2.35)] and the Fourier modes of the Mukhanov-Sasaki variable v_k satisfy the following differential equation:

$$v_k'' + \left[c_s^2 k^2 - \left(\frac{z''}{z} \right) \right] v_k = 0. \quad (2.74)$$

2.5 Evolution of the curvature perturbations at super-Hubble scales

The equation (2.72) that describes the evolution of the curvature perturbations is completely equivalent to the equation of motion of a harmonic oscillator with the time-dependent damping term (z'/z) . It is evident from this correspondence that the curvature perturbations can be expected to grow at super-Hubble scales if there exists a period during which the damping term proves to be negative [99, 100]. Actually, as we shall see, if (z'/z) turns out to be negative for some amount of time, then, for a certain range of modes, the amplitude of the curvature perturbations is enhanced at super-Hubble scales, while the amplitude of another range of modes is suppressed, when compared to their values at Hubble exit. We shall now outline as to how the quantity (z'/z) turns out to be negative for the tachyonic case during a period of fast roll inflation or when there is a break in inflation.

As we had mentioned in the previous chapter, the slow roll approximation is an expansion in terms of small parameters that are defined as derivatives either of the potential $V(T)$ or the Hubble parameter H [42]. However, for our discussion below, we shall make use of the horizon flow parameters which are defined as the derivatives of the Hubble parameter H

2.5. EVOLUTION OF THE CURVATURE PERTURBATIONS AT SUPER-HUBBLE SCALES

with respect to the number of e -folds N as follows [119]:

$$\epsilon_0 \equiv \left(\frac{H_*}{H} \right) \quad \text{and} \quad \epsilon_{i+1} \equiv \left(\frac{d \ln |\epsilon_i|}{dN} \right) = \left(\frac{\dot{\epsilon}_i}{H \epsilon_i} \right) \quad \text{for } i \geq 0, \quad (2.75)$$

where H_* is the Hubble parameter evaluated at some given time, and inflation occurs when $\epsilon_1 < 1$. For the case of the tachyon we are considering here, the first two horizon flow functions are given by [92]

$$\epsilon_1 = \left(\frac{3 \dot{T}^2}{2} \right) \quad \text{and} \quad \epsilon_2 = \left(\frac{2 \ddot{T}}{H \dot{T}} \right). \quad (2.76)$$

We find that the quantity (z'/z) can be expressed in terms of these two horizon flow functions as follows:

$$\left(\frac{z'}{z} \right) = (a H) \left(1 + \left(\frac{\epsilon_2}{2} \right) \left[\frac{1}{1 - (2 \epsilon_1/3)} \right] \right). \quad (2.77)$$

It is apparent from this expression that, in the slow roll limit, i.e. when $(\epsilon_1, \epsilon_2) \ll 1$, $(z'/z) \simeq (a H) = \dot{a}$ which, in an expanding universe, is a positive definite quantity. Clearly, (z'/z) cannot be negative in the slow roll regime. However, note that (z'/z) can become negative if the following condition is satisfied:

$$\epsilon_2 < -2 \left[1 - \left(\frac{2 \epsilon_1}{3} \right) \right]. \quad (2.78)$$

Such a situation can occur either when there is a break in inflation, say, when $\epsilon_1 \simeq 1$ and $\epsilon_2 < -(2/3)$ or during a period of fast roll inflation, i.e. when $\epsilon_1 \ll 1$ and $\epsilon_2 < -2$. In the following subsection, we shall discuss a specific example of the second scenario.

2.5.1 A specific example

To explicitly illustrate the phenomenon of the enhancement or the suppression of the amplitude of the curvature perturbations at super-Hubble scales, we shall work with the following potential

$$V(T) = V_0 (1 + V_1 T^4), \quad (2.79)$$

where V_0 and V_1 are positive constants. For this potential, we find that, in the T - \dot{T} plane, there exists only one finite critical point at $(T = 0, \dot{T} = 0)$ for the equation of motion (2.65). A linear stability analysis about this point immediately suggests that the critical point is a stable fixed point. This implies that, regardless of the initial conditions that the tachyon

starts rolling from, it will always approach the critical point asymptotically. Also, we find that, for certain values of the parameters V_0 and V_1 , all the trajectories in the phase space rapidly approach an attractor trajectory which has the following three regimes for the field evolution: $\dot{T} \ll 1$, $\dot{T} \lesssim 1$, and $\dot{T} \ll 1$ again. It is then clear from the expressions (2.76) for ϵ_1 and ϵ_2 that, as the field starts rolling down the potential from a large value, ϵ_1 can grow from a small value to some maximum value and then decrease to a small value again. Also, this behavior will allow ϵ_2 to become negative during the period when the field is decelerating—a feature that is necessary to achieve the condition (2.78). However, the minimum value attained by ϵ_2 and the duration for which it remains negative depends on the values of the parameters V_0 and V_1 that describe the potential.

We now need to choose the values of the parameters V_0 and V_1 of the potential so that the condition (2.78) is satisfied. A general analysis in terms of the horizon flow functions is not possible without explicitly solving the equation of motion for T . Hence, instead of the horizon flow functions, we shall now make use of the PSR parameters to estimate these values [120]. For the case of the tachyon we are considering here, the first two PSR parameters are defined as [56]

$$\varepsilon_v = \left(\frac{M_P^2}{2} \right) \left(\frac{V_T^2}{V^3} \right), \quad (2.80a)$$

$$\delta_v = M_P^2 \left[3 \left(\frac{V_T^2}{V^3} \right) - 2 \left(\frac{V_{TT}}{V^2} \right) \right], \quad (2.80b)$$

where $V_{TT} \equiv (d^2V/dT^2)$. For M_P set to unity, we find that $\delta_v < -2$ provided $V_1 > 0.036^4$.

We have solved the background equations and the equation describing the curvature perturbation numerically. The results that we present here are for the following values of the potential parameters: $V_0 = 0.5$ and $V_1 = 0.18$. We have chosen the standard initial conditions at sub-Hubble scales corresponding to the Bunch-Davies vacuum for the curvature perturbations [cf. Eq. (2.48)]. The initial conditions we have imposed are easily expressed in terms of the Mukhanov-Sasaki variable v_k which are as follows:

$$v_k = \left(\frac{1}{2\omega_k} \right)^{1/2} \quad \text{and} \quad v'_k = -i \left(\frac{\omega_k}{2} \right)^{1/2}, \quad (2.81)$$

⁴Actually, the PSR parameters and the horizon flow functions are of the same order only in the slow roll limit. Their equivalence will necessarily break down in the fast roll regime we are interested in. However, we find that the value for V_1 we shall work with (which is greater than 0.036) indeed leads to the required behavior.

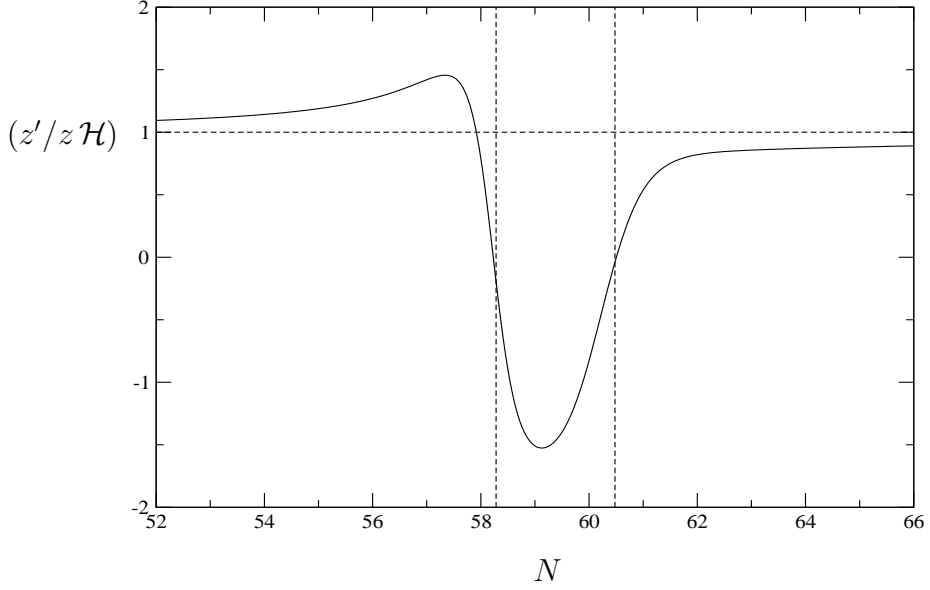


Figure 2.1: The evolution of the quantity $(z'/z\mathcal{H})$ has been plotted as a function of the number of e -folds N . The vertical lines indicate the regime where $(z'/z\mathcal{H})$ is negative. Note that it remains close to unity during the two slow roll regimes, but it turns negative for a little less than three e -folds between N of 58 and 61 during the fast roll phase.

where

$$\omega_k^2 = [(k c_s)^2 - (z''/z)], \quad (2.82)$$

and we have imposed these conditions at a time when all the modes of interest are well inside the Hubble radius [121, 122].

In Fig. 2.1, we have plotted the quantity $(z'/z\mathcal{H})$ as a function of the number of e -folds N . It is clear from the figure that $(z'/z\mathcal{H})$ is negative during $58 < N < 61$. In Fig. 2.2, we have plotted the amplitude of the curvature perturbation \mathcal{R}_k as a function of N for two modes which are at super-Hubble scales when the slow roll to fast roll transition takes place. It is evident from the figure that, while the amplitude of \mathcal{R}_k corresponding to the mode with wavenumber $k = 0.1 \text{ Mpc}^{-1}$ is enhanced at super-Hubble scales, the amplitude of the mode with wavenumber $k = 0.03 \text{ Mpc}^{-1}$ is suppressed at late times, when compared to their values at Hubble exit⁵. We should mention that, to highlight these behavior, we have

⁵In Refs. [99, 100], the authors emphasize the point that, a period of deviation from slow roll inflation can

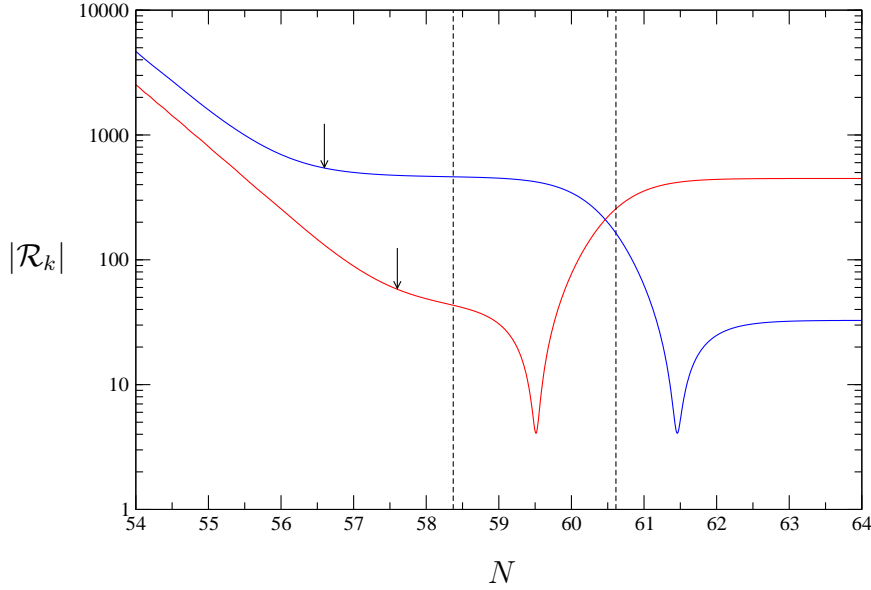


Figure 2.2: The evolution of the amplitude of the curvature perturbation \mathcal{R}_k has been plotted as a function of the number of e -folds N for the modes with wavenumbers $k = 0.03 \text{ Mpc}^{-1}$ (in blue) and $k = 0.1 \text{ Mpc}^{-1}$ (in red). As in the previous figure, the vertical lines delineate the regime where $(z'/z\mathcal{H})$ is negative. The arrows indicate the time at which the modes leave the Hubble radius, i.e. when $(k c_s) = (a H)$. Note that the amplitude of the curvature perturbation for the $k = 0.1 \text{ Mpc}^{-1}$ mode is enhanced at super-Hubble scales (by a factor of about 10), while the amplitude of the $k = 0.03 \text{ Mpc}^{-1}$ mode is suppressed (by a factor of about 20), when compared to their values at Hubble exit. We should mention that these two particular modes have been chosen for the reason that, in the specific example that we are considering, they exhibit sufficient extent of amplification or suppression at super-Hubble scales.

chosen modes that exhibit sufficient amplification or suppression for the specific model and parameters we are considering here. Finally, we should also stress the point that, had there been no transition to the fast roll regime, the amplitude of the curvature perturbations would have frozen at their value at Hubble exit [123].

enhance the amplitude of the curvature perturbations at super-Hubble scales, but seem to overlook the fact that it can also lead to their suppression. Actually, they also encounter the suppression of the amplitude in the examples they consider. In Figs. 1 and 2 of Ref. [100], they plot the power spectrum evaluated at the end of inflation as well as at a time soon after the modes leave the Hubble radius. It is clear from these two figures that, while a certain range of modes are amplified at super-Hubble scales, another range of modes are suppressed.

2.6 Entropy perturbations as the source of evolution at super-Hubble scales

In this section, we shall outline as to how the entropy perturbation \mathcal{S} grows during the fast roll regime, and how such a growth in turn acts as the source for the change in the amplitude of the curvature perturbation at super-Hubble scales.

On using the expression (2.70) for the entropy perturbation \mathcal{S} , we find that the differential equations (2.25) and (2.72) describing the evolution of \mathcal{R} can be written in Fourier space as the following two first order equations [99]:

$$\left(\frac{\mathcal{R}'_k}{aH}\right) = \mathcal{A} \mathcal{S}_k, \quad (2.83a)$$

$$\left(\frac{\mathcal{S}'_k}{aH}\right) = \mathcal{B} \mathcal{S}_k - \mathcal{C} \left(\frac{k^2}{a^2 H^2}\right) \mathcal{R}_k. \quad (2.83b)$$

The quantities \mathcal{A} , \mathcal{B} and \mathcal{C} appearing in the above two equations can be expressed in terms of the first three horizon flow parameters as

$$\mathcal{A} = (3 - 2\epsilon_1) \left(\frac{3 - 6\epsilon_1 + \epsilon_2}{6 - 12\epsilon_1 + \epsilon_2}\right), \quad (2.84a)$$

$$\begin{aligned} \mathcal{B} = & \left(\frac{1}{(3 - 2\epsilon_1)(6 - 12\epsilon_1 + \epsilon_2)(3 - 6\epsilon_1 + \epsilon_2)}\right) \\ & \times \left[(2\epsilon_1\epsilon_2 [3 - 72\epsilon_1^2 + \epsilon_2(12 + \epsilon_2) - 6\epsilon_1(12 + 2\epsilon_2 + \epsilon_3)] - 9\epsilon_2\epsilon_3) \right. \\ & \left. - (6 - 12\epsilon_1 + \epsilon_2)(3 - 6\epsilon_1 + \epsilon_2)(9 - 9\epsilon_1 + 3\epsilon_2 + 2\epsilon_1^2) \right], \end{aligned} \quad (2.84b)$$

$$\mathcal{C} = \left(\frac{1}{3}\right) \left(\frac{6 - 12\epsilon_1 + \epsilon_2}{3 - 6\epsilon_1 + \epsilon_2}\right), \quad (2.84c)$$

with the third horizon flow parameter ϵ_3 given by

$$\epsilon_3 = \left(\frac{1}{H}\right) \left[\left(\frac{\ddot{T}}{\dot{T}}\right) - \left(\frac{\ddot{T}}{\dot{T}}\right) - \left(\frac{\dot{H}}{H}\right) \right]. \quad (2.85)$$

We shall now make use of the coupled first order differential equations (2.83) to understand the evolution of the entropy perturbations at super-Hubble scales and its effect on the curvature perturbations during the slow roll and the fast roll regimes.

Let us first discuss the behavior in the slow roll regime. During slow roll, we can ignore the horizon flow parameters when compared to the numerical constants in the above expressions for \mathcal{A} , \mathcal{B} and \mathcal{C} . Since we are interested in the evolution at super-Hubble scales, one

would be tempted to ignore the term involving \mathcal{R}_k in Eq. (2.83b). If we can indeed do so, we can immediately conclude that $\mathcal{S}_k \propto e^{-3N}$ during an epoch of slow roll inflation. However, the self-consistent numerical solutions we have obtained to equations (2.83) indicate otherwise. In Fig. 2.3, using the numerical solutions to the curvature perturbations \mathcal{R}_k we had discussed in the last section and the relation (2.83a), we have plotted the evolution of the entropy perturbation \mathcal{S}_k for the two modes $k = 0.03 \text{ Mpc}^{-1}$ and $k = 0.1 \text{ Mpc}^{-1}$ as a function of the number of e -folds. It is clear from the figure that while there is indeed an intermediate period in the slow roll phase when $\mathcal{S}_k \propto e^{-3N}$, the late time behavior actually has the form $\mathcal{S}_k \propto e^{-2N}$. In fact, we find that all the modes that leave the Hubble radius before the transition to fast roll exhibit such a behavior. We should point out here that similar conclusions have been arrived at earlier for the case of the perturbations induced by the canonical scalar field [99].

During a period of fast roll inflation, in contrast to the slow roll case, we cannot ignore the horizon flow parameters in the quantities \mathcal{A} , \mathcal{B} and \mathcal{C} . If we now choose to neglect the term involving \mathcal{R}_k in Eq. (2.83b), we find that the equation reduces to

$$\left(\frac{\mathcal{S}'_k}{aH} \right) \simeq (\mathcal{B} \mathcal{S}_k). \quad (2.86)$$

Moreover, we find that, on using the background equations, we can rewrite the expression (2.85) for ϵ_3 as follows:

$$\begin{aligned} \epsilon_3 = & -\left(\frac{3}{2}\right) + \left(\frac{7\epsilon_1}{2}\right) - \left(\frac{\epsilon_2}{4}\right) - \left(\frac{\epsilon_1 \epsilon_2}{2(3-2\epsilon_1)}\right) \\ & + \left(\frac{3\epsilon_1}{\epsilon_2}\right) - \left(\frac{V_{TT}}{VH^2}\right) \left(\frac{1}{\epsilon_2}\right) \left[1 - \left(\frac{2\epsilon_1}{3}\right)\right]. \end{aligned} \quad (2.87)$$

If we now assume that $\epsilon_1 \ll 1$, and make the additional assumption that $(V_{TT}/VH^2) \ll 1^6$, we find that ϵ_3 simplifies to [99]

$$\epsilon_3 \simeq -\left(\frac{3}{2}\right) - \left(\frac{\epsilon_2}{4}\right). \quad (2.88)$$

On substituting this value in the expression (2.84b) for \mathcal{B} and assuming that $\epsilon_2 \simeq -5$ (which is roughly the largest value of ϵ_2 in the fast roll regime for our choice of parameters), we

⁶We should point out here that, for the case of the standard scalar field, the quantity (V_{TT}/H^2) is actually the second potential slow roll parameter. However, for the tachyon, the equivalent quantity turns out to be (V_{TT}/VH^2) , and the extra factor of V in the denominator is due to the form of the tachyonic action.

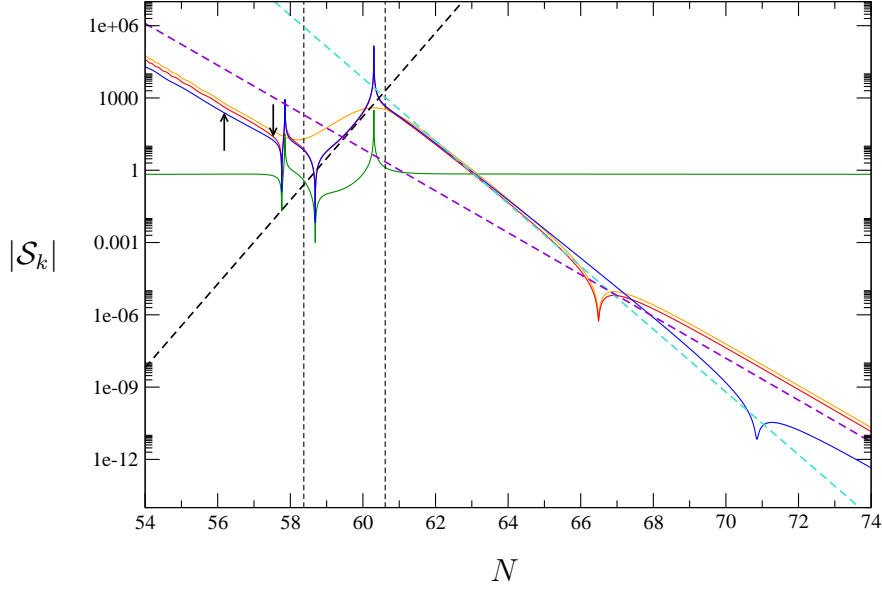


Figure 2.3: The evolution of the amplitude of the entropy perturbation \mathcal{S}_k is plotted as a function of the number of e -folds N for the two modes $k = 0.03 \text{ Mpc}^{-1}$ (in blue) and $k = 0.1 \text{ Mpc}^{-1}$ (in red) we had considered in the previous figure. The dashed lines in black, turquoise and violet indicate the $e^{(4N)}$, $e^{-(3N)}$ and $e^{-(2N)}$ behavior, respectively. The vertical lines again delineate the fast roll regime and, as before, the arrows indicate the time at which the modes leave the Hubble radius. We have also plotted the quantities $(1/\mathcal{A})$ (in green) and $(|\mathcal{R}'_k|/aH)$ (in orange) for the mode $k = 0.1 \text{ Mpc}^{-1}$. The former is discontinuous while the latter is continuous, and it is the former quantity that leads to the discontinuities in the evolution of \mathcal{S}_k . The conclusions we have discussed in the text—the $e^{(4N)}$ growth of the entropy perturbation during fast roll, the intermediate $e^{-(3N)}$ slow roll behavior and the late time $e^{-(2N)}$ slow roll decay—are evident from the figure. It is also important to note that the entropy perturbations associated with both the modes evolve in a similar fashion during the fast roll phase.

obtain that

$$\mathcal{S}_k \propto e^{4N}. \quad (2.89)$$

As we have illustrated in Fig. 2.3, this rough estimate is corroborated by the numerical result we obtain. It is then evident from equation (2.83a) that it is such a rapid growth of the entropy perturbation during the fast roll regime (instead of a slow roll decay) that is responsible for the change in the amplitude of the curvature perturbation at super-Hubble scales. However, we should add that a rapid growth of entropy perturbations is exhibited

only by modes that leave the Hubble radius just before the transition to the fast roll phase. We find that the earlier the modes leave the Hubble radius, less rapidly do their entropy perturbations grow during the fast roll phase. Evidently, the longer a mode has been outside the Hubble radius before the fast roll transition, the more suppressed the entropy perturbation is, and lesser is its growth during the fast roll phase. Therefore, its ability to affect the curvature perturbation gets suppressed correspondingly [123].

The following clarifying remarks are in order at this stage of our discussion. To begin with, we should reiterate the point we had made earlier, viz. that, in the absence of a transition to the fast roll regime, the amplitude of the curvature perturbations would have frozen at their value at Hubble exit. Also, since, at sub-Hubble scales, the modes do not feel the effect of the background quantities, the transition has virtually no effect on those modes that are well within the Hubble radius during the period of fast roll inflation. In fact, the fast roll regime has the maximum effect on the modes that leave the Hubble radius just before the transition. (As we mentioned, it is for this reason that, in Figs. 2.2 and 2.3, we have chosen modes that leave the Hubble scale just before the transition to the fast roll regime takes place and which exhibit sufficient extent of amplification or suppression.) While the amplitude of a certain range of modes is indeed enhanced at super-Hubble scales as has been noticed earlier in the case of the canonical scalar field [99], we find that, actually, there also exists a range of modes whose amplitude is *suppressed* at super-Hubble scales, when compared to their value at Hubble exit. This is evident from Fig. 2.6 wherein we have plotted the power spectrum evaluated soon after Hubble exit as well as the spectrum computed at the end of inflation. Moreover, the extent of the change in the amplitude of the curvature perturbations proves to be smaller and smaller for modes that leave the Hubble radius earlier and earlier before the transition. Clearly, this is due to the combined effect of the slower growth during the fast roll phase and the exponential suppression of the entropy perturbations far outside the Hubble radius.

2.7 The long wavelength approximation

In the previous section, working in the fluid picture, we had discussed as to how the growth of entropy perturbations acts as the source for the evolution of the curvature perturbations at super-Hubble scales during a period of fast roll inflation. In this section, extending the

earlier result for the canonical scalar field [100], we evaluate the power spectrum in the long wavelength approximation and show that it matches the exact spectrum obtained numerically, quite well. Since the analysis for the tachyon is essentially similar to that of the canonical scalar field, rather than repeat the discussion, we shall simply point out the difference between the two cases and present the final results.

As far as the evolution of the curvature perturbation goes, the only difference between the canonical scalar field and the tachyon is the factor of c_s^2 that appears as the coefficient of k^2 in Eq. (2.72). The effective speed of sound c_s turns out to be unity for the standard scalar field. In the earlier analysis for the canonical scalar field [100], the amplitude of curvature perturbation at the end of inflation was related to its value soon after Hubble exit in terms of quantities involving the function z at the $\mathcal{O}(k^2)$ in the long wavelength approximation. Therefore, the corresponding result for the tachyon essentially involves suitably replacing the quantity k^2 with $(c_s^2 k^2)$. We find that, at the $\mathcal{O}(k^2)$, the amplitude of the curvature perturbation at the end of inflation, say, at η_* , can be related to its amplitude soon after Hubble exit, say, at η_k , by the following relation:

$$\mathcal{R}_k(\eta_*) = [\alpha_k \mathcal{R}_k(\eta_k)], \quad (2.90)$$

where α_k is given by

$$\alpha_k = [1 + D_k(\eta_k) - F_k(\eta_k)]. \quad (2.91)$$

The quantities D_k and F_k in the above expression for α_k are described by the following integrals involving the functions $z(\eta)$ and $c_s(\eta)$:

$$D_k(\eta) \simeq \mathcal{H}_k \int_{\eta}^{\eta_*} d\eta_1 \left(\frac{z^2(\eta_k)}{z^2(\eta_1)} \right) \quad (2.92)$$

and

$$F_k(\eta) \simeq k^2 \int_{\eta}^{\eta_*} \frac{d\eta_1}{z^2(\eta_1)} \int_{\eta_k}^{\eta_1} d\eta_2 [c_s^2(\eta_2) z^2(\eta_2)] \quad (2.93)$$

with \mathcal{H}_k denoting the conformal Hubble parameter evaluated at η_k .

As we had pointed out earlier, during slow roll inflation, $(z'/z) \simeq (aH) = \dot{a}$. In other words, in the slow roll regime, z is a monotonically increasing quantity. Therefore, in such a regime, the quantity D_k remains small and the contribution due to F_k —since it is proportional to k^2 —can be ignored at extreme super-Hubble scales. However, the contributions

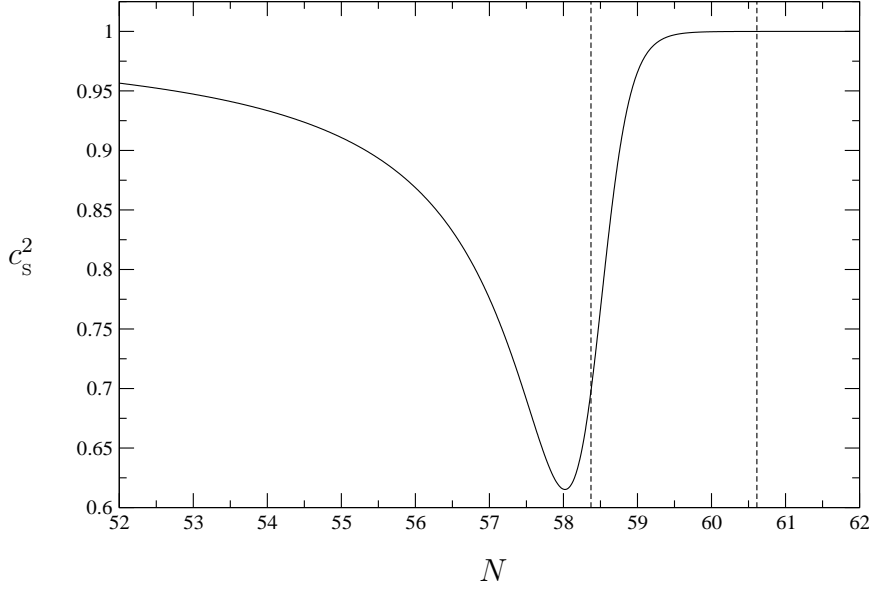


Figure 2.4: The evolution of the effective speed of sound c_s^2 has been plotted as a function of the number of e -folds N . As in the earlier figures, the vertical lines indicate the fast roll regime. We find that $0.62 < c_s^2 < 1$ for the potential and the parameters we are working with.

due to these two terms cannot be neglected if these quantities turn out to be larger than unity. Recall that $c_s^2 = (1 - \dot{T}^2)$ and, hence, $0 \leq c_s^2 \leq 1$. It is then clear from the above integrals for D_k and F_k that they can be large if, for a given mode, there exists an epoch during which $z(\eta)$ at super-Hubble scales is much smaller than the corresponding value when the mode left the Hubble radius. We find that indeed such a situation arises during the fast roll regime in the specific example we had discussed in the last section. For the potential and the parameters we are working with, we find that $0.62 < c_s^2 < 1$, which we have plotted in Fig. 2.4. And, in Fig. 2.5, we have plotted the quantity z^2 as a function of the number of e -folds N . It is the dip in the quantity z^2 during the fast roll regime that turns out to be responsible for the change in the amplitude of the curvature perturbations at super-Hubble scales.

In Fig. 2.6, using the numerical integration of the modes we had discussed in the last section, we have plotted the power spectrum evaluated at the end of inflation as well as the spectrum that has been obtained in the long wavelength approximation using the rela-

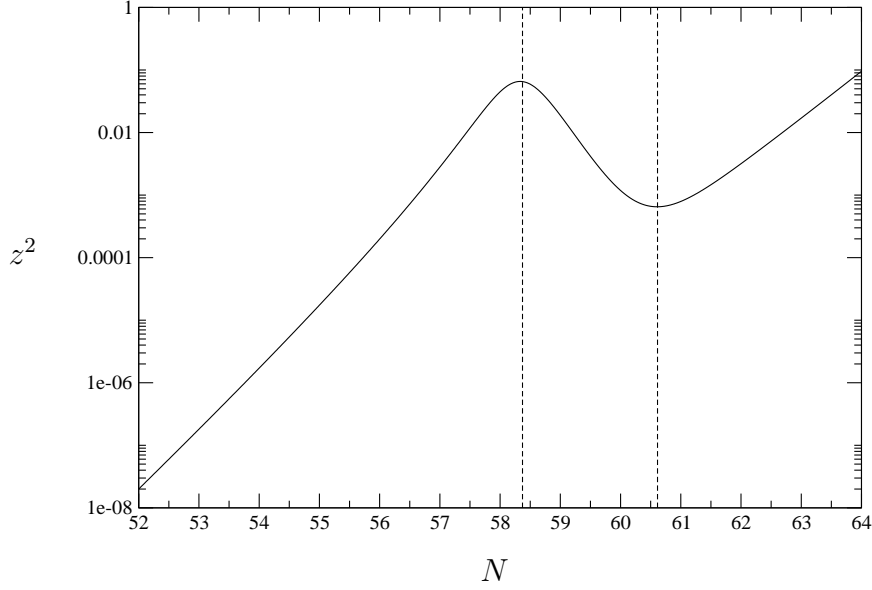


Figure 2.5: The evolution of the quantity z^2 has been plotted as a function of the number of e -folds N . Note the dip during the fast roll regime that is outlined by the vertical lines. It is this dip that is responsible for $(z'/z\mathcal{H})$ being negative, which, in turn, leads to the change in the amplitude of the curvature perturbations at super-Hubble scales.

tion (2.90). We have also plotted the power spectrum evaluated soon after the modes leave the Hubble radius. The figure clearly illustrates the following three points. Firstly, the spectrum evaluated at the $\mathcal{O}(k^2)$ in the long wavelength limit proves to be quite a good fit of the actual spectrum. Secondly, there is a considerable difference between the power spectrum that has been evaluated at the end of inflation and the spectrum that has been evaluated soon after Hubble exit. The difference is, in particular, large for the modes that leave the Hubble radius just before the fast roll regime. Thirdly, while the amplitude of the modes at super-Hubble scales in the wavenumber range $0.01 \lesssim k \lesssim 0.04 \text{ Mpc}^{-1}$ is suppressed when compared to its value soon after Hubble exit, the amplitude of the modes in the range $0.04 \lesssim k \lesssim 0.1 \text{ Mpc}^{-1}$ is enhanced.

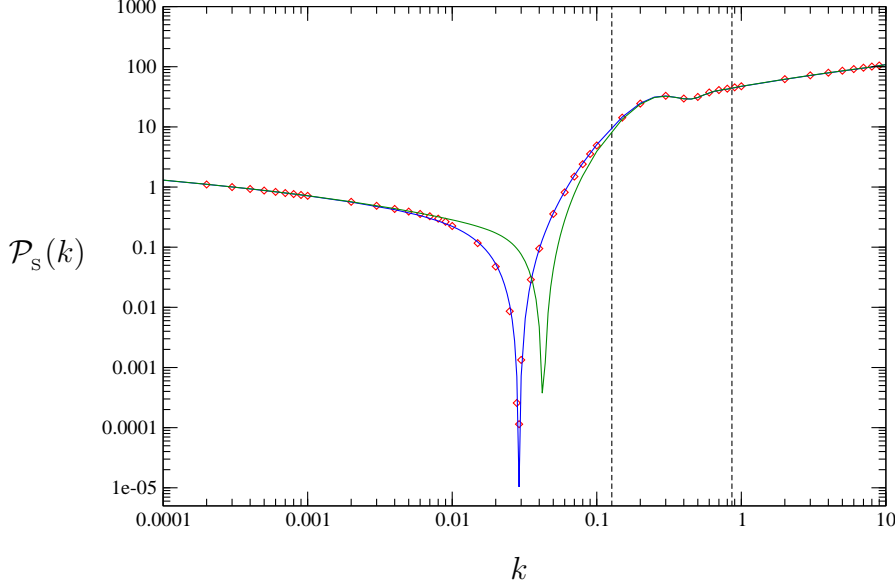


Figure 2.6: Plots of the scalar power spectrum that has been evaluated at the end of inflation through the numerical integration of the modes (in blue) as well as the spectrum that has been obtained using the long wavelength approximation (in red). The spectrum evaluated soon after the modes leave the Hubble radius (when $(k c_s / a H) = 0.1$) has also been plotted (in green). The modes within the vertical lines leave the Hubble radius during the fast roll regime. It is clear from the figure that the power spectrum evaluated in the long wavelength approximation agrees quite well with the actual spectrum. However, there is a substantial difference between the power spectrum evaluated near Hubble exit and the spectrum evaluated at the end of inflation. The difference is, in particular, large for those modes whose Hubble exit occurs just before the period of fast roll inflation. Note that, while the amplitude of the modes at super-Hubble scales in the wavenumber range $0.01 \lesssim k \lesssim 0.04 \text{ Mpc}^{-1}$ is suppressed when compared to its value near Hubble exit, the amplitude of the modes in the range $0.04 \lesssim k \lesssim 0.1 \text{ Mpc}^{-1}$ is enhanced. Essentially, the valley in the power spectrum computed near Hubble exit has shifted towards smaller k when the spectrum is evaluated in the super-Hubble limit.

2.8 Non-trivial evolution of the curvature perturbations at super-Hubble scales—Simple analytic examples

As we had discussed earlier, the amplitude of the curvature perturbations can be affected at super-Hubble scales if there exists a period during which the time-dependent damping term (z'/z) turns out to be negative. An equivalent condition for the amplification of the

curvature perturbations at super-Hubble scales seems to be that there exists an epoch during which $z^2(\eta) \ll z^2(\eta_k)$, where $\eta = \eta_k$ is some instant shortly after the mode crosses the Hubble radius [100]. In this section, we shall present two simple and analytically tractable examples wherein the amplitude of the curvature perturbations induced by the canonical scalar field is enhanced at super-Hubble scales, when compared to their values at Hubble exit.

2.8.1 Example I

Note that when z is a constant or when it is proportional to η , the quantity (z''/z) vanishes and, hence, the solutions to the Mukhanov-Sasaki equation (2.36) are just plane wave solutions i.e. $e^{\pm i k \eta}$ [124, 125]. We shall utilize these solutions to illustrate the non-trivial evolution of the curvature perturbations at super-Hubble scales. Consider a scenario where $z(\eta)$ makes a transition from a constant value to another constant value at late times. The behavior of $z(\eta)$ can be described as follows:

$$z(\eta) = \alpha, \quad \eta \leq \eta_1, \quad (2.94a)$$

$$z(\eta) = -\beta \eta + \gamma, \quad \eta_1 \leq \eta \leq \eta_2, \quad (2.94b)$$

$$z(\eta) = \delta, \quad \eta \geq \eta_2. \quad (2.94c)$$

where α, β, γ and δ are constants and $\eta = \eta_1$ indicates the time when the mode crosses the Hubble radius. Demanding the continuous behavior of $z(\eta)$ at η_1 and η_2 , the coefficients β and γ can be written as

$$\beta = - \left(\frac{\alpha - \delta}{\eta_1 - \eta_2} \right) \quad \text{and} \quad \gamma = \left(\frac{\delta \eta_1 - \alpha \eta_2}{\eta_1 - \eta_2} \right). \quad (2.95)$$

For the choice of $z(\eta)$ in Eq. (2.94), the solutions to the Mukhanov-Sasaki equation (2.36) can be written as

$$v_k(\eta) = \frac{1}{\sqrt{2k}} e^{-i k \eta}, \quad \eta \leq \eta_1, \quad (2.96a)$$

$$v_k(\eta) = B e^{-i k \eta} + C e^{i k \eta}, \quad \eta_1 \leq \eta \leq \eta_2, \quad (2.96b)$$

$$v_k(\eta) = D e^{-i k \eta} + E e^{i k \eta}, \quad \eta \geq \eta_2. \quad (2.96c)$$

where the standard Bunch-Davies initial conditions have been imposed on the Fourier modes in the first region [cf. Eq. (2.48)]. The coefficients B, C, D and E are k -dependent

functions, which are determined by applying the matching conditions at the interface of different regimes. Upon imposing the matching conditions at the first transition point $\eta = \eta_1$, the continuity of v_k and v'_k leads to

$$B(k) = \frac{1}{\sqrt{2k}} \left(1 - \frac{i}{2k} \right), \quad (2.97a)$$

$$C(k) = \frac{1}{\sqrt{2k}} \left(\frac{i}{2k} \right) e^{2ik\eta_1}. \quad (2.97b)$$

In a similar way, applying the matching conditions at the second transition point $\eta = \eta_2$, we obtain

$$D(k) = \frac{1}{\sqrt{2k}} \left[\left(1 + \frac{1}{4k^2} \right) - \frac{1}{4k^2} e^{2ik(\eta_1 - \eta_2)} \right], \quad (2.98a)$$

$$E(k) = \frac{1}{\sqrt{2k}} \frac{(1 + 2ik)}{4k^2} \left[e^{2ik\eta_1} - e^{2ik\eta_2} \right]. \quad (2.98b)$$

In Fig. 2.7, we have plotted the evolution of the amplitude of the curvature perturbation \mathcal{R}_k [$\equiv (v_k/z)$; cf. Eq. (2.35)] for the mode with wavenumber $k = 0.01 \text{ Mpc}^{-1}$ as a function of the number of e -folds N . It is evident from the figure that, the amplitude of the mode is enhanced at super-Hubble scales as compared to its value at Hubble exit. And, in Fig. 2.8, we have plotted the corresponding power spectrum of the curvature perturbations $\mathcal{P}_s(k)$ [cf. Eq. (2.39)]. As is well known, the perturbation spectrum for the case wherein $z(\eta)$ is a constant for all times turns out to be blue with the spectral index $n_s = 3$ [124]. In our case, though $z(\eta)$ makes a transition from one constant value to another constant value, the term (z''/z) vanishes everywhere. As a result, the perturbation spectrum again proves to be blue with superimposed oscillations that arise due to the transition from one regime to another regime.

2.8.2 Example II

We shall now consider a scenario where $z(\eta)$ makes a transition from a constant value at early times to a de Sitter phase at late times.

Though pathological, we consider the de Sitter case for its simplicity. It is straightforward to extend this to the power law or the slow roll cases. The behavior of $z(\eta)$ can be described

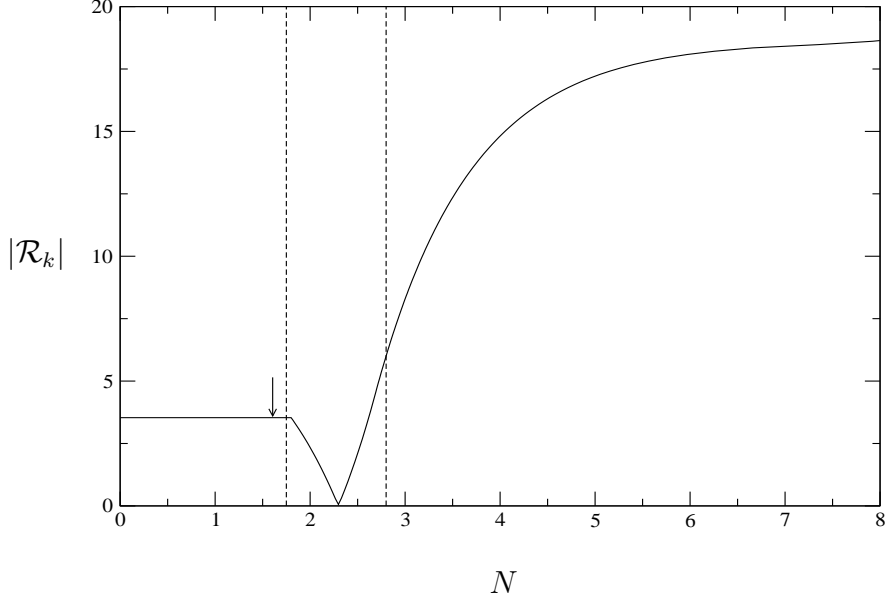


Figure 2.7: The evolution of the amplitude of the curvature perturbation \mathcal{R}_k for the mode with wavenumber $k = 0.01 \text{ Mpc}^{-1}$ has been plotted as a function of the number of e -folds N . The arrow indicates the time at which the mode leaves the Hubble radius. The vertical dashed lines indicate the regime where the quantity (z'/z) is negative. The figure clearly illustrates that the amplitude of the curvature perturbation is enhanced at super-Hubble scales, when compared to its value at Hubble exit.

as follows:

$$z(\eta) = \alpha, \quad \eta \leq \eta_1, \quad (2.99a)$$

$$z(\eta) = -\beta\eta + \gamma, \quad \eta_1 \leq \eta \leq \eta_2, \quad (2.99b)$$

$$z(\eta) = -\left(\frac{\delta}{H\eta}\right), \quad \eta \geq \eta_2, \quad (2.99c)$$

where, as earlier, α, β, γ and δ are constants and H is the Hubble parameter during the de Sitter phase. The coefficients β and γ are given by,

$$\beta = -\left(\frac{1}{\eta_1 - \eta_2}\right) \left[\alpha + \left(\frac{\delta}{H\eta_2}\right) \right], \quad (2.100a)$$

$$\gamma = -\left(\frac{1}{\eta_1 - \eta_2}\right) \left[\alpha\eta_2 + \left(\frac{\delta\eta_1}{H\eta_2}\right) \right]. \quad (2.100b)$$

In this case, the term (z''/z) vanishes in first and second regimes but not in the de Sitter regime. Solving the Mukhanov-Sasaki equation (2.36) for this case, the mode solutions can

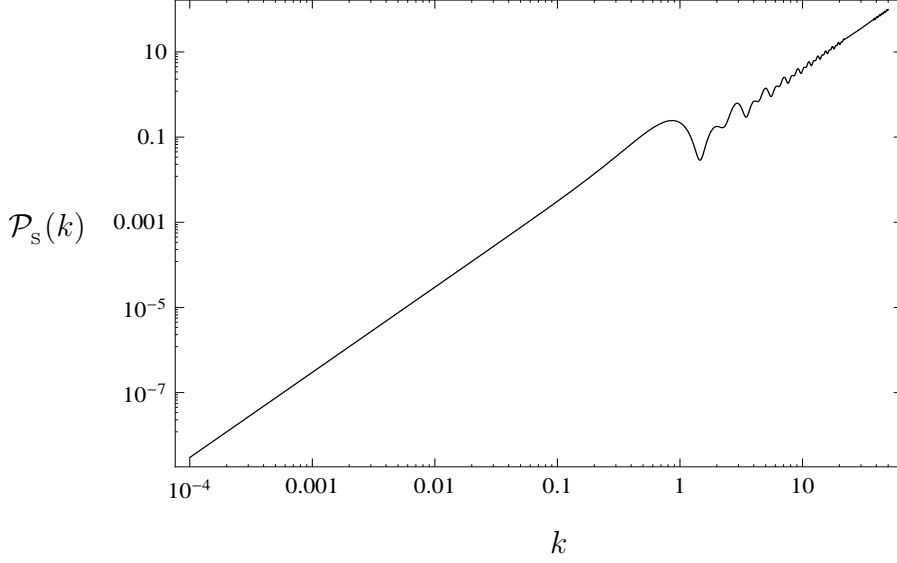


Figure 2.8: The spectrum of the curvature perturbations $\mathcal{P}_s(k)$ has been plotted as a function of the wavenumber k . As is well known, the perturbation spectrum for the case wherein $z(\eta)$ is a constant for all times turns out to be blue with the spectral index $n_s = 3$ [124]. In our case, the spectrum also proves to be blue with the spectral index $n_s = 3$. Note that there exists superimposed modulations on the spectrum which essentially arise due to the fact that the quantity z makes a transition from one constant value to another constant value.

be written as

$$v_k(\eta) = \frac{1}{\sqrt{2k}} e^{-ik\eta}, \quad \eta \leq \eta_1, \quad (2.101a)$$

$$v_k(\eta) = B e^{-ik\eta} + C e^{ik\eta}, \quad \eta_1 \leq \eta \leq \eta_2, \quad (2.101b)$$

$$v_k(\eta) = -\frac{\sqrt{\pi}\eta}{2} \left[D H_{3/2}^{(1)}(k\eta) + E H_{3/2}^{(2)}(k\eta) \right], \quad \eta \geq \eta_2. \quad (2.101c)$$

where $H_{3/2}^{(1)}$ and $H_{3/2}^{(2)}$ are the first and second kind of Hankel functions with order $(3/2)$ respectively, and B, C, D and E are k -dependent functions. Upon using the matching conditions at the first transition point $\eta = \eta_1$ i.e. the continuity of the mode solution and its derivative implies that

$$B(k) = \frac{1}{\sqrt{2k}} \left(1 - \frac{i}{2k} \right), \quad (2.102a)$$

$$C(k) = \frac{1}{\sqrt{2k}} \left(\frac{i}{2k} \right) e^{2ik\eta_1}. \quad (2.102b)$$

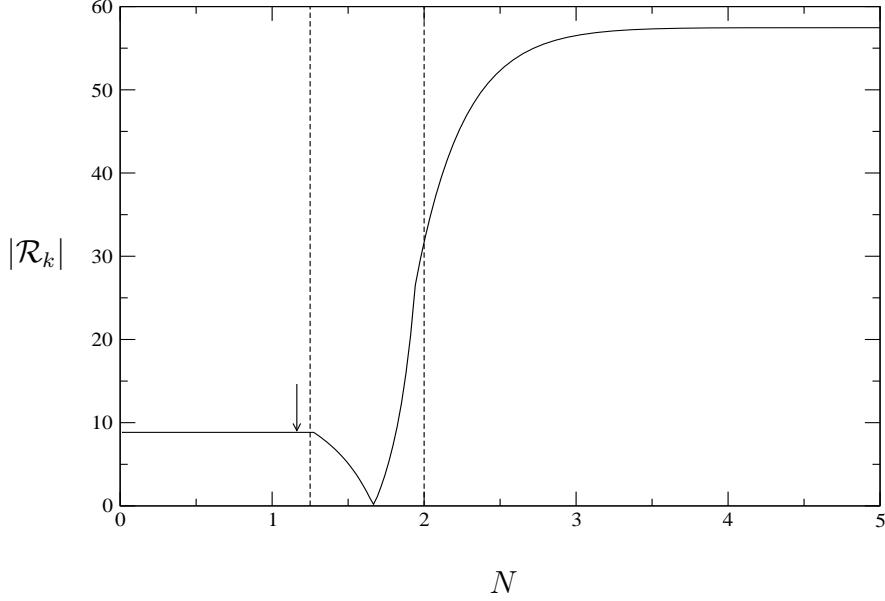


Figure 2.9: The evolution of the amplitude of the curvature perturbation \mathcal{R}_k for the mode with wavenumber $k = 0.01 \text{ Mpc}^{-1}$ has been plotted as a function of the number of e -folds N . As in Fig. 2.7, the arrow indicates the time at which the mode leaves the Hubble radius. The vertical dashed lines again delineate the regime where the quantity (z'/z) is negative. The figure again clearly demonstrates that the amplitude of the curvature perturbation is enhanced at super-Hubble scales, when compared to its value at Hubble exit.

Again, applying the matching conditions at the second transition point $\eta = \eta_2$, we obtain

$$D(k) = \frac{1}{2(i - k\eta_2)} \left[2(i + k\eta_2) e^{(1+2ik\eta_2)} + \eta_2(i - 2k) - i\eta_2 e^{2ik(\eta_1+\eta_2)} \right], \quad (2.103a)$$

$$E(k) = \frac{e^{-2ik\eta_2}}{2(i + k^3\eta_2^3)} \left[2(i - k^3\eta_2^3) e^{(1+2ik\eta_2)} + \eta_2 \left\{ (1 + 2ik) \left(i + \eta_2(i - k\eta_2) \right) - e^{2ik(\eta_1+\eta_2)} \left(i + \eta_2(1 + 2ik)(i - k\eta_2) \right) \right\} \right]. \quad (2.103b)$$

In Fig. 2.9, we have plotted the evolution of the amplitude of the curvature perturbation \mathcal{R}_k for the mode with wavenumber $k = 0.01 \text{ Mpc}^{-1}$ as a function of the number of e -folds N . The figure clearly illustrates that the amplitude of the curvature perturbation is enhanced at super-Hubble scales, when compared to its value at Hubble exit. And, in Fig. 2.10, we have plotted the corresponding power spectrum of the curvature perturbations. As is well known, while the spectrum is blue at large scales (for small values of k) with the spectral

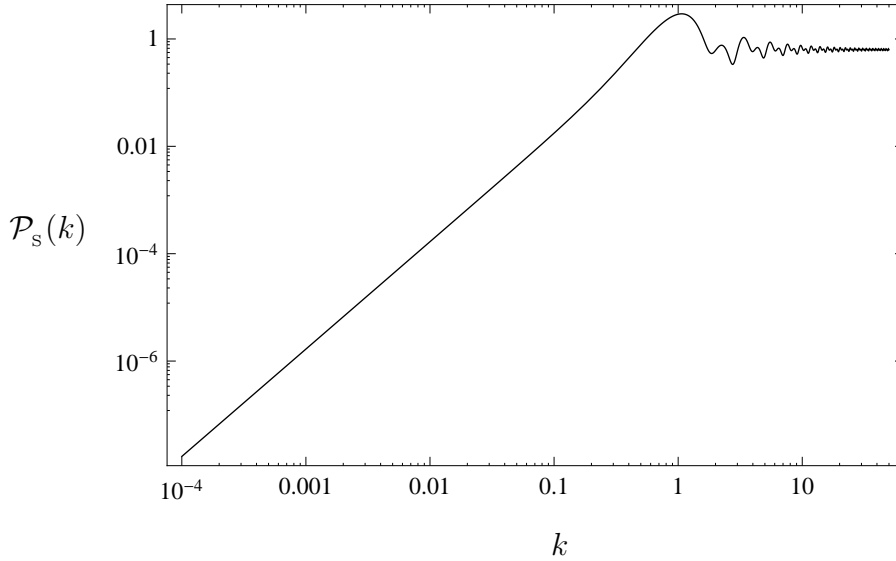


Figure 2.10: The spectrum of the curvature perturbations $\mathcal{P}_s(k)$ has been plotted as a function of the wavenumber k . As is well known, while the spectrum is blue at large scales with the spectral index $n_s = 3$ [124], it turns a scale invariant spectrum at small scales. The superimposed modulations on the spectrum essentially arise due to the fact that the quantity z makes a transition from a constant value to a de Sitter phase.

index $n_s = 3$ [124], it turns scale invariant at small scales (for large values of k), corresponding to the modes that leave the Hubble radius during the de Sitter phase. As in the previous example, tiny features in the power spectrum are present in this case as well.

2.9 Summary and discussion

In this chapter, with the help of a specific example, we have shown that the amplitude of the curvature perturbations induced by the tachyon can be *enhanced or suppressed* at super-Hubble scales if there exists a period of deviation from slow roll inflation. Working in the fluid picture, we have illustrated that, as in the case of the canonical scalar field, the change in the amplitude of the curvature perturbations arises due to the growth of the entropy perturbations in the fast roll regime. Moreover, following the results obtained earlier for the canonical scalar field, we have shown that the power spectrum evaluated in the long

wavelength approximation matches the exact spectrum obtained numerically very well. We have also discussed two simple analytical examples wherein the amplitude of the curvature perturbations induced by the canonical scalar field is enhanced at super-Hubble scales. We have also obtained the power spectrum associated with the curvature perturbations in these cases.

Transitions from slow roll to fast roll inflation lead to deviations from a nearly scale-invariant power spectrum. The possibility that specific deviations from the standard scale independent power spectrum may fit the CMB observations better have been explored recently in the literature [126, 127, 128, 129]. If we can systematically understand the effects of the quantity z on the curvature perturbation \mathcal{R}_k , we will be able to fine tune the transitions such as the ones we have discussed in this chapter to obtain the desired features in the power spectrum (in this context, see Refs. [128, 129]). For instance, the sharp drop in the power spectrum in our model in the wavelength range $0.03 \lesssim k \lesssim 0.1 \text{ Mpc}^{-1}$ may provide a better fit to the lower power observed in the quadrupole moment of the CMB [130, 131]. In the following chapter, we shall make use of such a feature to arrive at a spectrum that leads to a better fit to the recent CMB observations.

Chapter 3

Punctuated inflation, features in the primordial spectrum and the low CMB multipoles

3.1 Motivation

As we have repeatedly mentioned, the concordant cosmological model—viz. a spatially flat, Λ CDM model with a nearly scale invariant primordial spectrum—seems to fit the recent CMB data rather well [19]. However, the measurements of the CMB anisotropies—from the early days of the COBE satellite until the most recent observations of the WMAP—have consistently indicated a low value of the quadrupole, below the cosmic variance of the concordant Λ CDM model [12, 13, 14, 15, 16, 17, 19]. While there has been a recurring debate about the statistical significance of the quadrupole (corresponding to the multipole $\ell = 2$) and the other outliers at the low multipoles (notably, near the multipoles $\ell = 22$ and 40, see Fig. 1.4) in the CMB angular power spectrum (see Refs. [132, 133, 134, 135] and references therein), there has also been persistent efforts in understanding possible underlying physical reasons for the outliers (see, for an inexhaustive list, Refs. [117, 126, 127, 128, 129, 136, 137, 138, 139, 140, 141, 142, 143, 144, 145, 146, 147, 148, 149, 150, 151, 152, 153, 154, 155, 156, 157, 158, 159, 160, 161, 162]).

Given the CMB observations, different model independent approaches have been used to recover the primordial spectrum (see, for example, Refs. [17, 130, 131, 163, 164, 165, 166, 167, 168, 169]). While all these approaches arrive at a spectrum that is nearly scale invariant at the smaller scales, most of them inevitably seem to point to a sharp drop in power at the

scales corresponding to the Hubble scale today. Within the inflationary scenario, a variety of single and two field models have been constructed to produce such a drop in power at the large scales [126, 127, 136, 139, 148, 149, 155, 156, 158, 161]. However, in single field inflationary models, in order to produce such a spectrum, we find that many of the scenarios either assume a specific pre-inflationary regime, say, a radiation dominated epoch, or special initial conditions for the background scalar field, such as an initial period of fast roll [126, 127, 148, 158]. Moreover, some of them impose the initial conditions on the perturbations when the largest scales are outside the Hubble radius during the pre-inflationary or the fast roll regime [126, 127, 158]. Such requirements are rather artificial and, ideally, it would be preferable to produce the desired power spectrum during an inflationary epoch without invoking any specific pre-inflationary phase or special initial conditions for the inflaton. Furthermore, though a very specific pre-inflationary phase such as the radiation dominated epoch may allow what can be considered as natural (i.e. Minkowski-like) initial conditions for the perturbations even at super-Hubble scales, we believe that choosing to impose initial conditions for a small subset of modes when they are outside the Hubble radius, while demanding that such conditions be imposed on the rest of the modes at sub-Hubble scales, can be considered unsatisfactory.

It has long been known that power spectra with large deviations from scale invariance can be generated in inflationary models that admit one or more periods of departure from the slow roll phase (see, for instance, Refs. [136, 170, 171, 172, 173, 174, 175, 176, 177, 178]). The degree of the deviation from a nearly scale invariant spectrum would be determined by the extent and duration of the departure, which are, in turn, controlled by the parameters of the model. A departure from slow roll affects the evolution of modes that leave the Hubble radius just before the departure. Rather than remaining constant, the curvature perturbations \mathcal{R}_k , corresponding to these modes evolve at super-Hubble scales, sourced by the intrinsic entropy perturbations of the inflaton field which, typically, exhibit a rapid growth during the fast roll regime [99, 100, 123]. Such an evolution on super-Hubble scales results in dips or bursts of oscillations in the scalar power spectrum. Usually, such a departure is induced by introducing a sharp feature in the potential of the inflaton field, such as a step or a sudden change in the slope [128, 129, 136, 159, 160, 178]. However, this is not necessary, and transitions to fast roll for brief periods can be generated even with smooth and better

motivated effective potentials [99, 100, 170, 172].

In this chapter, our purpose is to present a simple model of inflation that suppresses the power spectrum on large scales, a feature—as we discussed above—that seems to be necessary to fit the lower power in the quadrupole (and, to some extent, in the deviant power at other lower multipoles such as the octopole and the multipole $\ell = 22$) of the CMB angular power spectrum, using an effective potential of the canonical scalar field *without* introducing any ad hoc sharp feature. We find that the form of the potentials motivated by a class of certain minimal supersymmetric extensions of the standard model provide us with the desired behavior [179, 180, 181, 182]. These large field models allow a period of fast roll sandwiched between two stages of slow roll inflation¹. We shall refer to such an inflationary scenario as punctuated inflation. The first phase of slow roll inflation allows us to impose the standard Bunch-Davies initial conditions on the modes which exit the Hubble radius during the subsequent fast roll regime, an epoch due to which the curvature perturbations on the super-Hubble scales are suppressed. The second slow roll phase lasts for about 50-60 e -folds, thereby allowing us to overcome the standard horizon problem associated with the hot big bang model. The advantages of our approach over other single field models mentioned earlier are twofold. Firstly, we do not need to assume any specific pre-inflationary phase. The entire evolution of the inflationary era is described by a single inflaton potential and, therefore, is much simpler. Secondly, the modes which exit the Hubble radius during the fast roll regime are inside the Hubble radius during the first stage of slow roll inflation and, hence, we do not have to impose any special initial conditions on the large scale modes.

This chapter is organized as follows. In Sec. 3.2, we shall review the essential features of the effective inflaton potential that we shall consider, and describe the background dynamics in situations of our interest. In Sec. 3.3, after an outline of the slow roll ‘expectations’ of the scalar spectrum that can arise in such a background, we shall discuss the spectra that we obtain through numerical integration. In Sec. 3.4, using the cosmological Boltzmann code CAMB and the Monte Carlo code COSMOMC, we shall compare the power spectra from the models we consider with the recent WMAP 5-year data. Finally, in Sec. 3.5, after a brief summary of our results, we shall discuss as to how the results from our model compare with

¹Earlier, in the literature, two successive stages of slow roll inflation have often been driven by two scalar fields [183, 184, 185, 186, 187, 188, 189, 190]. Instead, we achieve the two stages of slow roll inflation including a brief period of departure from inflation, all with just a single scalar field.

those that have been obtained in another closely related single field model. Note that, unless we mention otherwise, we shall set $M_{\text{P}} = 1$ in this chapter.

3.2 The inflaton potential and the background dynamics

The effective potential for the inflation field that we shall consider is described by two parameters m and λ , and is given by

$$V(\phi) = \left(\frac{m^2}{2}\right) \phi^2 - \left(\frac{\sqrt{2\lambda(n-1)}m}{n}\right) \phi^n + \left(\frac{\lambda}{4}\right) \phi^{2(n-1)}, \quad (3.1)$$

where $n > 2$ is an integer. Such potentials are known to arise in certain minimal supersymmetric extensions of the standard model [179], and their role as an inflaton and its related effects have been studied recently [180, 181, 182]. (We should also hasten to add that the specific case of $n = 3$ has been considered much earlier for reasons similar to ours, viz. producing certain features in the primordial spectrum [170].) In the above potential, the coefficient of the ϕ^n term has been chosen in such a way that the potential has a point of inflection at $\phi = \phi_0$ (i.e. the location where both V_ϕ and $V_{\phi\phi}$ vanish), with ϕ_0 given by

$$\phi_0 = \left[\frac{2m^2}{(n-1)\lambda} \right]^{\frac{1}{2(n-2)}}. \quad (3.2)$$

Near this point of inflection, the potential exhibits a plateau with an extremely small curvature, which, as we shall discuss below, proves to be crucial for the desired evolution of the inflaton field. The potential (3.1) for the case $n = 3$ is depicted in Fig. 3.1.

Note that the potential (3.1) roughly behaves as

$$V(\phi) \sim \begin{cases} \phi^{2(n-1)}, & \text{for } \phi > \phi_0, \\ \phi^2, & \text{for } \phi < \phi_0. \end{cases} \quad (3.3)$$

Recall that, inflation ends when the first PSR parameter ϵ_v crosses unity [cf. Eq. (1.27a)]. It is then clear that, in a power law potential of the form $V \sim \phi^{2(n-1)}$, slow roll inflation will occur (i.e. $\epsilon_v \ll 1$) when $\phi \gg 1$ (in $M_{\text{P}} = 1$ units), and inflation will end when $\phi_{\text{end}} \simeq [\sqrt{2}(n-1)] \sim \mathcal{O}(1)$. Thus, for a transition from slow roll to fast roll to occur, we need to choose the two parameters in the potential (3.1) so that $\phi_0 \sim \mathcal{O}(1)$, i.e. of the order of the (reduced) Planck scale. Restarting inflation after the fast roll phase and the number of e -folds

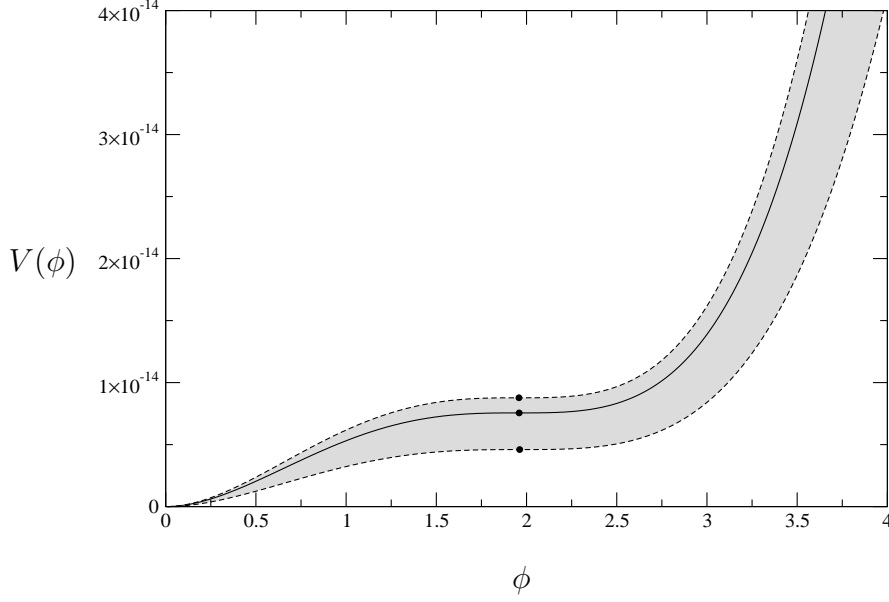


Figure 3.1: Illustration of the inflaton potential (3.1) for the case of $n = 3$. The solid line corresponds to the following values for the potential parameters: $m = 1.5368 \times 10^{-7}$ and $\lambda = 6.1517 \times 10^{-15}$ (corresponding to $\phi_0 = 1.9594$), values which turn out to provide the best fit to the WMAP 5-year data (cf. Tab. 3.4.2). The dashed lines correspond to values that are $1\text{-}\sigma$ away from the best fit ones. The black dots denote the points of inflection.

that can be achieved during the second phase of slow roll crucially depends on the value of ϕ_0 . We rely on the numerics to choose this parameter carefully since the above slow roll estimate only provides a rough order of magnitude. Choosing ϕ_0 in such a way is actually fine tuning, but it seems to be inevitable if we are to achieve the desired slow-fast-slow roll transition as well as the required number of e -folds. Once the point of inflection has been identified, we find that the normalization to the CMB angular power spectrum data provides the second constraint, thereby determining the value of the other free parameter m .

The equation of motion governing the scalar field described by the potential (3.1), when expressed as two first order equations for the coupled variables ϕ and $\dot{\phi}$, has one attractive fixed point located at the origin, i.e. at $(\phi, \dot{\phi}) = (0, 0)$. For positive values of ϕ , we find that there exists an attractor trajectory towards which all other trajectories with arbitrary initial conditions on ϕ and $\dot{\phi}$ quickly converge. For a suitably chosen ϕ_0 , we find that the attractor trajectory exhibits two regimes of slow roll inflation sandwiching a period of fast

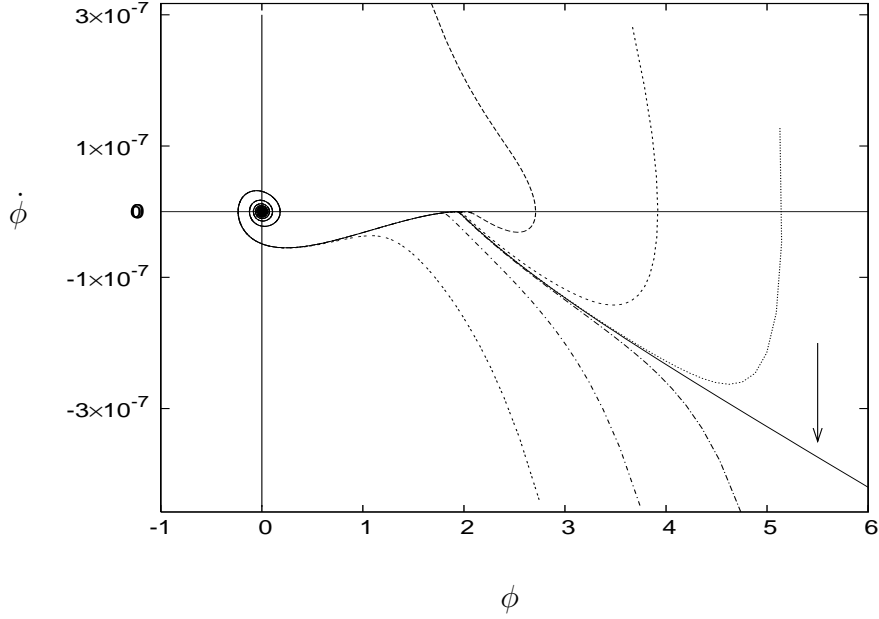


Figure 3.2: The phase portrait of the scalar field described by the potential (3.1) in the case of $n = 3$ and for the values of the parameters m and λ mentioned in the last figure. The arrow points to the attractor. Note that, as discussed in the text, all the trajectories quickly approach the attractor. We should mention that, though we have plotted the phase portrait for just the $n = 3$ case, we find that such a behavior is exhibited by higher values of n (such as, for example, $n = 4, 6$) as well.

roll. Hence, if we start the evolution with $\phi \gg \phi_0$, then the initial values of ϕ and $\dot{\phi}$ prove to be irrelevant for the subsequent dynamics as they approach the attractor. This behavior is evident from Fig. 3.2 where we have plotted the phase portrait for the $n = 3$ case. Once the field reaches close to ϕ_0 , due to the extreme flatness of the potential (3.1), it relaxes and then moves very slowly, commencing the second stage of the slow roll inflation. This stage ends when the field finally rolls down towards the minima of the potential at $\phi = 0$.

We had mentioned earlier that potentials of the type (3.1) are encountered in the Minimal Supersymmetric Standard Model (MSSM) [179], and that their role as an inflaton has been analyzed recently [180, 181, 182]. At this point it is important that we highlight the differences between MSSM inflation and the scenario we are considering. In MSSM inflation, the point of inflection is located at sub-Planckian values (i.e. $\phi_0 \ll 1$) which can be an advantage as it avoids the problems associated with having super-Planckian values for the field.

In contrast, in our case, as emphasized above, the saddle point should be located around the Planck scale (i.e. $\phi_0 \gtrsim 1$), if we are to achieve the second period of slow roll before the end of inflation. However, in the MSSM case, to have successful inflation, the initial values of ϕ and $\dot{\phi}$ have to be finely tuned so that $\phi_{\text{ini}} \simeq \phi_0$ and $\dot{\phi}_{\text{ini}} \simeq 0$. But, in our scenario, we do not require such fine tuning of the initial conditions on ϕ and $\dot{\phi}$. Instead, we require for the location of ϕ_0 .

Though the parameters of the potential that we work with are different from the MSSM case, we nevertheless believe that it may be possible to realize the potential (3.1) in theories beyond the standard model, such as, for instance, string theory (in this context, see Refs. [191, 192, 193]). For example, it is known that the existence of a number of string axion fields can give rise to the following potential describing multi-field chaotic inflation [48]:

$$V(\phi_i) = \sum_i \left(\frac{1}{2} \right) m_i^2 \phi_i^2, \quad (3.4)$$

with the initial field displacements smaller than unity. The dynamics and the inflationary predictions in such examples are surprisingly similar to the corresponding single field chaotic inflation models [194, 195, 196], due to the assisted inflation mechanism [47]. Similarly, with enough number of fields and with the non-renormalizable superpotential

$$W = \left(\frac{\lambda}{n} \right) \left(\frac{\phi^n}{M_{\text{P}}^{n-3}} \right), \quad (3.5)$$

and the corresponding A term and the soft mass term, one might be able to build an inflation model that is effectively equivalent to the single field one described by the potential (3.1). (Note that, for clarity, we have temporarily restored M_{P} in the expression (3.5) above.)

3.3 The scalar power spectrum

In this section, after providing general arguments for the form of the scalar spectra that we can expect from our model, we present the spectra evaluated numerically.

3.3.1 Physical ‘expectations’

Before we evaluate the scalar spectra numerically, let us broadly try and understand the spectra that we can expect to arise in the slow-fast-slow roll scenario that we are interested in.

The evolution of the scalar modes and the scalar spectrum

Consider modes that exit the Hubble scale during an epoch of slow roll inflation. Provided there is no deviation from slow roll soon after the modes leave the Hubble radius, the amplitude of these modes will remain constant at super-Hubble scales. Therefore, their amplitude is determined by their value at Hubble exit, and the scalar power spectrum corresponding to these modes can be expressed in terms of the potential and its derivative [cf. Eq. (2.61)]. However, if there is a period of deviation from slow roll inflation, as we had discussed in the last chapter, the asymptotic (i.e. the extreme super-Hubble) amplitude of the modes that leave the Hubble radius *just before* the deviation are enhanced when compared to their value at Hubble exit [99, 100]. While modes that leave well before the deviation remain unaffected, as we had illustrated in the previous chapter, it is found that there exists an intermediate range of modes whose amplitudes are actually *suppressed* at super-Hubble scales [123]. As a result, in the slow-fast-slow roll scenario of our interest, the scalar power spectrum is initially characterized by a sharp dip and a rise corresponding to modes that leave the Hubble radius just before the transition to fast roll. Then arises a regime of nearly scale invariant spectrum corresponding to modes that leave during the second stage of slow roll inflation (see, for instance, the scalar power spectrum we had plotted in Fig. 2.6 in the preceding chapter).

The effects on the tensor modes and the tensor spectrum

Let us now understand the behavior of the tensor modes. In the case of the scalar modes, the quantity (z'/z) that appears in the differential equation (2.33) turns out to be negative during a period of fast roll, and as we had seen in the last chapter, it is this feature that proves to be responsible for the amplification or the suppression of the modes at super-Hubble scales [99, 100, 123]. In contrast, the coefficient of the friction term in the equation (2.42) that describes the tensor modes, viz. $(2\mathcal{H})$, is a positive definite quantity. Hence, we do not expect any non-trivial super-Hubble evolution of \mathcal{U}_k . We find that, in the models that we consider, the tensor-to-scalar ratio r remains smaller than 10^{-4} over scales of cosmological interest (i.e. over $10^{-4} \lesssim k \lesssim 1 \text{ Mpc}^{-1}$), which is below the levels of possible detection by forthcoming missions such as, say, PLANCK [197] and CMBPol [198].

3.3.2 Numerical results

It is the background quantity (z'/z) that appears in the differential equation (2.33) for the curvature perturbation which essentially determines the form of the scalar power spectrum. The quantity $(z'/z\mathcal{H})$ can be expressed in terms of the first two HSR parameters², viz. $\epsilon_{\text{H}} = -(\dot{H}/H^2)$ and $\delta_{\text{H}} = (\ddot{\phi}/H\dot{\phi})$ [cf. Eq. (2.52)]. It is given by [99, 100]

$$\left(\frac{z'}{z\mathcal{H}}\right) = (1 + \epsilon_{\text{H}} + \delta_{\text{H}}), \quad (3.6)$$

and it is clear from this expression that, during slow roll inflation (i.e. when $\epsilon_{\text{H}} \ll 1$ and $\delta_{\text{H}} \ll 1$), the quantity $(z'/z\mathcal{H})$ will remain close to unity [99, 100, 123]. In Fig. 3.3, we have plotted the evolution of $(z'/z\mathcal{H})$ as a function of the number of e -folds N for the cases of $n = 3$ and $n = 4$ in the potential (3.1). And, in Fig. 3.4, we have plotted the evolution of the field in the plane of the HSR parameters ϵ_{H} and δ_{H} for the $n = 3$ case. It is manifest from these figures that the departure from slow roll occurs roughly between e -folds $7 \lesssim N \lesssim 15$ in the $n = 3$ case and between e -folds $4 \lesssim N \lesssim 12$ for $n = 4$. We should also point out that inflation is actually interrupted for about one e -fold during the fast roll. In Fig. 3.5, we have plotted the corresponding scalar spectra evaluated numerically. The broad arguments we had presented in the previous subsection are evidently corroborated by these two figures. Note that, in plotting all these figures, we have chosen parameters that eventually provide the best fit to the WMAP 5-year data. Also, in the inset in the top panel of Fig. 3.5, we have highlighted the difference between the scalar spectra in our model and the power law case (i.e. when $\mathcal{P}_{\text{s}}(k) = A_{\text{s}} k^{n_{\text{s}}-1}$, with $A_{\text{s}} = 2.1 \times 10^{-9}$ and $n_{\text{s}} \simeq 0.955$). Moreover, we should stress here that the standard sub-Hubble, Bunch-Davies, initial conditions have been imposed on *all* the modes in arriving at these spectra.

The scalar power spectrum with a drop in power at large scales is often approximated by an expression with an exponential cut-off of the following form [126, 148, 154]:

$$\mathcal{P}_{\text{s}}(k) = A_{\text{s}} \left(1 - \exp[-(k/k_*)^\alpha]\right) k^{n_{\text{s}}-1}. \quad (3.7)$$

In Fig. 3.5, we have also plotted this expression for values of A_{s} , n_{s} , α and k_* that closely approximate the spectra we obtain. It is useful to note that the spectra we obtain correspond

²We had already defined the first two HSR parameters in Eq. (2.50). However, note that the second HSR parameter δ_{H} that we have used here is 'negative' of what we defined earlier, i.e. $\delta_{\text{H}} = -\eta_{\text{H}}$.

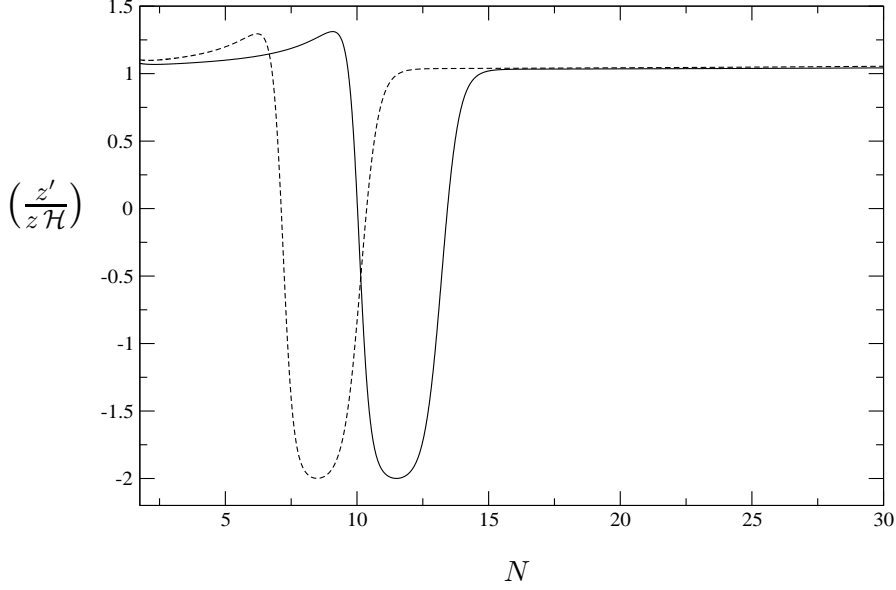


Figure 3.3: The background quantity $(z'/z\mathcal{H})$ has been plotted as a function of the number of e -folds N , for the cases of $n = 3$ and $n = 4$ in potential (3.1). The solid line represents the $n = 3$ case with the same values for the potential parameters as in the previous two figures. The dashed line corresponds to the $n = 4$ case with $m = 1.1406 \times 10^{-7}$ and $\lambda = 1.448 \times 10^{-16}$ (corresponding to $\phi_0 = 2.7818$) and, as in the $n = 3$ case, we have chosen these values as they provide the best fit to the WMAP 5-year data. Also, note that we have imposed the following initial conditions for the background field in both the cases: $\phi_{\text{ini}} = 10$ and $\dot{\phi}_{\text{ini}} = 0$. Evidently, the $n = 3$ case departs from slow roll when $7 \lesssim N \lesssim 15$, while the departure occurs during $4 \lesssim N \lesssim 12$ in the case of $n = 4$.

to $A_s = 2 \times 10^{-9}$, $n_s \simeq 0.945$, $\alpha = 3.35$ and $k_* = 2.4 \times 10^{-4} \text{ Mpc}^{-1}$ when $n = 3$, while $A_s = 2 \times 10^{-9}$, $n_s \simeq 0.95$, $\alpha = 3.6$ and $k_* = 9.0 \times 10^{-4} \text{ Mpc}^{-1}$ in the $n = 4$ case. We should emphasize here that we have arrived at these values for A_s , n_s , α and k_* by a simple visual comparison of the numerically evaluated result with the above exponentially cut-off spectrum.

3.4 Comparison with the recent WMAP 5-year data

In this section, we shall discuss as to how our model compares with the recent WMAP 5-year data.

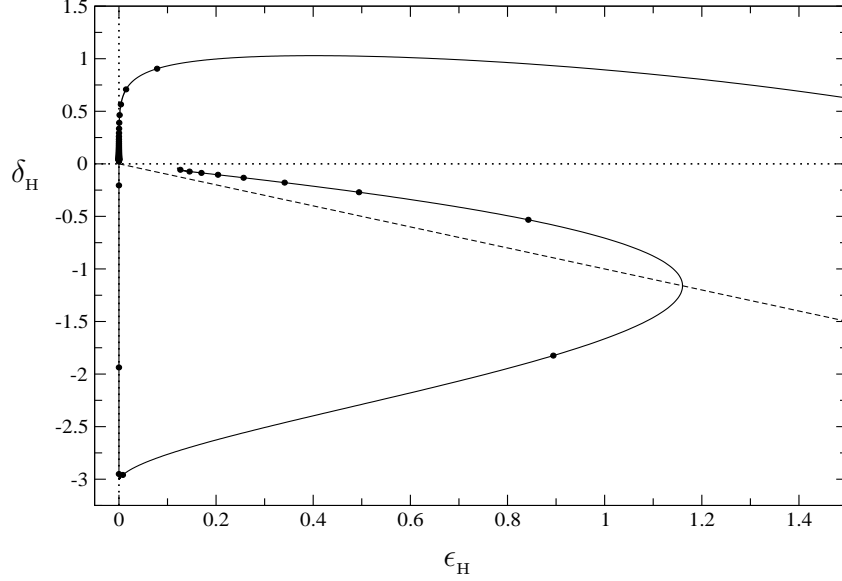


Figure 3.4: The evolution of the scalar field has been plotted (as the solid black line) in the plane of the first two HSR parameters ϵ_H and δ_H in the case of $n = 3$ and for the best fit values of the parameters m and λ we have used earlier in Figs. 3.1 and 3.2. The black dots have been marked at intervals of one e -fold, while the dashed line corresponds to $\epsilon_H = -\delta_H$. Note that $\epsilon_H > 1$ during $8 < N < 9$. In other words, during fast roll, inflation is actually interrupted for about one e -fold.

3.4.1 The parameters in our model and the priors we work with

In the standard concordant cosmological model—viz. the Λ CDM model with a power law inflationary perturbation spectrum—six parameters are introduced when comparing the theoretical results with the CMB data (see, for instance, Ref. [199]). Four of them are the following background parameters: the baryon density ($\Omega_b h^2$), the density of cold dark matter ($\Omega_c h^2$), the angular size of the acoustic horizon θ , and the optical depth τ , with h denoting the Hubble constant today (viz. H_0) expressed in units of $100 \text{ km s}^{-1} \text{ Mpc}^{-1}$ [cf. Eq. (1.2)]. The parameters that are introduced to describe the inflationary perturbation spectrum are the scalar amplitude A_s and the scalar spectral index n_s [cf. Eq. (1.29)]. The tensor-to-scalar ratio r is also introduced as a parameter provided the ratio is sufficiently large, say, when $r \gtrsim \mathcal{O}(10^{-2})$. However, in the models we consider, the tensor-to-scalar ratio proves to be smaller than 10^{-4} over the scales of cosmological interest (i.e. over $10^{-4} \lesssim k \lesssim 1 \text{ Mpc}^{-1}$). So,

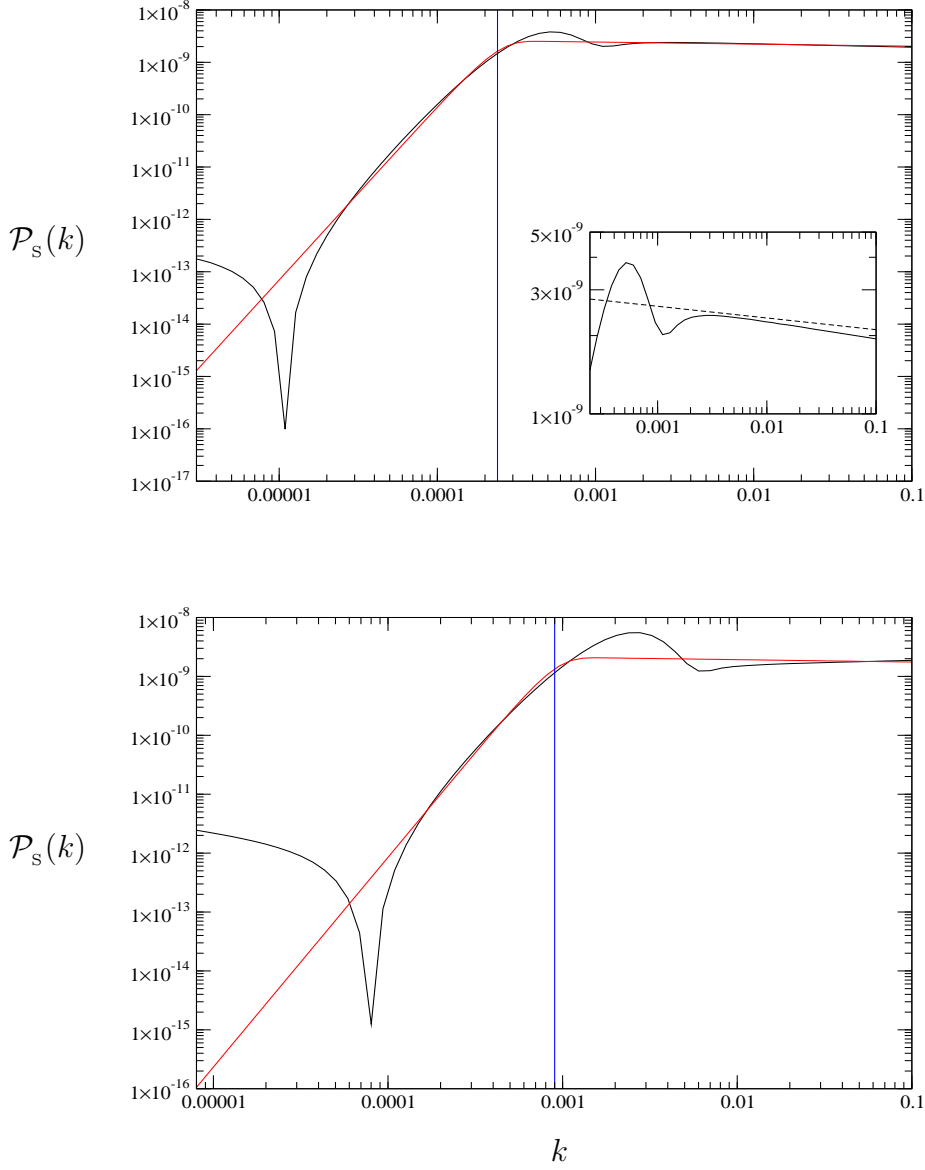


Figure 3.5: The scalar power spectrum $\mathcal{P}_s(k)$ (the solid black line) have been plotted as a function of the wavenumber k for the cases of $n = 3$ (on top) and $n = 4$ (at the bottom). We have chosen the same values for the potential parameters as in the earlier figures. Moreover, we should emphasize that we have arrived at these spectra by imposing the standard, Bunch-Davies, initial conditions on *all* the modes. The red line in these plots is the spectrum (3.7) with the exponential cut-off. It corresponds to $A_s = 2 \times 10^{-9}$, $n_s \simeq 0.945$, $\alpha = 3.35$ and $k_* = 2.4 \times 10^{-4} \text{ Mpc}^{-1}$ in the $n = 3$ case, while $A_s = 2 \times 10^{-9}$, $n_s \simeq 0.95$, $\alpha = 3.6$ and $k_* = 9.0 \times 10^{-4} \text{ Mpc}^{-1}$ in the case of $n = 4$. Note that the vertical blue line denotes k_* . The inset in the top panel illustrates the difference between our model and the standard power law case (i.e. when $\mathcal{P}_s(k) = A_s k^{n_s-1}$, with the best fit values $A_s = 2.1 \times 10^{-9}$ and $n_s \simeq 0.955$) at smaller scales. This disparity leads to a difference in the CMB angular power spectrum at the higher multipoles, which we have highlighted in the inset in Fig. 3.8.

Model	Parameter	Lower limit	Upper limit
Common parameters	$\Omega_B h^2$	0.005	0.1
	$\Omega_C h^2$	0.001	0.99
	θ	0.5	10.0
	τ	0.01	0.8
Reference model	$\log [10^{10} A_s]$	2.7	4.0
	n_s	0.5	1.5
Our model	$\log [10^{10} m^2]$	-9.0	-8.0
	ϕ_0	1.7	2.3
	a_0	0.1	2.0

Table 3.1: The priors on the various parameters describing the reference Λ CDM model with a power law primordial spectrum and our model. While the first four background cosmological parameters are common for both the models, the fifth and the sixth parameters describe the power law primordial spectrum of the reference model. As discussed in the text, in our model, we have traded off the scalar amplitude A_s for m and the spectral index n_s for ϕ_0 . The additional parameter in our model, viz. a_0 , represents the value of the scale factor at $N = 0$ and it essentially identifies the location of the cut-off in the power spectrum.

we completely ignore the contribution due to the gravitational waves in our analysis. We retain the standard background cosmological parameters, and we introduce the following three parameters to describe the inflationary perturbation spectrum: m , ϕ_0 and a_0 . While m appears explicitly in the potential (3.1), ϕ_0 has been chosen in place of λ . The quantity a_0 denotes the initial value of the scale factor (i.e. at $N = 0$), and it basically determines the location of the cut-off in the power spectrum. Thus, we have one additional parameter in comparison with the standard case. Essentially, we have traded off the scalar amplitude A_s for m , and the scalar spectral index n_s for ϕ_0 . In Tab. 3.4.1, we have listed the ranges of uniform priors that we have imposed on the various parameters.

3.4.2 The best fit values and the joint constraints

We have compared the power spectra for the $n = 3$ and the $n = 4$ cases with the recent WMAP 5-year data for the temperature-temperature, the temperature-electric polarization and the electric-electric polarization angular power spectra of the CMB anisotropies [19].

We have used a modified version of the cosmological Boltzmann code CAMB [200, 201] to calculate the angular power spectra of the CMB anisotropies, with the inflationary perturbation spectrum computed from a separate routine. We have evaluated the likelihood function using the likelihood code that has been made publicly available by the WMAP team [202]. We have obtained the best fit values for the parameters of our model using COSMOMC [203, 204], the publicly available, Markov Chain Monte Carlo (MCMC) code for the parameter estimation of a given cosmological model. The MCMC convergence diagnostics are done on multiple parallel chains using the Gelman and Rubin (“variance of chain means”/“mean of chain variances”) R statistics for each parameter, demanding that $(R - 1) < 0.01$, a procedure that essentially looks at the fluctuations amongst the different chains and decides when to terminate the run. We find that, while the $n = 3$ case provides a better fit to the data than the reference concordant model [199], the $n = 4$ case leads to such a poor fit to the data that we do not consider it hereafter. We attribute the poor fit by the $n = 4$ case (and also in the cases wherein $n > 4$) to the large bump in the scalar power spectrum that arises just before the spectrum turns scale invariant (cf. Fig. 3.5). We have plotted the one-dimensional marginalized and mean likelihood curves for the various parameters in the $n = 3$ case in Fig. 3.6. And, in Fig. 3.7, we have plotted the corresponding $1\text{-}\sigma$ and $2\text{-}\sigma$ two-dimensional joint constraints on the various parameters. We have listed the best fit values and the $1\text{-}\sigma$ constraints on the various parameters describing the reference model and the $n = 3$ case in Tab. 3.4.2. We find that the $n = 3$ case provides a much better fit to the data than the reference model with an improvement in χ^2_{eff} of 6.62 [205]. It is clear from Figs. 3.6 and 3.7 that the constraint on the parameter m is prior dominated. In our model, it is the parameter m that determines the amplitude of the power spectrum when it is nearly scale invariant. This amplitude, in turn, is essentially determined by the first peak of the CMB angular power spectrum. We should mention here that our choice of priors for the parameter m has been arrived at by a simple visual fit to the first peak.

3.4.3 The CMB angular power spectra for the best fit values

In Fig. 3.8, we have plotted the angular power spectrum of the CMB temperature anisotropies for the best fit values of the parameters for the $n = 3$ case. For comparison, we have also plotted the angular power spectrum for the best fit reference model. It is im-

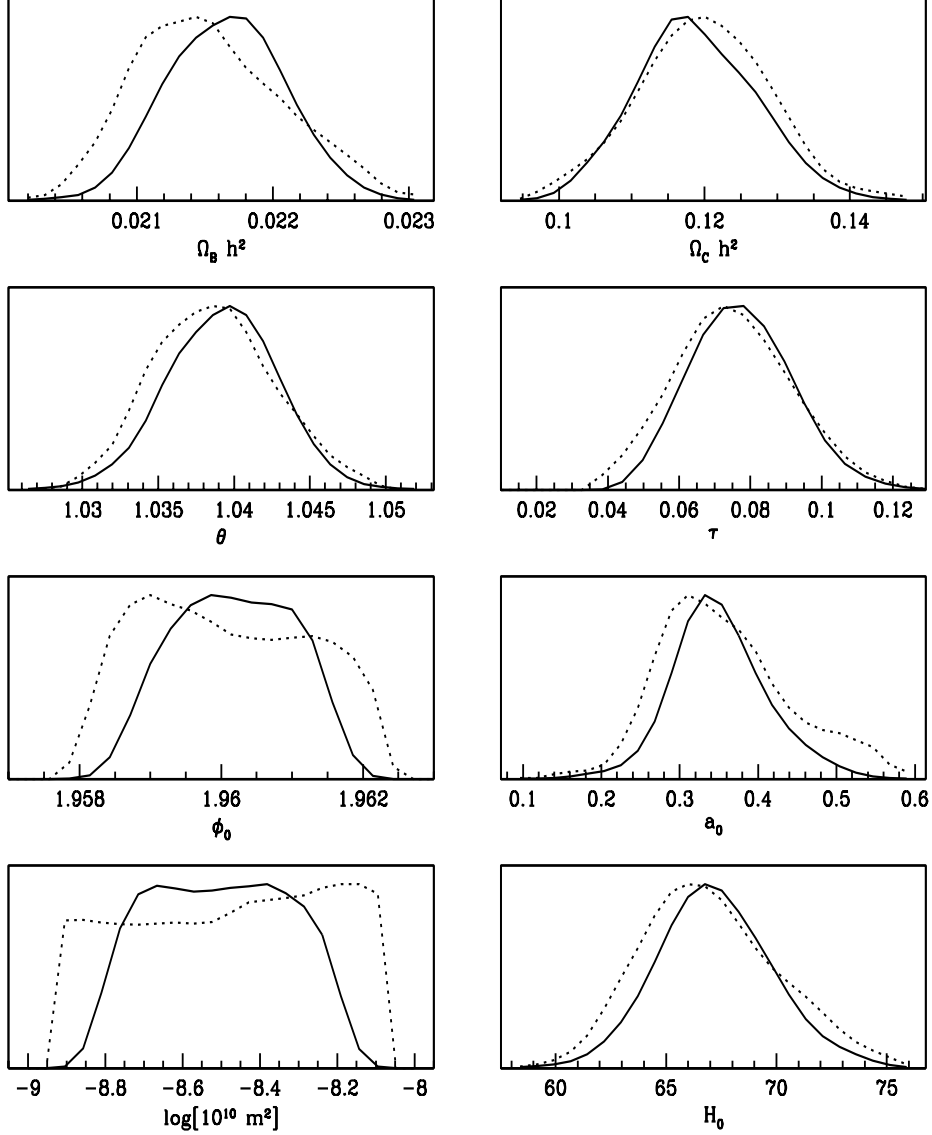


Figure 3.6: The one-dimensional mean (the solid lines) and marginalized (dashed lines) likelihood curves for all the input parameters (and the derived parameter H_0) in the $n = 3$ case.

mediately obvious from the figure that our model fits the lower multipoles much better than the reference model. As we have mentioned above, we obtain an improvement in χ^2_{eff} of 6.62 at the cost of introducing just one additional parameter when compared to the standard power law case. We should also emphasize here that the improvement in the fit that we have achieved is not only due to the cut-off in the scalar power spectrum, but also because

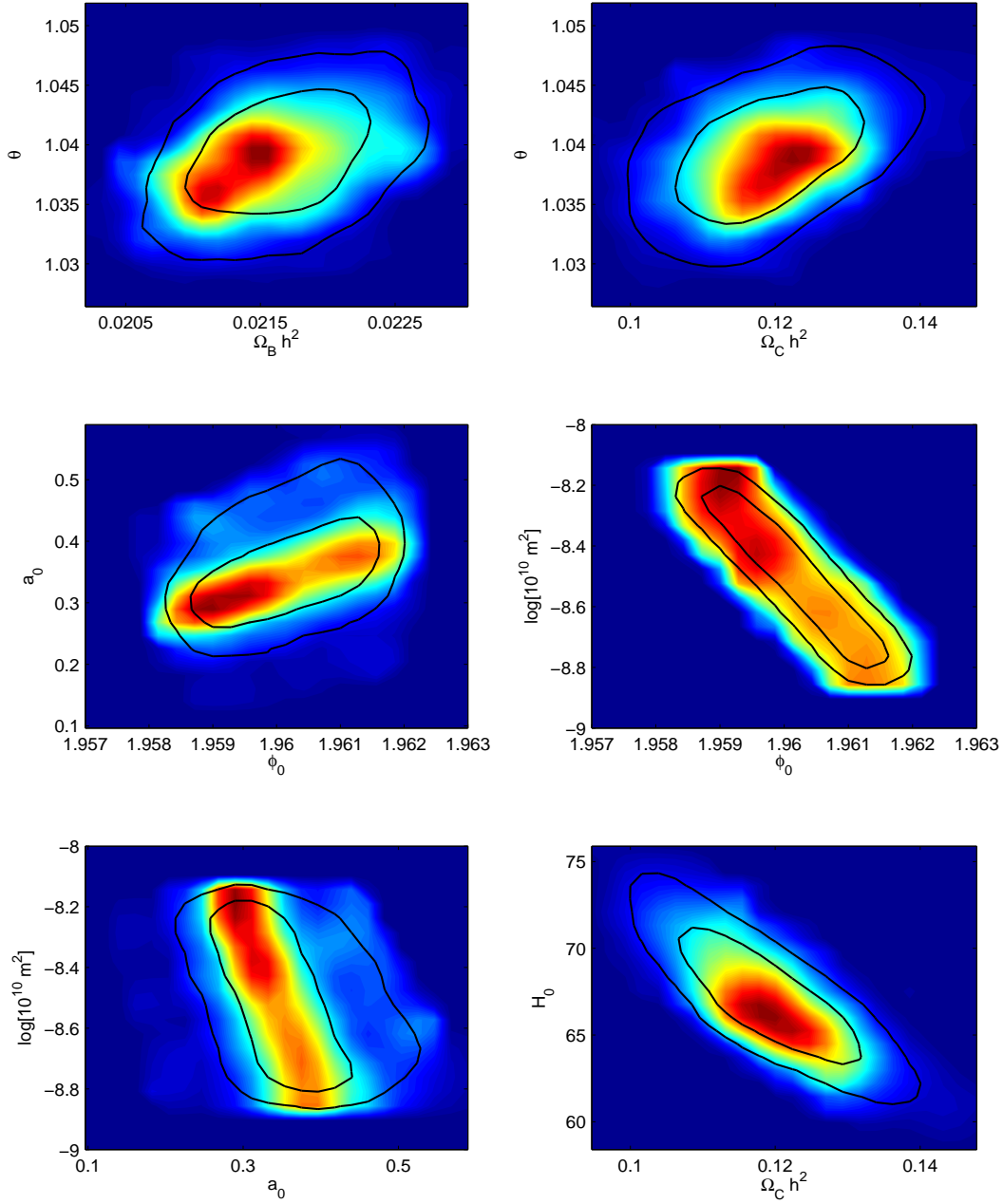


Figure 3.7: The $1\text{-}\sigma$ and $2\text{-}\sigma$ two-dimensional joint constraints on the different input parameters (and the derived parameter H_0) in the $n = 3$ case.

of the presence of the oscillations at the top of the spectrum, just before it turns scale invariant [205]. Also, note the difference in the angular power spectrum for our model and

Parameter	Reference model	Our model
$\Omega_{\text{B}} h^2$	$0.02242^{+0.00155}_{-0.00127}$	$0.02146^{+0.00142}_{-0.00108}$
$\Omega_{\text{C}} h^2$	$0.1075^{+0.0169}_{-0.0126}$	$0.12051^{+0.02311}_{-0.02387}$
θ	$1.0395^{+0.0075}_{-0.0076}$	$1.03877^{+0.00979}_{-0.00931}$
τ	$0.08695^{+0.04375}_{-0.03923}$	$0.07220^{+0.04264}_{-0.02201}$
$\log [10^{10} A_{\text{s}}]$	$3.0456^{+0.1093}_{-0.1073}$	—
n_{s}	$0.9555^{+0.0394}_{-0.0305}$	—
$\log [10^{10} m^2]$	—	$-8.3509^{+0.1509}_{-0.1473}$
ϕ_0	—	$1.9594^{+0.00290}_{-0.00096}$
a_0	—	$0.31439^{+0.02599}_{-0.02105}$

Table 3.2: The mean values and the $1\text{-}\sigma$ constraints on the various parameters that describe the reference model and our model. As we mentioned in the text, we find that the $n = 3$ case provides a much better fit to the data than the reference model with an improvement in χ^2_{eff} of 6.62.

the standard power law spectrum at the higher multipoles, which we have illustrated in the inset in Fig. 3.8. This disparity essentially arises due to the difference in the asymptotic spectral index in our model (which proves to be about $n_{\text{s}} \simeq 0.945$) and the spectral index in the power law case (which is about $n_{\text{s}} \simeq 0.955$, cf. Tab. 3.4.2). The PLANCK mission [197] is expected to provide more accurate data at these higher multipoles and, therefore, may aid us discriminate between these models better.

3.5 Summary and discussion

In this section, after a quick summary of our results, we shall compare the results we have obtained with those obtained in another single scalar field model that has been considered earlier. We emphasize the fact that the difference between these models has immediate observational consequences.

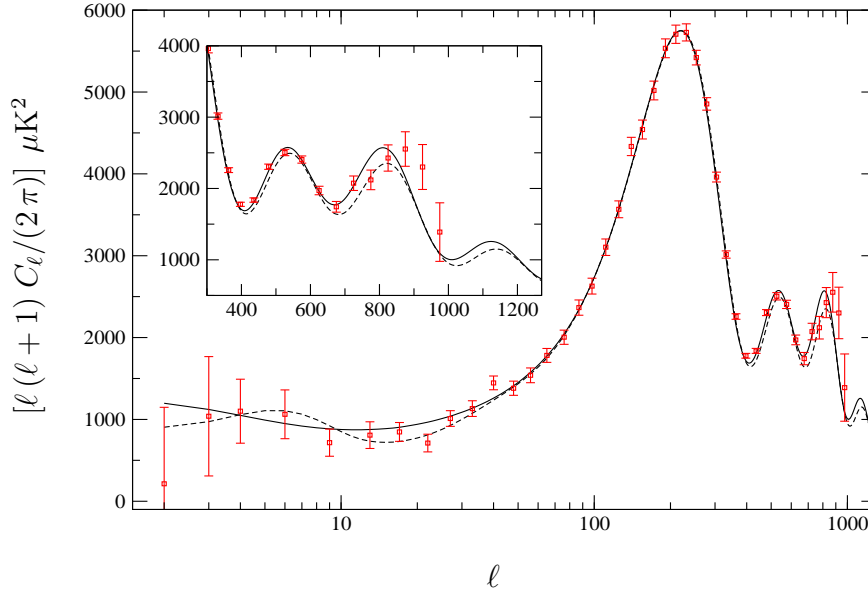


Figure 3.8: The CMB angular power spectrum for the best fit values of the $n = 3$ case (dashed line) and the best fit power law, reference model (solid line) [cf. Tab. 3.4.2]. Visually, it is evident that our model fits the data much better than the standard power law case at the lower multipoles. The inset highlights the difference between our model and the power law spectrum at the higher multipoles. This difference arises due to the fact that, while the spectral index in the power law case is about $n_s \simeq 0.955$, the asymptotic spectral index in our case turns out to be $n_s \simeq 0.945$.

3.5.1 Summary

In this chapter, we have discussed a two stage slow roll inflationary scenario sandwiching an intermediate period of deviation from inflation, driven by potentials that are similar in shape to certain MSSM potentials [180]. In the MSSM case, inflation occurs when the field values are much smaller than the Planck scale [180, 181, 182]. However, in our case, since we demand two epochs of slow roll, it necessarily requires that the initial values of the field (assuming, say, about 60 e -folds of inflation) be greater than M_p . The period of fast roll period produces a sharp drop in the scalar power spectrum for the modes that leave the Hubble radius just before the second slow roll phase. We choose our scales such that the drop in power corresponds to the largest cosmological scales observable today. We find that the resulting scalar power spectrum provides a much better fit to the recent WMAP data

than the canonical, nearly scale invariant, power law, primordial spectrum.

3.5.2 Discussion

At this stage, it is important that we compare our results with those obtained in another single field model that has been studied before. As we had mentioned in Sec. 3.1, an initial kinetic dominated (i.e. fast roll) stage preceding slow roll inflation, driven by a quadratic potential has been considered earlier to provide a sharp drop in the scalar power spectrum at large scales [126, 127]. At first glance, one may be tempted to conclude that the model we have studied here is equivalent to such a scenario if we disregard the first slow roll stage, since we have a kinetic dominated phase preceding a period of slow roll inflation. However, there are crucial differences between the two models which we have outlined below.

To begin with, in the model that we have considered, there is no freedom to choose the type of fast roll (say, the equation of state parameter during the epoch of fast roll). It is fixed once we have chosen the parameters so as to fit the observations. Secondly, in the scenario considered earlier, the modes which are outside the Hubble radius during the kinetic dominated phase *would have always remained so* in the past [126, 127]. The authors assume that somehow there may have been a previous phase of inflation, during which they were inside the Hubble radius and began life in the Bunch-Davies vacuum. While it is not impossible to think of situations where there may have been a previous inflationary epoch—for instance, it can be achieved by invoking another scalar field [186, 187, 188, 189, 190]—the consequences can be quite different. In contrast, in the scenario that we have considered here, the standard, sub-Hubble, Bunch-Davies, initial conditions have been imposed on *all* the modes. Thirdly, it was argued that, since the suppression of power for the scalar spectrum proves to be sharper than that of the tensor, the tensor-to-scalar ratio r displays a sharp rise towards large physical scales [127], a feature that may possibly be detected by upcoming missions such as, for instance, PLANCK [197] and CMBPol [198]. However, in the models that we consider, the tensor amplitude on scales of cosmological interest proves to be too small ($r < 10^{-4}$) to be detectable in the near future. In conclusion, we would like to mention that a detection of the C_ℓ^{BB} modes corresponding to, say, $r > 10^{-4}$, can rule out the class of models that we have considered here.

In the following chapter, we shall consider the effects of punctuated inflation on the tensor

spectrum and the resulting tensor-to-scalar ratio.

Chapter 4

The tensor spectrum and the tensor-to-scalar ratio in punctuated inflationary scenarios

4.1 Introduction and motivation

As we have discussed in the previous chapters, the concordant cosmological model—viz. a spatially flat, Λ CDM model and a nearly scale invariant primordial spectrum, with or without a small tensor contribution (say, with a tensor-to-scalar ratio r of less than 0.1)—seems to fit the recent CMB data rather well [19]. However, different observations have indicated that there exist a few outliers (corresponding to the quadrupole at $\ell = 2$, and near other lower multipoles at $\ell = 22$ and 40), in the observed CMB angular power spectrum which lie outside the cosmic variance associated with the concordant model [12, 13, 14, 15, 16, 18]. These discrepancies have remained in subsequent updates of the data [12, 13, 14, 15, 16, 18, 19], and have also survived in other independent estimates of the angular power spectrum (see, for instance, Refs. [206, 207, 208]). Given the CMB observations, a handful of model independent approaches have been constructed over the last few years to recover the primordial power spectrum [130, 131, 163, 164, 165, 166, 167, 168, 169]. At the smaller scales, all these approaches arrive at a spectrum that is nearly scale invariant. However, many of the approaches seem to unambiguously point to a sharp drop in power (with specific features) at the scales corresponding to the Hubble scale today.

Even as the debate about the statistical significance of the outliers in the CMB data has continued [132, 133, 134, 135], as we had mentioned in the last chapter, a considerable

amount of effort has been devoted to understand the possible physical reasons behind these outliers (for an inexhaustive list, see Refs. [117, 126, 128, 129, 137, 138, 139, 140, 141, 142, 143, 144, 145, 146, 147, 148, 150, 151, 152, 153, 154, 155, 156, 158, 159, 160, 161, 162, 178]). Within the inflationary paradigm, different models have been constructed to produce a sharp drop in the scalar power at large scales, so as to lead to a better fit to the low quadrupole (see Refs. [117, 126, 138, 139, 145, 148, 152, 153, 154, 155, 156, 158, 161]; for earlier efforts that discuss generating features in the inflationary perturbation spectrum, see Refs. [136, 170, 171, 173, 174, 175, 176, 177, 186, 187]). However, many of the scenarios that have been considered in this context seem rather artificial—they either assume a specific pre-inflationary regime or specific initial conditions for the inflaton [117, 126, 148, 155, 156, 158, 161]. Also, in some cases, either certain special initial conditions are chosen for the perturbations or the initial conditions are imposed when a subset of the modes are outside the Hubble radius [117, 126, 148, 155, 156, 158, 161]. Such requirements clearly contradict the spirit of inflation.

Motivated by the aim of arriving at the desired power spectrum without any special initial conditions on either the background or the perturbations, in the preceding chapter, we had considered a setting involving two stages of slow roll inflation that sandwich an intermediate period of departure from inflation [205]. In such a *punctuated inflationary scenario*, the first phase of slow roll inflation allows us to impose the standard, sub-Hubble initial conditions on the perturbations which may leave the Hubble radius during the subsequent rapid roll regime (i.e. a period wherein the first slow roll parameter $\epsilon \gtrsim 1$). The second slow roll phase lasts for, say, 50–60 e -folds, thereby enabling us to overcome the well known horizon problem associated with the hot big bang model. As we had discussed in the last chapter, such a background behavior can be achieved in certain large field inflationary models wherein the potentials contain a point of inflection [the form of the potentials we had considered are encountered in the Minimal Supersymmetric Standard Model (MSSM)]. As we had shown in the previous chapter, the slow-rapid-slow roll transition leads to a step like feature in the scalar power spectrum. Importantly, we had found that, if we set the scales such that the drop in the power spectrum occurs at a length scale that roughly corresponds to the Hubble radius today, then a spectrum we had obtained leads to a much better fit to the recent WMAP 5-year data (with just one extra parameter, χ^2_{eff} improves by 6.6) when compared to

the best fit reference Λ CDM model with the standard, power law, primordial spectrum [205].

All models of inflation generate tensor perturbations that can potentially have an observable effect on the measured CMB temperature and polarization spectra [209, 210, 211, 212]. Barring an exception [127], most of the efforts in the literature have focused on suppressing the scalar power spectrum on large scales, and have overlooked the corresponding effects on the tensors. In this chapter, we discuss the effects of the slow-rapid-slow roll transition on the tensor perturbations in the canonical scalar field and the tachyonic [49, 50, 51, 52, 53, 54, 55, 56, 92] inflationary models. Aided by a few different examples (including the specific model that we had considered in the last chapter), we show that, in punctuated inflation, a drop in the scalar power on large scales is *always* associated with an increase in the tensor power and, hence, a dramatic rise in the tensor-to-scalar ratio r , on these scales. In fact, we find that the strong rise leads to a small range of modes for which the tensor-to-scalar ratio actually proves to be *much greater than unity*¹. We believe that this is the first instance in the literature wherein examples of single scalar field inflationary models resulting in $r \gg 1$ are being presented. However, if we are to utilize the drop in the scalar power to provide a better fit to the low CMB quadrupole, then the modes with rather large tensor-to-scalar ratio turn out to be bigger than the Hubble scale today.

The rapid rise in the tensor-to-scalar ratio r at large scales translates to a dramatic enhancement in the angular power spectrum, C_ℓ^{BB} , of the B-mode polarization of the CMB at the low multipoles. This could potentially be a characteristic signature of punctuated inflationary scenarios that match the CMB data well. But, in the specific models of punctuated inflation that we have explored to match the low multipoles of CMB temperature power spectrum, the enhanced C_ℓ^{BB} is not at an observable level. This is due to the following two reasons. Firstly, the band of scales where $r \gg 1$ is far beyond the Hubble scale and, secondly, because r is extremely small at large wavenumbers. However, it is readily conceivable that there exist models of punctuated inflation where either one or both of these features can be modified favorably to arrive at observable levels of C_ℓ^{BB} . In this chapter, we highlight the extremely large values of the tensor-to-scalar ratio attainable in the punctuated inflationary scenario.

¹In the models we consider, r attains a maximum value of about 100. Though the tensor-to-scalar ratio is large, the actual amplitude of the tensor perturbations still remains small for the linear perturbation theory to be valid.

This chapter is organized as follows. In Sec. 4.2, we outline the broad features of the scalar and tensor spectra that result in punctuated inflation. In Sec. 4.3, we discuss the spectra that arise in two different punctuated inflationary models involving the canonical scalar field, while, in Sec. 4.4, we discuss the spectra in a particular tachyonic model. In Sec. 4.5, we consider the corresponding effects on the angular power spectrum of the B-mode polarization of the CMB. In Sec. 4.6, to highlight the peculiar feature that the tensor-to-scalar ratio turns out to be greater than unity for a range of modes in punctuated inflation, we illustrate the evolution of the scalar and tensor amplitudes for a particular mode from this domain. Finally, in Sec. 4.7, we conclude with a brief discussion on the implications of this feature.

4.2 Characteristics of the scalar and the tensor perturbation spectra in punctuated inflation

In this section, we shall discuss the broad features of the scalar and the tensor spectra that arise in the punctuated inflationary scenario.

As we have repeatedly mentioned in the earlier chapters, it is often remarked that, during inflation, the amplitude of the curvature perturbations freezes at its value at Hubble exit in the single scalar field models. Actually, this happens to be true only if there is no departure from slow roll inflation soon after the modes leave the Hubble radius [99, 100, 123]. But, as we have discussed in the second chapter, when there is a period of deviation from slow roll, then, it is found that the asymptotic (i.e. the extreme super-Hubble) amplitude of the modes that exit the Hubble scale just before the deviation are enhanced when compared to their value at Hubble exit. While modes that leave well before the departure from slow roll are unaffected, it has been shown that there exists an intermediate range of modes whose amplitudes are suppressed at super-Hubble scales [123]. Due to these behavior, punctuated inflation leads to a step like feature in the scalar power spectrum. Evidently, the two nearly flat regions of the step correspond to modes that exit the Hubble scale during the two stages of slow roll. The step actually contains a sharp dip before the rise, and this feature is associated with the modes that leave the Hubble radius just before the transition to the rapid roll regime.

Let us now understand the tensor spectrum that can result in a similar situation. In the

case of the scalar modes, the quantity (z'/z) that appears in the differential equation for the curvature perturbation \mathcal{R}_k in Eq. (2.33) turns out to be negative during a period of fast roll, and, as discussed in the earlier chapters, it is this feature that proves to be responsible for the amplification or the suppression of the modes at super-Hubble scales [99, 100, 123]. In contrast, the coefficient of the friction term in the equation for the tensor amplitude \mathcal{U}_k in Eq. (2.42)—viz. (a'/a) —is a positive definite quantity at all times. Hence, we do not expect any non-trivial super-Hubble evolution of the tensor perturbations. However, recall that, during a period of slow roll, the tensor amplitude is proportional to the potential of the scalar field [1, 3, 5, 6, 94, 95, 96, 97, 213]. It is then immediately clear that, in the slow-rapid-slow roll scenario of our interest, the tensor spectrum will also be in the shape of a step, with the modes that leave during the second slow roll phase having lower power than those which exit during the first phase [since, unless the potential is negative, the inflaton always rolls *down* the potential (see, for example, Ref. [214])]. In other words, in punctuated inflation, the tensor step happens to be in exactly the opposite direction as the step in the scalar spectrum. The fact that the scalar power drops at large scales, while the tensor power rises on these scales, leads to a sharp increase in the tensor-to-scalar ratio r . Interestingly, we find that the steep rise can result in the tensor-to-scalar ratio being greater than unity for a small range of modes. (These range of modes correspond to those for which the scalar spectrum exhibits a sharp dip before the rise.) However, as we shall discuss below, in the specific models of punctuated inflation that we consider, in spite of the rise, the tensor-to-scalar ratio remains too small to be observed (r proves to be less than 10^{-4}) for the modes of cosmological interest (say, $10^{-4} \lesssim k \lesssim 1 \text{ Mpc}^{-1}$). But, we believe that the increase in the tensor-to-scalar ratio at large scales considerably improves the prospects of constructing punctuated inflationary models wherein C_ℓ^{BB} at the low multipoles is within the observational reach of upcoming missions such as PLANCK [197] or CMBPol [198].

4.3 Punctuated inflation with canonical scalar fields

In this section, we shall discuss punctuated inflationary scenarios in models where inflation is driven by the canonical scalar field. We shall first present the model that we had considered in the previous chapter, and then discuss a hybrid inflation model.

Before proceeding to discuss the specific models, we shall outline as to how one can ar-

arrive at the potential and the parameters that result in punctuated inflation and the desired scalar spectrum. Needless to say, not all potentials will allow punctuated inflation. Therefore, to begin with, one has to identify a potential, or a class of potentials, that lead to such a scenario. Even amongst the limited class of potentials, the required slow-rapid-slow roll transition may occur only for a certain range of values of the parameters describing the potential. The form of the potential and the range of the parameters can be arrived at, say, based on the behavior of the first two PSR parameters. Once the potential and the range of the parameters that allow punctuated inflation have been identified, we need to ensure that the following two observational requirements are also satisfied. Firstly, the second stage of slow roll inflation has to last for about 60 e -folds in order to overcome the horizon problem. Secondly, the nearly scale invariant higher step in the scalar power spectrum has to match the COBE amplitude. These two conditions further restrict the allowed range of the parameters describing the potential.

4.3.1 The model motivated by MSSM

As we had discussed in the preceding chapter, the model motivated by MSSM contains two parameters m and λ , and is described by the potential [179, 180, 181, 182]

$$V(\phi) = \left(\frac{m^2}{2}\right) \phi^2 - \left(\frac{\sqrt{2\lambda(n-1)}m}{n}\right) \phi^n + \left(\frac{\lambda}{4}\right) \phi^{2(n-1)}, \quad (4.1)$$

where $n > 2$ is an integer. This potential has a point of inflection at $\phi = \phi_0$ (i.e. the location where both V_ϕ and $V_{\phi\phi}$ vanish), with ϕ_0 given by

$$\phi_0 = \left[\frac{2m^2}{(n-1)\lambda} \right]^{\frac{1}{2(n-2)}}. \quad (4.2)$$

Note that the potential (4.1) reduces to a typical large field model when the field is sufficiently far away from the point of inflection. It is then clear that the first stage of slow roll can be achieved in the domain $\phi \gg \phi_0$, and a period of rapid roll can occur when $\phi \simeq [\sqrt{2}(n-1)]$. Also, since the first two PSR parameters vanish at the point of inflection, a second stage of slow roll can be expected to arise when the field is very close to ϕ_0 . We find that restarting inflation after the rapid roll phase and the number of e -folds that can be achieved during the second stage of slow roll crucially depends on the location of the point

of inflection. We depend on the numerics to arrive at a suitable value of ϕ_0 . Once ϕ_0 has thus been identified, we find that the COBE normalization determines the value of the other free parameter m .

In Fig. 4.1, we have plotted the scalar and the tensor power spectra for the cases of $n = 3$ and $n = 4$. These spectra correspond to the parameters that provide the best fit to the recent WMAP 5-year data (for the values of the various parameters and other relevant details, see the previous chapter and also Ref. [205]). We should mention that in these cases inflation is actually interrupted for about one e -fold during the rapid roll regime. As we had discussed in the previous chapter, we found that, while the $n = 3$ case provides a much better fit to the data than the reference concordant model (as we had pointed out earlier, with just one more parameter than the concordant model, χ^2_{eff} improves by 6.6), the $n = 4$ case leads to a very poor fit to the data. We believe that the poor fit by the $n = 4$ case can be attributed to the large bump in the scalar power spectrum that arises just before it turns scale invariant. Since the bump grows with n , we feel that the cases with $n > 4$ will fit the data much more poorly and, hence, we have not compared these cases with the data. As we had mentioned in the last chapter, the scalar power spectrum with a drop in power at large scales is often approximated by a spectrum with an exponential cut off [cf. Eq. (3.7)]. In Fig. 4.1, we have also plotted this spectrum for values of the different parameters that closely approximate the exact spectra we obtain.

In Fig. 4.2, we have plotted the resulting tensor-to-scalar ratio for the two cases of $n = 3$ and $n = 4$. Clearly, the broad characteristics of the scalar and the tensor spectra as well as the tensor-to-scalar ratio that we had outlined in the previous section are corroborated by these two figures.

4.3.2 A hybrid inflation model

Another model that is known to lead to a punctuated inflationary scenario is a hybrid model that can be effectively described by the following potential (see, for instance, Ref. [99]; for the earliest discussion of the model, see Ref. [46]):

$$V(\phi) = \left(\frac{M^4}{4} \right) (1 + B \phi^4). \quad (4.3)$$

For suitable values of the parameter B , this potential admits two stages of slow roll inflation, broken by a brief period of rapid roll. The first slow roll phase is driven by the ϕ^4 term and,

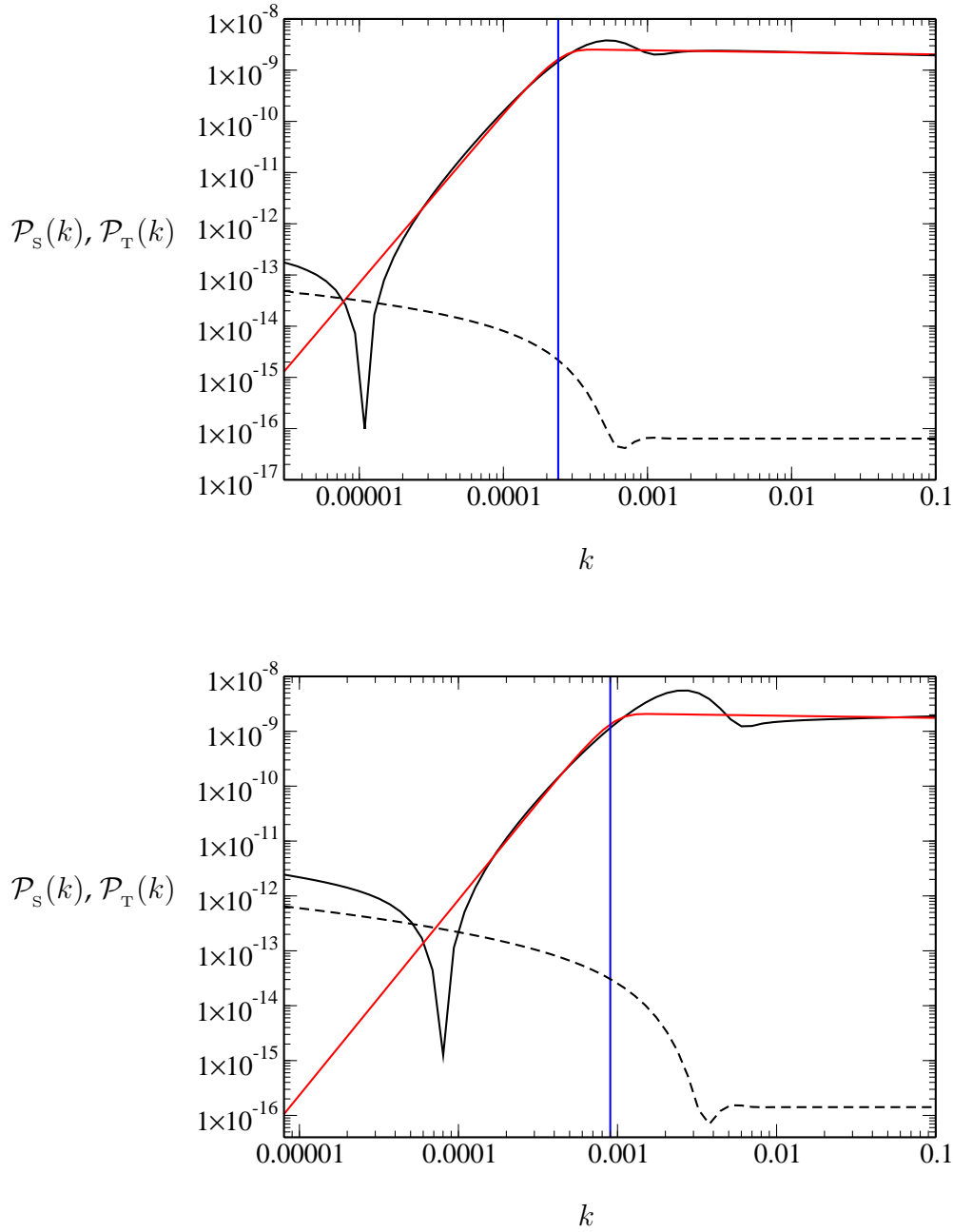


Figure 4.1: The scalar power spectrum $\mathcal{P}_s(k)$ (the solid black line) and the tensor power spectrum $\mathcal{P}_T(k)$ (the dashed black line) have been plotted as a function of the wavenumber k for the cases of $n = 3$ (top) and $n = 4$ (bottom). The red curve in these plots is the spectrum (3.7) with the exponential cut off, whose parameters have been arrived at by a simple visual comparison with the numerically evaluated scalar spectrum. Note that the vertical blue line denotes k_* . The actual values of the different parameters have been mentioned in the previous chapter [cf. the caption of Fig. 3.5] and also in Ref. [205].

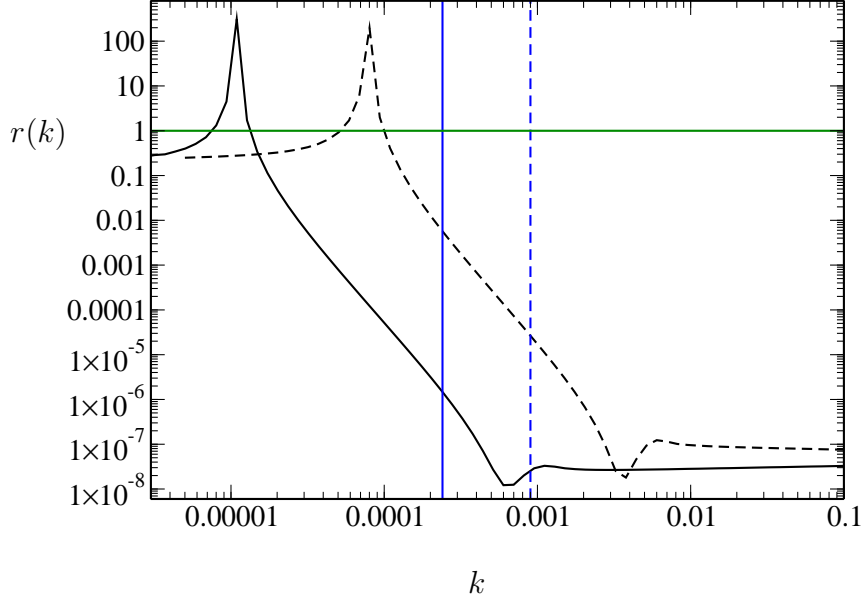


Figure 4.2: The tensor-to-scalar ratio $r(k)$ for the cases of $n = 3$ (the solid black line) and $n = 4$ (the dashed black line) has been plotted as a function of the wavenumber k . These plots have been drawn for the same choice of parameters as in the previous figure. The vertical solid and dashed blue lines denote the k_* corresponding to the $n = 3$ and $n = 4$ cases, respectively. Note that, despite the rise at the larger wavelengths, the tensor-to-scalar ratio remains smaller than 10^{-4} for modes of cosmological interest (i.e. for $k \gtrsim k_*$). For this reason, in the previous chapter, we had ignored the tensor contribution when comparing these models with the WMAP data. Interestingly, we find that there arises a domain wherein the tensor-to-scalar ratio $r(k)$ is actually *much greater than unity* [215]. To highlight this feature, we have included the horizontal green line which denotes $r = 1$. In Sec. 4.6, we have plotted the evolution of the scalar and tensor amplitudes for a mode from this domain.

when ϕ has rolled down the potential and has become sufficiently small, the false vacuum term drives the second phase. The parameter M determines the amplitude of nearly scale invariant lower step in the scalar spectrum (associated with the modes that leave during the first stage of slow roll inflation), with a mild dependence on B . However, B very strongly affects the rise in scalar power (corresponding to the modes that leave just before the rapid roll stage) and the asymptotic spectral index (associated with the modes that leave during the second stage of inflation), since it determines the extent and the duration of the departure from slow roll.

We are able to achieve COBE normalization for a suitable combination of the parameters M and B . For these values of the parameters, we find that, as in the MSSM case, a departure from inflation occurs (again, for about one e -fold) during the rapid roll phase. In Fig. 4.3, we have plotted the resulting scalar and the tensor power spectra as well as the associated tensor-to-scalar ratio. We should hasten to clarify that we have not compared the hybrid model with the CMB data, as we had done in the $n = 3$ and $n = 4$ cases of MSSM. A well known property of the hybrid models is that they lead to blue scalar spectra. We believe that, the blue tilt, along with the rather large bump (which turns out to be larger than the one in $n = 4$, MSSM case) will considerably spoil the fit to the CMB data.

4.4 An example of tachyonic punctuated inflation

In this section, we shall consider a tachyonic model that allows punctuated inflation. Since our experience suggests that a point of inflection in the potential is an assured way of achieving a slow-rapid-slow roll transition, we shall construct a tachyonic potential containing a point of inflection.

Tachyonic potentials are usually written in terms of two parameters, say, λ and T_0 , in the following form [49, 50, 51, 52, 53, 54, 55, 56, 92]:

$$V(T) = \lambda V_1(T/T_0), \quad (4.4)$$

where $V_1(T/T_0)$ is a function which has a maximum at the origin and it vanishes as $T \rightarrow \infty$. In order to achieve the necessary amount of inflation and the correct amplitude for the scalar perturbations, suitable values for the two parameters λ and T_0 that describe the above potential can be arrived at as follows. One finds that, in these potentials, inflation typically occurs around $T \simeq T_0$ corresponding to an energy scale of about $\lambda^{1/4}$. Moreover, it turns out that, the quantity (λT_0^2) has to be much larger than unity (in units wherein $M_p = 1$) for the PSR parameters to be small and, thereby ensure that, at least, 60 e -folds of inflation takes place. One first chooses a sufficiently large value of (λT_0^2) by hand in order to guarantee slow roll. The COBE normalization condition for the scalar perturbations then provides the second constraint, thereby determining the values of both the parameters λ and T_0 [92].

Now, consider a tachyon potential of the form

$$V(x) = \left(\frac{\lambda}{1 + g(x)} \right), \quad (4.5)$$

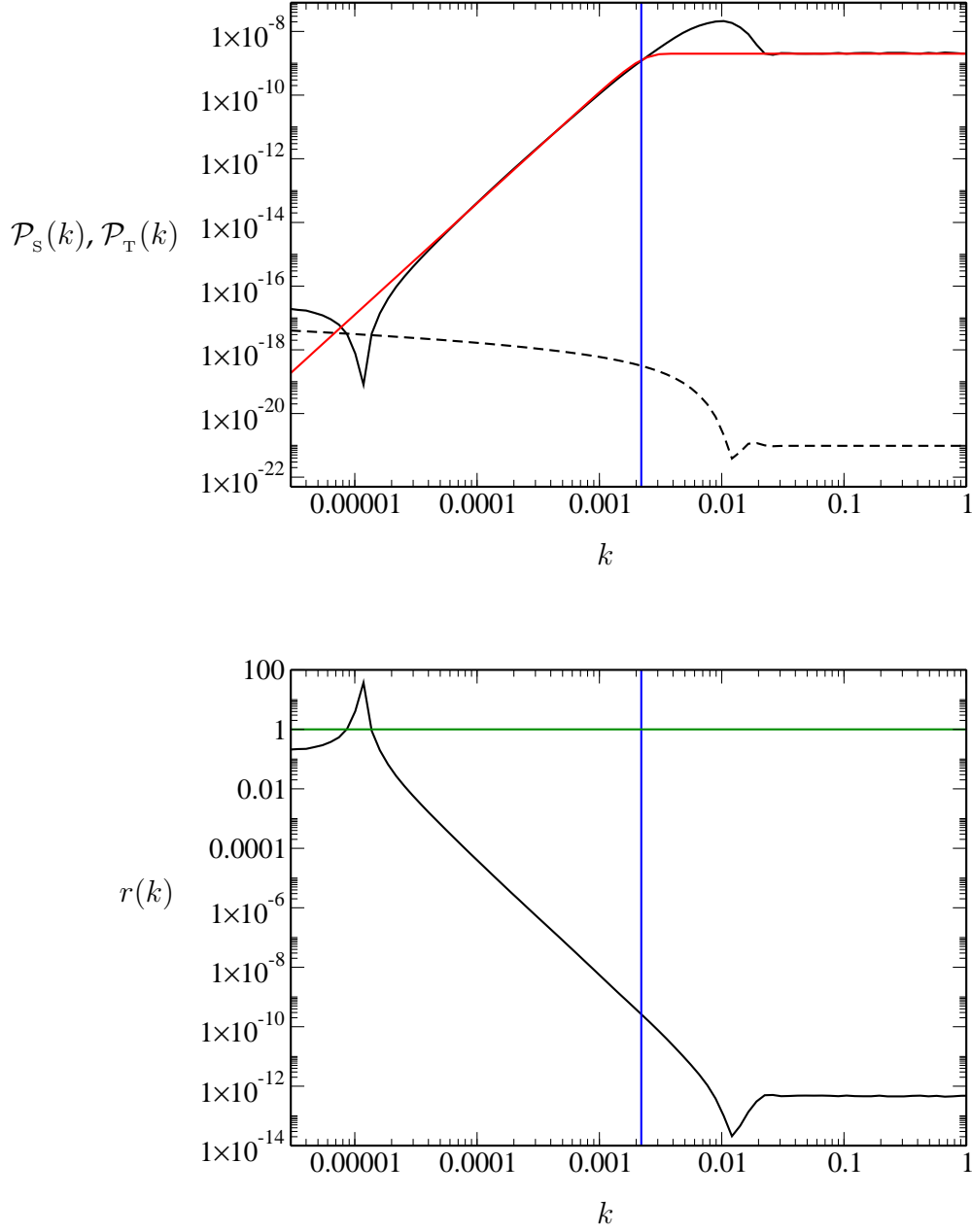


Figure 4.3: The scalar power spectrum $\mathcal{P}_s(k)$ (the solid black line) and the tensor power spectrum $\mathcal{P}_T(k)$ (the dashed black line) have been plotted (top) as a function of the wavenumber k for the hybrid inflation model described by the potential (4.3). The corresponding tensor-to-scalar ratio $r(k)$ has also been plotted (bottom). As in the previous figure, the horizontal green line in the graph at the bottom denotes $r = 1$. These spectra correspond to following values of the potential parameters: $M = 2.6 \times 10^{-5}$ and $B = 0.552$. The solid red curve in the graph on top is the exponential cut off spectrum (3.7) corresponding to $A_s = 2 \times 10^{-9}$, $n_s = 1.0$, $k_* = 2.2 \times 10^{-3} \text{ Mpc}^{-1}$ and $\alpha = 3.5$. The vertical blue line in both the graphs denotes k_* . We should mention that the blue tilt in the scalar spectrum is very small and, hence, is not evident from the figure.

where $x = (T/T_0)$. Let the function $g(x)$ be defined as an integral of yet another function $f(x)$ as follows:

$$g(x) = \int dx f(x), \quad (4.6)$$

with the constant of integration assumed to be zero. If we choose $f(x)$ to be a polynomial that vanishes at least quadratically at a point, say, x_1 , then, it is clear that the resulting potential $V(x)$, in addition to satisfying the above mentioned conditions (i.e. having a maxima at the origin and a minima at infinity), will also contain a point of inflection at x_1 . A simple function that satisfies our requirements turns out to be²

$$f(x) = [(x - x_1)^2 x^2]. \quad (4.7)$$

For this choice of the function $f(x)$ and appropriate values of the parameters λ and T_0 , we find that the corresponding potential gives rise to punctuated inflation. However, it is important to note that, unlike the earlier examples, the rapid roll phase *does not* result in a deviation from inflation. In Fig. 4.4, we have plotted the scalar and the tensor power spectra, and the corresponding tensor-to-scalar ratio that we obtain in this case. It is clear from the figure that the spectra broadly behave in the same fashion as in the earlier examples.

4.5 The effects on the B-modes of the CMB

As is well known, the polarization of the CMB can be decomposed into the E and B-components. While the E-mode polarization is affected by both the scalar as well as the tensor perturbations, the B-modes are generated *only* by the tensor perturbations³. Therefore, the B-mode provides a direct signature of the primordial tensor perturbations (see, for instance, Ref. [6]). The detection of the B-mode is a coveted, prime goal of the experimental community (see, for example, the recent white paper [216]). We feel that the punctuated inflationary scenario can provide additional theoretical motivation for this endeavor.

We have evaluated the angular power spectrum of the B-mode polarization of the CMB (i.e. C_ℓ^{BB}) using the Boltzmann code CAMB [201]. In Fig. 4.5, we have plotted C_ℓ^{BB} for the best fit values of the parameters in the $n = 3$ and the $n = 4$ cases of MSSM. For comparison,

²Actually, this function contains another point of inflection at the origin. But, as we shall restrict ourselves to the domain $x > 0$, it is not useful to us.

³In fact, the B-modes are created by the vector perturbations too. However, inflation does not generate any vector perturbations (see, for instance, Ref. [6], p. 116).

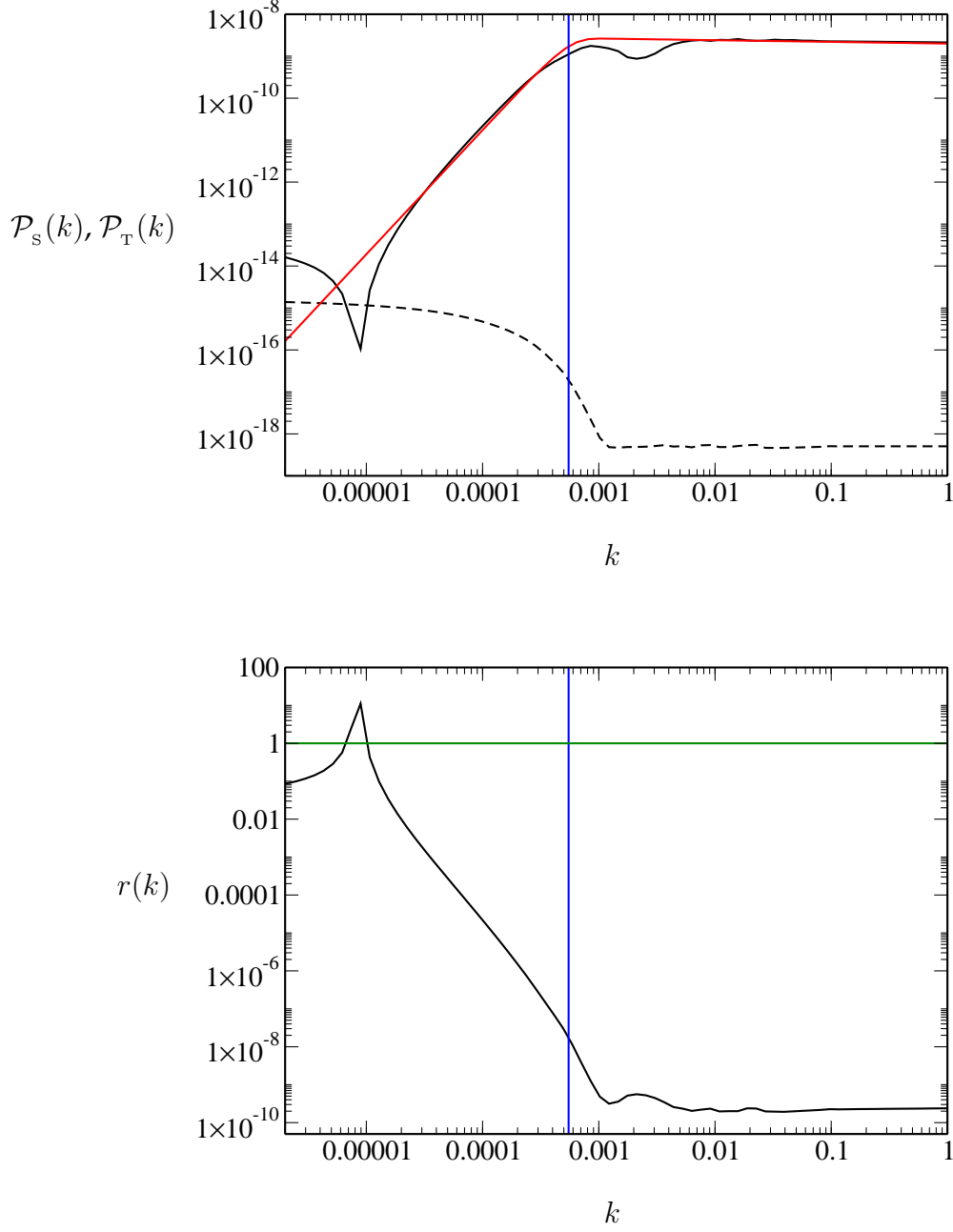


Figure 4.4: The scalar and the tensor power spectra and the corresponding tensor-to-scalar ratio for the case of tachyonic punctuated inflation as well as the exponential cut off spectrum have been plotted exactly in the same fashion as in the previous figure. These figures correspond to the following values of the parameters: $\lambda = 10^{-13}$, $T_0 = 3.55 \times 10^7$, $x_1 = 10$, $A_s = 2 \times 10^{-9}$, $n_s = 0.96$, $k_* = 5.5 \times 10^{-4} \text{ Mpc}^{-1}$, and $\alpha = 3$.

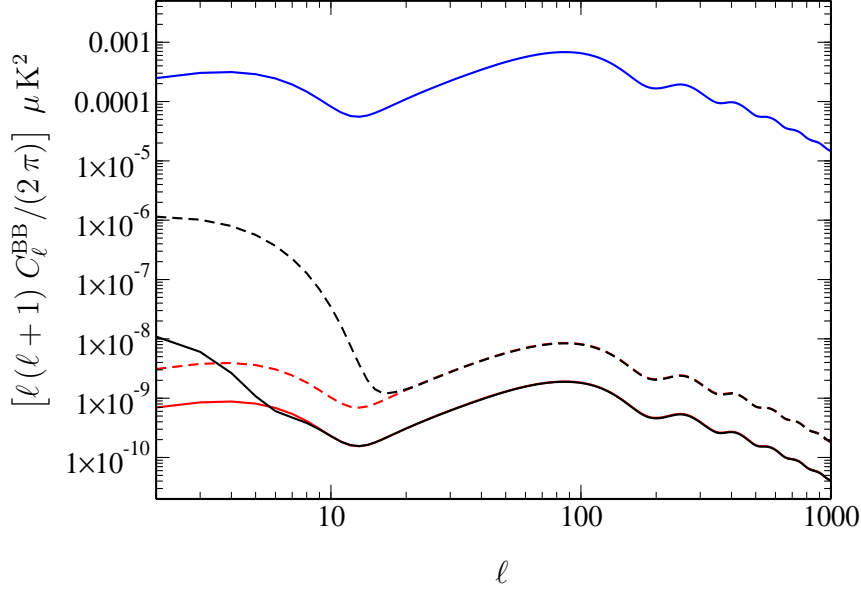


Figure 4.5: The B-mode CMB angular power spectrum C_ℓ^{BB} has been plotted as a function of the multipole ℓ for the best fit values of the $n = 3$ (the solid black line) and $n = 4$ (the dashed black line) MSSM models. For comparison, we have also plotted the C_ℓ^{BB} for the concordant cosmological model with a strictly scale invariant tensor spectrum and a tensor-to-scalar ratio of $r = 0.01$ (the solid blue line), $r = 2 \times 10^{-8}$ (the solid red line) and $r = 10^{-7}$ (the dashed red line). The latter two curves match the $n = 3$ and $n = 4$ MSSM cases at the small angular scales, and they help in highlighting the effects of punctuated inflation at the lower multipoles.

we have also plotted the corresponding angular power spectra for the concordant cosmological model with a strictly scale invariant tensor spectrum and a tensor-to-scalar ratio of $r = 0.01$, $r = 2 \times 10^{-8}$ and $r = 10^{-7}$ (the last two values have been chosen since they match the $n = 3$ and $n = 4$ MSSM cases at the small angular scales). The C_ℓ^{BB} for the two MSSM cases clearly exhibit an increase in their amplitude at the lower multipoles, reflecting the rise in the tensor-to-scalar ratio on these scales⁴. But, despite the rise at the lower multipoles, the amplitude of C_ℓ^{BB} in these cases proves to be way too smaller than what is possibly de-

⁴We should point out that, in order to evaluate the CMB angular power spectra, CAMB integrates over the following range of wavenumber of the primordial scalar and tensor spectra: $7.79 \times 10^{-6} < k < 2.78 \times 10^{-1} \text{ Mpc}^{-1}$. Note that, in both the MSSM cases, the lower limit on the k -integral is actually smaller than the wavenumber where r attains its maximum value (cf. Fig. 4.2). In other words, though the $r > 1$ region is well beyond the Hubble scale today (i.e. $k \lesssim 10^{-4} \text{ Mpc}^{-1}$), the C_ℓ^{BB} evaluated by CAMB seems to be sensitive to the contributions from these scales.

tectable in the near future (upcoming missions such as PLANCK [197] and CMBPol [198] are expected to be sensitive to $r \gtrsim 0.01$). However, since the increase in the B-mode power at large angular scales is a generic feature of punctuated inflation, we feel that it improves the possibility that the effect may be detected in the future. It is conceivable that there exist punctuated inflationary models that predict a significantly larger tensor-to-scalar ratio, while still providing a good fit to the CMB temperature angular power spectrum. It seems a worthwhile exercise to hunt for such models.

4.6 The evolution of the scalar and tensor perturbations for a mode with $r > 1$

In the various examples of punctuated inflation that we had discussed earlier, though the tensor-to-scalar ratio remains too small ($r < 10^{-4}$) on the scales of cosmological interest (i.e. for $10^{-4} \lesssim k \lesssim 1 \text{ Mpc}^{-1}$), we find that there exists a small range of modes for which the tensor-to-scalar ratio turns out to be greater than unity. This indicates that the amplitude of the tensor perturbation is larger than that of the scalar perturbation for modes that correspond to this range. We believe that this is an interesting feature which may have potential observational consequences. To highlight this feature, in Fig. 4.6, we have plotted the evolution of the amplitudes of the curvature and the tensor perturbations for a mode corresponding to the wavenumber $k = 10^{-5} \text{ Mpc}^{-1}$ that has a tensor-to-scalar ratio greater than unity in the $n = 3$, MSSM case. While the amplitude of the tensor perturbation freezes at its value at Hubble exit, the amplitude of the curvature perturbation is suppressed at super-Hubble scales, when compared to its value at Hubble exit. As is clearly illustrated in the figure, such a behavior of the perturbations leads to a large tensor-to-scalar ratio that actually proves to be greater than unity.

4.7 Conclusions

In the last chapter, we had performed a Markov Chain Monte Carlo analysis to determine the values of the MSSM parameters that provide the best fit to the recent WMAP 5-year data for the CMB angular power spectrum. We had found that a scalar spectrum in the $n = 3$ case leads to a much better fit of the observed data than the concordant model. We

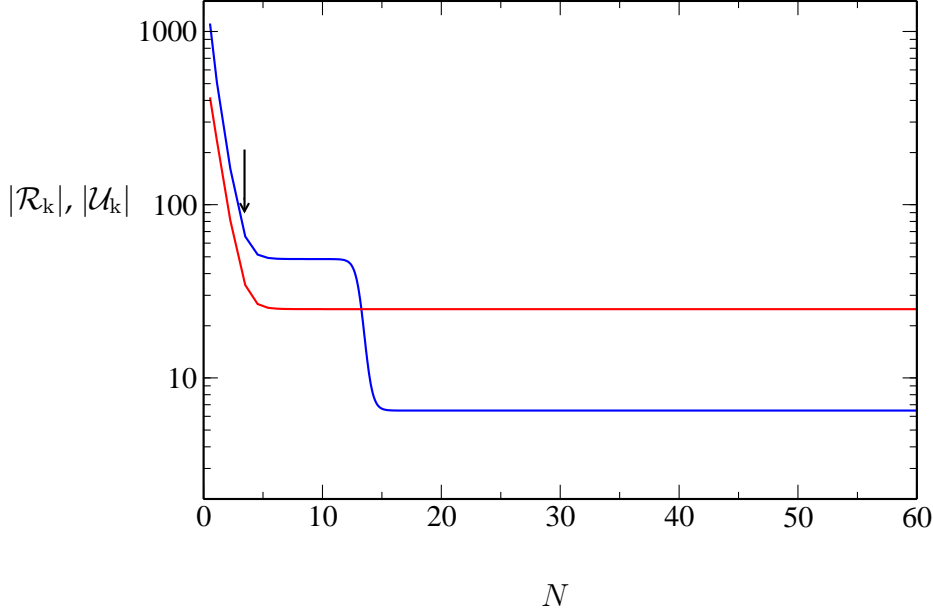


Figure 4.6: The evolution of the amplitudes of the curvature perturbation \mathcal{R}_k (in blue) and the tensor perturbation \mathcal{U}_k (in red) has been plotted as a function of the number of e -folds N for the best fit values of the $n = 3$, MSSM case. These perturbations correspond to the mode $k = 10^{-5} \text{ Mpc}^{-1}$, and the arrow denotes the time when the mode leaves the Hubble radius. Note that, as expected, the tensor amplitude freezes at its value at Hubble exit. Evidently, the large tensor-to-scalar ratio arises due to the suppression of the amplitude of the curvature perturbation at super-Hubble scales.

should emphasize again that we have not carried out such a comparison with the data for the hybrid or the tachyon model. In the $n = 3$, MSSM case, we had found that, in addition to the drop in the power at large scales, the bump present in the spectrum before it turns scale invariant had led to the improvement in the fit. In the $n = 4$ case, a rather large bump had led to a poor fit to the data. We find that, a similar, large bump arises in the hybrid model as well. Also, as we had mentioned, in the hybrid model, the scalar spectral index proves to be greater than unity at small scales. We feel that these two features will not allow a better fit in the hybrid case. In the tachyonic model, though the spectral index is close to the observed value, we find that no bump (*above* the asymptotic, nearly scale invariant amplitude) arises in the spectrum. We expect that this feature will spoil the fit to the data. Also, we believe that the lack of such a bump is due to the fact that inflation is not interrupted in this case.

In models which start with a period of fast roll, along with the scalar power, the tensor power is also suppressed at large scales [127]. But, the drop in the scalar power proves to be sharper than that of the tensors and, as a result, the tensor-to-scalar ratio displays a rise over these scales in such models. It has been argued that such a feature may be detected by forthcoming missions such as, for instance, PLANCK [197]. We too encounter an increase in the tensor-to-scalar ratio on the large scales, though the reason is somewhat different. In punctuated inflation, the rise in the tensor-to-scalar ratio turns out to be much stronger due to the fact that the tensor amplitude itself increases on large scales. Intriguingly, we find that the rapid rise leads to the tensor-to-scalar ratio being much larger than unity for a small range of modes. However, in the specific models we have considered, the tensor amplitude on scales of cosmological interest (say, $10^{-4} \lesssim k \lesssim 1 \text{ Mpc}^{-1}$) proves to be too small ($r < 10^{-4}$) for the effect to be possibly detected in the very near future.

The sharper the drop in the scalar spectrum at large scales, the better seems to be the fit to the low CMB quadrupole. In punctuated inflation, the steeper the drop in the scalar power, the faster will be the corresponding rise in the tensor power at large scales. Therefore, if the scalar power drops fast, the tensor-to-scalar ratio can be larger on the small scales, thereby improving the prospects of its detection through the B-modes of the CMB polarization. However, empirical evidence indicates that, in punctuated inflation, a steeper drop in the scalar power requires a larger value of the first slow roll parameter ϵ during the rapid roll. But, such a large ϵ also leads to a bigger bump (above the asymptotic amplitude) in the scalar spectrum before it turns scale invariant. While a suitable bump seems to provide a better fit to the data at a few lower multipoles after the quadrupole, too large a bump seems to spoil the fit to the data (as in the $n = 4$, MSSM case). In other words, to lead to a good fit, there appears to be a trade off between the sharpness of the cut off and the size of the bump in the scalar power spectrum. It will be a worthwhile exercise to look for punctuated inflationary models that will lead to a sufficiently steep drop in the scalar power at large scales, a suitably sized bump at the top of the spectrum, and also a reasonable tensor amplitude at small scales that may be detectable by forthcoming missions [197, 198].

Chapter 5

Reheating and its effects on the large scale perturbations

5.1 Effects of inflationary and post-inflationary dynamics on the evolution of the super-Hubble perturbations

In the standard inflationary scenario, the scales of cosmological interest exit the Hubble radius within the first few (about 8-10) e -folds of inflation and, hence, are outside the Hubble scale during the later epochs. When comparing the predictions of the inflationary models with the CMB and the large scale structure data, as we had pointed out, it is often assumed that the amplitude of the curvature perturbations remain constant at super-Hubble scales. In such a situation, the observed CMB anisotropies directly determine the amplitude and the shape of the perturbation spectrum imprinted on the modes when they left the Hubble radius during inflation. Typically, the amplitude of the perturbations constrain the parameters that describe the inflaton potential, while the shape of the spectrum limits its form (see, for instance, any of the standard texts [1, 3, 5, 6] or one of the following reviews [94, 95, 96, 97, 98]).

Provided inflation is of the slow roll type for *all* of the required number of e -folds, it is indeed true that the amplitude of the curvature perturbations freeze at their value at Hubble exit. However, if there is a period of deviation from slow roll inflation, as we had discussed in chapter 2, the asymptotic (i.e. the extreme super-Hubble) amplitude of the modes that leave the Hubble radius just before the deviation are enhanced when compared to their value at Hubble exit [99, 100, 123]. While modes that leave well before the deviation remain

unaffected, it is found that there exists an intermediate range of modes whose amplitudes are actually suppressed at super-Hubble scales [123, 217]. Depending on the form of the departure from slow roll, these effects lead to certain features in the scalar perturbation spectrum. If such deviations occur either during or soon after the cosmological scales leave the Hubble radius, then the CMB observations constrain the resulting features rather well (for an inexhaustive list, see Refs. [126, 127, 128, 129, 136, 139, 148, 150, 151, 154, 155, 156, 158, 159, 160, 161, 170, 171, 173, 174, 175, 176, 177, 178, 205]). But, at smaller scales, only theoretical tools are currently available to restrict the form of the primordial spectrum. These constraints are essentially based on the number density of primordial black holes that are formed towards the end of inflation (for recent discussions in this context, see, for example, Refs. [218, 219, 220, 221]).

Since the cosmological scales are well outside the Hubble radius by the early stages of inflation, clearly, the *shape* of the perturbation spectrum on such large scales is indeed unlikely to be affected by subsequent dynamics. But, over the past decade, it has been recognized that post-inflationary dynamics can alter the *amplitude* of the curvature perturbations at super-Hubble scales, in particular, when more than one component of matter is present. As we had mentioned in the introductory chapter, preheating, the curvaton scenario and the modulated reheating mechanism are popular examples that illustrate the interesting possibilities of post-inflationary dynamics. Preheating—a mechanism that transfers energy from the inflaton to radiation through an explosive production of quanta corresponding to an intermediate scalar field—is known to even lead to an exponential growth in the amplitude of the super-Hubble perturbations (for the earlier discussions, see Refs. [67, 68, 69, 70, 71, 72, 73, 74, 75, 76, 77, 78, 79, 80] and, for more recent efforts, see, for instance, Refs. [81, 82, 83, 84]). In the curvaton scenario, while the inflationary epoch still remains the source of the perturbations, these perturbations are amplified after inflation due to the presence of entropic perturbations (see, for example, Refs. [85, 86]). The modulated reheating scenario is an extreme case wherein inflation is essentially required only to resolve the horizon problem, whereas the perturbations are generated due to an inhomogeneous decay rate when the energy is being transferred from the inflaton to radiation through other fields [87, 88, 89, 90]. These different alternatives indicate that the post-inflationary evolution of the large scale curvature perturbations can be highly model dependent and, therefore,

5.1. INFLATIONARY AND POST-INFLATIONARY EFFECTS ON THE PERTURBATIONS

requires a careful and systematic study.

With these motivations in mind, we investigate the problem of the more conventional (perturbative) reheating [62, 63, 64, 65, 66], and its effects on the evolution of the curvature perturbations in tachyonic inflationary models (for the original discussions on the tachyon, see Refs. [49, 50, 51, 52, 53, 54]; for efforts on treating the tachyon as an inflaton, see, for instance, Refs. [55, 56, 92]; for discussions on reheating in such inflationary models, see Refs. [222, 223, 224, 225]). We shall consider two types of potentials to describe the tachyon and construct scenarios of transition from inflation to radiation domination for the following two possible cases of the decay rate Γ of the tachyon into radiation: (i) a constant, and (ii) dependent on the tachyon. We solve the coupled equations for the system numerically and study the evolution of the perturbations from the sub-Hubble to the super-Hubble scales. Importantly, we shall consider the effects of the transition from inflation to the radiation dominated epoch on the evolution of the large scale (i.e. those that correspond to cosmological scales today) curvature and non-adiabatic pressure (i.e. the intrinsic entropy as well as the relative entropy or the isocurvature) perturbations. We shall evaluate the spectrum of curvature perturbations at the end of inflation as well as at the early stages of the radiation dominated epoch. As we shall illustrate, reheating does not affect the amplitude of the curvature perturbations in any of these cases. We shall also show that, before the transition to the radiation dominated epoch, the relative non-adiabatic pressure perturbation between the tachyon and radiation decays in a fashion very similar to that of the intrinsic entropy perturbation associated with the tachyon. Moreover, we demonstrate that, after the transition, the relative non-adiabatic pressure perturbation dies down extremely rapidly during the early stages of the radiation dominated epoch. It is these behavior which ensure that the amplitude of the curvature perturbations remains unaffected during reheating. Our results corroborate similar conclusions that have been arrived at earlier in the literature based on the study of the evolution of the perturbations in the super-Hubble limit [87]. We shall also discuss similar effects in the case of the canonical scalar field.

A few clarifying remarks are in order at this stage of the discussion. We should stress that the set up we are considering is the standard cold inflationary scenario, followed by an epoch of reheating achieved by the standard method of introducing a coarse-grained decay rate in the equation of motion describing the inflaton [62, 63, 64, 65]. Recently, an

analysis somewhat similar to what we shall consider here has been studied in the context of warm inflationary scenarios involving tachyonic fields [226, 227]. Though there can exist similarities in the form of the equations in the cold and the warm inflationary scenarios, the physics in these two scenarios are rather different (for a recent discussion, see, for example, Ref. [228]). Moreover, to analyze the effects of reheating on the large scale perturbations, one could have possibly studied the evolution of the perturbations in the super-Hubble limit, say, the first order (in time) differential equations usually considered in the literature (cf. Refs. [87, 88, 229]). However, some concerns have been raised that the coupling between the inflaton and radiation may affect the amplitude as well as the scalar spectral index in certain situations [65, 66]. Also, the modified background dynamics preceding reheating can effect the extent of small scale primordial black holes that are formed towards the end of inflation. If we are to address such issues, it requires that we study the evolution of the perturbations from the sub-Hubble to the super-Hubble scales.

This chapter is organized as follows. In the following section, we shall summarize the essential background equations for the system consisting of the tachyon and a perfect fluid and set up scenarios of transition from inflation to radiation domination. In Sec. 5.3, we shall obtain the equations describing the scalar perturbations for the system of the tachyon and a perfect fluid. In Sec. 5.4, we shall evolve the coupled system of equations describing the perturbations and study the effects of the transition from inflation to the radiation dominated epoch on the super-Hubble curvature perturbations. We shall plot the spectrum of curvature perturbations at the end of inflation as well as at the early stages of the radiation dominated epoch. We shall also explicitly illustrate that the intrinsic entropy perturbation associated with the tachyon and the relative non-adiabatic pressure perturbation between the tachyon and radiation decay in a similar fashion before and after the transition to the radiation dominated epoch. It is the behavior of these non-adiabatic pressure perturbations which ensure that the amplitude of the curvature perturbations remains unaffected during reheating. In Sec. 5.5, we shall discuss the corresponding results for the case of the canonical scalar field. Finally, in Sec. 5.6, we conclude with a summary and a discussion on the results we have obtained.

5.2 The transition from tachyon driven inflation to the radiation dominated epoch

In this section, we shall discuss the background equations describing the evolution of the tachyon that is interacting with a perfect fluid. Assuming the perfect fluid to be radiation, we shall construct scenarios of transition from tachyon driven inflation to radiation domination for the following two possible types of the decay rate Γ [cf. Eq. (5.5) below] of the inflaton into radiation: (i) a constant, and (ii) dependent on the tachyon [87].

5.2.1 Background equations in the presence of interacting components

In the presence of multiple components, the total energy density and the total pressure of the system can be expressed as the sum of the energy density ρ_α and the pressure p_α of the individual components as follows:

$$\rho = \sum_{\alpha} \rho_{\alpha} \quad \text{and} \quad p = \sum_{\alpha} p_{\alpha}. \quad (5.1)$$

If the different components of fields and fluids do not interact, then, in addition to the total energy density, the energy density of the individual components will be conserved as well. Hence, in such a situation, the energy density ρ_α of each component will individually satisfy the continuity equation [cf. Eq. (1.8)]

$$\dot{\rho}_\alpha + 3H(\rho_\alpha + p_\alpha) = 0. \quad (5.2)$$

On the other hand, when the different components interact, the continuity equation for the individual components can be expressed as (see, for instance, Refs. [87, 230, 231])

$$\dot{\rho}_\alpha + 3H(\rho_\alpha + p_\alpha) = Q_\alpha, \quad (5.3)$$

where Q_α denotes the rate at which energy density is transferred to the component α from the other components. The conservation of the energy of the complete system then leads to the following constraint on the total rate of transfer of the energy densities:

$$\sum_{\alpha} Q_{\alpha} = 0. \quad (5.4)$$

5.2.2 The case of the tachyon and a perfect fluid

Let us now consider the system of a tachyon (which we shall denote as T) that is interacting with a perfect fluid (referred to, hereafter, as F), so that $\alpha = (T, F)$. We shall assume that the rate at which energy density is transferred to the perfect fluid, i.e. Q_F , is given by [225]

$$Q_F = \Gamma \dot{T}^2 \rho_T, \quad (5.5)$$

where ρ_T is the energy density of the tachyon. Such a transfer of energy is assumed to describe—albeit, in a course grained fashion—the perturbative decay of the tachyon into particles that constitute the perfect fluid. The quantity Γ represents the corresponding decay rate and, as we shall discuss below, it can either be a constant, or depend on the tachyon [87].

For the above choice of Q_F , the continuity equation (5.3) corresponding to the perfect fluid is given by

$$\dot{\rho}_F + 3 H (1 + w_F) \rho_F = \Gamma \dot{T}^2 \rho_T, \quad (5.6)$$

where $w_F = (p_F/\rho_F)$ is the equation of state parameter describing the perfect fluid, which we shall assume to be a constant. Also, it is evident from Eq. (5.4) that

$$Q_T = -Q_F = -\Gamma \dot{T}^2 \rho_T. \quad (5.7)$$

Therefore, the continuity equation for the tachyon energy density ρ_T reduces to

$$\dot{\rho}_T + 3 H (\rho_T + p_T) = -\Gamma \dot{T}^2 \rho_T, \quad (5.8)$$

where p_T is the pressure associated with the tachyon. Given a potential $V(T)$ describing the tachyon, the corresponding energy density ρ_T and pressure p_T are given by the expressions in Eqs. (2.64a) and (2.64b). On substituting the expressions for the energy density and pressure in the continuity equation (5.8), we arrive at the following equation of motion for the tachyon T [225]:

$$\left(\frac{\ddot{T}}{1 - \dot{T}^2} \right) + 3 H \dot{T} + \Gamma \dot{T} + \left(\frac{V_T}{V} \right) = 0. \quad (5.9)$$

Before we proceed, the following clarification on the choice of Q_F in Eq. (5.5) is in order at this stage of the discussion. Recall that, in a situation wherein the canonical scalar field, say ϕ , drives inflation, it is common to introduce a $(\Gamma \dot{\phi})$ term in the field equation to describe the perturbative decay of the inflaton [see Refs. [1, 3, 5, 6, 35, 63, 64, 65, 66, 94, 95, 96, 97,

98]; also see Eq. (5.38)]. Motivated by the canonical case, the choice of Q_F in Eq. (5.5) has been specifically made so as to lead to the $(\Gamma \dot{T})$ term in the equation of motion (5.9) for the tachyon [225]. Needless to add, the choice (5.5) is but one of the many possibilities that can help in achieving reheating at the end of inflation.

5.2.3 Tachyonic inflationary models, different possible Γ and reheating

Assuming the perfect fluid to be radiation with $w_F = (1/3)$, we shall construct specific scenarios of transition from tachyon driven inflation to an epoch of radiation domination.

We shall consider two different types of potentials in order to describe the tachyon.

- The first potential we shall consider is given by

$$V_1(T) = \left(\frac{\lambda}{\cosh(T/T_0)} \right), \quad (5.10)$$

a potential that is well motivated from the string theory perspective [53, 54].

- Our second choice will be the following phenomenologically motivated power law potential that has been considered earlier in the literature (see, for example, Ref. [92]):

$$V_2(T) = \left(\frac{\lambda}{1 + (T/T_0)^4} \right). \quad (5.11)$$

As we had discussed in the previous chapter, in order to achieve the necessary amount of inflation and the correct amplitude for the scalar perturbations, suitable values for the two parameters λ and T_0 that describe the above potentials can be arrived at as follows. Firstly, one finds that, in these potentials, inflation typically occurs around $T \simeq T_0$ corresponding to an energy scale of about $\lambda^{1/4}$. Secondly, it turns out that, the quantity $(\lambda T_0^2/M_{\text{P}}^2)$ has to be much larger than unity for the PSR parameters to be small and thereby ensure that, at least, 60 e -folds of inflation takes place. As we had mentioned while considering the tachyonic example in the last chapter, one first chooses a sufficiently large value of $(\lambda T_0^2/M_{\text{P}}^2)$ by hand in order to guarantee slow roll. The COBE normalization condition for the scalar perturbations then provides the second constraint, thereby determining the values of both the parameters λ and T_0 [92].

In the absence of the fluid, we find that the two potentials $V_1(T)$ and $V_2(T)$ above allow about 60 e -folds of slow roll inflation and lead to the correct COBE amplitude for the

Potential	λ	T_0	(T_i/T_0)	\dot{T}_i
$V_1(T)$	10^{-6}	10^5	5.81	0.1
$V_2(T)$	$10^{-5.15}$	3.7×10^4	4.56	0.1

Table 5.1: Achieving inflation: The values for the parameters of the tachyon potential and the initial conditions for the inflaton (the initial value T_i of the tachyon and its initial velocity \dot{T}_i) that we work with. These choices for the parameters and initial conditions lead to the required 60 e -folds of slow roll inflation and the observed amplitude for the scalar perturbations.

choice of the parameters and initial conditions listed in Tab. 5.1. Also, in such a situation, it is known that, at the end of inflation, the tachyon leads to an epoch of dust like behavior [55, 92], thereby making a radiation dominated epoch difficult to achieve. However, as we shall illustrate below, when the tachyon is interacting with the fluid, we can ensure that a transition from inflation to the radiation dominated regime occurs with a suitable choice of the amplitude for the decay rate Γ .

As we mentioned before, we shall consider the following two possible choices for the decay rate Γ : (i) $\Gamma_1 = \bar{\mathcal{A}} = \text{constant}$, and (ii) $\Gamma_2 = \Gamma(T)$. We shall work with the following specific form of $\Gamma(T)$:

$$\Gamma_2 = \Gamma(T) = \bar{\mathcal{A}} \left(1 - \bar{\mathcal{B}} \tanh \left[(T - \bar{\mathcal{C}}) / \bar{\mathcal{D}} \right] \right), \quad (5.12)$$

where $\bar{\mathcal{A}}$, $\bar{\mathcal{B}}$, $\bar{\mathcal{C}}$ and $\bar{\mathcal{D}}$ are constants that we shall choose suitably to achieve the desired evolution. (It turns out that the above form of $\Gamma(T)$ proves to be convenient in the numerical calculations, helping us illustrate the required behavior.) We find that a transition from inflation to radiation domination can be achieved provided the amplitude of Γ (viz. $\bar{\mathcal{A}}$) is chosen to be less than the Hubble parameter H (which is almost a constant) during the epoch of slow roll inflation. In Tab. 5.2, we have listed the values of the initial energy density of radiation (viz. ρ_γ^i) and the various parameters describing the decay rates (for the tachyon, we have used the same values listed in Tab. 5.1) that lead to about 60 e -folds of slow roll inflation, the correct scalar amplitude, while also reheating the universe within 2-3 e -folds after the end of inflation. In the left column of Fig. 5.1, we have plotted the fractional contributions (with respect to the total energy density) of the energy densities of the tachyon and

Potential	Γ	ρ_γ^i	$\bar{\mathcal{A}}$	$\bar{\mathcal{B}}$	$\bar{\mathcal{C}}$	$\bar{\mathcal{D}}$
$V_1(T)$	Γ_1	10^{-40}	5λ	–	–	–
	Γ_2	10^{-40}	5λ	10^{-2}	$2T_0$	T_0
$V_2(T)$	Γ_1	10^{-40}	$1.43 \times 10^{-2}\lambda$	–	–	–
	Γ_2	10^{-40}	$10^{-2}\lambda$	10^{-2}	$2T_0$	T_0

Table 5.2: Achieving inflation *and* reheating: The values of the initial energy density of radiation ρ_γ^i and the parameters describing the decay rates that we work with when the interaction of the tachyon with radiation is taken into account. For the tachyon, we use the same values listed in the previous table. These parameters and initial conditions lead to about 60 e -folds of slow roll inflation, the required amplitude for the perturbations, and also reheat the universe within a couple of e -folds after inflation.

radiation, i.e. $\Omega_T = (\rho_T/\rho)$ and $\Omega_\gamma = (\rho_\gamma/\rho)$, as a function of the number of e -folds N for the potential $V_1(T)$. It is evident from the figure that the two choices for the decay rate Γ ensure the completion of reheating (i.e. $\Omega_\gamma \simeq 1$) within a couple of e -folds after the end of inflation. In the right column of the figure, we have plotted the corresponding effective equation of state parameter, viz. $w = (p/\rho)$, and also the first HSR parameter, viz. $\epsilon_H = -(\dot{H}/H^2)$, of the entire system, for the same tachyon potential. These plots, while confirming that inflation has indeed ended and reheating has been realized, also indicate the nature of the composite matter during the transition. We should add that a very similar behavior occurs for the potential $V_2(T)$.

5.3 Equations of motion governing the scalar perturbations for the system

In this section, using the first order Einstein equations and the equations describing the conservation of the perturbed energy density of the tachyon and the perfect fluid, we shall arrive at the coupled, second order (in time) differential equations governing the scalar perturbations for the system consisting of the tachyon and the fluid. For convenience, we shall work in the Uniform Curvature Gauge (UCG), a gauge that is also referred to, often, as the spatially flat gauge.

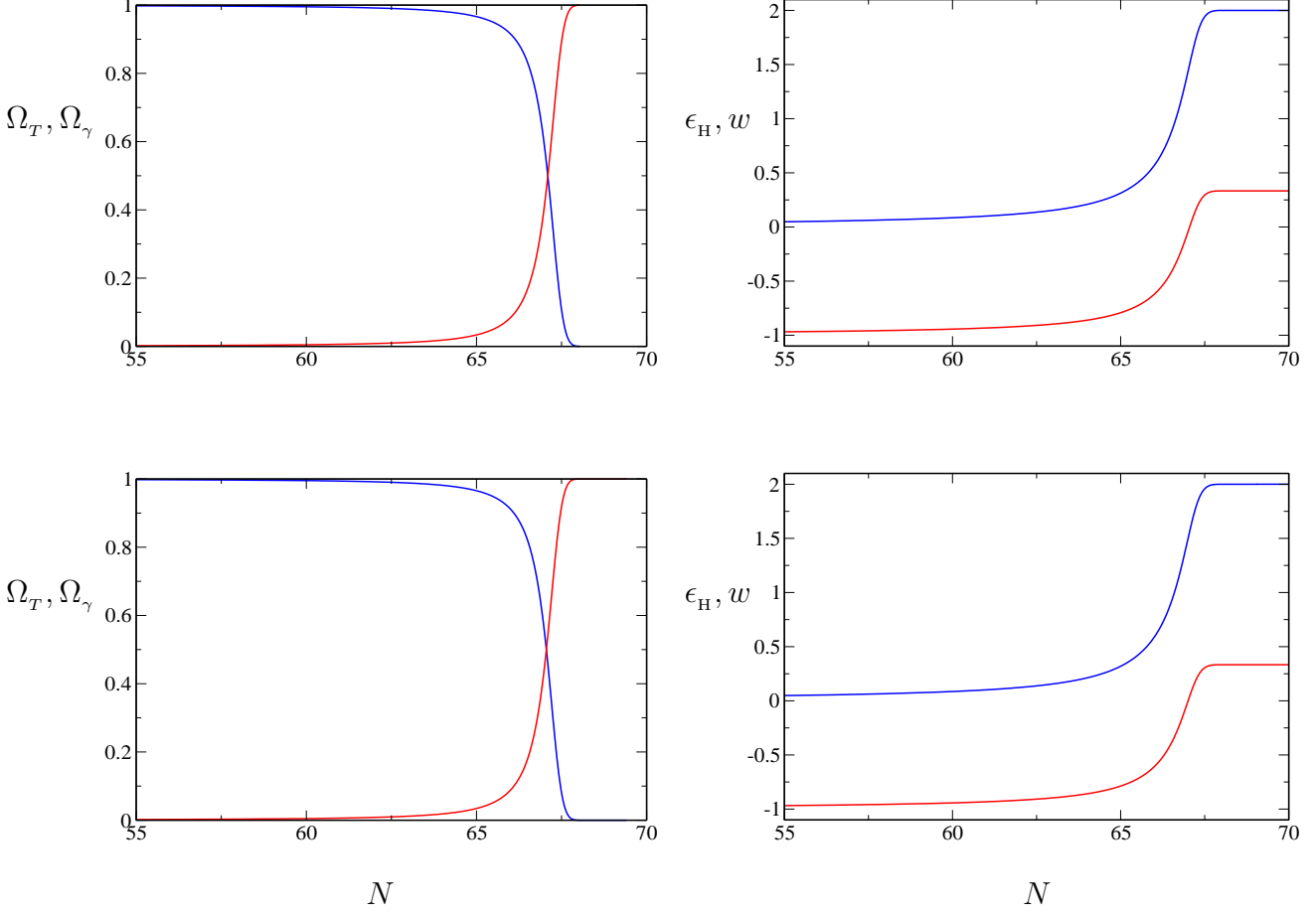


Figure 5.1: In the left column, the evolution of the quantities Ω_T (in blue) and Ω_γ (in red) has been plotted as a function of the number of e -folds N for the tachyon potential $V_1(T)$ and the two cases of Γ , viz. $\Gamma_1 = \text{constant}$ (on top) and $\Gamma_2 = \Gamma(T)$ (at the bottom), with $\Gamma(T)$ given by Eq. (5.12). Similarly, in the right column, the evolution of the first HSR parameter ϵ_H (in blue) and the equation of state parameter of the entire system w (in red) has been plotted as a function of the number of e -folds for the same potential and the different cases of Γ , as indicated above. All these plots correspond to the values for the various parameters and the initial conditions that we have listed in Tabs. 5.1 and 5.2. The figures clearly illustrate the transfer of energy from the inflaton to radiation. (Note that $\epsilon_H = 2$ during the radiation dominated epoch.) We have chosen the various parameters in such a fashion that there is a sufficiently rapid transition from inflation to radiation domination without any intermediate regime, as suggested by the evolution of ϵ_H and w . We find that a very similar behavior occurs for the potential $V_2(T)$.

5.3.1 First order Einstein equations

If we take into account the scalar perturbations to the spatially flat background metric (2.1), then, in the UCG, the Friedmann line-element is given by [1, 3, 5, 6, 94, 95, 96, 97, 98]

$$ds^2 = (1 + 2A) dt^2 - 2a(\partial_i B) dx_i dt - a^2(t) dx^2, \quad (5.13)$$

where A and B are functions that describe the two degrees of freedom associated with the perturbations. Being a scalar field, the tachyon, evidently, does not possess any anisotropic stress at the linear order in the perturbations. We shall assume that the perfect fluid does not contain any anisotropic stress either. In such a case, at the first order in the perturbations, the Einstein equations in the UCG can be written as [1, 3, 5, 6, 94, 95, 96, 97, 98]

$$-(3H^2)A - \left(\frac{H}{a}\right) \nabla^2 B = (4\pi G) \delta\rho, \quad (5.14a)$$

$$H(\partial_i A) = (4\pi G)(\partial_i \delta q), \quad (5.14b)$$

$$H\dot{A} + (2\dot{H} + 3H^2)A = (4\pi G)\delta p, \quad (5.14c)$$

where the quantities $\delta\rho$, $(\partial_i \delta q)$, and δp denote the perturbations in the total energy density, the total momentum flux, and the total pressure of the complete system, respectively. The absence of the anisotropic stress leads to the following additional relation between the two functions A and B describing the scalar perturbations:

$$A + a(\dot{B} + 2HB) = 0. \quad (5.15)$$

For the system of our interest, viz. that of the tachyon and a perfect fluid described by a constant equation of state parameter w_F , the quantities $\delta\rho$, δq and δp are given by [cf. Eqs. (2.66)]

$$\delta\rho = (\delta\rho_T + \delta\rho_F) = \left(\frac{V_T \delta T}{\sqrt{1 - \dot{T}^2}}\right) + \left(\frac{V\dot{T}}{(1 - \dot{T}^2)^{3/2}}\right) (\delta\dot{T} - A\dot{T}) + \delta\rho_F, \quad (5.16a)$$

$$\delta q = (\delta q_T + \delta q_F) = \left(\frac{V\dot{T} \delta T}{\sqrt{1 - \dot{T}^2}}\right) - \psi_F, \quad (5.16b)$$

$$\delta p = (\delta p_T + \delta p_F) = -\left(V_T \delta T \sqrt{1 - \dot{T}^2}\right) + \left(\frac{V\dot{T}}{\sqrt{1 - \dot{T}^2}}\right) (\delta\dot{T} - A\dot{T}) + w_F \delta\rho_F, \quad (5.16c)$$

where δT denotes the perturbation in the tachyon and ψ_F is proportional to the potential that determines the three (i.e. the spatial) velocity of the perfect fluid¹.

5.3.2 Equations of motion describing the perturbed matter components

In the UCG, at the first order in the perturbations, the equation describing the conservation of the energy density of the component α is given by [94, 95, 96, 97, 98, 229, 230, 231]

$$\dot{\delta\rho}_\alpha + 3H(\delta\rho_\alpha + \delta p_\alpha) - \left(\frac{1}{a^2}\right) \nabla^2 [\delta q_\alpha + (\rho_\alpha + p_\alpha) a B] - Q_\alpha A - \delta Q_\alpha = 0, \quad (5.17)$$

where the quantities $\delta\rho_\alpha$, δq_α and δp_α denote the perturbations at the linear order in the energy density, the momentum flux, and the pressure of the particular component α , while Q_α and δQ_α indicate the rate at which the energy is transferred to the component α and the perturbation in the rate, respectively. The equation of motion that governs the perturbation δT in the tachyon can now be obtained upon using the expressions (5.16) for $\delta\rho_T$, δq_T and δp_T in above equation for the conservation of the perturbed energy density. We find that the equation of motion describing the perturbation δT is given by

$$\begin{aligned} \left(\frac{\ddot{\delta T}}{1 - \dot{T}^2}\right) &+ \left[(3H + \Gamma) (1 - 3\dot{T}^2) - 2\dot{T} \left(\frac{V_T}{V}\right) \right] \left(\frac{\dot{\delta T}}{1 - \dot{T}^2}\right) \\ &+ \left[\left(\frac{d^2 \ln V}{dT^2}\right) - \left(\frac{1}{a^2}\right) \nabla^2 \right] \delta T - \left(\frac{\dot{T} \dot{A}}{1 - \dot{T}^2}\right) \\ &+ \left[6H\dot{T}^3 + 2\left(\frac{V_T}{V}\right) + \Gamma\dot{T}(1 + \dot{T}^2) \right] \left(\frac{A}{1 - \dot{T}^2}\right) \\ &- \left(\frac{\dot{T}}{a}\right) \nabla^2 B + \dot{T} \delta\Gamma = 0, \end{aligned} \quad (5.18)$$

where $\delta\Gamma$ denotes the first order perturbation in the decay rate. Upon using Eq. (5.17), we find that the equation describing the conservation of the perturbed energy density of the

¹Usually, for a perfect fluid, the quantity δq_F is written as $[(\rho_F + p_F) \chi_F]$, where χ_F is the potential whose spatial gradient describes the three velocity of the fluid (see, for instance, Refs. [1, 3, 5, 6, 94, 95, 96, 97, 98]). For convenience, we have instead defined the entire quantity $[(\rho_F + p_F) \chi_F]$ as $-\psi_F$ [65]. As we shall point out later, we have ensured that suitable sub-Hubble initial conditions are imposed on ψ_F .

fluid $\delta\rho_F$ can be written as

$$\begin{aligned} \delta\dot{\rho}_F + 3H(1+w_F)\delta\rho_F + \left(\frac{1}{a^2}\right)\nabla^2\psi_F - \left(\frac{\Gamma V \dot{T}(2-\dot{T}^2)}{(1-\dot{T}^2)^{3/2}}\right)\delta\dot{T} - \left(\frac{\Gamma V_T \dot{T}^2}{\sqrt{1-\dot{T}^2}}\right)\delta T \\ + \left(\frac{\Gamma V \dot{T}^2}{(1-\dot{T}^2)^{3/2}}\right)A - \left(\frac{(1+w_F)\rho_F}{a}\right)\nabla^2 B - \left(\frac{V \dot{T}^2}{\sqrt{1-\dot{T}^2}}\right)\delta\Gamma = 0. \end{aligned} \quad (5.19)$$

Also, upon using the Einstein equations (5.14b) and (5.14c), we obtain the following first order (in time) differential equation for the quantity ψ_F that describes the spatial velocity of the fluid:

$$\dot{\psi}_F + 3H\psi_F + w_F\delta\rho_F + (1+w_F)\rho_F A + \left(\frac{\Gamma V \dot{T}}{\sqrt{1-\dot{T}^2}}\right)\delta T = 0. \quad (5.20)$$

We should emphasize here that the above equations take into account both the possibilities of the decay rate Γ (i.e. it can either be a constant, or depend on the tachyon) that we had discussed earlier.

5.3.3 The coupled perturbation variables and the initial conditions

The variables describing the perturbations in the tachyon and the fluid that we shall eventually evolve numerically are [65, 94, 95, 96, 97, 98]

$$\mathcal{Q}_T = \delta T \quad \text{and} \quad \mathcal{Q}_F = \left(\frac{\psi_F}{\sqrt{(1+w_F)\rho_F}}\right). \quad (5.21)$$

We have already obtained a second order differential equation (in time) describing the evolution of \mathcal{Q}_T [viz. Eq. (5.18)]. A similar equation for \mathcal{Q}_F can be obtained by differentiating Eq. (5.20) with respect to time, and upon using Eq. (5.19) that describes the conservation of the perturbed energy density of the fluid. Then, on utilizing the first order Einstein equations (5.14a), (5.14b) and (5.15) to eliminate the scalar metric perturbations A and B , we can arrive at a set of coupled, second order (in time, again!) differential equations for the quantities \mathcal{Q}_T and \mathcal{Q}_F .

For simplicity, let us first discuss the case wherein the decay rate Γ is a constant. We shall later indicate as to how certain coefficients in the differential equations change when Γ is assumed to be dependent on the tachyon. Upon suitably using the background equations (2.2),

(5.6) and (5.9), we find that the differential equations satisfied by the perturbation variables \mathcal{Q}_T and \mathcal{Q}_F can be written as

$$\ddot{\mathcal{Q}}_\alpha + \sum_\beta \left(\mathcal{F}_{\alpha\beta} \dot{\mathcal{Q}}_\beta + \mathcal{G}_{\alpha\beta} \mathcal{Q}_\beta \right) = 0, \quad (5.22)$$

where, as before, $(\alpha, \beta) = (T, F)$. The coefficients $\mathcal{F}_{\alpha\beta}$ and $\mathcal{G}_{\alpha\beta}$ appearing in the above equations are given by

$$\mathcal{F}_{TT} = (3H + \Gamma) (1 - 3\dot{T}^2) - 2\dot{T} \left(\frac{V_T}{V} \right), \quad (5.23a)$$

$$\mathcal{F}_{TF} = \left(\frac{4\pi G}{H} \right) \left[1 - \left(\frac{1 - \dot{T}^2}{w_F} \right) \right] \dot{T} \sqrt{(1 + w_F) \rho_F}, \quad (5.23b)$$

$$\begin{aligned} \mathcal{F}_{FT} = \left(\frac{V \dot{T}}{\sqrt{1 - \dot{T}^2}} \right) \left\{ \left(\frac{4\pi G}{H} \right) \left[1 - \left(\frac{w_F}{1 - \dot{T}^2} \right) \right] \sqrt{(1 + w_F) \rho_F} \right. \\ \left. + \left[1 + w_F \left(\frac{2 - \dot{T}^2}{1 - \dot{T}^2} \right) \right] \left(\frac{\Gamma}{\sqrt{(1 + w_F) \rho_F}} \right) \right\}, \end{aligned} \quad (5.23c)$$

$$\mathcal{F}_{FF} = 3H + \left(\frac{\Gamma V \dot{T}^2}{\sqrt{1 - \dot{T}^2}} \right) \left(\frac{1}{\rho_F} \right), \quad (5.23d)$$

$$\begin{aligned} \mathcal{G}_{TT} = (1 - \dot{T}^2) \left[\left(\frac{d^2 \ln V}{dT^2} \right) - \left(\frac{1}{a^2} \right) \nabla^2 \right] \\ + \left(\frac{4\pi G}{H} \right) \left(\frac{V \dot{T}}{\sqrt{1 - \dot{T}^2}} \right) \left[(2 - \dot{T}^2) \left(\frac{2V_T}{V} \right) + (2 + \dot{T}^2) (3H + \Gamma) \dot{T} \right. \\ \left. - \left(\frac{\Gamma \dot{T}}{w_F} \right) (1 - \dot{T}^2) \right] \\ - \left(\frac{4\pi G}{H} \right)^2 \left\{ \left(\frac{2V^2 \dot{T}^4}{1 - \dot{T}^2} \right) - \left(\frac{V \dot{T}^2}{\sqrt{1 - \dot{T}^2}} \right) \left[1 + \left(\frac{1 - \dot{T}^2}{w_F} \right) \right] (1 + w_F) \rho_F \right\}, \end{aligned} \quad (5.23e)$$

$$\begin{aligned}
 \mathcal{G}_{TF} = & \left(\frac{4\pi G}{H} \right) \left\{ - \left(\frac{3H\dot{T}}{2} \right) \left[1 + \left(\frac{1-\dot{T}^2}{w_F} \right) \right] (1+w_F) \right. \\
 & + \left(\frac{1}{2\rho_F} \right) \left[1 - \left(\frac{1-\dot{T}^2}{w_F} \right) \right] \left(\frac{\Gamma V \dot{T}^3}{\sqrt{1-\dot{T}^2}} \right) \\
 & \left. - \left(6H\dot{T}^3 + 2 \left(\frac{V_T}{V} \right) + (\Gamma\dot{T}) (1+\dot{T}^2) \right) \right\} \sqrt{(1+w_F)\rho_F} \quad (5.23f)
 \end{aligned}$$

$$\begin{aligned}
 & + \left(\frac{4\pi G}{H} \right)^2 \left\{ \left(\frac{2V\dot{T}^3}{\sqrt{1-\dot{T}^2}} \right) + \left[1 + \left(\frac{1-\dot{T}^2}{w_F} \right) \right] \dot{T} [(1+w_F)\rho_F] \right\} \sqrt{(1+w_F)\rho_F}, \\
 \mathcal{G}_{FT} = & - \left(\frac{4\pi G}{H} \right) \left\{ \left[1 + \left(\frac{w_F}{1-\dot{T}^2} \right) \right] [(1+w_F)\rho_F] V_T \sqrt{1-\dot{T}^2} \right. \\
 & + \left(\frac{3HV\dot{T}}{\sqrt{1-\dot{T}^2}} \right) (1+w_F)^2 \rho_F - \left(\frac{\Gamma V^2 \dot{T}^3}{1-\dot{T}^2} \right) \left[1 - \left(\frac{w_F \dot{T}^2}{1-\dot{T}^2} \right) \right] \left\{ \left(\frac{1}{\sqrt{(1+w_F)\rho_F}} \right) \right. \\
 & - \left(\frac{4\pi G}{H} \right)^2 \left\{ \left(\frac{V^2 \dot{T}^3}{1-\dot{T}^2} \right) \left[1 + \left(\frac{w_F}{1-\dot{T}^2} \right) \right] [(1+w_F)\rho_F] \right. \\
 & \left. - \left(\frac{2V\dot{T}}{\sqrt{1-\dot{T}^2}} \right) [(1+w_F)\rho_F]^2 \right\} \left(\frac{1}{\sqrt{(1+w_F)\rho_F}} \right) \\
 & \left. + \left(\frac{\Gamma V}{\sqrt{1-\dot{T}^2}} \right) \left[\left(\frac{V_T}{V} \right) (1-\dot{T}^2) - \left(\frac{V_T}{V} \right) w_F \dot{T}^2 + \Gamma\dot{T} - 3Hw_F\dot{T} \right] \right. \\
 & \left. \times \left(\frac{1}{\sqrt{(1+w_F)\rho_F}} \right) \right\}, \quad (5.23g)
 \end{aligned}$$

$$\begin{aligned}
 \mathcal{G}_{FF} = & - \left(\frac{w_F}{a^2} \right) \nabla^2 + \left(\frac{9H^2}{4} \right) (1-w_F^2) \\
 & + \left(\frac{4\pi G}{H} \right) \left\{ \left(\frac{3H}{2} \right) (1+w_F) (1+3w_F) \rho_F + \left(\frac{3H}{2} \right) \left(\frac{V\dot{T}^2}{\sqrt{1-\dot{T}^2}} \right) (w_F-1) \right. \\
 & \left. - \left(\frac{\Gamma V \dot{T}^2}{\sqrt{1-\dot{T}^2}} \right) \left[1 - \left(\frac{w_F \dot{T}^2}{1-\dot{T}^2} \right) \right] \right\} \\
 & - \left(\frac{4\pi G}{H} \right)^2 \left\{ \left(\frac{V\dot{T}^2}{\sqrt{1-\dot{T}^2}} \right) \left[1 + \left(\frac{w_F}{1-\dot{T}^2} \right) \right] [(1+w_F)\rho_F] + 2 [(1+w_F)\rho_F]^2 \right\} \\
 & - \left(\frac{\Gamma V \dot{T}}{\sqrt{1-\dot{T}^2}} \right) \left\{ \left(\frac{\Gamma\dot{T}}{2\rho_F} \right) (2-\dot{T}^2) + \left(\frac{V_T}{V} \right) (1-\dot{T}^2) \left(\frac{1}{\rho_F} \right) \right. \\
 & \left. - \left(\frac{3H\dot{T}}{2\rho_F} \right) (w_F + \dot{T}^2) + \left(\frac{\Gamma V \dot{T}^3}{4\rho_F^2 \sqrt{1-\dot{T}^2}} \right) \right\}. \quad (5.23h)
 \end{aligned}$$

As we had pointed out, the coefficients $\mathcal{F}_{\alpha\beta}$ and $\mathcal{G}_{\alpha\beta}$ above have been derived assuming that the decay rate Γ is a constant. For the case wherein the decay rate is a function of the tachyon, the coefficients \mathcal{G}_{TT} and \mathcal{G}_{FT} are modified to

$$\mathcal{G}_{TT} \rightarrow \mathcal{G}_{TT} + (1 - \dot{T}^2) \dot{T} \Gamma_T, \quad (5.24a)$$

$$\mathcal{G}_{FT} \rightarrow \mathcal{G}_{FT} + \left(\frac{V \dot{T}^2}{\sqrt{1 - \dot{T}^2}} \right) \left(\frac{w_F}{\sqrt{(1 + w_F) \rho_F}} \right) \Gamma_T, \quad (5.24b)$$

where $\Gamma_T \equiv (d\Gamma/dT)$. The other coefficients remain unaffected in this case.

We should mention here that we have checked that we indeed recover the standard equations in the different limiting cases from the coupled equations (5.22) for \mathcal{Q}_T and \mathcal{Q}_F . For instance, when the fluid is ignored and the decay rate is assumed to vanish, the equation for the variable \mathcal{Q}_T reduces to the equation that has been derived earlier in the literature for describing the perturbation in the tachyon (see, for instance, Refs. [92, 123, 226, 227]). Moreover, when the tachyon is assumed to vanish and its coupling to the fluid is also ignored, we find that we arrive at the well known equation governing the fluid perturbation, as required [1, 3, 5, 6, 94, 95, 96, 97, 98].

5.4 Effects of reheating on the scalar power spectrum

In this section, we shall discuss the effects of reheating on the large scale curvature perturbations and the scalar power spectrum. We shall also investigate the behavior of the non-adiabatic pressure perturbations at large scales, when reheating is achieved through the two different choices for the decay rate.

5.4.1 Evolution of the curvature perturbations and the scalar power spectrum

We shall solve the coupled equations (5.22) for the two variables \mathcal{Q}_T and \mathcal{Q}_F numerically. Imposing the standard Bunch-Davies initial conditions [cf. Eq. (2.48)], we shall evolve the perturbations from the sub-Hubble to the super-Hubble scales, and analyze the effects of the transition from inflation to the radiation dominated epoch on the evolution of the large scale perturbations. We shall compute the scalar power spectrum at the end of inflation

and soon after reheating is complete. Let us begin by quickly summarizing the essential quantities of interest and the initial conditions that we shall be imposing.

Let \mathcal{R}_T and \mathcal{R}_F denote the curvature perturbations associated with the tachyon and the fluid, respectively. We find that these curvature perturbations are related to the variables \mathcal{Q}_T and \mathcal{Q}_F as follows [92, 94, 95, 96, 97, 98, 123, 226, 227]:

$$\mathcal{R}_T = \left(\frac{H}{\dot{T}} \right) \delta T = \left(\frac{H}{\dot{T}} \right) \mathcal{Q}_T, \quad (5.25a)$$

$$\mathcal{R}_F = - \left(\frac{H}{\rho_F + p_F} \right) \psi_F = - \left(\frac{H}{\sqrt{(1 + w_F) \rho_F}} \right) \mathcal{Q}_F. \quad (5.25b)$$

The total curvature perturbation of the system, say, \mathcal{R} , can then be expressed as a weighted sum of the individual curvature perturbations in the following fashion (see, for instance, Refs. [230, 231]):

$$\mathcal{R} = \sum_{\alpha} \left(\frac{\rho_{\alpha} + p_{\alpha}}{\rho + p} \right) \mathcal{R}_{\alpha}. \quad (5.26)$$

Therefore, for our system of interest, the total curvature perturbation is given by

$$\mathcal{R} = H \left[\left(\frac{V \dot{T}^2}{\sqrt{1 - \dot{T}^2}} \right) + [(1 + w_F) \rho_F] \right]^{-1} \left[\left(\frac{V \dot{T}}{\sqrt{1 - \dot{T}^2}} \right) \mathcal{Q}_T - \sqrt{[(1 + w_F) \rho_F]} \mathcal{Q}_F \right]. \quad (5.27)$$

The scalar power spectrum is then defined in terms of the Fourier mode \mathcal{R}_k of the total curvature perturbation in the standard fashion [cf. Eq. (2.39)]. The Mukhanov-Sasaki variable, say, v_T , associated with the tachyon is given by Eq. (2.35) with z_T as defined in Eq. (2.73). The corresponding variable, say, v_F , associated with the fluid is related to the curvature perturbation \mathcal{R}_F in a similar way and can be expressed as

$$v_F = (\mathcal{R}_F z_F). \quad (5.28)$$

The quantity z_F for the fluid can be written in terms of the background quantities as in the case of the tachyon [cf. Eq. (2.73)], and is given by [1, 3, 5, 6, 92, 94, 95, 96, 97, 98, 123]

$$z_F = \left(\frac{a}{H} \right) \left[\frac{(1 + w_F) \rho_F}{w_F} \right]^{1/2}. \quad (5.29)$$

As we had discussed in the earlier chapters, we shall impose the following initial conditions on the Fourier modes of the perturbation variables v_T and v_F [cf. Eq. (2.48)]:

$$v_k = \left(\frac{1}{2 \omega_k} \right)^{1/2} \quad \text{and} \quad \dot{v}_k = - \left(\frac{i}{a} \right) \left(\frac{\omega_k}{2} \right)^{1/2}, \quad (5.30)$$

where

$$\omega_k^2 = \left((k c_s)^2 - a^2 [(\ddot{z}/z) + (H \dot{z}/z)] \right), \quad (5.31)$$

with $c_s^2 = (1 - \dot{T}^2)$ in the case of the tachyon and $c_s^2 = w_F$ in the case of the fluid. Also, we shall impose these conditions when the modes are well inside the Hubble radius during the inflationary epoch. We shall transform these initial conditions to the corresponding conditions on the variables \mathcal{Q}_T and \mathcal{Q}_F when numerically integrating the coupled equations (5.22).

We shall focus on modes that correspond to the cosmological scales today. We shall choose our parameters in such a fashion that modes spread over four orders of magnitude (say, $10^{-4} \lesssim k \lesssim 1 \text{ Mpc}^{-1}$) leave the Hubble radius during the early stages of inflation (they actually leave during $5 \lesssim N \lesssim 15$). As we have discussed earlier, for our choice of the parameters and initial conditions on the background variables, reheating is achieved after about 65 odd e -folds (also see Fig. 5.1). Moreover, the transition from inflation to radiation domination occurs within about 2-3 e -folds after inflation has terminated. We evaluate the scalar power spectrum towards the end of inflation as well as soon after the transition to the radiation dominated epoch is complete. In the left column of Fig. 5.2, we have plotted the evolution of the amplitudes of the individual (viz. $|\mathcal{R}_T|$ and $|\mathcal{R}_\gamma|$ corresponding to the tachyon and radiation, respectively) as well as the total curvature perturbation (i.e. $|\mathcal{R}|$) for a typical cosmological scale (we have chosen $k = 0.1 \text{ Mpc}^{-1}$) across the transition from inflation to radiation domination. And, in the right column of the figure, we have plotted the scalar power spectrum (constructed out of the total curvature perturbation) evaluated before and after the transition. It is evident from the plots that the amplitude of the total curvature perturbation remains unaffected during reheating when the decay rate Γ is either a constant, or is a function of the tachyon [232]. These results confirm similar conclusions that have been arrived at earlier based on the first order (in time) super-Hubble equations [87].

5.4.2 Evolution of the entropy perturbations

In this section, we shall discuss the evolution of the entropic (i.e. the non-adiabatic pressure) perturbations across the transition from inflation to the radiation dominated epoch.

Let us recall the key quantities and equations. In the UCG, the gauge invariant Bardeen potential Φ is given by

$$\Phi = A + a \left(\dot{B} + H B \right). \quad (5.32)$$

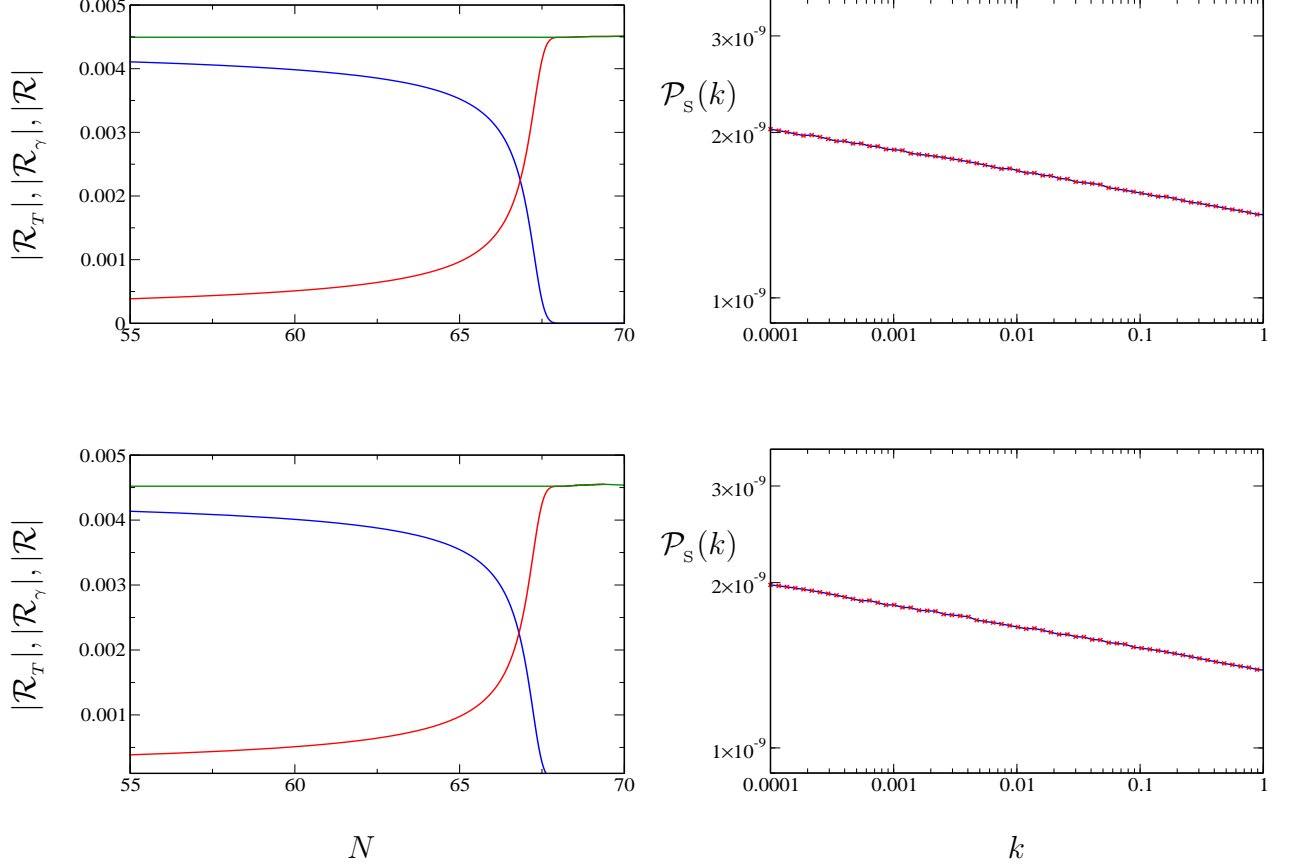


Figure 5.2: In the left column, the evolution of the amplitudes of the curvature perturbations associated with the tachyon ($|\mathcal{R}_T|$, in blue) and radiation ($|\mathcal{R}_\gamma|$, in red) as well as the weighted sum of the two ($|\mathcal{R}|$, in green) has been plotted as a function of the number of e -folds N for the two possible cases of Γ , viz. $\Gamma_1 = \text{constant}$ (on top), $\Gamma_2 = \Gamma(T)$ (at the bottom). In these plots, we have chosen a typical cosmological scale with the wavenumber $k = 0.1 \text{ Mpc}^{-1}$. Clearly, the amplitude of the total curvature perturbation remains constant across the transition in both the cases. In the right column, the scalar power spectrum has been plotted towards the end of inflation (in blue) and soon after complete reheating has been achieved (in red) for the two cases of Γ , as mentioned above. These plots unambiguously illustrate that the amplitude of the nearly scale invariant power spectrum is unaffected in both the cases (In these plots, the blue line lies right beneath the red one.) Note that all these plots correspond to the potential $V_1(T)$ with values for the various parameters and the initial conditions that are listed in Tabs. 5.1 and 5.2. We find that a very similar behavior occurs for the potential $V_2(T)$.

Upon using the first order Einstein equations (5.14a), (5.14c) and (5.15), it can be shown that the Bardeen potential Φ satisfies a second order differential equation (in time), viz. Eq. (2.22). Now, using the Einstein equations (5.14b) and (5.15), the definition of the curvature perturbation \mathcal{R} [cf. Eq. (2.24)] and the second order differential equation for the Bardeen potential Φ [cf. Eq. (2.22)], it can be demonstrated that, at super-Hubble scales, any change in the amplitude of the curvature perturbations has to be due to the non-trivial evolution of the non-adiabatic pressure perturbation of the system.

The perfect fluid, by definition, does not possess any intrinsic entropy perturbation. Therefore, the non-adiabatic pressure perturbation, say, δp^{NA} of our composite system depends on the intrinsic non-adiabatic pressure perturbation of the tachyon, say, δp_T^{NA} , and the relative non-adiabatic pressure perturbation between the tachyon and the perfect fluid (i.e. the isocurvature perturbation), which we shall denote as $\delta p_{TF}^{\text{NA}}$. Hence, we can write

$$\delta p^{\text{NA}} = (\delta p_T^{\text{NA}} + \delta p_{TF}^{\text{NA}}). \quad (5.33)$$

While the quantity δp_T^{NA} is defined by the standard relation [cf. Eq. (2.23)], the relative non-adiabatic pressure perturbation $\delta p_{TF}^{\text{NA}}$ is given by (see, for instance, Refs. [87, 118, 233])

$$\begin{aligned} \delta p_{TF}^{\text{NA}} = (3H + \Gamma) \left(\frac{\rho_T + p_T}{\rho + p} \right) & \left[(\rho_F + p_F) - (\Gamma/3H) (\rho_T + p_T) \right] \\ & \times (w_F - c_T^2) \left[\left(\frac{\delta \rho_T}{\dot{\rho}_T} \right) - \left(\frac{\delta \rho_F}{\dot{\rho}_F} \right) \right], \end{aligned} \quad (5.34)$$

where $c_T^2 = (\dot{p}_T/\dot{\rho}_T)$. Upon using the expressions (5.16a) and (5.16c), and the Einstein equations (5.14a), (5.14c) and (5.15), we find that we can write the quantities $\delta \rho_T$, δp_T and $\delta \rho_F$ in terms of the variables \mathcal{Q}_T and \mathcal{Q}_F as follows:

$$\begin{aligned} \delta \rho_T = & \left[\left(\frac{V_T}{\sqrt{1 - \dot{T}^2}} \right) - \left(\frac{4\pi G}{H} \right) \left(\frac{V^2 \dot{T}^3}{(1 - \dot{T}^2)^2} \right) \right] \mathcal{Q}_T + \left(\frac{V \dot{T}}{(1 - \dot{T}^2)^{3/2}} \right) \dot{\mathcal{Q}}_T \\ & + \left(\frac{4\pi G}{H} \right) \left(\frac{V \dot{T}^2}{(1 - \dot{T}^2)^{3/2}} \right) \sqrt{(1 + w_F) \rho_F} \mathcal{Q}_F, \end{aligned} \quad (5.35a)$$

$$\begin{aligned} \delta p_T = & - \left[V_T \sqrt{1 - \dot{T}^2} + \left(\frac{4\pi G}{H} \right) \left(\frac{V^2 \dot{T}^3}{1 - \dot{T}^2} \right) \right] \mathcal{Q}_T + \left(\frac{V \dot{T}}{\sqrt{1 - \dot{T}^2}} \right) \dot{\mathcal{Q}}_T \\ & + \left(\frac{4\pi G}{H} \right) \left(\frac{V \dot{T}^2}{\sqrt{1 - \dot{T}^2}} \right) \sqrt{(1 + w_F) \rho_F} \mathcal{Q}_F, \end{aligned} \quad (5.35b)$$

$$\begin{aligned}
 \delta\rho_F = & - \left[\left(\frac{4\pi G}{H} \right) \left(\frac{V\dot{T}}{\sqrt{1-\dot{T}^2}} \right) (1+w_F) \left(\frac{\rho_F}{w_F} \right) + \left(\frac{\Gamma V\dot{T}}{w_F\sqrt{1-\dot{T}^2}} \right) \right] \mathcal{Q}_T \\
 & - \left[\left(\frac{3H}{2w_F} \right) (1-w_F) \sqrt{(1+w_F)\rho_F} + \left(\frac{\Gamma V\dot{T}^2}{\sqrt{1-\dot{T}^2}} \right) \left(\frac{1+w_F}{4w_F^2\rho_F} \right)^{1/2} \right. \\
 & \left. - \left(\frac{4\pi G}{H} \right) \left(\frac{1}{w_F} \right) [(1+w_F)\rho_F]^{3/2} \right] \mathcal{Q}_F - \left(\frac{1}{w_F} \right) \sqrt{(1+w_F)\rho_F} \dot{\mathcal{Q}}_F. \quad (5.35c)
 \end{aligned}$$

These three relations allow us to express the non-adiabatic pressure perturbations δp_T^{NA} and $\delta p_{TF}^{\text{NA}}$ in terms of \mathcal{Q}_T , \mathcal{Q}_F , and their time derivatives.

In Fig. 5.3, we have plotted the amplitudes of the Bardeen potential (i.e. $|\Phi|$) and the non-adiabatic pressure perturbations (viz. $|\delta p_T^{\text{NA}}|$ and $|\delta p_{T\gamma}^{\text{NA}}|$) as a function of the number of e -folds. For convenience in numerical computation, we have chosen a very small scale mode (corresponding to $k = 10^{16} \text{ Mpc}^{-1}$) that leaves the Hubble radius around 58 e -folds or so during inflation². The following points are evident from these two plots. To begin with, barring a very small change in its amplitude—which is expected during the transition from inflation to the radiation dominated epoch—the Bardeen potential Φ remains a constant at super-Hubble scales. Secondly, it is clear from the plots that the intrinsic entropy perturbation associated with the tachyon $|\delta p_T^{\text{NA}}|$ decays as $e^{-(2N)}$ at super-Hubble scales during inflation, a result that is well known in the literature (see, for instance, Refs. [99, 100, 123]). Lastly, and interestingly, we find that the isocurvature perturbation $|\delta p_{T\gamma}^{\text{NA}}|$ behaves in almost the same fashion as the intrinsic entropy perturbation both before and after the transition, a feature that has been noticed earlier [233]. While they both behave as $e^{-(2N)}$ at super-Hubble scales before the transition, they die down *extremely* rapidly (roughly as $e^{-(80N)}$!) during the radiation dominated epoch. It is these behavior which ensure that the amplitude of the total curvature perturbation remains unaffected [232].

²The amplitude of the non-adiabatic pressure perturbations corresponding to the cosmological scales (i.e. $10^{-4} \lesssim k \lesssim 1 \text{ Mpc}^{-1}$) prove to be very small when they are well outside the Hubble radius. As a result, evolving these scales reliably until the transition to the radiation dominated epoch requires considerable numerical accuracy, which is difficult to achieve. For this reason, to illustrate the evolution of the non-adiabatic pressure perturbations, we choose to work with a very small scale mode that leaves the Hubble radius close to the end of inflation. Since the inflationary epoch is of the slow roll type for all the e -folds, the non-adiabatic pressure perturbations associated with the cosmological scales can be expected to behave in a fashion similar to that associated with such a small scale mode.

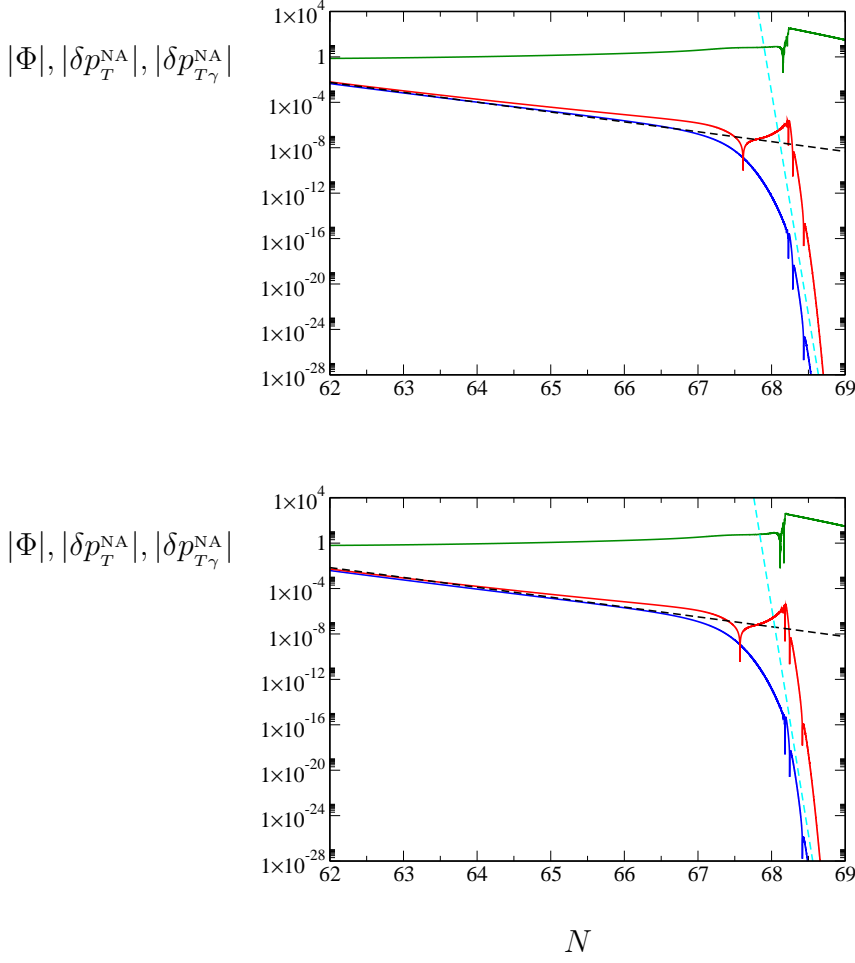


Figure 5.3: The evolution of the amplitudes of the Bardeen potential $|\Phi|$ (in green), the intrinsic entropy perturbation $|\delta p_T^{\text{NA}}|$ (in blue) and the isocurvature perturbation $|\delta p_{T\gamma}^{\text{NA}}|$ (in red) has been plotted as a function of the number of e -folds N for the two cases of Γ , as in the previous two figures. For computational reasons, we have chosen a very small scale mode with wavenumber $k = 10^{16} \text{ Mpc}^{-1}$ that exits the Hubble radius during inflation around 58 e -folds or so. Also, we have normalized the values of all the three quantities to be unity at Hubble exit. Clearly, while the Bardeen potential remains nearly a constant across the transition, both the intrinsic entropy and the isocurvature perturbations decay in almost the same fashion before as well as after the transition. The dashed lines in black and cyan indicate the $e^{-(2N)}$ and $e^{-(80N)}$ behavior, respectively. Interestingly, the non-adiabatic pressure perturbations die down extraordinarily rapidly after reheating is complete. It is these decay which ensure that the amplitude of the total curvature perturbation remains unaffected. Note that these plots correspond to the potential $V_1(T)$ with values for the various parameters and the initial conditions that we have used in the last two figures. As in the earlier figures, we find that a very similar behavior occurs for the potential $V_2(T)$.

5.5 The case of the canonical scalar field and a perfect fluid

In this section, we shall illustrate the corresponding effects for the case of the canonical scalar field that was considered recently in the literature [65]. We shall rapidly summarize the essential equations describing the background evolution and the perturbations, and present the results.

5.5.1 Background equations

In the case of a canonical scalar field, say, ϕ , that is interacting with a perfect fluid, if one assumes that $Q_F = (\Gamma \dot{\phi}^2)$, then the equation (5.3) that describes the conservation of the energy density of the fluid is given by

$$\dot{\rho}_F + 3 H (1 + w_F) \rho_F = \Gamma \dot{\phi}^2. \quad (5.36)$$

Then, Eq. (5.4) implies that $Q_\phi = -Q_F = -(\Gamma \dot{\phi}^2)$ and, hence, the continuity equation governing the energy density ρ_ϕ of the scalar field reduces to

$$\dot{\rho}_\phi + 3 H (\rho_\phi + p_\phi) = -\Gamma \dot{\phi}^2, \quad (5.37)$$

where p_ϕ denotes the pressure of the field [cf. Eqs. (1.21)]. Upon using the expressions for the energy density and the pressure of the field in the continuity equation (5.37), we arrive at the following equation of motion governing the scalar field [62, 63, 64, 65, 66]:

$$\ddot{\phi} + 3 H \dot{\phi} + \Gamma \dot{\phi} + V_\phi = 0. \quad (5.38)$$

In Fig. 5.4, we have illustrated the transition from inflation to the radiation dominated epoch by plotting the dimensionless energy density parameters Ω_ϕ and Ω_γ for the two possible types of decay rate Γ : (i) $\Gamma_1 = \text{constant}$, and (ii) $\Gamma_2 = \Gamma(\phi)$. We have also plotted the evolution of the first HSR parameter ϵ_H and the equation of state parameter w for the entire system. Note that we have considered the quadratic potential $V(\phi) = (m^2 \phi^2/2)$, and have chosen suitable values for the parameters and initial conditions to achieve the desired behavior.

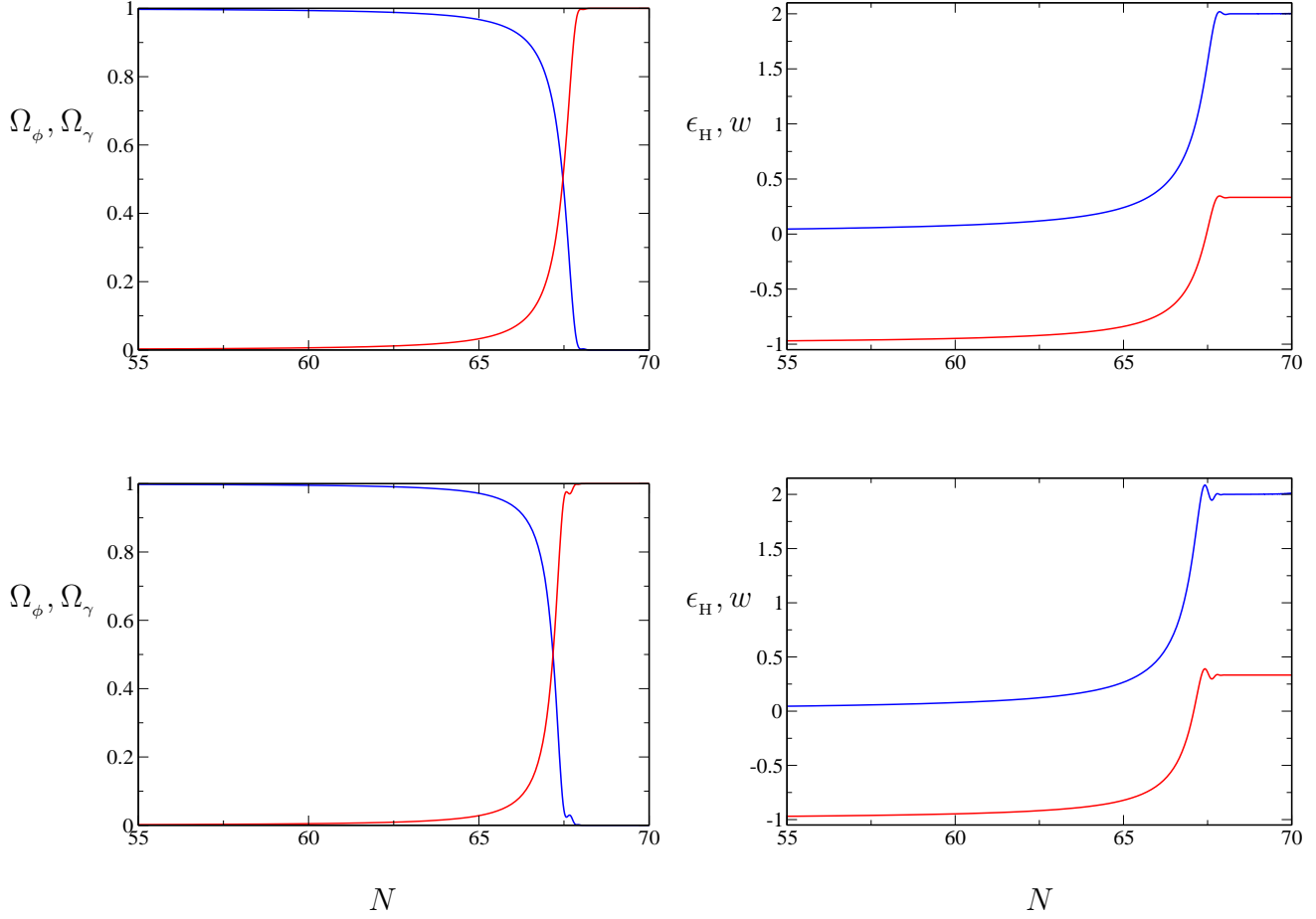


Figure 5.4: In the left column, the evolution of the quantities Ω_ϕ (in blue) and Ω_γ (in red) has been plotted as a function of the number of e -folds N for the two types of Γ , as discussed in the earlier figures. In the right column, we have plotted the evolution of the first slow roll parameter ϵ_H (in blue) and the equation of state of the entire system w (in red). We have considered the popular quadratic potential to describe the scalar field, and we have worked with suitable parameters and initial condition to arrive at the required behavior. These plots clearly illustrate the transfer of energy from the inflaton to radiation.

5.5.2 Equations governing the scalar perturbations

Upon using the expressions for the perturbed energy density, momentum flux and pressure of the scalar field in Eq. (5.17), we can arrive at the equation of motion for the perturbation in the scalar field, say, $\delta\phi$, exactly as we did for the perturbation in the tachyon. In the UCG, we find that $\delta\phi$ satisfies the differential equation

$$\begin{aligned} \ddot{\delta\phi} + (3H + \Gamma) \dot{\delta\phi} + \left[V_{\phi\phi} - \left(\frac{1}{a^2} \right) \nabla^2 \right] \delta\phi \\ - \dot{\phi} \dot{A} + \left(2V_{\phi} + \Gamma \dot{\phi} \right) A - \left(\frac{\dot{\phi}}{a} \right) \nabla^2 B + \dot{\phi} \delta\Gamma = 0, \end{aligned} \quad (5.39)$$

where, as before, $\delta\Gamma$ denotes the first order perturbation in the decay rate. Again, on using Eq. (5.17), we find that the equation describing the conservation of the perturbed energy density of the fluid $\delta\rho_F$ can be written as

$$\begin{aligned} \delta\dot{\rho}_F + 3H(1 + w_F) \delta\rho_F + \left(\frac{1}{a^2} \right) \nabla^2 \psi_F \\ - 2\Gamma \dot{\phi} \delta\phi + \Gamma \dot{\phi}^2 A - \left[\frac{(1 + w_F) \rho_F}{a} \right] \nabla^2 B - \dot{\phi}^2 \delta\Gamma = 0. \end{aligned} \quad (5.40)$$

Also, from the first order Einstein equations (5.14b) and (5.14c), we can arrive at the following differential equation for the quantity ψ_F that describes the spatial velocity of the fluid:

$$\dot{\psi}_F + 3H\psi_F + w_F \delta\rho_F + (1 + w_F) \rho_F A + \Gamma \dot{\phi} \delta\phi = 0. \quad (5.41)$$

The perturbation variables that we shall evolve numerically are $\mathcal{Q}_\phi = \delta\phi$ and the quantity \mathcal{Q}_F that we had introduced earlier [cf. Eq. (5.21)]. As in the case of the tachyon and the perfect fluid, using the background equations, the first order Einstein equations for the system and the energy conservation equations for the scalar field and the fluid, we can arrive at the coupled second order differential equations (5.22) for \mathcal{Q}_ϕ and \mathcal{Q}_F , with $(\alpha, \beta) = (\phi, F)$ [65]. For the case wherein the decay rate Γ is a constant, the coefficients $\mathcal{F}_{\alpha\beta}$ and $\mathcal{G}_{\alpha\beta}$ are now

given by

$$\mathcal{F}_{\phi\phi} = (3H + \Gamma), \quad (5.42a)$$

$$\mathcal{F}_{\phi F} = \left(\frac{4\pi G}{H}\right) \left(\frac{w_F - 1}{w_F}\right) \dot{\phi} \sqrt{(1 + w_F) \rho_F}, \quad (5.42b)$$

$$\mathcal{F}_{F\phi} = \left(\frac{4\pi G}{H}\right) \dot{\phi} (1 - w_F) \sqrt{(1 + w_F) \rho_F} + (1 + 2w_F) \left(\frac{\Gamma \dot{\phi}}{\sqrt{(1 + w_F) \rho_F}}\right), \quad (5.42c)$$

$$\mathcal{F}_{FF} = 3H + \left(\frac{\Gamma \dot{\phi}^2}{\rho_F}\right), \quad (5.42d)$$

$$\begin{aligned} \mathcal{G}_{\phi\phi} = & V_{\phi\phi} - \left(\frac{1}{a^2}\right) \nabla^2 + \left(\frac{4\pi G}{H}\right) \left[4V_{\phi} \dot{\phi} + 2(3H + \Gamma) \dot{\phi}^2 - \left(\frac{\Gamma \dot{\phi}^2}{\rho_F}\right)\right] \\ & - \left(\frac{4\pi G}{H}\right)^2 \dot{\phi}^2 \left[2\dot{\phi}^2 + \left(\frac{(1 + w_F)^2}{w_F}\right) \rho_F\right], \end{aligned} \quad (5.42e)$$

$$\begin{aligned} \mathcal{G}_{\phi F} = & \left(\frac{4\pi G}{H}\right) \left[-\left(\frac{3H \dot{\phi}}{2}\right) \left(\frac{(1 + w_F)^2}{w_F}\right)\right. \\ & \left. + \left(\frac{1}{2\rho_F}\right) \left(\frac{w_F - 1}{w_F}\right) \Gamma \dot{\phi}^3 - 2V_{\phi} - \Gamma \dot{\phi}\right] \sqrt{(1 + w_F) \rho_F} \\ & + \left(\frac{4\pi G}{H}\right)^2 \dot{\phi} \left[2\dot{\phi}^2 + \left(\frac{(1 + w_F)^2}{w_F}\right) \rho_F\right] \sqrt{(1 + w_F) \rho_F}, \end{aligned} \quad (5.42f)$$

$$\begin{aligned} \mathcal{G}_{FF} = & -\left(\frac{4\pi G}{H}\right) \left[V_{\phi} (1 + w_F)^2 \rho_F + 3H V_{\phi} \dot{\phi} (1 + w_F)^2 \rho_F - \Gamma \dot{\phi}^3\right] \left(\frac{1}{\sqrt{(1 + w_F) \rho_F}}\right) \\ & + \left(\frac{4\pi G}{H}\right)^2 (\dot{\phi}^2 + 2\rho_F) \left[\frac{(1 + w_F^2) \rho_F \dot{\phi}}{\sqrt{(1 + w_F) \rho_F}}\right] \\ & - \left(\frac{\Gamma}{\sqrt{(1 + w_F) \rho_F}}\right) (V_{\phi} - 3H w_F \dot{\phi} + \Gamma \dot{\phi}), \end{aligned} \quad (5.42g)$$

$$\begin{aligned} \mathcal{G}_{FF} = & -\left(\frac{w_F}{a^2}\right) \nabla^2 + \left(\frac{9H^2}{4}\right) (1 - w_F^2) \\ & + \left(\frac{4\pi G}{H}\right) \left[\left(\frac{3H}{2}\right) (1 + w_F) (1 + 3w_F) \rho_F + \left(\frac{3H}{2}\right) \dot{\phi}^2 (w_F - 1) - \Gamma \dot{\phi}^2\right] \\ & - \left(\frac{4\pi G}{H}\right)^2 \left[(1 + w_F)^2 \rho_F \dot{\phi}^2 + 2((1 + w_F) \rho_F)^2\right] \\ & - \left(\frac{\Gamma \dot{\phi}}{\rho_F}\right) \left[V_{\phi} + \Gamma \dot{\phi} - \left(\frac{3H}{2}\right) w_F \dot{\phi} + \left(\frac{\Gamma \dot{\phi}^3}{4\rho_F}\right)\right]. \end{aligned} \quad (5.42h)$$

For the case wherein the decay rate is a function of the scalar field ϕ , the coefficients $\mathcal{G}_{\phi\phi}$ and $\mathcal{G}_{F\phi}$ are modified to

$$\mathcal{G}_{\phi\phi} \rightarrow \mathcal{G}_{\phi\phi} + \dot{\phi} \Gamma_{\phi}, \quad (5.43a)$$

$$\mathcal{G}_{F\phi} \rightarrow \mathcal{G}_{F\phi} + \left(\frac{w_F}{\sqrt{(1+w_F) \rho_F}} \right) \dot{\phi}^2 \Gamma_{\phi}, \quad (5.43b)$$

where $\Gamma_{\phi} \equiv (d\Gamma/d\phi)$. The other coefficients remain unchanged.

5.5.3 Evolution of the curvature perturbations and the scalar power spectrum

Let \mathcal{R}_{ϕ} and \mathcal{R}_F denote the curvature perturbations associated with the canonical scalar field and the fluid, respectively. As earlier, we find that these curvature perturbations are related to the variables \mathcal{Q}_{ϕ} and \mathcal{Q}_F as follows [65, 66, 92, 94, 95, 96, 97, 98, 123, 226, 227]:

$$\mathcal{R}_{\phi} = \left(\frac{H}{\dot{\phi}} \right) \delta\phi = \left(\frac{H}{\dot{\phi}} \right) \mathcal{Q}_{\phi}, \quad (5.44a)$$

$$\mathcal{R}_F = - \left(\frac{H}{\rho_F + p_F} \right) \psi_F = - \left(\frac{H}{\sqrt{(1+w_F) \rho_F}} \right) \mathcal{Q}_F. \quad (5.44b)$$

As mentioned earlier, the total curvature perturbation of the system, say, \mathcal{R} , can then be expressed as a weighted sum of the individual curvature perturbations [cf. Eq. (5.26)] and, for the system of our interest, the total curvature perturbation is given by

$$\mathcal{R} = H \left[\dot{\phi}^2 + (1+w_F) \rho_F \right]^{-1} \left[\dot{\phi} \mathcal{Q}_{\phi} - \sqrt{(1+w_F) \rho_F} \mathcal{Q}_F \right]. \quad (5.45)$$

As usual, the scalar power spectrum is then defined in terms of the Fourier mode \mathcal{R}_k of the total curvature perturbation [cf. Eq. (2.39)].

In Fig. 5.5, as in the case of the tachyon discussed earlier, we have plotted evolution of the amplitude of the individual and the total curvature perturbations, as well as the scalar power spectrum before and after the transition. It is evident from these figures that the conclusions we had arrived at for the tachyon apply equally well to the case involving the canonical scalar field too.

5.5.4 Evolution of the entropy perturbations

As in the case of the tachyon coupled with the perfect fluid, the non-adiabatic pressure perturbation δp^{NA} of the system containing a canonical scalar field and the perfect fluid depends

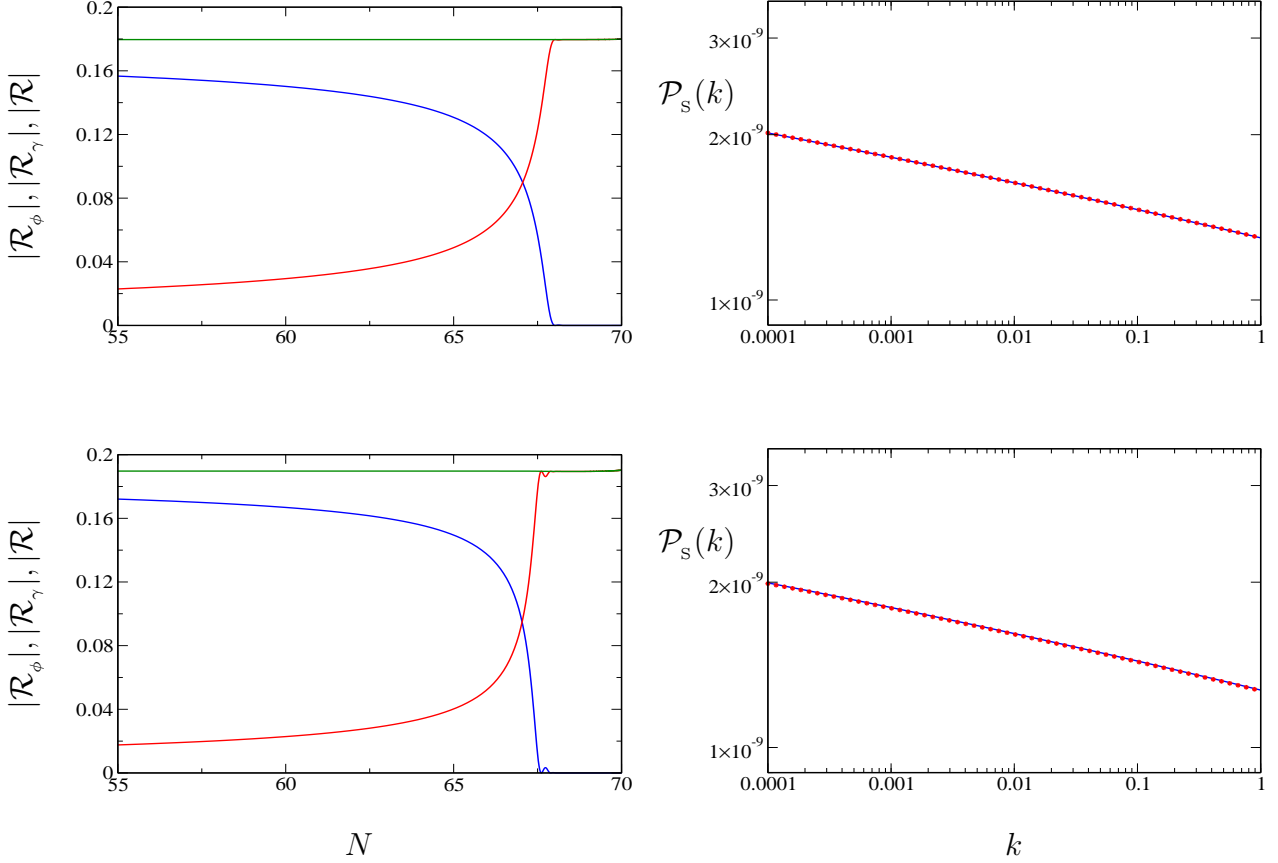


Figure 5.5: In the left column, the evolution of the amplitudes of the curvature perturbations associated with the scalar field ($|\mathcal{R}_\phi|$, in blue), radiation ($|\mathcal{R}_\gamma|$, in red) and the total curvature perturbation of the entire system ($|\mathcal{R}|$, in green) has been plotted as a function of the number of e -folds N for the two types of the decay rate. For illustration, we have again chosen a typical cosmological mode with wavenumber $k = 0.01 \text{ Mpc}^{-1}$. In the right column, as before, we have plotted the scalar power spectrum before (in blue) and after (in red) the transition. It is evident that, as in the case of the tachyon, the amplitude of the nearly scale invariant power spectrum remains unaffected for both types of decay.

on the intrinsic non-adiabatic pressure perturbation of the scalar field, say, $\delta p_\phi^{\text{NA}}$, and the relative non-adiabatic pressure perturbation between the scalar field and the fluid, say, $\delta p_{\phi F}^{\text{NA}}$.

While, the quantity $\delta p_\phi^{\text{NA}}$ is defined by the standard relation [cf. Eq. (2.23)], the relative non-adiabatic pressure perturbation $\delta p_{\phi F}^{\text{NA}}$ is given by [cf. Eq. (5.34)]

$$\delta p_{\phi F}^{\text{NA}} = (3H + \Gamma) \left(\frac{\rho_\phi + p_\phi}{\rho + p} \right) \left[(\rho_F + p_F) - (\Gamma/3H) (\rho_\phi + p_\phi) \right] \times (w_F - c_\phi^2) \left[\left(\frac{\delta \rho_\phi}{\dot{\rho}_\phi} \right) - \left(\frac{\delta \rho_F}{\dot{\rho}_F} \right) \right], \quad (5.46)$$

where $c_\phi^2 = (\dot{p}_\phi/\dot{\rho}_\phi)$. We find that the quantities $\delta \rho_\phi$, δp_ϕ and $\delta \rho_F$ can be written in terms of the variables \mathcal{Q}_ϕ and \mathcal{Q}_F as follows:

$$\delta \rho_\phi = \left[V_\phi - \left(\frac{4\pi G}{H} \right) \dot{\phi}^3 \right] \mathcal{Q}_\phi + \dot{\phi} \dot{\mathcal{Q}}_\phi + \left(\frac{4\pi G}{H} \right) \dot{\phi}^2 \sqrt{(1+w_F) \rho_F} \mathcal{Q}_F, \quad (5.47a)$$

$$\delta p_\phi = - \left[V_\phi + \left(\frac{4\pi G}{H} \right) \dot{\phi}^3 \right] \mathcal{Q}_\phi + \dot{\phi} \dot{\mathcal{Q}}_\phi + \left(\frac{4\pi G}{H} \right) \dot{\phi}^2 \sqrt{(1+w_F) \rho_F} \mathcal{Q}_F, \quad (5.47b)$$

$$\begin{aligned} \delta \rho_F = & - \left[\left(\frac{4\pi G}{H} \right) \dot{\phi} (1+w_F) \left(\frac{\rho_F}{w_F} \right) + \left(\frac{\Gamma \dot{\phi}}{w_F} \right) \right] \mathcal{Q}_\phi \\ & - \left[\left(\frac{3H}{2w_F} \right) (1-w_F) \sqrt{(1+w_F) \rho_F} + \Gamma \dot{\phi}^2 \left(\frac{1+w_F}{4w_F^2 \rho_F} \right)^{1/2} \right. \\ & \left. - \left(\frac{4\pi G}{H} \right) \left(\frac{1}{w_F} \right) [(1+w_F) \rho_F]^{3/2} \right] \mathcal{Q}_F - \left(\frac{1}{w_F} \right) \sqrt{(1+w_F) \rho_F} \dot{\mathcal{Q}}_F. \end{aligned} \quad (5.47c)$$

These relations can be used to express the non-adiabatic pressure perturbations $\delta p_\phi^{\text{NA}}$ and $\delta p_{\phi F}^{\text{NA}}$ in terms of \mathcal{Q}_ϕ , \mathcal{Q}_F , and their time derivatives.

In Fig. 5.6, we have plotted the amplitudes of the Bardeen potential (i.e. $|\Phi|$) and the non-adiabatic pressure perturbations (viz. $|\delta p_\phi^{\text{NA}}|$ and $|\delta p_{\phi F}^{\text{NA}}|$) as a function of the number of e -folds. It is again clear from these figures that the various quantities behave in a similar fashion as in the case involving the tachyon.

5.6 Summary and discussion

In this chapter, we have studied the evolution of perturbations in an interacting system consisting of a tachyon and radiation. Treating the tachyon as an inflaton, we have investigated the effects of reheating—i.e. the perturbative transfer of energy from the tachyon

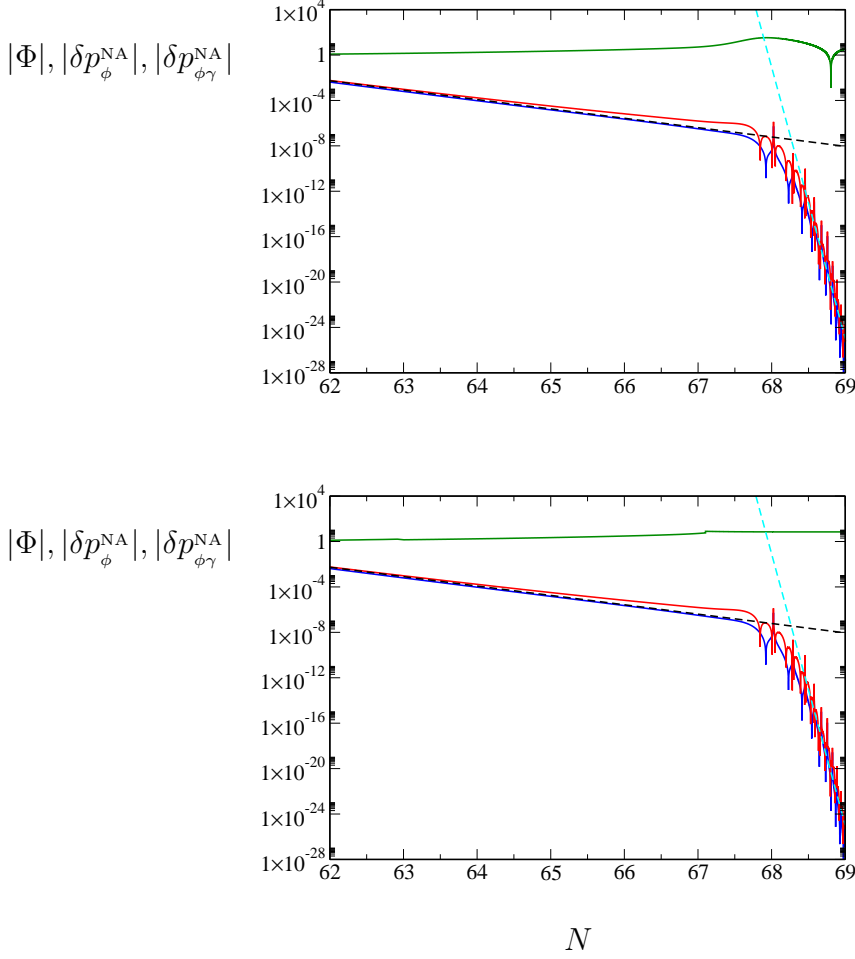


Figure 5.6: The evolution of the amplitudes of the Bardeen potential $|\Phi|$ (in green), the intrinsic entropy perturbation $|\delta p_\phi^{\text{NA}}|$ (in blue) and the isocurvature perturbation $|\delta p_{\phi\gamma}^{\text{NA}}|$ (in red) has been plotted as a function of the number of e -folds N for the two cases of Γ , as in the previous two figures. Again, for computational reasons, we have chosen a very small scale mode with wavenumber $k = 10^{16} \text{ Mpc}^{-1}$. As earlier, we have normalized the values of all the three quantities to be unity at Hubble exit. Clearly, while the Bardeen potential remains nearly a constant across the transition, both the intrinsic entropy and the isocurvature perturbations decay in almost the same fashion before as well as after the transition. The dashed lines in black and cyan indicate the $e^{-(2N)}$ and $e^{-(55N)}$ behavior, respectively. The non-adiabatic pressure perturbations die down extraordinarily rapidly after reheating is complete.

to radiation—on the large scale curvature perturbations. We have shown that the transition does not alter the amplitude of the total curvature perturbation of the system when the rate describing the decay of the inflaton into radiation is either a constant or a function of the tachyon. We have also illustrated that, before the transition to the radiation dominated epoch, the relative non-adiabatic pressure perturbation between the tachyon and radiation decays in a fashion very similar to that of the intrinsic entropy perturbation associated with the tachyon. Moreover, we have shown that, after the transition, the relative non-adiabatic pressure perturbation between the tachyon and radiation dies down extremely rapidly during the early stages of the radiation dominated epoch. It is these behavior which ensure that the amplitude of the curvature perturbations remain unaffected during reheating. We have also discussed the corresponding results for the popular chaotic inflation model in the case of the canonical scalar field.

It may be considered an overkill to integrate the second order differential equations rather than work with the much simpler first order equations [87, 229, 230]. Our motivations were threefold. Importantly, our effort allowed us to cross-check certain previous results [87]. Also, our aim is to later study the effects of deviations from slow roll inflation as well as the effects of the modified dynamics close to the transition to the radiation dominated epoch on the small scale perturbations. As we had mentioned in the introductory section of this chapter, these effects can have interesting implications for the number density of primordial black holes that are formed towards the end of inflation [218, 219, 220, 221]. Moreover, in possibilities such as the warm inflationary scenario, the decay rate, in addition to depending on the inflaton, can also depend on the temperature (see, for example, Refs. [226, 227, 228, 234]). In such a case, the transfer of the energy from the inflaton to radiation may affect the amplitude and possibly the spectral index as well [66].

We would like to conclude this chapter by commenting on our choice of $\Gamma(T)$. As we had pointed out earlier, our choice is motivated by convenience in the numerical evolution rather than physics. Obviously, better motivated functional forms of the decay rate needs to be investigated. It may be worth exploring these issues further.

Chapter 6

Non-gravitating scalar field in the Friedmann universe

6.1 Introduction

Over the last couple of decades, several mechanisms have been proposed for the generation of the initial inhomogeneities in the early universe. As discussed in the earlier chapters, the inflationary phase wherein the quantum fluctuations associated with the scalar field prove to be responsible for the generation of the inhomogeneities in the early universe, seems to provide a viable scenario for the origin of the primordial perturbations. The inflationary paradigm is now widely accepted and its predictions are fairly well supported by observations. Apart from the inflationary scenario, topological defects that form during the phase transitions in the very early universe have also been considered as alternative sources for the generation of the primordial perturbations [235, 236]. As we had mentioned in the introductory chapter, there are a number of possible types of defects, such as magnetic monopoles, domain walls, cosmic strings and textures. With the aim of providing another possible mechanism for the origin of the perturbations, in this chapter, we consider the behavior of an inhomogeneous, self-interacting, scalar field that is coupled non-minimally to gravity in the Friedmann background. Though, we do not quite achieve the goal we set out to, we, nevertheless, shall discuss the peculiar properties of a non-gravitating scalar field that is coupled non-minimally to gravity in various backgrounds, including the Friedmann universe.

Non-minimal coupling of the dilaton and the metric is a generic feature of any string theory (see, for instance, Ref. [237]). While usual compactifications do not generate any poten-

tial, in the low energy limit for the dilaton or other massless scalars coming from the string theory, it is generally believed that a potential is generated for them when one considers flux compactifications [238, 239]. The generation of potential for the scalar fields in the flux compactification makes them an arena for study of physics of the early universe. However, if one looks at models of inflation in these compactifications, a generic problem crops up in realizing slow roll inflation. One of the slow roll parameters turns out to be sensitive to the size of the compactified space and, as a result, the slow roll conditions often prove to be harder to achieve [240, 241, 242].

As we had discussed, the slow roll conditions arise when the kinetic energy of the inflaton (the scalar field which drives inflation) is neglected when compared to its potential energy and the acceleration term is also ignored when compared to the friction term in the equation of motion for the inflaton [2, 3, 5, 97]. Since, the Right Hand Side (RHS) of the Einstein equations contains the stress-energy tensor of the scalar field, this condition reflects upon the nature of the potential. However, if we have a non-minimally coupled scalar field with a potential such that it does not gravitate, i.e. its stress-energy tensor vanishes identically, then the smallness of the slow roll parameters becomes irrelevant. This is because of the fact that throughout the rolling of the non-gravitating scalar field, there is no contribution of it on the RHS of the Einstein equations. The shape of the potential and rolling of the scalar field becomes relevant only when, by some other mechanism, it starts gravitating. If we achieve sufficient amount of inflation before the scalar field starts gravitating then the subsequent time dependence of the scalar field has no bearing on the model of inflation. As we shall see below, for a specific choice of non-minimal coupling, one gets a fixed potential for the scalar field so that it does not gravitate. It is not obvious if such a non-minimal coupling and/or the potential can be obtained from a generic flux compactification. Nevertheless, inflation in the theory with a non-gravitating scalar field is a novel way of by-passing the ‘ η -problem’ that one encounters in models of inflation with flux compactifications [239, 240].

If we are looking for a non-gravitating scalar field background, it could generically depend on the spatial coordinates as well. This question was addressed recently in the Minkowski spacetime [243] and, in this chapter, we shall obtain similar results for the Friedmann and the Anti-de Sitter (AdS) backgrounds. As discussed in the earlier papers [243, 244], we find that the classical non-gravitating solution allows space dependent

scalar field profile in all these cases, including the Minkowski spacetime. However, in every case, this solution is singular, i.e. the scalar field profile diverges at some point in space or spacetime. This singularity begs for a careful evaluation of the stress-energy tensor in its neighborhood. We analyze the stress-energy tensor by regularizing the singular scalar field profile and find that there is a subtle contribution to the stress-energy tensor from the singularity. This contribution is proportional to the Dirac δ -function but with an infinite multiplicative coefficient. Due to this contribution, the space dependent scalar field profile actually gravitates. While this rules out non-constant solution in the Minkowski spacetime, purely time dependent solution is an allowed class of non-gravitating solutions in the Friedmann background. Similarly, purely radial dependent solution can be non-gravitating in the AdS background.

Since purely time dependent solution in the Friedmann background can be non-gravitating, we build a hybrid inflation model by coupling the non-gravitating solution to another scalar field χ , which is gravitating. Inflation is obtained by rolling of the non-gravitating scalar field and is exited by rolling of the gravitating scalar field, i.e. χ . The rolling of χ is triggered by that of the non-gravitating field. Interesting feature of this model is that the non-gravitating scalar field starts gravitating as soon as χ starts rolling.

This chapter is organized as follows. In Sec. 6.2, we review the essential results for a non-gravitating scalar field and its interaction potential functional in the Minkowski background and also obtain the same in the Friedmann and the AdS backgrounds. In Sec. 6.3, we perform the regularized stress-energy tensor calculation in the vicinity of the singularity of the scalar field profile. We also discuss the subtleties related to the issue of finding the backreacted metric in the presence of the non-vanishing stress-energy tensor. In Sec. 6.4, we propose a novel model of hybrid inflation by considering another scalar field χ . Finally, in Sec. 6.5, we summarize our results.

6.2 Non-gravitating scalar field in various backgrounds

In this section, we shall study a scalar field $\phi(\mathbf{x}, t)$ non-minimally coupled to gravity. We shall first summarize as to how the non-gravitating solution is obtained in the Minkowski spacetime [243]. We shall then obtain the non-gravitating solutions in the Friedmann background as well as in the AdS background. We shall refer to the non-gravitating solution as

a solution to the equations of motion such that the stress-energy tensor for the field $\phi(\mathbf{x}, t)$ evaluated on this background vanishes. It imposes constraints which are sufficient to determine the form of the classical solution as well as the potential $V(\phi)$. The equation of motion of the field then becomes a consistency condition for the solution and the potential energy functional.

Let us consider a self-interacting scalar field $\phi(\mathbf{x}, t)$ that is non-minimally coupled to gravity. We shall also assume the presence of the cosmological constant Λ . The action for such a scalar field is given by

$$I_\phi = \int d^4x \sqrt{-g} \left(\frac{M_p^2}{2} (R + 2\Lambda) + \frac{1}{2} \phi \square \phi - \frac{1}{2} \xi R \phi^2 - V(\phi) \right). \quad (6.1)$$

The parameter ξ is a measure of non-minimality. In $(3 + 1)$ dimensions, $\xi = (1/6)$ leads to conformal coupling of the scalar field to the gravity and $\xi = 0$ corresponds to the usual minimal coupling. The equation of motion of the scalar field is

$$(\square - \xi R) \phi = V_\phi, \quad (6.2)$$

where the additional term proportional to the Ricci scalar R is a consequence of the non-minimal coupling. The conserved stress-energy tensor is also modified due to the non-minimal coupling and can be written as

$$\Theta_{\mu\nu} \equiv T_{\mu\nu} + \xi (g_{\mu\nu} \square - \nabla_\mu \nabla_\nu + \Lambda g_{\mu\nu}) \phi^2, \quad (6.3)$$

where $T_{\mu\nu}$ is the standard stress-energy tensor for a minimally coupled scalar field and is given by

$$T_{\mu\nu} = \partial_\mu \phi \partial_\nu \phi - g_{\mu\nu} \left(\frac{1}{2} \partial_\alpha \phi \partial^\alpha \phi + V(\phi) \right). \quad (6.4)$$

The expression for the stress-energy tensor $\Theta_{\mu\nu}$ in Eq. (6.3) is obtained in the following way. We first assume that, in its original form, every component of the stress-energy tensor $\Theta_{\mu\nu}$ vanishes. In such a case, the Einstein equations become

$$G_{\mu\nu} = \Lambda g_{\mu\nu}. \quad (6.5)$$

Using this equation, we arrive at the form of $\Theta_{\mu\nu}$ as given in Eq. (6.3).

So far, we have been looking at the general features of a scalar field non-minimally coupled to the gravity. Our aim is to look for a scalar field solution which does not gravitate in a given background. The solution is obtained by first carrying out a change of variable

$$\phi = \sigma^\alpha, \quad (6.6)$$

in the expression for the stress-energy tensor (6.3) and then writing them in terms of σ and its derivatives. Setting every component of $\Theta_{\mu\nu}$ to zero leads to the following set of equations:

$$\begin{aligned} 0 &= \Theta_{\mu\nu} \\ &= \frac{(2\xi)^2}{(1-4\xi)} \frac{\phi^2}{\sigma} \nabla_\mu \partial_\nu \sigma, \quad \mu \neq \nu, \end{aligned} \quad (6.7a)$$

$$\begin{aligned} 0 &= g_{ii} \Theta_{tt} - g_{tt} \Theta_{ii} \\ &= \frac{(2\xi)^2}{(1-4\xi)} \frac{\phi^2}{\sigma} \left[g_{ii} \nabla_t \partial_t \sigma - g_{tt} \nabla_i \partial_i \sigma \right] \text{ (no sum)}, \end{aligned} \quad (6.7b)$$

$$\begin{aligned} 0 &= \Theta_{tt} \\ &= V(\phi) - \frac{(2\xi)^2 \phi^2}{(1-4\xi)\sigma} \left[\frac{\partial_\rho \sigma \partial^\rho \sigma}{2(1-4\xi)\sigma} - g^{ii} \sum_{i=1}^3 \nabla_i \partial_i \sigma \right] - \xi \phi^2 \Lambda. \end{aligned} \quad (6.7c)$$

These equations impose constraints on σ , and are obtained after choosing α to be

$$\alpha = \left[\frac{2\xi}{(4\xi-1)} \right], \quad (6.8)$$

where $\xi \neq 0$ or $(1/4)$. While the case $\xi = 0$ is excluded because it takes us back to the minimally coupled scalar field theory, $\xi = (1/4)$ can be treated separately, and it can be shown that a non-gravitating solution exists for $\xi = (1/4)$ as well [243]. We shall solve these constraints in various backgrounds below.

6.2.1 The Minkowski background

Let us start with the Minkowski background. The equations (6.7a) and (6.7b) are solved in the Minkowski background by [243]

$$\sigma(x^\mu) = a_1 x^\mu x_\mu + p^\mu x_\mu + a_2, \quad (6.9)$$

and the self interacting potential is given by

$$V(\phi) = \frac{2\xi^2}{(1-4\xi)^2} \left[\lambda \phi^{(1-2\xi)/\xi} + 48 \left(\xi - \frac{1}{6} \right) a_1 \phi^{1/2\xi} \right], \quad (6.10)$$

where $\lambda = (p^\mu p_\mu - 4 a_1 a_2)$. We shall get back to this solution in the next section.

6.2.2 The Friedmann background

Let us now turn our attention to the Friedmann background. The background metric in this case is given by¹

$$ds^2 = -dt^2 + a^2(t) [dx^2 + dy^2 + dz^2], \quad (6.11)$$

where $a(t)$ is the scale factor of the spatial section of the Friedmann background. Making use of the change of variable (6.6) and rearranging the components of the stress-energy tensor (6.3) appropriately, we arrive at three independent set of expressions, all of which are set to zero. Eq. (6.7a) imposes constraints on the profile of σ . When neither of the indices μ or ν is equal to t , the constraints on σ are such that we can choose

$$\sigma = f(t) [X_1(x) + X_2(y) + X_3(z)]. \quad (6.12)$$

If instead, either μ or ν is equal to t , then the constraint arising from the equation (6.7a) implies that the function $f(t)$ is proportional to the scale factor $a(t)$ i.e.

$$f(t) = c_0 a(t). \quad (6.13)$$

The linear combination of the diagonal components of the stress-energy tensor in Eq. (6.7b) determines the solution completely. While on one hand, it can be used to obtain the behavior of the scale factor, on the other hand, it also determines the functional forms of $X_1(x)$, $X_2(y)$ and $X_3(z)$ up to the constants of integration. This equation also requires exponential behavior of the scale factor. This is consistent with the Einstein equation (6.5) which can be written in terms of the Hubble parameter H and the cosmological constant Λ as

$$3H^2 = -\Lambda, \quad a(t) = a_0 \exp(Ht). \quad (6.14)$$

Vanishing of the double spatial derivative of σ in Eq. (6.7b) implies that the functions X_i are at most linear in their arguments for all i , as given by

$$X_1(x) = p_1 x + c_1. \quad (6.15)$$

Using Eqs. (6.12)–(6.15) in the relation (6.6), we get

$$\phi(\mathbf{x}, t) = \sigma^{2\xi/(4\xi-1)} = [c_0 a(t) (p_i x^i + c)]^{2\xi/(4\xi-1)}, \quad (6.16)$$

¹We should emphasize here that, for calculational convenience, in this chapter, we shall be working with the metric signature of $(-, +, +, +)$.

where, $c = (c_1 + c_2 + c_3)$ and $p_i x^i = (p_1 x + p_2 y + p_3 z)$. Using the Θ_{tt} equation (6.7c) and the solution (6.16), the potential $V(\phi)$ can be determined to be

$$V(\phi) = \left[\frac{2\xi^2}{(4\xi - 1)^2} (5 - 24\xi) - 3\xi \right] H^2 \phi^2 + \frac{2\xi^2}{(4\xi - 1)^2} \left(c_0^2 \sum_{i=1}^3 p_i^2 \right) \phi^{(1-2\xi)/\xi}. \quad (6.17)$$

Let us first notice that, for all $\xi < (1/4)$, the second term in the potential is dominant for large ϕ , and if ξ is such that the potential $V(\phi)$ is even under $\phi \rightarrow -\phi$, then the potential is bounded from below. Since the first term is negative, for the parity symmetric cases, we have a double well potential, as shown in the top panel of Fig. 6.1. The solution (6.16) obtained by solving the stress-energy tensor constraints also satisfies the equation of motion for the field (6.2). This consistency condition ensures that the stress-energy tensor is conserved in this background. This solution diverges for large x^i when $\xi > (1/4)$ (or, $\alpha > 0$), on the other hand, for $\xi < (1/4)$ (or, $\alpha < 0$), it diverges at a point where $(p_i x^i + c) = 0$ (as displayed in the bottom panel of Fig. 6.1). We choose ξ in such a way that α , which is, in general, a fraction, has an odd denominator. This ensures that at least one real solution always exists. The classical solution $\phi(\mathbf{x}, t)$ depends on the scale factor $a(t)$ and when $\xi < (1/4)$, the field $\phi(\mathbf{x}, t)$ is inversely proportional to a ξ dependent power of $a(t)$. Thus, in addition to having the space dependent profile, the amplitude of the classical solution depends on the scale factor and decreases rapidly for $\xi < (1/4)$ [245].

For the sake of completeness, let us consider the case of $\xi = (1/4)$. In this case, we carry out the similar analysis as in Ref. [243] and obtain the classical solution $\phi(\mathbf{x}, t)$ and the potential $V(\phi)$ exactly as

$$\phi(\mathbf{x}, t) = \exp \left[c_0 e^{Ht} (p_i x^i + c) \right], \quad (6.18)$$

$$V(\phi) = \phi^2 \left[\sum_{i=1}^3 \frac{(c_0 p_i)^2}{2} - \frac{3H^2}{4} - \frac{(H \ln \phi)^2}{2} - \frac{3H^2}{2} \ln \phi \right]. \quad (6.19)$$

6.2.3 The AdS background

Let us now turn our attention to the AdS background. The metric of the AdS background can be written as

$$ds^2 = -\frac{r^2}{b^2} dt^2 + \frac{b^2}{r^2} dr^2 + \frac{r^2}{b^2} (dx^2 + dy^2), \quad (6.20)$$

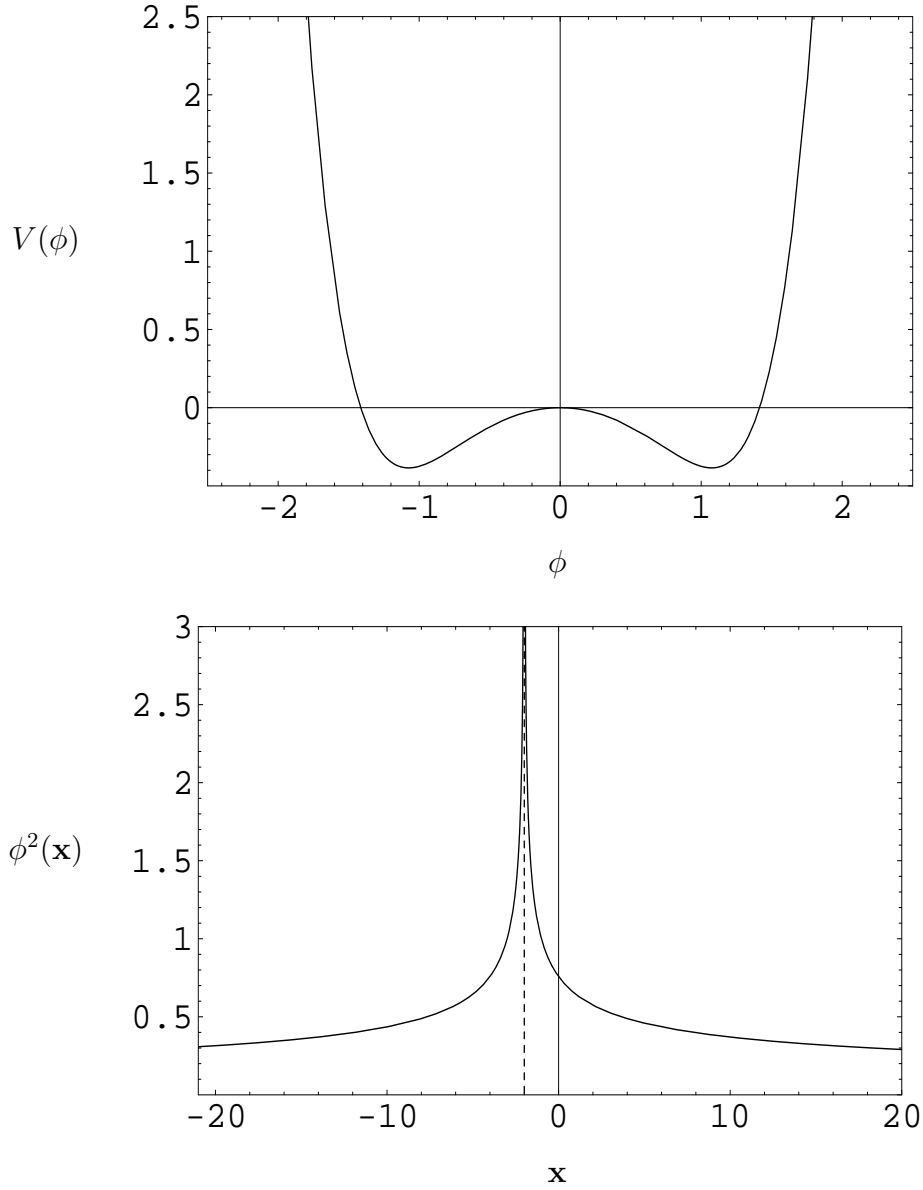


Figure 6.1: The top figure shows the generic form of the potential for the non-gravitating field ϕ in the Friedmann background, while the figure at the bottom denotes ϕ^2 , the square of the classical solution at a fixed time.

where b is the radius of the AdS space. The conditions coming from the $\Theta_{\mu\nu}$ ($\mu \neq \nu$) can be satisfied by choosing the following ansatz for σ :

$$\sigma = a(r) \left[f_1(t) + f_2(x) + f_3(y) \right]. \quad (6.21)$$

The diagonal components of the stress-energy tensor then lead to

$$a(r) = C r, \quad (6.22)$$

where C is the integration constant and

$$\sigma = C r [t + x + y + d], \quad (6.23)$$

with d denoting another constant of integration. The potential functional $V(\phi)$ is obtained by solving $\Theta_{tt} = 0$ and is given by

$$V(\phi) = \alpha^2 b^2 C^2 \phi^{\frac{(1-2\xi)}{\xi}} + \left(8\xi\alpha + 5\xi + \frac{\alpha^2}{2} \right) \frac{\phi^2}{b^2}. \quad (6.24)$$

It is worth emphasizing that, this solution satisfies the equation of motion (6.2), ensuring the conservation of the stress-energy tensor.

While we have managed to obtain non-gravitating solutions to the equations of motion in various backgrounds, we find that all these solutions are singular. If one chooses $\xi > (1/4)$, then the solution diverges at infinity and if $\xi < (1/4)$, then it diverges for some finite value of the spacetime coordinates. This divergence in the solution has a subtle contribution to the stress-energy tensor which we shall carefully analyze using the solution and show that the naive conclusion of vanishing of the stress-energy tensor is flawed.

6.3 The regularized stress-energy tensor

In this section, we shall show that the naive computation of the stress-energy tensor for the ‘non-gravitating’ solution in the previous section fails in the vicinity of the singularity. The singular nature of the solution, depending on the choice of ξ , leads to either discontinuous profile for ϕ or its derivative $\partial_\mu \phi$. Since the stress-energy tensor contains terms up to second derivative of ϕ , this discontinuity can lead to a potential δ -function contribution. To analyze this, we need to regularize the solution in the neighborhood of singularity. We shall illustrate this method for the Minkowski background as well as for the Friedmann background, a similar analysis carries through for the AdS spacetime. For concreteness, we shall carry out our analysis for $\xi < (1/4)$, but it can be easily extended to $\xi > (1/4)$. While, in the former case, the singularity is in the finite domain, it is at infinity for the latter case.

6.3.1 The Minkowski background

In this case, we regularize the solution by regularizing the function σ as follows:

$$\sigma = \sqrt{(x+t)^2 + \epsilon^2} \sqrt{(x-t)^2 + \epsilon^2}, \quad (6.25)$$

where, for illustration, we have chosen $a_1 = 1$, $p_\mu = 0$ and $a_2 = 0$ in Eq. (6.9). It is evident that as $\epsilon \rightarrow 0$, we recover the original form for σ viz. $\sigma = (x^2 - t^2)$. Notice that, we choose the profile for σ such that it depends only on one spatial dimension. This suffices to illustrate our point and reinstating its full space dependence does not alter our conclusion. Using this regularized form of σ , and therefore ϕ , we can write down any component of the stress-energy tensor $\Theta_{\mu\nu}$ at an arbitrary point in the Minkowski space. The non-vanishing off-diagonal component of $\Theta_{\mu\nu}$ is,

$$\Theta_{tx} = -2 \xi \alpha \sigma^{2\alpha} \left[\frac{\epsilon^2}{[(x+t)^2 + \epsilon^2]^2} - \frac{\epsilon^2}{[(x-t)^2 + \epsilon^2]^2} \right]. \quad (6.26)$$

At any spacetime point, where the field profile ϕ is finite, we can show using independent methods that every component of the stress-energy tensor vanishes. We, therefore, need to restrict ourselves to the neighborhood of the singularity. Taking $(x+t) \sim \epsilon$ and $(x-t) \sim \epsilon$, we get

$$\Theta_{tx} = -2 \xi \alpha \epsilon^{4\alpha} f_1 \left(\frac{x}{\epsilon}, \frac{t}{\epsilon}, \epsilon \right). \quad (6.27)$$

As expected, the function f_1 is such that when $(x, t) \gg \epsilon$, it vanishes as $\epsilon \rightarrow 0$, and when $(x, t) \sim \epsilon$, $f_1 \sim \epsilon^{-2}$. Therefore, in the neighborhood of the singular point, i.e. when $(x, t) \sim \epsilon$, we arrive at

$$\Theta_{tx} \sim \epsilon^{(4\alpha-2)}. \quad (6.28)$$

Since $(4\alpha - 2)$ is negative for $\xi < (1/4)$, we find that the component Θ_{tx} of the stress-energy tensor is divergent in the limit $\epsilon \rightarrow 0$. In fact, an analysis of the diagonal components of the stress-energy tensor shows that they also diverge as $\epsilon^{(4\alpha-2)}$ in the neighborhood of the singular point. Notice that, in the limit $\epsilon \rightarrow 0$, the function f_1 has δ -function support at the location of the singularity. However, the coefficient multiplying this δ -function diverges as we remove the regulator. This severe singular contribution to $\Theta_{\mu\nu}$ invalidates the naive derivation of the non-gravitating solution in the previous section.

6.3.2 The Friedmann background

The situation is not any better in the Friedmann background. We write the regularized solution as

$$\phi = a(t)^\alpha x (x^2 + \epsilon^2)^\beta. \quad (6.29)$$

where $\beta = [(\alpha - 1)/2]$. Upon substituting this regularized form of the solution in the stress-energy tensor, we find that all the off-diagonal components of $\Theta_{\mu\nu}$ vanish identically at the singular point. On the other hand, the diagonal components take the following form:

$$\Theta_{tt} = a(t)^{2\alpha} \epsilon^{4\beta} f_2\left(\frac{x}{\epsilon}\right). \quad (6.30)$$

The function f_2 vanishes when $x \gg \epsilon$ and $\epsilon \rightarrow 0$, and when $x \sim \epsilon$, it is constant. Therefore, near the singular point, i.e. when $x \sim \epsilon$ and $\epsilon \rightarrow 0$, Θ_{tt} diverges as $\epsilon^{4\beta}$. All other diagonal components exhibit the similar divergent behavior as

$$\Theta_{ii} = a(t)^{2\alpha+2} \epsilon^{4\beta-2} f_2\left(\frac{x}{\epsilon}\right). \quad (6.31)$$

This divergence is as severe as in the case of the Minkowski background. The analysis of the stress-energy tensor of the scalar field in the AdS background proceeds in the similar fashion as in the Friedmann case [245].

We can now ask as to what is the backreaction of this contribution to the stress-energy tensor on the background metric. Notice that, in the Friedmann case, the Dirac δ -function contribution exists only for the diagonal components of the stress-energy tensor and all the off-diagonal components continue to vanish. With this in mind, we consider the metric ansatz for the backreacted geometry to be

$$g_{\mu\nu} = \text{diag.} \left[-f_1(x, t), f_2(x, t), f_3(x, t), f_3(x, t) \right]. \quad (6.32)$$

Substituting this ansatz in the Einstein equations gives us a set of coupled non-linear inhomogeneous partial differential equations. To make things even harder, we find that the coefficient of the inhomogeneous term is time dependent. In order to seek a solution, we shall attempt a separable ansatz for the solution. We shall also look at the solution on one side of the singularity. A similar solution on the other side of the singularity can then be matched with the first one along with the contribution from the singularity. Since the stress-energy

tensor vanishes away from the singularity, the RHS of the Einstein equation is proportional to the cosmological constant term only. As an illustration, let us consider an ansatz

$$f_i(x, t) = (cx + d)^{\alpha_i} g_i(t). \quad (6.33)$$

With this ansatz, we get one sided solution with $\alpha_1 = \alpha_3 = 0$ and $\alpha_2 = -2$ and two classes of time dependent terms are $g_1(t) = c_1, g_2(t) = c_2 e^{-2t}, g_3(t) = c_3 e^t$ or $g_1(t) = c_1, g_2(t) = c_2 e^{2t}, g_3(t) = c_3 e^{-t}$, where c_1, c_2 and c_3 are integration constants. We can now take the δ -function contribution into account to match the solutions on either side of the singularity. Due to the time dependent coefficient of the δ -function, we end up with inconsistent powers of the scale factor on the right and left hand side of the Einstein equation. We therefore conclude that the separable ansatz does not give a solution to our coupled inhomogeneous partial differential equations. We have tried out more general separable ansatz but all of them have suffered the same fate.

Since the vanishing of the stress-energy tensor also gives rise to coupled non-linear, but homogeneous, partial differential equations, we can attempt to get another solution of these equations which are not singular. This does not seem to lead to any new solution. Noticing the fact that the scalar field profile is proportional to $\exp(Ht)$, we can try a field redefinition viz. $\phi = \exp(\psi)$ and attempt to seek a solution

$$\psi(x, t) = At + f(x). \quad (6.34)$$

This ansatz gives us back the singular solution. Instead of the additive ansatz, if we take a multiplicative ansatz, i.e. $\psi(x, t) = [At f(x)]$, we end up with a contradiction. While one equation demands the scale factor to be a function of time only, the other equation is satisfied only if the scale factor has spatial dependence. Replacing (At) in the product ansatz by any other time dependent function does not alter the result.

6.4 The hybrid inflation model

In the previous section, we discussed that the space dependent scalar field profile fails to be a non-gravitating solution. However, if we look at purely time dependent scalar field profile in the Friedmann background, it does not lead to any subtle contribution to the stress-energy

tensor. We can therefore use the space independent scalar field profile to construct a model of inflation.

To do that, we shall couple another scalar field $\chi(\mathbf{x}, t)$ to the model studied above. For simplicity, we consider the minimal coupling between $\chi(\mathbf{x}, t)$ and gravity. The additional term in the action corresponding to the field $\chi(\mathbf{x}, t)$ is

$$I_\chi = \int d^4x \sqrt{-g} \left(\frac{1}{2} \chi \square \chi - \mathcal{V}(\phi, \chi) \right), \quad (6.35)$$

where $\mathcal{V}(\phi, \chi)$ is the interaction term which we choose to be

$$\mathcal{V}(\phi, \chi) = \frac{\lambda_1}{2} (\phi^2 - \phi_0^2) \chi^2 + \lambda_2 \chi^4, \quad (6.36)$$

where λ_i are positive for $i = (1, 2)$. We define the total action to be $I = I_\phi + I_\chi$. We can now justify the cosmological constant term in I_ϕ by interpreting it as the value of the potential \mathcal{V} at $\chi = 0$. This essentially amounts to redefining the value of \mathcal{V} at $\chi = 0$. For the model to be studied here, we shall choose $\xi < (1/4)$ and therefore, in this case, the magnitude of the classical solution $\phi(\mathbf{x}, t)$ decreases as a function of time as the scale factor $a(t)$ grows.

For a fixed value of ϕ_0 , it is easy to see from the potential (6.36), that we have two regimes corresponding to $\phi > \phi_0$ and $\phi < \phi_0$. As we discussed in the previous section, the space dependent profile for ϕ is singular and it gives rise to a subtle contribution to the stress-energy tensor. The space dependent solution (6.16) therefore, is not a bona fide non-gravitating solution. Purely time dependent configuration for ϕ , however, does not suffer from this problem and is a legitimate non-gravitating field configuration. For $\phi > \phi_0$, the potential for the field χ has a unique minimum at $\chi = 0$ and in this case, the field ϕ does not gravitate. The exponential growth of scale factor is then determined solely by the cosmological constant $\Lambda = \langle \mathcal{V} \rangle_{\chi=0}$ and the rate at which the field ϕ is rolling is irrelevant. In particular, the slow roll parameters determined from the potential $V(\phi)$ have no bearing on the nature of the inflation as $\phi(\mathbf{x}, t)$ is non-gravitating in this domain. This situation continues until $\phi(\mathbf{x}, t_0) = \phi_0$ at some time $t = t_0$. For all subsequent times after t_0 , we are in a situation where $\phi < \phi_0$. A sufficient amount of inflation can be obtained by adjusting initial value of ϕ .

Once $\phi < \phi_0$, the field χ develops a tachyonic instability at $\chi = 0$. This instability makes χ roll towards the true minimum. The rolling of χ affects exponential growth of the scale

factor. This is because of the fact that two new terms are generated due to rolling of the field χ . First of all, rolling of χ brings in I_χ into the picture, i.e. the field χ contributes to the stress-energy tensor and consequently to the RHS of the Einstein equations. Secondly, the non-zero vacuum expectation value of χ changes the potential $V(\phi)$ by adding a ϕ^2 term which modifies the mass of ϕ . Due to this additional term, the field ϕ ceases to be a non-gravitating field and starts contributing to the RHS of the Einstein equations. The first term is identical to the scalar field in the hybrid inflation models, which is responsible for the exit from the inflationary regime. It would be really interesting to study the predictions of this model further and check its validity against currently available data from various CMB observations [18, 19, 246].

6.4.1 Conformal transformation

It is known for some time that, the action of the scalar field non-minimally coupled to gravity can be brought into the canonical minimally coupled form by conformal transformation (in this context, see, for instance, Ref. [247]). Consider the action

$$S = \int d^4x \sqrt{-g} \left[\frac{\Omega^2 M_{\text{P}}^2}{2} R - \frac{1}{2} g^{\mu\nu} \partial_\mu \phi \partial_\nu \phi - V(\phi) \right], \quad (6.37)$$

where $\Omega^2 = (1 - M_{\text{P}}^{-2} \xi \phi^2)$. From this action, a minimally coupled scalar field theory can be obtained by doing the conformal transformation as

$$\Omega^2 g_{\mu\nu} = \tilde{g}_{\mu\nu}, \quad (6.38)$$

and followed by a redefinition of the scalar field as

$$d\tilde{\phi} = \frac{[1 - M_{\text{P}}^{-2} \xi (1 - 6\xi) \phi^2]^{1/2}}{\Omega^2} d\phi. \quad (6.39)$$

The new action written in terms of $\tilde{\phi}$ with the potential energy functional

$$\tilde{V}(\tilde{\phi}) = \frac{V(\phi)}{\Omega^4}, \quad (6.40)$$

is minimally coupled to gravity. The equation (6.39) can be integrated to write $\tilde{\phi}$ as a function of ϕ as

$$\left(\frac{\tilde{\phi}}{M_{\text{p}}}\right) = \frac{1}{\sqrt{2}\xi} \left[2\sqrt{3}\xi \tanh^{-1} \left(\frac{\sqrt{6}\xi(\phi/M_{\text{p}})}{\sqrt{1-\xi(1-6\xi)(\phi/M_{\text{p}})^2}} \right) - \sqrt{2\xi(-1+6\xi)} \sinh^{-1} \left(\sqrt{\xi(-1+6\xi)}(\phi/M_{\text{p}}) \right) \right]. \quad (6.41)$$

Substituting this redefinition in the action gives rise to a rather complicated potential energy functional. Nevertheless, in principle, it is possible to obtain non-gravitating scalar field background even in the minimally coupled case. This result holds for all backgrounds including the Minkowski space [243]. Clearly, the non-minimally coupled situation is much easier to deal with.

In case of the hybrid inflation model, we have an added complication in the minimally coupled situation. This is due to the fact that the conformal transformation which relates the non-minimally coupled theory to the minimally coupled one shows up in front of the kinetic energy term of χ as well as the potential energy term. The action for χ then becomes

$$\mathcal{L}_{\chi} = -\Omega^{-2} \tilde{g}^{\mu\nu} \partial_{\mu}\chi \partial_{\nu}\chi - \Omega^{-4} \mathcal{V}(\tilde{\phi}, \chi). \quad (6.42)$$

Since Ω is field dependent, it generates a non-trivial metric in the field space. Therefore, in this context, it is not advisable to work in the frame when the scalar field is minimally coupled to gravity.

6.5 Discussion and summary

In this chapter, we have considered a novel model for inflation with a non-minimally coupled *non-gravitating* scalar field. We find that the naive non-gravitating classical solution for the scalar field has space dependent profile which turns out to be singular. This singularity gives rise to a subtle but divergent contribution to the stress-energy tensor of the scalar field. Due to this contribution, the space dependent profile of the scalar field fails to be a non-gravitating solution. The divergent contribution to the stress-energy tensor has a delta function support at the location of the singularity of the classical solution. The divergence

turns out to be more severe than just the delta function because for any $\alpha \neq 0$, the coefficient multiplying the delta function also diverges. This problem is not specific only to the space dependent profile of the scalar field in the Friedmann universe. This problem exists for solutions in the Minkowski and the AdS backgrounds as well. We had attempted to determine the backreaction of this divergent contribution on the geometry. This gives rise to a set of coupled inhomogeneous non-linear partial differential equations. Several obvious and not-so-obvious ansatz fail to solve these equations.

Space independent profile for ϕ , however, does retain the non-gravitating property. We used this fact to write down a hybrid inflation model by coupling ϕ to another scalar field χ . Utility of this model is in the non-gravitating nature of the scalar field ϕ . Due to this property, inflation is completely driven by the cosmological constant, which is the value of the potential $\mathcal{V}(\phi, \chi)$ at $\chi = 0$. The expansion of the universe is independent of how ϕ rolls down and enters into the gravitating regime. Therefore, the value of the slow roll parameters is of little consequence. Although, after a conformal transformation, a non-minimally coupled scalar field can be brought into a minimally coupled form, we show that such a field redefinition is not very convenient. It is, in fact, more efficient to work with the non-minimal coupling.

Space dependent profiles for the inflaton have been considered earlier in the context of inflation as they lead to the formation of the topological defects (in this context, see, for instance, Refs. [235, 246] and references therein). We had strived to provide an alternative scenario wherein the inhomogeneities are generated by the classical field configuration of a non-gravitating scalar field. However, the proposal could not succeed as the inhomogeneous scalar field turned out to be gravitating and it may be worth exploring further in this direction. Nevertheless, our approach is novel in the fact that, unlike in all other models of inflation, the homogeneous part of the inflaton does not gravitate during the inflationary regime.

Chapter 7

Summary and outlook

This thesis work was aimed at studying certain issues related to the origin and evolution of cosmological perturbations during inflation and reheating, and the resulting signatures on the CMB. In what follows, we shall rapidly summarize the results obtained in this thesis and shall also briefly discuss a couple of problems that we believe require immediate attention.

7.1 Summary

We began with a brief overview of inflationary cosmology in the introductory chapter. In chapter 2, we had shown that the amplitude of the curvature perturbations induced by the tachyon can be enhanced or suppressed at super-Hubble scales if there exists a period of deviation from slow roll inflation. We had illustrated that the growth of the intrinsic entropy perturbation associated with the tachyon in the fast roll regime turns out to be responsible for the change in the amplitude of the curvature perturbations. We had shown that the power spectrum of the curvature perturbations evaluated in the long wavelength approximation matches the exact spectrum obtained numerically very well. Towards the end, we had discussed two simple analytical examples wherein the amplitude of the curvature perturbations induced by the canonical scalar field is enhanced at super-Hubble scales. We had also obtained the power spectrum evaluated analytically for these cases.

In chapter 3, we had investigated inflationary scenarios driven by a class of potentials that are similar in shape to certain MSSM potentials. We had discovered that these potentials lead to ‘punctuated inflation’, i.e. a scenario wherein a brief period of deviation from inflation is sandwiched between two stages of slow roll inflation. We had shown that punctuated

inflation leads to a step like feature in the scalar power spectrum. We had performed a Markov Chain Monte Carlo analysis to determine the values of the model parameters that provide the best fit to the recent WMAP 5-year data for the CMB angular power spectrum. We had found that an inflationary spectrum with a suppression of power at large scales with certain additional features leads to a much better fit of the observed data when compared to the best fit concordant model.

In chapter 4, we had studied the effects of punctuated inflation on the tensor power spectrum. We had illustrated that, in punctuated inflation, a drop in the scalar power on large scales is always accompanied by a rise in the tensor power and, hence, an even more pronounced increase in the tensor-to-scalar ratio on these scales. We had found that, in the examples from the canonical scalar field as well as the tachyonic inflationary models that we had considered, the tensor-to-scalar ratio actually exceeds well beyond unity over a small range of scales. We had also shown that such a rise in tensor-to-scalar ratio on large scales translates to a rapid increase in the angular power spectrum, C_ℓ^{BB} , of the B-mode polarization of the CMB at the low multipoles. However, the enhanced C_ℓ^{BB} is not at an observable level. We had highlighted the essential requirements for constructing a model of punctuated inflation that leads to lower power in the scalar power spectrum on large scales and also observable levels of C_ℓ^{BB} .

In chapter 5, we had investigated the problem of perturbative reheating and its effects on the evolution of the curvature perturbations in tachyonic inflationary model. We had shown that the transition from tachyon driven inflation to the radiation dominated epoch does not alter the amplitude of the total curvature perturbation of the system when the rate describing the decay of the inflaton into radiation is either a constant, or a function of the tachyon. We had also illustrated that, while the intrinsic entropy perturbation associated with the tachyon and the relative non-adiabatic pressure perturbation between the tachyon and radiation decay in a similar fashion before the transition to the radiation dominated epoch, the relative non-adiabatic pressure perturbation dies down extremely rapidly after the transition during the early stages of the radiation dominated epoch. We had discussed that it is these behavior which ensure that the amplitude of the curvature perturbations remain unaffected during reheating. We had also presented the corresponding results for the case of the canonical scalar field model.

In chapter 6, with the aim of providing another possible mechanism for the generation of perturbations, we had considered the behavior of an inhomogeneous, interacting, scalar field that is coupled non-minimally to gravity in the Friedmann background. For a specific choice of the interaction terms, we had found that the scalar field does not gravitate. We had noticed that the naive space dependent solution to the equations of motion leads to a singular field profile and, as a result, it gives a subtle contribution to the stress-energy tensor of the scalar field. We had illustrated that the emergence of the space dependent singular field profile is not specific to the Friedmann universe but it exists in the Minkowski and the AdS backgrounds as well. We had also studied the hybrid inflation scenario in this model when a purely time dependent non-gravitating field is coupled to another scalar field.

7.2 Outlook

In what follows, we shall describe a few problems that are a natural outcome of the issues related to inflation, reheating, and the CMB studied in this thesis.

Generating features in the primordial spectrum in tachyonic inflationary models

As we have repeatedly mentioned, while a power law inflationary perturbation spectrum fits the recent CMB data quite well, there exist a few data points which lie outside the cosmic variance. While the outlier at the quadrupole ($\ell = 2$) has cornered most of the attention, there exist (at least) two more outliers near $\ell = 22$ and 40, which have not been studied in equal measure [128, 162]. It will be interesting to construct examples of inflationary models involving non-canonical scalar fields (such as, say, a tachyon, or the DBI field) that result in features in the primordial spectrum and can possibly provide a better fit to the CMB data at the low multipoles.

Deviations from slow roll inflation and non-Gaussianities

It is well known that models of inflation driven by single, slowly rolling, canonical scalar fields generically predict a negligible amount of primordial non-Gaussianity (see, for instance, Ref. [248]). On the other hand, a re-analysis of the WMAP 3-year data seems to indicate a fairly large amount of non-Gaussianity [249]. A recent analysis of the WMAP 5-year data has also provided seemingly strong evidence for large non-Gaussianity [250, 251].

It has been noticed that periods of deviation from slow roll inflation that lead to features in the perturbation spectrum (so as to fit the CMB outliers) can also result in sufficiently large non-Gaussianities [252]. With more accurate measurements of the CMB anisotropies by forthcoming missions, such as PLANCK [197], non-Gaussianity will soon become a powerful tool to constrain inflationary models. In such a situation, it becomes important to construct better motivated and more natural inflationary potentials (both in canonical and non-canonical models of scalar fields) that generate features in the primordial spectrum while at the same time lead to larger non-Gaussianities.

Effects of reheating on curvature perturbations in warm inflationary scenarios

Warm inflationary scenarios consist of situations wherein the inflaton decays into radiation even during the inflationary epoch (see, for example, Ref. [253]). Such an effect is typically produced by explicitly coupling the inflaton to radiation as is done, for example, in achieving reheating in the cold inflationary scenario. It will be interesting to examine whether there can be a non-trivial evolution of the super-Hubble perturbations in warm inflationary scenarios, in particular, in the strong dissipative regime [254, 255].

Primordial black hole formation

While the scalar power spectrum is well constrained on cosmological scales by observations of the CMB anisotropies, the power spectrum at small scales can only be constrained by theoretical arguments essentially involving the formation and evaporation of primordial black holes (see, for example, Refs. [256]). Since a nearly scale invariant power spectrum fits the CMB data fairly well, inflation needs to be of the slow roll type when the cosmological scales leave the Hubble radius. However, there can be later periods of deviation from slow roll inflation, which can affect the extent of formation of primordial black holes. It will be worthwhile to systematically examine the effects of such deviations from slow roll inflation on the abundance of primordial black holes and the asymptotic, small scale, index of the perturbation spectrum [219]. In particular, it will be interesting to study the non-Gaussian effects due to the higher order interactions on the abundance of the primordial black holes [221].

We intend to study these issues in the near future.

Bibliography

- [1] E. W. Kolb and M. S. Turner, *The Early Universe* (Addison-Wesley, Redwood City, California, USA, 1990).
- [2] A. Linde, *Particle Physics and Inflationary Cosmology* (Harwood Academic, Chur, Switzerland, 1990).
- [3] A. R. Liddle and D. H. Lyth, *Cosmological Inflation and Large-Scale Structure* (Cambridge University Press, Cambridge, England, 1999); *The Primordial Density Perturbation: Cosmology, Inflation and the Origin of Structure* (Cambridge University Press, Cambridge, England, 2009).
- [4] S. Dodelson, *Modern Cosmology* (Academic Press, New York, USA, 2003).
- [5] V. F. Mukhanov, *Physical Foundations of Cosmology* (Cambridge University Press, Cambridge, England, 2005).
- [6] R. Durrer, *The Cosmic Microwave Background* (Cambridge University Press, Cambridge, England, 2008).
- [7] S. Weinberg, *Cosmology* (Oxford University Press, Oxford, England, 2008).
- [8] E. Hubble, *Proc. Nat. Acad. Sci.* **15**, 168 (1929).
- [9] W. L. Freedman *et al.*, *Astrophys. J.* **553**, 47 (2001).
- [10] A. A. Penzias and R. W. Wilson, *Astrophys. J.* **142**, 419 (1965).
- [11] J. C. Mather, D. J. Fixsen, R. A. Shafer, C. Mosier and D. T. Wilkinson, *Astrophys. J.* **512**, 511 (1999).

BIBLIOGRAPHY

- [12] C. L. Bennett *et al.*, *Astrophys. J.* **436**, 423 (1994).
- [13] E. L. Wright, G. F. Smoot, C. L. Bennett and P. M. Lubin, *Astrophys. J.* **436**, 443 (1994).
- [14] E. L. Wright, C. L. Bennett, K. Gorski, G. Hinshaw and G.F. Smoot, *Astrophys. J.* **464**, L21 (1996).
- [15] M. Tegmark, *Astrophys. J. Lett.* **464**, L35 (1996).
- [16] H. V. Peiris *et al.*, *Astrophys. J. Suppl.* **148**, 213 (2003).
- [17] G. Hinshaw *et al.*, *Astrophys. J. Suppl.* **170**, 288 (2007).
- [18] D. N. Spergel *et al.*, *Astrophys. J. Suppl.* **170**, 377 (2007).
- [19] M. R. Nolta *et al.*, *Astrophys. J. Suppl.* **180**, 296 (2009).
- [20] J. Dunkley *et al.*, *Astrophys. J. Suppl.* **180**, 306 (2009).
- [21] E. Komatsu *et al.*, *Astrophys. J. Suppl.* **180**, 330 (2009).
- [22] G. Hinshaw *et al.*, *Astrophys. J. Suppl.* **180**, 225 (2009).
- [23] F. Iocco, G. Mangano, G. Miele, O. Pisanti and P. D. Serpico, *Phys. Rep.* **472**, 1 (2009).
- [24] A. Coc, E. Vangioni-Flam, P. Descouvemont, A. Adahchour and C. Angulo, *Astrophys. J.* **600**, 544 (2004).
- [25] J. Yadav, S. Bharadwaj, B. Pandey and T. R. Seshadri, *Mon. Not. Roy. Astron. Soc.* **364**, 601 (2005).
- [26] A. Friedmann, *Z. Phys.* **10**, 377 (1922) [*Gen. Rel. Grav.* **31**, 1991 (1999)].
- [27] A. Friedmann, *Z. Phys.* **21**, 326 (1924) [*Gen. Rel. Grav.* **31**, 2001 (1999)].
- [28] H. P. Robertson, *Astrophys. J.* **82**, 248 (1935).
- [29] H. P. Robertson, *Astrophys. J.* **83**, 187 (1936).
- [30] H. P. Robertson, *Astrophys. J.* **83**, 257 (1936).

- [31] A. G. Walker, Proc. London Math. Soc. **42** 90 (1937).
- [32] M. Kowalski *et al.*, Astrophys. J. **686**, 749 (2008).
- [33] A. H. Guth, Phys. Rev. D **23**, 347 (1981).
- [34] A. D. Linde, Phys. Lett. B **108**, 389 (1982).
- [35] A. J. Albrecht and P. J. Steinhardt, Phys. Rev. Lett. **48**, 1220 (1982).
- [36] S. Dodelson and L. Hui, Phys. Rev. Lett. **91**, 131301 (2003).
- [37] A. R. Liddle and S. M. Leach, Phys. Rev. D **68**, 103503 (2003).
- [38] C. Kiefer, D. Polarski and A. A. Starobinsky, Int. J. Mod. Phys. D **7**, 455 (1998).
- [39] C. Kiefer, I. Lohmar, D. Polarski and A. A. Starobinsky, Class. Quant. Grav. **24**, 1699 (2007).
- [40] J. Martin, Lect. Notes Phys. **738**, 193 (2008).
- [41] C. Kiefer and D. Polarski, Adv. Sci. Lett. **2**, 164 (2009).
- [42] A. R. Liddle, P. Parsons and J. D. Barrow, Phys. Rev. D **50**, 7222 (1994).
- [43] L. Sriramkumar, arXiv:0904.4584 [astro-ph.CO].
- [44] A. D. Linde, Phys. Lett. B **129**, 177 (1983).
- [45] K. Freese, J. A. Frieman and A. V. Olinto, Phys. Rev. Lett. **65**, 3233 (1990).
- [46] A. D. Linde, Phys. Rev. D **49**, 748 (1994).
- [47] A. R. Liddle, A. Mazumdar and F. E. Schunck, Phys. Rev. D **58**, 061301 (1998).
- [48] S. Dimopoulos, S. Kachru, J. McGreevy and J. G. Wacker, JCAP **0808**, 003 (2008).
- [49] A. Sen, JHEP **9910**, 008 (1999).
- [50] M. Garousi, Nucl. Phys. B **584** 284, (2000).
- [51] E. Bergshoeff, M. de Roo, T. de Wit, E. Eyras and S. Panda, JHEP **0005**, 009 (2000).

BIBLIOGRAPHY

- [52] J. Kluson, Phys. Rev. D **62**, 126003 (2000).
- [53] A. Sen, JHEP **0204**, 048 (2002).
- [54] A. Sen, JHEP **0207**, 065 (2002).
- [55] M. Sami, P. Chingangbam and T. Qureshi, Phys. Rev. D **66**, 043530 (2002).
- [56] P. Chingangbam, S. Panda and A. Deshamukhya, JHEP **0502**, 052 (2005).
- [57] E. Silverstein and D. Tong, Phys. Rev. D **70**, 103505 (2004).
- [58] M. Alishahiha, E. Silverstein and D. Tong, Phys. Rev. D **70**, 123505 (2004).
- [59] C. Armendariz-Picon, T. Damour and V. F. Mukhanov, Phys. Lett. B **458**, 209 (1999).
- [60] J. Garriga and V. F. Mukhanov, Phys. Lett. B **458**, 219 (1999).
- [61] A. A. Starobinsky, Phys. Lett. B **91**, 99 (1980).
- [62] A. Albrecht, P. J. Steinhardt, M. S. Turner and F. Wilczek, Phys. Rev. Lett. **48**, 1437 (1982).
- [63] M. S. Turner, Phys. Rev. D **28**, 1243 (1983).
- [64] E. W. Kolb, A. Notari and A. Riotto, Phys. Rev. D **68**, 123505 (2003).
- [65] F. Di Marco, F. Finelli and A. Gruppuso, Phys. Rev. D **76**, 043530 (2007).
- [66] A. Cerioni, F. Di Marco, F. Finelli and A. Gruppuso, Phys. Rev. D **78**, 021301(R) (2008).
- [67] J. H. Traschen and R. Brandenberger, Phys. Rev. D **42**, 2491 (1990).
- [68] A. D. Dolgov and D. P. Kirilova, Sov. J. Nucl. Phys. **51**, 172 (1990).
- [69] L. Kofman, A. D. Linde and A. A. Starobinsky, Phys. Rev. Lett. **73**, 3195 (1994).
- [70] Y. Shtanov, J. H. Traschen and R. H. Brandenberger, Phys. Rev. D **51**, 5438 (1995).
- [71] L. Kofman, A. D. Linde and A. A. Starobinsky, Phys. Rev. D **56**, 3258 (1997).
- [72] B. A. Bassett and F. Tamburini, Phys. Rev. Lett. **81**, 2630 (1998).

- [73] B. A. Bassett, C. Gordon, R. Maartens and D. I. Kaiser, Phys. Rev. D **61**, 061302(R) (2000).
- [74] B. A. Bassett and F. Viniegra, Phys. Rev. D **62**, 043507 (2000).
- [75] B. A. Bassett and S. Tsujikawa, Phys. Rev. D **63**, 123503 (2001).
- [76] P. Ivanov, Phys. Rev. D **61**, 023505 (1999).
- [77] F. Finelli and R. Brandenberger, Phys. Rev. Lett. **82**, 1362 (1999).
- [78] F. Finelli and R. Brandenberger, Phys. Rev. D **62**, 083502 (2000).
- [79] R. Easther and M. Parry, Phys. Rev. D **62**, 103503 (2000).
- [80] S. Tsujikawa and B. A. Bassett, Phys. Lett. B **536**, 9 (2002).
- [81] T. Suyama and S. Yokoyama, Class. Quant. Grav. **24**, 1615 (2007).
- [82] P. R. Anderson, C. Molina-Paris, D. Evanich and G. B. Cook, Phys. Rev. D **78**, 083514 (2008).
- [83] D. Battefeld and S. Kawai, Phys. Rev. D **77**, 123507 (2008).
- [84] D. Battefeld, arXiv:0809.3455 [astro-ph].
- [85] D. H. Lyth and D. Wands, Phys. Lett. B **524**, 5 (2002).
- [86] D. H. Lyth, C. Ungarelli and D. Wands, Phys. Rev. D **67**, 023503 (2003).
- [87] S. Matarrese and A. Riotto, JCAP **0308**, 007 (2003).
- [88] A. Mazumdar and M. Postma, Phys. Lett. B **573**, 5 (2003).
- [89] S. Tsujikawa, Phys. Rev. D **68**, 083510 (2003).
- [90] G. Dvali, A. Gruzinov and M. Zaldarriaga, Phys. Rev. D **69**, 023505 (2004).
- [91] K. Dimopoulos and D. H. Lyth, Phys. Rev. D **69**, 123509 (2004).
- [92] D. A. Steer and F. Vernizzi, Phys. Rev. D **70**, 043527 (2004).
- [93] G. N. Felder, L. Kofman and A. Starobinsky, JHEP **0209**, 026 (2002).

BIBLIOGRAPHY

- [94] H. Kodama and M. Sasaki, Prog. Theor. Phys. Suppl. **78**, 1 (1984).
- [95] V. F. Mukhanov, H. A. Feldman and R. H. Brandenberger, Phys. Rep. **215**, 203 (1992).
- [96] J. E. Lidsey, A. Liddle, E. W. Kolb, E. J. Copeland, T. Barreiro and M. Abney, Rev. Mod. Phys. **69**, 373 (1997).
- [97] B. Bassett, S. Tsujikawa and D. Wands, Rev. Mod. Phys. **78**, 537 (2006).
- [98] K. A. Malik and D. Wands, Phys. Rep. **475**, 1 (2009).
- [99] S. M. Leach and A. R. Liddle, Phys. Rev. D **63**, 043508 (2001).
- [100] S. M. Leach, M. Sasaki, D. Wands and A. R. Liddle, Phys. Rev. D **64**, 023512 (2001).
- [101] F. Quevedo, Class. Quant. Grav. **19**, 5721 (2002).
- [102] K. Enqvist, A. Jokinen, A. Mazumdar, T. Multamaki and A. Vaihkonen, JCAP **0503**, 010 (2005).
- [103] K. Enqvist, A. Jokinen, A. Mazumdar, T. Multamaki and A. Vaihkonen, JHEP **0508**, 084 (2005).
- [104] M. R. Garousi, JHEP **0312**, 036 (2003).
- [105] M. R. Garousi, M. Sami and S. Tsujikawa, Phys. Rev. D **70**, 043536 (2004).
- [106] M. R. Garousi, M. Sami and S. Tsujikawa, Phys. Lett. B **606**, 1 (2005).
- [107] M. R. Garousi, M. Sami and S. Tsujikawa, Phys. Rev. D **71**, 083005 (2005).
- [108] P. Chingangbam and T. Qureshi, Int. J. Mod. Phys. A **20**, 6083 (2005).
- [109] M. Sasaki, Prog. Theor. Phys. **70**, 394 (1983).
- [110] M. Sasaki, Prog. Theor. Phys. **76**, 1036 (1986).
- [111] J. M. Bardeen, Phys. Rev. D **22**, 1882 (1980).
- [112] V. F. Mukhanov, JETP Lett. **41**, 493 (1985).

- [113] J. Martin, Lect. Notes Phys. **669**, 199 (2005).
- [114] T. Bunch and P. C. W. Davies, Proc. Roy. Soc. Lond. A **360**, 117 (1978).
- [115] E. D. Stewart and D. H. Lyth, Phys. Letts. B **302**, 171 (1993).
- [116] J. C. Hwang and H. Noh, Phys. Rev. D **54**, 1460 (1996).
- [117] L. Sriramkumar and T. Padmanabhan, Phys. Rev. D **71**, 103512 (2005).
- [118] C. Gordon, D. Wands, B. A. Bassett and R. Maartens, Phys. Rev. D **63**, 023506 (2001).
- [119] D. J. Schwarz, C. A. Terrero-Escalante, A. A. Garcia, Phys. Lett. B **517**, 243 (2001).
- [120] D. Roberts, A. R. Liddle, and D. H. Lyth, Phys. Rev. D **51**, 4122 (1995).
- [121] D. S. Salopek, J. R. Bond and J. M. Bardeen, Phys. Rev. D **40**, 1753 (1989).
- [122] C. Ringeval, Lect. Notes Phys. **738**, 243 (2008).
- [123] R. K. Jain, P. Chingangbam and L. Sriramkumar, JCAP **0710**, 003 (2007).
- [124] R. Easther, Class. Quantum Grav. **13**, 1775 (1996).
- [125] J. Martin and D. J. Schwarz, Phys. Lett. B **500**, 1 (2001).
- [126] C. R. Contaldi, M. Peloso, L. Kofman and A. Linde, JCAP **0307**, 002 (2003).
- [127] G. Nicholson, C. R. Contaldi, JCAP **0801**, 002 (2008).
- [128] L. Covi, J. Hamann, A. Melchiorri, A. Slosar and I. Sorbera, Phys. Rev. D **74**, 083509 (2006).
- [129] J. Hamann, L. Covi, A. Melchiorri and A. Slosar, Phys. Rev. D **76**, 023503 (2007).
- [130] A. Shafieloo and T. Souradeep, Phys. Rev. D **70**, 043523 (2004).
- [131] A. Shafieloo, T. Souradeep, P. Manimaran, P. K. Panigrahi and R. Rangarajan, Phys. Rev. D **75**, 123502 (2007).
- [132] I.J. O'Dwyer *et al.*, Astrophys. J. **617**, L99 (2004).

BIBLIOGRAPHY

- [133] J. Magueijo and R. D. Sorkin, *Mon. Not. Roy. Astron. Soc. Lett.* **377**, L39 (2007).
- [134] C.-G. Park, C. Park and J. R. Gott III, *Astrophys. J.* **660**, 959 (2007).
- [135] L.-Y. Chiang, P. D. Naselsky and P. Coles, *Astrophys. J.* **694**, 339 (2009).
- [136] A. A. Starobinsky, *Sov. Phys. JETP Lett.* **55**, 489 (1992).
- [137] Y. P. Jing and L. Z. Fang, *Phys. Rev. Lett.* **73**, 1882 (1994).
- [138] J. Yokoyama, *Phys. Rev. D* **59**, 107303 (1999).
- [139] B. Feng and X. Zhang, *Phys. Lett. B* **570**, 145 (2003).
- [140] G. Efstathiou, *Mon. Not. R. Astron. Soc.* **343**, L95 (2003).
- [141] J. P. Luminet *et al.*, *Nature (London)* **425**, 593 (2003).
- [142] A. Hajian and T. Souradeep, *Astrophys. J. Lett.* **597**, L5 (2003).
- [143] A. Hajian, T. Souradeep and N. Cornish, *Astrophys. J.* **618**, L63 (2005).
- [144] A. Hajian and T. Souradeep, *Phys. Rev. D* **74**, 123521 (2006).
- [145] M. Kawasaki and F. Takahashi, *Phys. Lett. B* **570**, 151 (2003).
- [146] M. Kawasaki, F. Takahashi and T. Takahashi, *Phys. Lett. B* **605**, 223 (2005).
- [147] C. Gordon and W. Hu, *Phys. Rev. D* **70**, 083003 (2004).
- [148] J. M. Cline, P. Crotty and J. Lesgourgues, *JCAP* **0309**, 010 (2003).
- [149] T. Moroi and T. Takahashi, *Phys. Rev. Lett.* **92**, 091301 (2004).
- [150] P. Hunt and S. Sarkar, *Phys. Rev. D* **70**, 103518 (2004).
- [151] P. Hunt and S. Sarkar, *Phys. Rev. D* **76**, 123504 (2007).
- [152] S. Shankaranarayanan and L. Sriramkumar, *Phys. Rev. D* **70**, 123520 (2004).
- [153] S. Shankaranarayanan and L. Sriramkumar, *arXiv:hep-th/0410072*.

- [154] R. Sinha and T. Souradeep, Phys. Rev. D **74**, 043518 (2006).
- [155] D. Boyanovsky, H. J. de Vega and N. G. Sanchez, Phys. Rev. D **74**, 123006 (2006).
- [156] D. Boyanovsky, H. J. de Vega and N. G. Sanchez, Phys. Rev. D **74**, 123007 (2006).
- [157] J. F. Donoghue, K. Dutta and A. Ross, arXiv:astro-ph/0703455.
- [158] B. A. Powell and W. H. Kinney, Phys. Rev. D **76**, 063512 (2007).
- [159] M. Joy, V. Sahni, A. A. Starobinsky, Phys. Rev. D **77**, 023514 (2008).
- [160] M. Joy, A. Shafieloo, V. Sahni, A. A. Starobinsky, arXiv:0807.3334 [astro-ph].
- [161] C. Destri, H. J. de Vega and N. G. Sanchez, Phys. Rev. D **78**, 023013 (2008).
- [162] M. J. Mortonson, C. Dvorkin, H. V. Peiris and W. Hu, Phys. Rev. D **79**, 103519 (2009).
- [163] S. L. Bridle, A. M. Lewis, J. Weller and G. Efstathiou, Mon. Not. Roy. Astron. Soc. **342**, L72 (2003).
- [164] P. Mukherjee and Y. Wang, Astrophys. J. **599**, 1 (2003).
- [165] S. Hannestad, JCAP **0404**, 002 (2004).
- [166] A. Shafieloo and T. Souradeep, Phys. Rev. D **78**, 023511 (2008).
- [167] D. Tocchini-Valentini, Y. Hoffman and J. Silk, Mon. Not. Roy. Astron. Soc. **367**, 1095 (2006).
- [168] R. Nagata and J. Yokoyama, Phys. Rev. D **79**, 043010 (2009).
- [169] G. Nicholson and C. R. Contaldi, arXiv:0903.1106 [astro-ph.CO].
- [170] H. M. Hodges, G. R. Blumenthal, L. A. Kofman and J. R. Primack, Nucl. Phys. B **335**, 197 (1990).
- [171] V. F. Mukhanov and M. I. Zelnikov, Phys. Lett. B **263**, 169 (1991).
- [172] T. Souradeep, Ph.D. Thesis, University of Pune (Inter-University Centre for Astronomy and Astrophysics), Pune, India (1995).

BIBLIOGRAPHY

- [173] J. A. Adams, G. G. Ross and S. Sarkar, Nucl. Phys. B **503**, 405 (1997).
- [174] J. Lesgourgues, Nucl. Phys. B **582**, 593 (2000).
- [175] J. Barriga, E. Gaztanaga, M. Santos and S. Sarkar, Mon. Not. Roy. Astron. Soc. **324**, 977 (2001).
- [176] J. Barriga, E. Gaztanaga, M. Santos and S. Sarkar, Nucl. Phys. Proc. Suppl. **95**, 66 (2001).
- [177] J. A. Adams, B. Cresswell, R. Easter, Phys. Rev. D **64**, 123514 (2001).
- [178] J.-O. Gong, JCAP **0507**, 015 (2005).
- [179] R. Allahverdi, J. Garcia-Bellido, K. Enqvist and A. Mazumdar Phys. Rev. Lett. **97**, 191304 (2006).
- [180] R. Allahverdi, K. Enqvist, J. Garcia-Bellido, A. Jokinen and A. Mazumdar, JCAP **0706**, 019 (2007).
- [181] J. C. B. Sanchez, K. Dimopoulos and D. H. Lyth, JCAP **0701**, 015 (2007).
- [182] R. Allahverdi, A. Mazumdar and T. Multamaki, arXiv:0712.2031 [astro-ph].
- [183] L. A. Kofman, A. D. Linde and A. A. Starobinsky, Phys. Lett. B **157**, 361 (1985).
- [184] J. Silk and M. S. Turner, Phys. Rev. D **35**, 419 (1987).
- [185] M. S. Turner, J. V. Villumsen, N. Vittorio, J. Silk and R. Juszkiewicz, Astrophys. J. **323**, 423 (1987).
- [186] D. Polarski and A. A. Starobinsky, Nucl. Phys. B **385**, 623 (1992).
- [187] D. Polarski, Phys. Rev. D **49**, 6319 (1994).
- [188] D. Polarski and A. A. Starobinsky, Phys. Lett. B **356**, 196 (1995).
- [189] D. Langlois, Phys. Rev. D **59**, 123512 (1999).
- [190] S. Tsujikawa, D. Parkinson and B. A. Bassett, Phys. Rev. D **67**, 083516 (2003).
- [191] N. Itzhaki and E. D. Kovetz, JHEP **0710**, 054 (2007).

- [192] A. Ashoorioon and A. Krause, arXiv:hep-th/0607001.
- [193] A. Ashoorioon, A. Krause and K. Turzynski, JCAP **0902**, 014 (2009).
- [194] L. Alabidi and D. H. Lyth, JCAP **0605**, 016 (2006).
- [195] S. A. Kim and A. R. Liddle, Phys. Rev. D **74**, 023513 (2006).
- [196] J.-O. Gong, Phys. Rev. D **75**, 043502 (2007).
- [197] See, <http://www.rssd.esa.int/index.php?project=Planck>.
- [198] See, <http://cmbpol.uchicago.edu/>.
- [199] A. Lewis, Phys. Rev. D **78**, 023002 (2008).
- [200] A. Lewis, A. Challinor and A. Lasenby, Astrophys. J. **538**, 473 (2000).
- [201] See, <http://camb.info/>.
- [202] See, <http://lambda.gsfc.nasa.gov/>
- [203] A. Lewis and S. Bridle, Phys. Rev. D **66**, 103511 (2002).
- [204] See, <http://cosmologist.info/cosmomc/>.
- [205] R. K. Jain, P. Chingangbam, J.-O. Gong, L. Sriramkumar and T. Souradeep, JCAP **0901**, 009 (2009).
- [206] R. Saha, P. Jain and T. Souradeep, Astrophys. J. **645**, L89 (2006).
- [207] R. Saha, S. Prunet, P. Jain and T. Souradeep, Phys. Rev. D **78**, 023003 (2008).
- [208] P. K. Samal, R. Saha, J. Delabrouille, S. Prunet, P. Jain and T. Souradeep, arXiv:0903.3634 [astro-ph.CO].
- [209] A. A. Starobinsky, Sov. Astron. Lett. **11**, 133 (1985).
- [210] R. Davis, H. M. Hodges, G. F. Smoot, P. J. Steinhardt and M. S. Turner, Phys. Rev. Lett. **69**, 1856 (1992).

BIBLIOGRAPHY

- [211] T. Souradeep and V. Sahni, *Mod. Phys. Lett. A* **7**, 3541 (1992).
- [212] B. C. Friedman, A. Cooray and A. Melchiorri, *Phys. Rev. D* **74**, 123509 (2006).
- [213] W. H. Kinney, arXiv:0902.1529 [astro-ph.CO].
- [214] G. Felder, A. Frolov, L. Kofman and A. Linde, *Phys. Rev. D* **66**, 023507 (2002).
- [215] R. K. Jain, P. Chingangbam, L. Sriramkumar and T. Souradeep, arXiv:0904.2518 [astro-ph.CO].
- [216] S. Dodelson *et al.*, arXiv:0902.3796 [astro-ph.CO].
- [217] E. Bugaev and P. Klimai, *Phys. Rev. D* **78**, 063515 (2008).
- [218] I. Zaballa, A. M. Green, K. A. Malik and M. Sasaki, *JCAP* **0703**, 010 (2007).
- [219] S. Chongchitnan and G. Efstathiou, *JCAP* **0701**, 011 (2007).
- [220] K. Kohri, D. H. Lyth and A. Melchiorri, *JCAP* **0804**, 038 (2008).
- [221] R. Saito, J. Yokoyama and R. Nagata, *JCAP* **0806**, 024 (2008).
- [222] C. Campuzano, S. del Campo and R. Herrera, *Phys. Rev. D* **72**, 083515 (2005).
- [223] C. Campuzano, S. del Campo and R. Herrera, *Phys. Lett. B* **633**, 149 (2006).
- [224] C. Campuzano, S. del Campo and R. Herrera, *JCAP* **0606** 017, (2006).
- [225] V. H. Cardenas, *Phys. Rev. D* **73**, 103512 (2006).
- [226] R. Herrera, S. del Campo and C. Campuzano, *JCAP* **0610**, 009 (2006).
- [227] S. del Campo, R. Herrera and J. Saavedra, *Eur. Phys. J. C* **59**, 913 (2009).
- [228] M. Bastero-Gil and A. Berera, *Int. J. Mod. Phys. A* **24**, 2207 (2009).
- [229] K. A. Malik, D. Wands and C. Ungarelli, *Phys. Rev. D* **67**, 063516 (2003).
- [230] K. A. Malik, arXiv:astro-ph/0101563.
- [231] K. A. Malik and D. Wands, *JCAP* **0502**, 007 (2005).

- [232] R. K. Jain, P. Chingangbam and L. Sriramkumar, arXiv:0902.1067 [astro-ph.CO].
- [233] N. Bartolo, P. S. Corasaniti, A. R. Liddle and M. Malquarti, Phys. Rev. D **70**, 043532 (2004).
- [234] A. Deshamukhya and S. Panda, arXiv:0901.0471 [hep-th].
- [235] A. Vilenkin and E. P. S. Shellard, *Cosmic Strings and Other Topological Defects* (Cambridge University Press, Cambridge, England, 1994).
- [236] R. Durrer, M. Kunz and A. Melchiorri, Phys. Rept. **364**, 1 (2002).
- [237] J. Polchinski, *String theory, Vol. 1: An introduction to the bosonic string* (Cambridge University Press, Cambridge, England, 1998).
- [238] J. Polchinski, *String theory, Vol. 2: Superstring theory and beyond* (Cambridge University Press, Cambridge, England, 1998).
- [239] M. R. Douglas and S. Kachru, Rev. Mod. Phys. **79**, 733 (2007).
- [240] J. McDonald, JHEP **0212**, 029 (2002).
- [241] A. Riotto, arXiv:hep-ph/0210162.
- [242] R. Holman and J. A. Hutasoit, arXiv:hep-th/0603246.
- [243] E. Ayon-Beato, C. Martinez, R. Troncoso and J. Zanelli, Phys. Rev. D **71**, 104037 (2005).
- [244] D. A. Demir and B. Pulice, Phys. Lett. B **638**, 1 (2006).
- [245] N. Banerjee, R. K. Jain and D. P. Jatkar, Gen. Rel. Grav. **40**, 93 (2008).
- [246] R. Jeannerot and M. Postma, JHEP **0505**, 071 (2005).
- [247] V. Faraoni, E. Gunzig and P. Nardone, Fund. Cosmic Phys. **20**, 121 (1999).
- [248] J. M. Maldacena, JHEP **0305**, 013 (2003).
- [249] A. P. S. Yadav and B. D. Wandelt, Phys. Rev. Lett. **100**, 181301 (2008).
- [250] K. M. Smith, L. Senatore and M. Zaldarriaga, arXiv:0901.2572 [astro-ph].

BIBLIOGRAPHY

- [251] L. Senatore, K. M. Smith and M. Zaldarriaga, arXiv:0905.3746 [astro-ph.CO].
- [252] X. Chen, R. Easther and E. A. Lim, JCAP **0706**, 023 (2007).
- [253] J. C. B. Sanchez, M. Bastero-Gil, A. Berera and K. Dimopoulos, Phys. Rev. D **77**, 123527 (2008).
- [254] T. Matsuda, JCAP **0906**, 002 (2009).
- [255] C. Graham and I. G. Moss, arXiv:0905.3500 [astro-ph.CO].
- [256] J. Yokoyama, Prog. Theor. Phys. Suppl. **136**, 338 (1999).